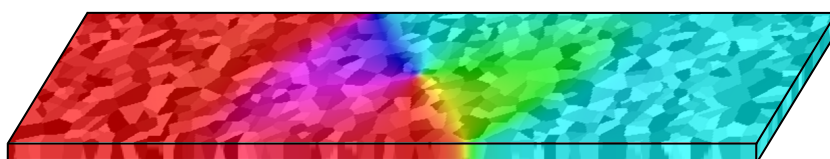


# MAGNETIC DISORDER AND THERMAL FLUCTUATIONS IN DOMAIN WALL MOTION AND NANOPARTICLE DYNAMICS



Jonathan Leliaert



FACULTY OF SCIENCES

# MAGNETIC DISORDER AND THERMAL FLUCTUATIONS IN DOMAIN WALL MOTION AND NANOPARTICLE DYNAMICS

Doctoral thesis  
by Jonathan Leliaert

Thesis submitted to obtain the degree of  
Doctor of Science: Physics

Public defense: May, 3th, 2016 at  
Department of Solid State Sciences  
Faculty of Sciences  
Ghent University

## **Promotors:**

prof. dr. Bartel Van Waeyenberge (promotor)  
prof. dr. ir. Luc Dupré (co-promotor)

Ghent University, Belgium  
Ghent University, Belgium

## **Examination Commission:**

Prof. dr. J. Ryckebusch (chairman)  
Prof. dr. ir. H. Vrielinck (secretary)  
Prof. dr. ir. K. Neyts  
Prof. dr. M. Milosevic  
Dr. A. Vansteenkiste  
Dr. ir. B. Van de Wiele  
Dr. G. Durin  
Dr. F. Wiekhorst

Ghent University, Belgium  
Ghent University, Belgium  
Ghent University, Belgium  
University of Antwerp, Belgium  
Ghent University, Belgium  
Ghent University, Belgium  
Istituto Nazionale di Ricerca Metrologica, Italy  
Physikalisch-Technische Bundesanstalt, Germany



*Voor mijn ouders, Geert en Ingrid  
voor mijn broer Matthias  
en mijn liefste Annelies*



---

## Dankwoord (*Acknowledgements*)

---

Ik wil beginnen met mijn promotoren, Bartel en Luc te bedanken voor alle kansen en hulp die ze mij de voorbije vier jaar geboden hebben. Zonder jullie was dit doctoraat er nooit geweest.

Binnen beide groepen waarin ik werkte heb ik ook het geluk gehad om heel goed begeleid te worden. Arne en Ben, bedankt voor alle bijdrages die jullie, elk op je eigen manier, geleverd hebben aan mijn doctoraat en de omkadering ervan.

*Next to the people directly involved with my work in Ghent I'm also indebted to all people who collaborated with us. Within this set of people, I'd like to especially mention (again in alphabetical order) Dietmar, Frank, Gianfranco, Lasse and Uwe.*

*Next, I would like to thank my (former) colleagues from S1 for the atmosphere during lunch and in the office. Especially Mykola's "educational moments" and Mathias' cynism, which is as rich as his coffee, have left a lasting impression. Among these colleagues, I have to especially thank Henk and Jevgenij for performing FMR measurements of nanoparticles, which taught me a lot about the difference between theory and experiments. I would also like to thank my colleagues from the technicum/913 for the wonderful times.*

*Ich möchte mich auch gerne bei meinen Kolleg(inn)en aus Berlin für die Gastlichkeit und die freundschaftliche Atmosphäre bedanken. Wir haben uns während unserer Bleibe wirklich gefreut und werden immer mit Freudigkeit zurückdenken an den Ausflug, den Picknick und die Biergartenbesuche. Außerdem freut es uns auch besonders, dass wir jetzt wissen, wo sich der beste Döner vom Bahnhof Zoo befindet.*

*Next, I'd like to thank all the members of the Jury, who tediously read my thesis and contributed to it with interesting questions and remarks. Here I'd like to especially thank Jan who guided me towards this PhD position when he was the promotor of my master thesis.*

*I should also thank BOF (Ghent University) for the projects which funded this research*

*and the FWO (Belgium), CWO (Ghent University) and PTB (Germany) for funding my mobility. I'm also grateful for computational resources provided by the Flemish Supercomputer centre (Belgium), INRIM (Italy), CSC (Finland) and Aalto University (Finland).*

Omdat de boog ook niet altijd gespannen kon staan is hier, net als in mijn hart, plaats voor alle vrienden die mij de laatste jaren altijd hebben kunnen doen genieten van alle ontspannende momenten op kot, op café, op de trein, op de krachtbal, op quizzen, . . .

Vervolgens wil ik ook mijn schoonouders en -zus bedanken voor de steun en interesse.

Mijn grootouders, marraine, opa, peter, en oma, wil ik ook bedanken om mij al van kleins af aan altijd met veel trots en aandacht te steunen in alles wat ik nastreefde.

Matthias, beste broer en dito man, onze diepe vriendschap waardeer ik bijzonder.

Mijn ouders, zonder wie niets van dit alles was mogelijk geweest, wil ik bedanken om alles mogelijk te maken op elk denkbaar gebied van mijn leven.

Als laatste wil ik mijn toekomstig vrouwtje, Annelies, nog het meest van iedereen bedanken om mij altijd te steunen, er voor mij te zijn en mij te begrijpen.

Jonathan Leliaert,  
Gent, 20 April 2016.

# Contents

<b>Contents</b>	<b>vii</b>
<b>1 Introduction</b>	<b>9</b>
1.1 The origin of ferromagnetism . . . . .	9
1.2 Historical overview of micromagnetism . . . . .	11
1.3 Micromagnetic theory . . . . .	14
<b>2 Domain wall motion</b>	<b>27</b>
2.1 Introduction . . . . .	27
2.2 Simulating disordered nanowires . . . . .	50
2.3 Domain wall motion in disordered nanowires . . . . .	56
<b>3 Domain wall motion at finite temperature</b>	<b>65</b>
3.1 Introduction . . . . .	65
3.2 Domain wall motion in non-disordered nanowires . . . . .	71
3.3 Domain wall motion in disordered nanowires . . . . .	78
<b>4 Magnetic nanoparticles</b>	<b>91</b>
4.1 Introduction . . . . .	91
4.2 Vinamax . . . . .	100
4.3 The Néel relaxation time constant . . . . .	117
4.4 Thermal magnetic noise spectra of nanoparticle ensembles . . . . .	124
<b>5 Conclusions and Outlook</b>	<b>131</b>
5.1 Conclusions . . . . .	131
5.2 Outlook . . . . .	133
<b>A Solvers</b>	<b>137</b>
<b>Bibliography</b>	<b>153</b>
<b>List of constants and symbols</b>	<b>173</b>
<b>Index</b>	<b>179</b>
<b>publications</b>	<b>183</b>



---

## Samenvatting (in Dutch)

---

In een wereld waarin computeronderdelen steeds kleiner en sneller worden, spelen magnetische structuren een belangrijke rol. Bijvoorbeeld, in klassieke harde schijven wordt data opgeslagen als uniform gemagnetiseerde gebiedjes (domeinen) op magnetische schijven. De uitdaging is om deze gebieden zo klein mogelijk te maken en zo snel mogelijk te kunnen schrijven en uitlezen.

Iets futuristischer is een alternatief voor huidige geheugens dat een aantal jaar geleden werd voorgesteld: het racetrack-geheugen. In deze toepassing wordt data opgeslagen in de richting van de magnetisatie van de grensgebieden tussen twee domeinen, genaamd domeinmuren. Deze domeinmuren kunnen door nanodraden met een typische doorsnede van enkele tientallen nanometer bewogen worden aan voldoende hoge snelheden om competitief te zijn met huidige geheugentechnologieën.

Een ander type magnetische structuren met veel toepassingen zijn magnetische nanodeeltjes. Deze deeltjes bestaan uit een magnetische kern van enkele (tientallen) nanometer diameter en eventueel een niet-magnetische coating die de deeltjes kan verhinderen om te clusteren of die ze bio-compatibel kan maken. De deeltjes worden onder meer gebruikt in biomedische toepassingen zoals hyperthermie, gerichte toediening van medicijnen en medische beeldvorming.

In geïdealiseerde systemen zonder wanorde werken al deze toepassingen probleemloos. In werkelijkheid is er echter altijd wanorde aanwezig. Wanorde is een breed begrip en hoeft ook niet noodzakelijk een negatieve invloed te hebben. In dit doctoraatsproefschrift zullen verschillende magnetische systemen met diverse vormen van wanorde besproken worden. Hieronder wordt een kort overzicht gegeven.

Bij het onderzoeken van bovenvermelde systemen zijn micromagnetische simulaties een onontbeerlijk hulpmiddel. Micromagnetisme is de theorie die de magnetische dynamica op nanometer lengteschaal en picoseconde tijdschaal beschrijft. Enerzijds is deze schaal voldoende groot om kwantummechanische effecten te mogen verwaarlozen en de magnetisatie als een continu

vectorveld te benaderen. Anderzijds is ze kleiner dan de macroschaal waarop de magnetisatie beschreven wordt door de wetten van Maxwell. Op deze tussenliggende schaal vinden we magnetische structuren en dynamica die interessant zijn voor verschillende toepassingen waarvan hierboven enkele kort aangehaald werden. In Hoofdstuk 1 wordt een uitgebreide inleiding tot micromagnetisme gegeven, waarbinnen de rest van dit proefschrift dan kadert.

Een eerste vorm van wanorde die we zullen beschouwen zijn imperfecte kristalstructuren, waarin eventueel magnetische defecten aanwezig zijn. Wanneer dit type defecten voorkomt in magnetische nanodraden spreken we van gedistribueerde wanorde. In Hoofdstuk 2 onderzoeken we hoe dergelijke materiaaldefecten en/of polykristallijne materialen zo realistisch mogelijk in micromagnetische simulaties opgenomen kunnen worden. Er wordt ook onderzocht wat het effect van wanorde op de beweging van magnetische domeinmuren in dergelijke materialen is en wat er precies gebeurt op het niveau van de lokale magnetisatie. Een belangrijk resultaat dat we vonden in stroomgedreven vortexdomeinmuren, is dat de vortexkern aan defecten kan ompolen wat zijn mobiliteit sterk beïnvloedt. Het gedrag van de domeinmuur wordt dan bepaald door effectieve materiaalparameters die sterk kunnen verschillen van hun werkelijke waarde. Onze bevinding kan zo een aantal tegenstrijdige experimentele resultaten verklaren.

Een tweede vorm van wanorde is temperatuur. Op de kleine tijd- en lengteschalen waarop wij naar de magnetisatie kijken, spelen thermische fluctuaties een belangrijke rol. In Hoofdstuk 3 leiden we een bewegingsvergelijking af die de stochastische beweging van domeinmuren door een nanodraad beschrijft en rekening houdt met zowel de invloed van temperatuur als van materiaaldefecten. Deze bewegingsvergelijking wordt numeriek opgelost en haar oplossingen worden vergeleken met micromagnetische simulaties. Nadat ze gevalideerd is, gebruiken we ze om de beweging van domeinmuren te onderzoeken in het “creep-regime”. In dit regime wordt de beweging van de domeinmuur volledig bepaald door het samenspel tussen de thermische fluctuaties en het potentiaallandschap ten gevolge van de wanorde in het materiaal. In brede nanodraden wordt hier (in overeenstemming met theoretische voorspellingen) typisch een sterk niet-lineair gedrag opgemeten. In dunnere draden, waarvoor onze bewegingsvergelijking geldt, is dit verrassend genoeg niet langer het geval en vinden we toch een lineaire relatie tussen de snelheid en de drijvende kracht. Dit resultaat wordt ook ondersteund door beschikbare experimentele data.

In Hoofdstuk 4 richten we onze aandacht op magnetische nanodeeltjes. De magnetische dynamica van deze deeltjes wordt door hun kleine afmetingen volledig bepaald door thermische fluctuaties. We stellen een nieuw micromagnetisch softwarepakket, Vinamax, voor dat speciaal ontwikkeld werd om nanodeeltjes efficiënt te kunnen simuleren. Dit pakket wordt eerst gevalideerd en daarna gebruikt om de magnetische relaxatie van een ensemble van deeltjes te onderzoeken. Nadat een ensemble in een extern veld gemagnetiseerd werd, zullen de thermische fluctuaties de magnetisatie van de deeltjes terug willekeurig oriënteren. Het opmeten van dit signaal noemt men magnetorelaxometrie. Door experimentele relaxometriedata te vergelijken met micromagnetische simulaties kunnen we de Gilbert damping in nanodeeltjes, een waarde

waarover in de literatuur bijna niets te vinden is, afschatten als  $\approx 0.001$ . Vervolgens gebruiken we Vinamax om de invloed van interacties tussen ijzeroxide nanodeeltjes te onderzoeken. Uit dit onderzoek besluiten we dat significante interacties plaatsvinden vanaf een concentratie van ongeveer 100 mmol/l ijzer. Magnetische ruis, het laatste onderwerp dat in dit Hoofdstuk behandeld wordt, werd onderzocht tijdens een 3-maand-durend onderzoeksverblijf aan de Physikalisch-Technische Bundesanstalt in Berlijn. Magnetische nanodeeltjes worden gewoonlijk onderzocht door hun respons op een externe excitatie op te meten. In afwezigheid van dergelijke excitatie wordt in een magnetisch afgeschermd omgeving echter toch nog een extreem kleine ruis opgemeten ten gevolge van de thermische fluctuaties in de magnetisatie. We hebben een theoretisch model opgesteld dat het experimenteel opgemeten spectrum van deze ruis kan relateren aan de fysieke eigenschappen van de deeltjes. Voor alle opgemeten deeltjes waren de eigenschappen, bepaald op basis van het ruisspectrum, in overeenstemming met deze bepaald uit andere methodes zoals magnetorelaxometrie.

Ten slotte worden in Hoofdstuk 5 algemene conclusies getrokken en wordt toekomstig werk dat op dit doctoraatsproefschrift kan voortbouwen besproken. In de toekomst kunnen we onze aandacht bijvoorbeeld richten op een vorm van wanorde die in dit proefschrift niet uitgebreid aan bod kwam (maar toch even werd aangeraakt in Hoofdstuk 4), namelijk geometrische wanorde. Hierbij bevinden de nanodeeltjes zich op willekeurige posities. Wanneer de interacties tussen de deeltjes sterk genoeg zijn, geven ze aanleiding tot een zeer merkwaardig gedrag van de totale magnetisatie, genaamd “glasachtig” gedrag. Een tweede mogelijk onderwerp voor toekomstig onderzoek zijn gefrustreerde systemen. Dit zijn systemen waarin zelfs in een globaal energiminimum de lokale magnetisatie niet overal in haar energetisch voordeligste toestand zit. Deze toestand is analoog aan waterijs en wordt daarom ook wel “spin-ijs” genoemd. De magnetische dynamica van deze spin-ijs systemen resulteert uit het samenspel van de gefrustreerde interacties tussen de individuele magnetische structuren en thermische fluctuaties. Deze systemen zijn nog maar een paar jaar experimenteel toegankelijk en er staan nog belangrijke uitdagingen in de weg om ze uitgebreid te onderzoeken met micromagnetische simulaties. De technieken die uitgewerkt werden in dit doctoraatsproefschrift kunnen een waardevolle bijdrage leveren om dit doel te bereiken.





In a world of ever faster and smaller ICT devices, magnetic structures play an important role. For example, in classic hard drives data is stored as uniformly magnetised areas, called domains, on magnetic platters. The big challenge is to make these domains as small as possible and to read and write them as quickly as possible.

Slightly more futuristic is an alternative memory technology which was presented some years ago: the racetrack memory. In this device, data is stored in the direction of the magnetisation of the boundaries between two domains, called domain walls. These domain walls can move sufficiently fast through nanowires with a typical cross-section of a few tens of nanometers to reach speeds competitive with current memory devices.

Magnetic nanoparticles are another type of magnetic structures with a lot of applications. They consist of a magnetic core with a diameter of a few nanometers and possibly a non-magnetic shell which can make them bio-compatible or prevent them from aggregating. The particles are used, among others, in medical applications like hyperthermia, drug targeting and medical imaging.

All these applications work perfectly in idealised systems without disorder. However, in reality there always is a certain degree of disorder present. Disorder is a broad concept and shouldn't necessarily have a negative influence. In this doctoral thesis we will discuss different magnetisation systems with various kinds of disorder.

To investigate the above mentioned systems, micromagnetic simulations are an essential tool. Micromagnetism is the theory which describes the magnetic dynamics at the nanometer length scale and the picosecond timescale. On the one hand, this scale is large enough to neglect quantum-mechanical effects and approximate the magnetisation as a continuous vector field. On the other hand, it is smaller than the macroscale where the magnetisation is described by the Maxwell equations. At this intermediate scale we encounter magnetic structures and

dynamics that are interesting for several applications, some of which were briefly described above. Chapter 1 contains an extensive introduction to micromagnetism, which provides the framework for the rest of the thesis.

The first type of disorder we will consider are imperfect crystal structures, which may contain magnetic defects. When these defects are abundant in magnetic nanowires, we talk about distributed disorder. In Chapter 2 we investigate how such defects and/or polycrystalline materials can be implemented in micromagnetic simulations. We also investigate the influence of such disorder on domain wall motion and what happens physically on the level of the local magnetisation. An important result we found in current-driven vortex domain walls is that the vortex core can switch its polarity at defects which strongly influences its mobility. Consequently, the domain wall behaviour is determined by effective material parameters strongly deviating from their real values, which explains some contradictory experimental results.

A second type of disorder is temperature. On the small time and length scales at which we look at the magnetisation, thermal fluctuations play an important role. In Chapter 3, we derive an equation of motion which describes the stochastic motion of domain walls through a nanowire and takes both temperature and material disorder into account. We numerically solve this equation of motion and compare its solutions to micromagnetic simulations. After validating the equation, we use it to investigate domain wall motion in the “creep regime”. In this regime, the motion of the domain wall is dominated by the interplay between the thermal fluctuations and the potential energy profile due to the material disorder. In wide nanowires a strong non-linear behaviour is expected (in agreement with theoretical results). Surprisingly, in thin wires in which our equation of motion is valid, this is no longer the case and we find a linear relation between the velocity and the driving force. This result is supported by available experimental data.

In Chapter 4 we turn our attention to magnetic nanoparticles. The magnetic dynamics of these particles is determined completely by thermal fluctuations due to their small dimensions. We present a new micromagnetic software package, Vinamax, which was developed specifically to efficiently simulate magnetic nanoparticles. First, we validate this package and then use it to investigate the magnetic relaxation of an ensemble of nanoparticles. This relaxation originates in the random reorientation of the magnetisation of the particles due to thermal fluctuations, after they were magnetised in an externally applied field. The measurement of this relaxation is called magnetorelaxometry. By comparing experimental relaxometry data with micromagnetic simulations, we can estimate the Gilbert damping parameter in nanoparticles, a value not found in literature, to be  $\approx 0.001$ . Subsequently, we use Vinamax to investigate the influence of interactions between iron-oxide nanoparticles. We conclude that significant interactions take place starting from concentrations of approximately 100 mmol/l iron. Magnetic noise, the last topic of this chapter, was investigated during a 3-month research stay at the Physikalisch-Technische Bundesanstalt in Berlin. Magnetic nanoparticles

are typically investigated by measuring their response to external excitations. However, in the absence of such excitations, one can still measure an extremely small noise signal in a magnetically shielded environment due to the thermal fluctuations in the magnetisation. We have developed a theoretical model which relates the noise spectrum to the physical properties of the particles. For all measured particles, the properties determined from the noise spectrum agreed with the ones determined from other methods like magnetorelaxometry.

Finally, in Chapter 5 we draw general conclusions and discuss possible future work building on the results of this thesis. In the future, we might investigate a type of disorder which was only considered briefly in Chapter 4, i.e. geometrical disorder. There, the particles are located on random positions. When the interactions between the particles are strong enough, they give rise to a strange magnetic behaviour, called “glassy” behaviour. A second possible topic of future research is frustrated systems. In these systems, the local magnetisation never is in its lowest energy state, not even when the system as a whole is in its global energy minimum state. This state resembles water-ice and therefore is called “spin-ice”. The magnetic dynamics of spin-ice systems result from the interplay between the frustrated interactions between individual magnetic structures and thermal fluctuations. Only recently such systems became experimentally accessible and significant challenges are hindering extensive micromagnetic studies. However, the methods developed in this doctoral thesis can provide valuable contributions towards this goal.



# CHAPTER 1

---

## Introduction

---

*magnet*, *n.* Something acted upon by magnetism.

*magnetism*, *n.* Something acting upon a magnet.

— Ambrose Bierce, *the devil's dictionary*

## 1.1 The origin of ferromagnetism

Ferromagnetic materials, like iron, are materials which show a spontaneous magnetisation in the absence of external fields. This effect originates in 1) the fact that the individual atoms have a magnetic moment and 2) that these magnetic moments display a long-range ordering. In this section we will explain where the magnetic moments come from and what causes their ordering.

Magnetism is related to the angular momentum of elementary particles[1]. In solids, the main source of magnetic moment are the *electrons*. They have an elementary charge  $e$  and mass  $m_e$ . They have two different angular momenta. First, there is the orbital moment. In the classical picture, an electron orbits the nucleus and is bound to it by the Coulomb interaction. This gives rise to a charge moving in a loop and thus a current loop, which has a magnetic moment associated to it. Consequently, the magnetic moment  $\mathfrak{M}$  is proportional to the angular momentum  $l$ .

$$\mathfrak{M} = \gamma l \tag{1.1}$$

with  $\gamma$  the *gyromagnetic ratio*, which equals  $-\frac{e}{2m_e}$  for the orbital motion of electrons. The *orbital angular momentum* is quantised in units of  $\hbar$ , so the natural unit for electronic magnetism is the *Bohr magneton*,

$$\mu_B = \frac{e\hbar}{2m_e} = 9.274 \times 10^{-24} \text{Am}^2. \tag{1.2}$$

The electron also possesses an intrinsic angular momentum (called *spin*) unrelated to its orbital motion. Because electrons are point particles, it is not meaningful to see them as actually spinning particles; the electron spin actually is a relativistic quantum mechanical effect unrelated to any actual spinning motion. This *spin angular momentum* also gives rise to a magnetic moment. The *gyromagnetic ratio*  $\gamma$  for this moments equals  $-\frac{e}{m_e}$  and consequently spin angular momentum is twice as efficient to generate magnetic moment as the orbital angular momentum. In most ferromagnetic materials like iron, the orbital angular momentum is negligible because it is *quenched* as a result of the interaction between the electrons and the crystal fields. In these materials, it is almost exclusively the intrinsic spin angular momentum which is responsible for the magnetic moment.

Although all substances contain electrons, most of them are not magnetic. The reason is that in most atoms the magnetic moment of one electron is cancelled out by the moment of another. Only when *unpaired electrons* are present, a net magnetic moment can remain.

We now know where the source of the magnetic moment lies, but not yet what causes its ordering. In most materials, the individual magnetic moments do not interact with each other and only line up in the presence of an external field, a phenomenon called *paramagnetism*.

The long-range ordering encountered in ferromagnetism is again a quantum mechanical effect and originates in the half-integer spin of the electrons. Because they are *fermions*, electrons have to obey *Pauli's exclusion principle* which states that two electrons cannot be in the same quantum state simultaneously. In practice this means that two electrons whose wave functions overlap cannot have their magnetic moments aligned.

This condition can be fulfilled in two ways. On the one hand, the two electrons could have an opposite spin, and have overlapping wave functions. On the other hand, the electrons could have their spins aligned, but then their wave-functions are not allowed to overlap and the electrons have to remain further apart. Due to the Coulomb repulsion the lowest energy state corresponds to the latter state where neighbouring atoms have the same spin, and the energy difference is called the exchange energy. The exchange interaction, further discussed in Section 1.3 thus lies at the origin of the ferromagnetic ordering.

## 1.2 Historical overview of micromagnetism

*Micromagnetism* is the continuum theory of magnetic materials at the picosecond timescale and nanometer to micrometer length scale. Its purpose was first described in the book “*Micromagnetics*” [2], written by W. F. Brown

*To understand ferromagnetic materials, we must examine them on a smaller scale than that of ordinary observations. On one such scale we speak of domains; on another, of lattice sites. This tract analyses them on an intermediate scale: small enough to reveal details of the transition regions between domains, yet large enough to permit the use of a continuous magnetisation vector rather than of individual atomic spins.*

**Micromagnetism** thus originates from a desire to understand ferromagnetic materials. The first achievement towards this goal was made by *Weiss* already in 1907[3]. Until then it was a mystery why some materials, for example iron, could sometimes display no net magnetisation although it was known that they were magnetic materials. *Weiss* came up with the idea that a ferromagnetic material can contain several uniformly magnetised *domains*. The magnetisation can point in different directions in different domains. Furthermore, knowing that uncoupled magnetic moments cannot give rise to the magnetisation observed in ferromagnets[4], he argued that the magnetic moments within these domains all lie in the same direction due to the influence of some unknown field, called the *Weiss molecular field*. At that time, the only thing that was known about this field was that the **magnetostatic interaction** due to the dipolar coupling alone is not sufficient for the observed long-range ordering. In 1928 *Heisenberg* realised that the quantum-mechanical **exchange interaction** lies at the origin of the **Weiss molecular field** [5].

In the meantime, in 1919, *Barkhausen* discovered that when a magnet is brought in the vicinity of another magnetic material, the magnetisation of this material changes in discrete jumps, leading to the well-known *Barkhausen noise*[6], which can be made audible by an amplifier. He explained this noise by attributing it to the switching of the individual domains. Today we know that this is not completely correct as the jumps result from the motion of **domain walls** between defects. Nonetheless, *Barkhausen* was correct in associating and explaining his observations with the help of domain theory, already 12 years before domains were first visualised by *Bitter*[7]. Simultaneously, *Sixtus and Tonks* investigated the reversal of magnetic wires in their famous experiments[8] and concluded that it is not the domains themselves which switch direction, but the boundaries between different domains which move and thus enlarge the domains with an energetically favourable direction at the cost of oppositely magnetised domains.

Also in the thirties, important theoretical insights were gained. Taking only material anisotropy and the exchange interaction into account, *Bloch* was the first to investigate domain walls[9] and calculated the size and shape of the boundary in between domains. In 1935 *Landau and Lifshitz*[10] were a huge step ahead of their time by taking into account all energy terms (see

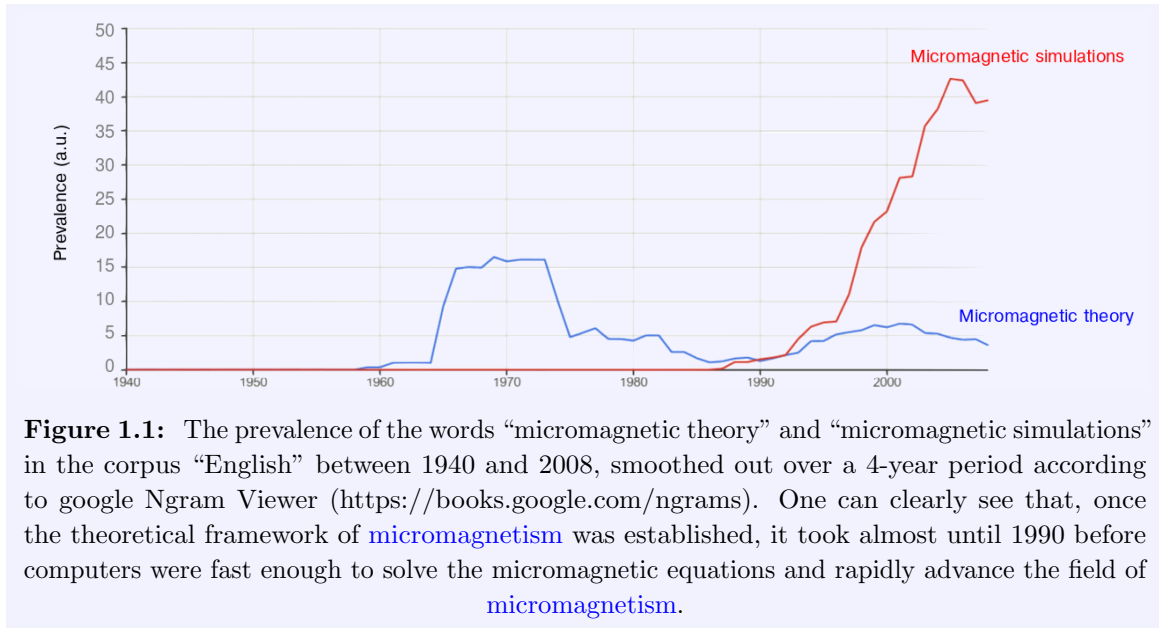
Section 1.3) when they redid Bloch’s calculation for domain walls. Their insights not only advanced the understanding of domain walls, but laid in fact the basis for all of micromagnetism by deriving the now famous Landau-Lifshitz equation. This equation describes the dynamics of magnetic moments while they minimise all these different energies. Following the work of Döring [11], the last step towards a complete framework of micromagnetism as it is still used today was done by Gilbert in 1955[12]. He investigated the description of *damping* in ferromagnetic materials and reformulated the Landau-Lifshitz equation as the Landau-Lifshitz-Gilbert equation.

As can be seen in the description above, the theory of micromagnetism gradually grew during a time span of roughly 50 years. By the sixties, all elements for a complete framework were there and Brown combined everything in a comprehensive overview[2]. Due to the complexity of the micromagnetic equations, it is only possible to analytically solve (relatively) simple problems. The most famous analytical calculation is the domain wall calculation of Landau and Lifshitz [10]. A second example, which is still as relevant today as it was 50 years ago, is the magnetisation of a single-domain particle [2, 13, 14]. Although it is possible to tackle more difficult problems by carefully analyzing and simplifying the micromagnetic equations (e.g. the 1D-model for domain wall motion by Schryer and Walker [15]), the field of micromagnetism did not advance very quickly. Only when increasingly faster computers became available, did it become possible to numerically solve micromagnetic problems and compare their solutions to their analytical counterparts. As Schryer and Walker [15] put it in 1974 (and 5 years after computers were used to put a man on the moon!):

*At the outset it was not at all clear how much could be accomplished with the computer simulation with a reasonable investment of effort. The numerical integration of the equations of motion presented in itself an interesting and difficult problem. It quickly became apparent that unless the character of the motion was reasonably simple, the integration would not be economically feasible.*

However, they were successful in their endeavor to perform the first micromagnetic simulation. Ever since, with the advent of increasingly faster computers, the field of micromagnetism has taken a high flight. Recently, the possibility to calculate on graphics cards[16] has further increased our possibilities to perform larger and larger simulations. This trend is presented visually in Fig. 1.1, where the prevalence of the words “micromagnetic theory” and “micromagnetic simulations” are shown as function of time.





### 1.3 Micromagnetic theory

We repeat that [micromagnetism](#) is a continuum theory of magnetisation. This means that we deal with spatial scales larger than that of individual atoms. The magnetisation is thus approximated as a continuum vector field  $\mathbf{M}$ . The length of the magnetisation vector at each point is assumed to be constant and equal to the *saturation magnetisation*,  $M_s$ . As we are only interested in the direction of the magnetic moment at each point in space, we can introduce the reduced magnetisation  $\mathbf{m} = \frac{\mathbf{M}}{M_s}$ . By definition, the norm of  $\mathbf{m}$  is thus equal to one everywhere.

The field of [micromagnetism](#) can be divided into two areas: static micromagnetics, where we are interested in the equilibrium configuration of the magnetic moments, defined as the state with minimal energy. The second area is dynamic micromagnetics, where the time evolution of the moments is investigated by solving the [Landau-Lifshitz-Gilbert equation](#).

#### 1.3.1 Micromagnetic energy terms

Static micromagnetics deals with finding the equilibrium magnetisation. This equilibrium state is found by minimising the total energy of the system.

$$E_{\text{total}} = E_{\text{exchange}} + E_{\text{Zeeman}} + E_{\text{anisotropy}} + E_{\text{magnetostatic}} + \dots \quad (1.3)$$

In the following sections an overview of the different micromagnetic energy terms will be given[17]. These energies are calculated as a volume integral of the local *energy densities*  $\mathcal{E}$  over the total considered volume  $V$

$$\mathcal{E} = \frac{dE}{dV}. \quad (1.4)$$

The energy densities can be calculated at each point in space and have expressions which are easy to interpret.

##### Exchange energy

The *exchange interaction* has a quantum-mechanical origin[5]. It is the result of the Coulomb repulsion between different electrons and [Pauli's exclusion principle](#) and tries to align neighbouring spins. It can be derived from the [Heisenberg](#) exchange Hamiltonian

$$\hat{\mathcal{H}}_{\text{exchange}} = -2\mathcal{J}\hat{\sigma}_i \cdot \hat{\sigma}_j. \quad (1.5)$$

In this equation,  $\hat{\sigma}_i$  and  $\hat{\sigma}_j$  are two neighbouring electron spins, and  $\mathcal{J}$  is the strength of the [exchange interaction](#). A positive  $\mathcal{J}$  results in a ferromagnetically ordered material and when  $\mathcal{J}$  is negative it is possible to find a ferrimagnetic or antiferromagnetic ordering.

In the continuum limit of [micromagnetism](#), this leads to an *exchange energy* density of

$$\mathcal{E}_{\text{exchange}} = A_{\text{ex}}(\nabla \mathbf{m})^2 \quad (1.6)$$

where  $A_{\text{ex}}$  denotes the *exchange stiffness constant* and  $(\nabla \mathbf{m})^2$  is shorthand for

$$(\nabla \mathbf{m})^2 = (\nabla m_x)^2 + (\nabla m_y)^2 + (\nabla m_z)^2. \quad (1.7)$$

The physical meaning of this expression is that there is an energy penalty whenever the magnetisation does not vary as smoothly as possible. If the [exchange interaction](#) would be the only interaction between magnetic moments, all equilibrium configurations would be states with all moments lying parallel to each other. Of course, this is not the case in reality, and due to the influence of other energy terms, the magnetisation will still vary on larger length scales. In the absence of an external field, there is a lower limit to the length scale at which the magnetisation can vary. This length is called the *exchange length*<sup>1</sup>,

$$l_{\text{ex}} = \sqrt{\frac{2A_{\text{ex}}}{\mu_0 M_s^2}}, \quad (1.8)$$

with  $\mu_0 = 4\pi \times 10^{-7} \text{ Tm/A}$  the *vacuum permeability*. To vary the magnetisation on a smaller length scale requires magnetic fields larger than  $M_s$ , which are impossible to find in magnetic materials without applying external fields or taking other effective field terms into account<sup>2</sup>.

### Zeeman energy

The *Zeeman energy* is the energy due to an externally applied magnetic field  $\mathbf{H}_{\text{ext}}$ . This energy is minimised when the magnetisation is aligned with the external field. The energy density is given by

$$\mathcal{E}_{\text{Zeeman}} = -\mu_0 \mathbf{M} \cdot \mathbf{H}_{\text{ext}}. \quad (1.9)$$

### Anisotropy energy

The structure of the crystal lattice can impose preferred directions on the magnetisation via spin-orbit coupling. In the simplest case, this *anisotropy* gives rise to one favourable direction. This is called *uniaxial anisotropy*, and appears for instance in crystals with a hexagonal structure.

The energy density for [uniaxial anisotropy](#) is given (up to the first order term) by

$$\mathcal{E}_{\text{anisotropy}} = K (1 - (\mathbf{m} \cdot \mathbf{u})^2). \quad (1.10)$$

The anisotropy constant  $K$  (expressed in  $\text{J/m}^3$ ) can be either positive or negative. When  $K > 0$ , the energy is minimised when the magnetisation is aligned with the anisotropy direction  $\mathbf{u}$ , which we then call an easy-axis. Alternatively, when  $K < 0$ , the magnetisation tries to

<sup>1</sup>Due to the way the [exchange interaction](#) is calculated in [MuMax3](#), the [finite difference cells](#) in the [micromagnetic simulations](#) should have a size which is preferably a bit smaller than the [exchange length](#).

<sup>2</sup>e.g. for the [anisotropy](#), discussed below, the characteristic length scale is given by  $\sqrt{(A_{\text{ex}}/K)}$ , with  $K$  the anisotropy constant. When considering other interactions, the size of the [finite difference cells](#) thus has to be chosen accordingly.

align with the plane perpendicular to the anisotropy axis to minimise the energy, which is then called a hard-axis. This is visualised in Figs. 1.2 and 1.3.

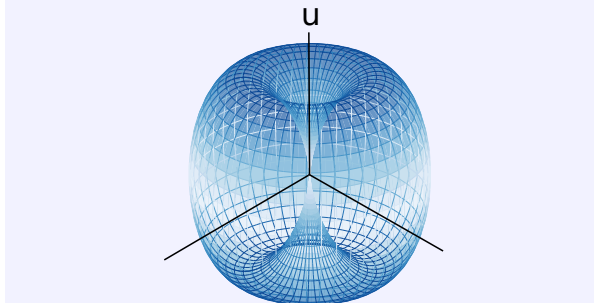


**Figure 1.2:** The energy surface for uniaxial anisotropy with  $\mathbf{u}$  along the z-axis and  $K > 0$ . The distance from the origin denotes the energy. The energetically favourable direction is  $\mathbf{u}$ .

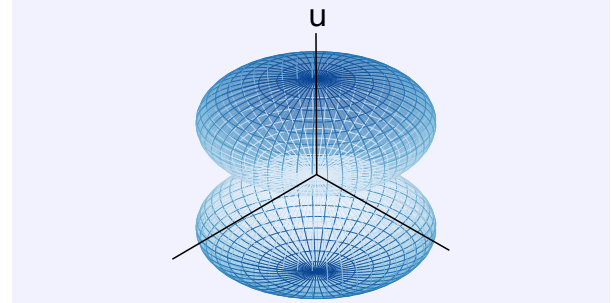


**Figure 1.3:** The same energy surface as in Fig. 1.2, here with  $K < 0$ . The energetically favourable directions lie perpendicular to  $\mathbf{u}$ .

A second case which is also often encountered (for instance in cubic crystals like iron) is *cubic anisotropy*. Here, the energy density (up to the first order term) is given by

$$\mathcal{E}_{\text{anisotropy}} = K ((\mathbf{c}_1 \cdot \mathbf{m})^2 (\mathbf{c}_2 \cdot \mathbf{m})^2 + (\mathbf{c}_1 \cdot \mathbf{m})^2 (\mathbf{c}_3 \cdot \mathbf{m})^2 + (\mathbf{c}_2 \cdot \mathbf{m})^2 (\mathbf{c}_3 \cdot \mathbf{m})^2) \quad (1.11)$$

with  $\mathbf{c}_1, \mathbf{c}_2$  and  $\mathbf{c}_3$ , three mutually perpendicular anisotropy directions.

The preferred axes are shown for a positive and negative anisotropy constant in Figs. 1.4 and 1.5.

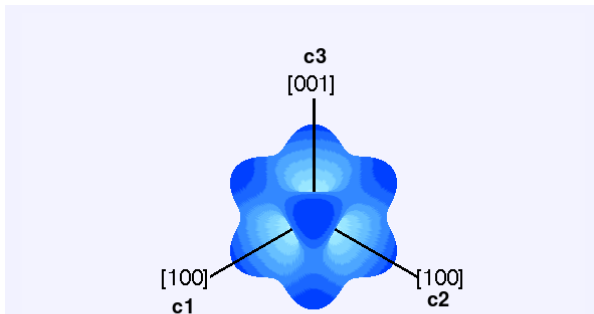


**Figure 1.4:** The energy surface for cubic anisotropy with  $\mathbf{c}_1, \mathbf{c}_2$  and  $\mathbf{c}_3$  along the x, y and z-axis respectively and  $K > 0$ . The distance from the origin denotes the energy. (By RockMagnetist (Own work) [CC0], via Wikimedia Commons)

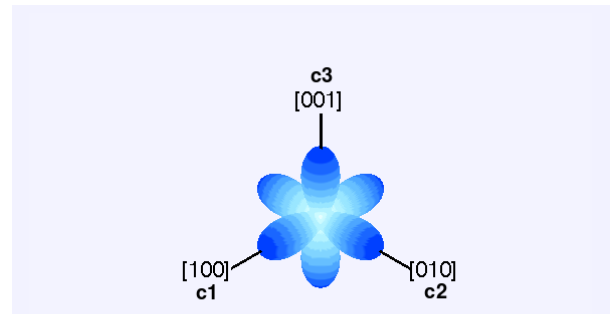


**Figure 1.5:** The same energy surface as in Fig. 1.4, here with  $K < 0$ . (By RockMagnetist (Own work) [CC0], via Wikimedia Commons)

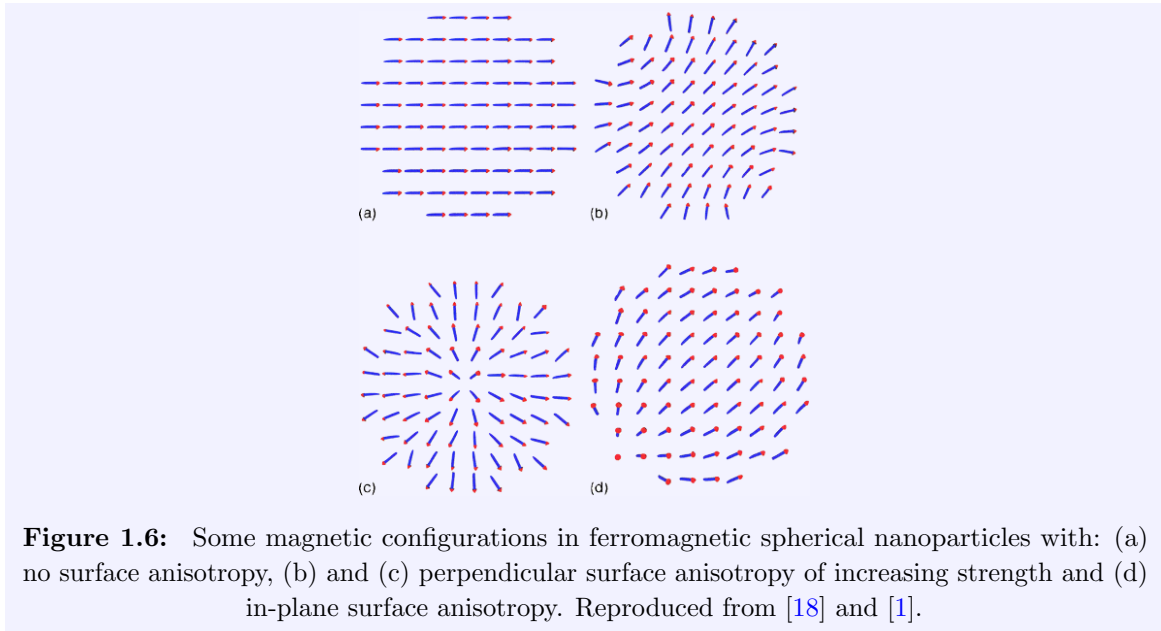
The anisotropies described above are examples of *magnetocrystalline anisotropy*. There also exists *shape anisotropy*. This anisotropy introduces easy axes due to the shape of the material and is magnetostatic in origin. Therefore it will be discussed in the next section.

Finally, *surface anisotropy* originates in the symmetry breaking in the crystal structure at the surface. In contrast to the other energy densities described in this chapter, its energy is given by an integral over the surface  $S$  of the sample:

$$E_{\text{surface anisotropy}} = \int_S K_s (1 - (\mathbf{m} \cdot \mathbf{e}_n)^2) dS, \quad (1.12)$$

where  $\mathbf{e}_n$  denotes the direction perpendicular to the surface and typical values for  $K_s$  are 0.1 to 1 mJ/m<sup>2</sup>[1]. In thin films this anisotropy can align the magnetisation perpendicular to the surface, leading to *perpendicular magnetic anisotropy* (PMA). As a side note, PMA can also have a magnetocrystalline origin when a thin film of a PMA material is grown on a suitable substrate which aligns its easy-axis perpendicular to the plane of the film.

The *surface anisotropy* can also influence the equilibrium state in materials with low Curie temperatures or with a weak *exchange energy* [1, 18] (see Fig. 1.6).



Chapters 2 and 3 mainly deal with the motion of domain walls in *permalloy*<sup>3</sup> *nanowires*. permalloy is an alloy of nickel and iron which was designed to have no magnetocrystalline anisotropy. This makes it very easy to magnetise (or demagnetise), and is why it is called a magnetically *soft material*. This contrasts magnetically *hard materials* which have large

<sup>3</sup>Most simulations in Chapters 2 and 3 are performed with the material parameters of permalloy. Without further mentioning them everywhere, the parameters used are: *spin polarisation* 0.56, *exchange stiffness constant*  $13 \times 10^{-12}$  J/m, *saturation magnetisation* 860 kA/m and *Gilbert damping parameter*  $\alpha = 0.02$  (Chapter 2) or 0.01 (Chapter 3).

anisotropies, and are able to form strong permanent magnets.

Chapter 4 deals with [magnetic nanoparticles](#). In these particles, the anisotropy is very important, as it is mainly the ratio between the *anisotropy energy* and the thermal energy which dictates the magnetic behaviour of these particles. For simplicity reasons, nanoparticles are often assumed to have [uniaxial anisotropy](#) [19, 20] and for the particles considered in that chapter the surface anisotropy is negligible.

### Magnetostatic energy

The *magnetostatic energy* is the energy of magnetic moments in the magnetic field resulting from all considered moments (including itself). This energy is minimised when all *flux loops* are closed and there are no stray fields outside of the magnet.

The *magnetostatic interaction* is also called the *dipole-dipole interaction* because it arises from the interaction between magnetic moments, which can be considered to be magnetic dipoles. This interaction gives rise to the *magnetostatic field* which is also called the *demagnetising field*, as it tries to close the flux loops which results in a zero net magnetisation outside the magnet.

In the expression for the energy density,

$$\mathcal{E}_{\text{magnetostatic}} = -\frac{1}{2}\mu_0\mathbf{M} \cdot \mathbf{H}_{\text{demag}}, \quad (1.13)$$

the factor  $\frac{1}{2}$  is necessary to avoid counting the interaction between two moments double.

In Eq. (1.13),  $\mathbf{H}_{\text{demag}}$  is the [demagnetising field](#)

$$\mathbf{H}_{\text{demag}} = \frac{\mu_0}{4\pi} \int_V M_s \left[ 3 \frac{(\mathbf{m} \cdot \mathbf{r}) \mathbf{r}}{\|\mathbf{r}\|^5} - \frac{\mathbf{m}}{\|\mathbf{r}\|^3} \right] d\mathbf{r}. \quad (1.14)$$

This expression can be derived from *Maxwell's equations*[1] and shows that the [demagnetising field](#) is the integral of all fields produced by all dipoles. The individual interaction between two dipoles is relatively weak, and is always smaller than the [exchange interaction](#) on short distances. However, unlike the exchange interaction which only acts between nearest neighbours, the [magnetostatic interaction](#) is a *long-range interaction*. In Chapter 2.1 it will be shown how this interaction is responsible for the formation of domains in magnetic materials. Another consequence of this long-range interaction is that micromagnetic calculations are computationally very challenging, which is discussed in further detail in Sections 1.3.3 and 4.2.

The [demagnetising field](#)  $\mathbf{H}_{\text{demag}}$  within a uniformly magnetised sample in the shape of an ellipsoid is uniform[1] and can be written as

$$\mathbf{H}_{\text{demag}} = \mathcal{N}\mathbf{M}. \quad (1.15)$$

In this equation,  $\mathcal{N}$  is the demagnetising tensor. If the 3 main axes of the sample coincide with the  $x, y$  and  $z$  axes of the coordinate system,  $\mathcal{N}$  can be written in diagonal form and  $\mathcal{N}_x$ ,  $\mathcal{N}_y$  and  $\mathcal{N}_z$  are then called *demagnetising factors*. These factors will be of use when describing the motion of domain walls in Chapter 3. They depend on the shape of the sample, which we illustrate with a few simple examples. The sum of  $\mathcal{N}_x$ ,  $\mathcal{N}_y$  and  $\mathcal{N}_z$  is always equal to 1. In a spherical magnet, they should all be equal to  $1/3$  for symmetry reasons. Likewise, for an infinitely long wire with circular cross-section, the demagnetising factor is 0 in the longitudinal direction of the wire, while the demagnetising factors in the two directions perpendicular to this direction are  $1/2$ . Finally, in an infinite plane, only the demagnetising factor in the direction perpendicular to the plane is different from 0 and thus equals 1. Consequently, the [demagnetising field](#) and the energy it costs to point the magnetisation in a certain direction depend on the shape of the sample. This *shape anisotropy* is responsible for the fact that the magnetisation in a nanowire (apart from any domain walls) lies in the length direction of the nanowire. This is consistent with the demagnetising factor 0 in this direction.

### Other energy terms

Apart from the ones described above, there still exist other energy terms which we will not discuss in detail as they are not important for the materials considered in this thesis. Two often encountered examples are:

- *Magnetoelastic energy*: This energy term describes the interaction between strains in the crystal lattice and the magnetisation. When a mechanical stress is applied to a magnetic material, the (small) deformations in its crystal lattice can influence the localised electrons and change the magnetisation. Also the inverse is possible; when a magnetic field is applied to such materials, the magnetic force on the electrons can displace the atoms in the crystal lattice and induce strains. This effect is called *magnetostriction*. The magnetostriction in iron and nickel is oriented in opposite directions, and an alloy of roughly 79% nickel and 21% iron ([permalloy](#)) does not show any magnetostriction at all.
- *Dzyaloshinskii-Moriya interaction* [21] (DMI): This interaction is an asymmetric exchange interaction which tries to orient closest neighbours perpendicular to each other. The DMI stabilises [skyrmions](#) [22]: bubble-like quasi-particles currently under investigation as a possible alternative to domain walls in [spintronics](#) applications [23, 24]. It is present in materials with no inversion symmetry or when the symmetry is broken at interfaces.

### 1.3.2 Dynamic micromagnetics

In the previous section we described the different micromagnetic energy terms. The minimisation of the total energy defines the ground state, which is the topic of static [micromagnetism](#). In this section the time dependent magnetisation, or dynamics, is described.

[Landau and Lifshitz](#) proposed that the time evolution of the magnetisation can be described by considering the effect of a local *effective field* on the magnetisation. This effective field can

be written as the derivative of the magnetic [energy densities](#) to the magnetisation,

$$\mathbf{H}_{\text{eff}} = -\frac{1}{\mu_0} \frac{d\mathcal{E}}{d\mathbf{M}}. \quad (1.16)$$

Without loss mechanisms, the magnetisation in an effective magnetic field will precess around this field.<sup>4</sup>

$$\dot{\mathbf{M}} = -\gamma \mathbf{M} \times \mu_0 \mathbf{H}_{\text{eff}} \quad (1.17)$$

The precession frequency (called the *Larmor frequency*) is then equal to

$$f = \frac{\gamma_0 \mathbf{H}_{\text{eff}}}{2\pi} \approx \mu_0 \mathbf{H}_{\text{eff}} 28 \text{ GHz/T} \quad (1.18)$$

where  $\gamma_0 = 2.21 \times 10^5 \text{ m/As}$  is the product of the [vacuum permeability](#)  $\mu_0$  and the [gyromagnetic ratio](#)

$$\gamma = \frac{ge}{2m_e} \quad (1.19)$$

where  $e$  and  $m_e$  are the charge and mass of the electron respectively and  $g \approx 2$  is the Landé factor.

Without loss mechanisms, *conservation of energy* would allow this precession to continue forever. However, in the real world, energy is dissipated by e.g. eddy currents and phonon excitations via spin-lattice coupling. [Landau and Lifshitz](#) [10] took this damping into account by adding a phenomenological torque to Eq. (1.17) which slowly damps the magnetisation towards the [effective field](#). The *Landau-Lifshitz equation* thus reads

$$\dot{\mathbf{m}} = -\gamma_0 \mathbf{m} \times \mathbf{H}_{\text{eff}} - \lambda \mathbf{m} \times (\mathbf{m} \times \mathbf{H}_{\text{eff}}). \quad (1.20)$$

In 1955, [Gilbert](#) [12] introduced a different approach to describe the damping. Also phenomenologically, but physically more intuitive, he assumed the damping to be proportional to the time derivative of the magnetisation  $\dot{\mathbf{m}}$ , with  $\alpha$  (the *Gilbert damping parameter*) as proportionality constant. Typically, an  $\alpha$  of 0.01 is measured in [permalloy](#), but this value can be as high as 0.3 in materials with [perpendicular magnetic anisotropy](#).

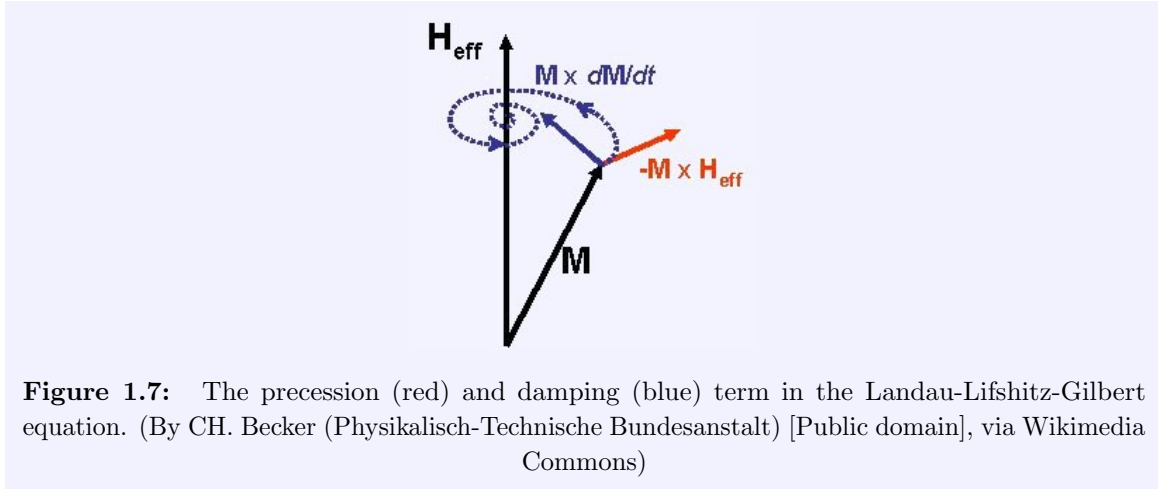
Using Gilbert's approach, the [Landau-Lifshitz equation](#) can be written in its Gilbert form (also called the *Landau-Lifshitz-Gilbert equation*)

$$\dot{\mathbf{m}} = -\gamma_0 \mathbf{m} \times \mathbf{H}_{\text{eff}} + \alpha \mathbf{m} \times \dot{\mathbf{m}}. \quad (1.21)$$

---

<sup>4</sup>In this thesis a time derivative will always be denoted with a dot, e.g.  $\dot{\mathbf{M}}$  stands for  $\frac{d\mathbf{M}}{dt}$ .





Both terms in Eq. (1.21) are intuitively explained in Fig. 1.7. The first term describes the precession of the magnetisation around the effective field  $\mathbf{H}_{\text{eff}}$ . The second term describes the damping of the magnetisation towards  $\mathbf{H}_{\text{eff}}$ . As shown in Fig. 1.7, this results in a spiralling motion for a static effective field.

Although Eqs. (1.20) and (1.21) look different, they can easily be transformed into one another by substituting  $\lambda$  and  $\gamma_0$  in the [Landau-Lifshitz equation](#) by  $\frac{\gamma_0 \alpha}{1+\alpha^2}$  and  $\frac{\gamma_0}{1+\alpha^2}$ , respectively.

Opposed to the original [Landau-Lifshitz equation](#) (without the correct rescaling of  $\lambda$  and  $\gamma_0$ ), the precession frequency is dependent on the damping in the [Landau-Lifshitz-Gilbert equation](#). Consequently, they only describe the same physics in the limit of low damping. As the phenomena investigated in this thesis have low damping, we will not explore the differences between both in more detail, but conclude with the remark that the [Landau-Lifshitz-Gilbert equation](#) is the only one describing physically correct behaviour in the limit of high damping.

### Spin-transfer torque

In Section 1.3.1 an overview of all energy terms contributing to the effective field was given. However, also the interaction between conduction electrons and the localised electrons responsible for the magnetisation can be taken into account in the [Landau-Lifshitz equation](#) [25]. One important phenomenon explained by this interaction is the *giant magnetoresistive effect* [26]. The interaction can be included as a *spin-transfer torque*.

Electrons possess a charge and a spin (due to their angular momentum). In an unpolarised electrical current, only the charge of the electrons is of importance and both spin directions (up or down) appear in equal amounts. In a *spin-polarised current*, this is no longer the case, and next to charge, also angular momentum is transported. There, the *spin polarisation* determines the relative abundance of one type of spin. In [permalloy](#), typically a [spin polarisation](#)  $P = 0.56$  is measured.

Zhang and Li[27] proposed a theoretical framework which accurately describes the interaction between a [spin-polarised current](#) and the magnetisation.

They added two [spin-transfer torque](#) terms to the [Landau-Lifshitz-Gilbert equation](#) describing the exchange of angular momentum between the conduction and localised electrons to arrive at

$$\dot{\mathbf{m}} = \gamma_0 \mathbf{H}_{\text{eff}} \times \mathbf{m} + \alpha \mathbf{m} \times \dot{\mathbf{m}} - [b\mathbf{J} \cdot \nabla] \mathbf{m} + \beta \mathbf{m} \times [b\mathbf{J} \cdot \nabla] \mathbf{m}. \quad (1.22)$$

In this equation,  $\mathbf{J}$  denotes the current density,  $\beta$  the *degree of non-adiabaticity* and

$$b = \frac{P\mu_B}{eM_s(1 + \beta^2)} \quad (1.23)$$

is a prefactor determined by  $P$ , the polarisation of the [spin-polarised current](#),  $e$ , the electron charge and  $\mu_B$ , the [Bohr magneton](#).

The first [spin-transfer torque](#) term in Eq. (1.22) is called the *adiabatic spin-transfer torque*. It is assumed that the spin polarisation follows the magnetisation adiabatically, except for the small degree of non-adiabaticity taken into account separately in the second term. This is the *non-adiabatic spin-transfer torque* and is proportional to  $\beta$ . It is related to the spatial mistracking of moments between conduction electrons and the local magnetisation[27] and is also called the *field-like torque*[28] because its effect on the magnetisation is similar to that of an externally applied field. The size of  $\beta$ [29] is still a topic of debate, which will be detailed in Chapter 2.

The exchange of angular momentum described by the [spin-transfer torque](#) allows to use spin-polarised currents as a driving force in domain wall motion. Further details about [current-driven domain wall motion](#) are given in Section 2.1.4.

## Nonzero temperatures

The [Landau-Lifshitz-Gilbert equation](#) shown in Eq. (1.21) describes the dynamics of the magnetic moments at zero temperature. However, magnets exist at *nonzero temperatures*. To accurately describe magnetic dynamics also *thermal fluctuations* should be taken into account.

Brown [13, 30] developed the theory to include thermal fluctuations when he investigated the thermal switching of [single-domain particles](#), a topic which will be discussed in detail in Chapter 4. Using the *fluctuation-dissipation theorem*, he determined the statistical properties of the thermal fluctuations acting on a [single-domain particle](#).

Lyberatos, in 1993[31], realised that this theory was also applicable to [micromagnetic simulations](#) as each [finite difference cell](#) can be seen as a single-domain “particle”. He adapted Brown’s equations and extended the effective field in the [Landau-Lifshitz-Gilbert equation](#) with a stochastic thermal field  $\mathbf{H}_{\text{th}}$  with the following properties.

$$\langle \mathbf{H}_{\text{th}} \rangle = 0 \quad (1.24)$$

$$\langle \mathbf{H}_{\text{th},i}(t) \mathbf{H}_{\text{th},j}(t') \rangle = q \delta_{\text{D}}(t - t') \delta_{\text{D},ij} \quad (1.25)$$

$$q = \frac{2k_{\text{B}}T\alpha}{M_{\text{s}}\gamma_0\mu_0V} \quad (1.26)$$

The operator  $\langle \cdot \rangle$  denotes an average over time,  $\langle \cdot \cdot \rangle$  a correlation,  $\delta_{\text{D}}$  the Dirac delta function and the indices  $i$  and  $j$  go over the  $x$ ,  $y$  and  $z$  axes in a Cartesian system. The thermal field has zero average [Eq. (1.24)], is uncorrelated in time and space [Eq. (1.25)] and its size  $q$  is given by Eq. (1.26). In this equation,  $k_{\text{B}}$  denotes the Boltzmann constant,  $T$  the temperature and  $V$  the volume in which the [thermal fluctuations](#) are considered.

Numerically, the thermal field is included in the effective field as:

$$\mathbf{H}_{\text{th}} = \boldsymbol{\eta} \sqrt{\frac{2\alpha k_{\text{B}}T}{\mu_0 M_{\text{s}}\gamma_0 V \Delta t}} \quad (1.27)$$

where  $\Delta t$  is the time step used to integrate the micromagnetic equations and  $\boldsymbol{\eta}$  denotes a vector containing 3 random numbers  $\eta$  drawn from a normal distribution with zero mean and standard deviation of one[32].

Equation (1.27) is determined so that the effect of the [thermal fluctuations](#) is independent on the space discretisation. E.g. when splitting up a volume into two smaller volumes and comparing the thermal fluctuations with those on the whole volume, one will on average recover the same behaviour.

In Eq. (1.27), one also sees an inverse proportionality to the square root of the time step  $\Delta t$ . Similarly as with larger volumes, when averaged out over a larger time, thermal fluctuations should become smaller. Again, this proportionality is determined so that the thermal fluctuations over long times do not depend on the time discretisation in the simulations. It is also the time step dependence of the thermal field which prohibits the use of [solvers](#) with an [adaptive time step](#). A more elaborate discussion on this topic can be found in appendix A.

The thermal fluctuations described above act on the same timescales as the other micromagnetic torques, i.e. picoseconds. However, when looking at e.g. ensembles of nanoparticles, macroscopic measurements are unable to capture any of these dynamics as they are averaged out over many particles and longer timescales. What we are interested in here is not the fast dynamics but the slower dynamics resulting from the thermally driven jumps over energy barriers, which can happen on a timescale of nanoseconds up to millions of years. In our simulations, however, we would rather not waste computational time by calculating billions of fluctuations, of which only one will eventually result in a macroscopically observable change in the magnetisation.

An alternative approach is to describe the effect of [thermal fluctuations](#) as a *jump noise process* [33–36]. Here, based on the energy landscape for each [finite difference cell](#), the switching time and final magnetisation direction are determined stochastically and thus only the resulting changes in the magnetisation instead of all random thermal fluctuations are calculated. This process is explained in further detail in Section 4.2, where an implementation for the stochastic switching of magnetic nanoparticles is presented.

Finally, by construction, the [Landau-Lifshitz equation](#) or [Landau-Lifshitz-Gilbert equation](#) conserve the norm of the magnetisation. However, close to the *Curie temperature*, this is no longer physical. To account for these effects, a term perpendicular to the precession and damping terms can be added to the equations. This term describes the variations in the norm of the magnetisation and allows the extension of [micromagnetism](#) to temperatures close to or even above the Curie temperature. The resulting equations, depending on the exact form, are called the *Landau-Lifshitz-Bloch equation* [37] or *Landau-Lifshitz-Baryakhtar equation* [38].

These equations have been implemented in several micromagnetic software packages [39]. E.g. in our group, Dvornik [40] transformed MuMax2 into *hotspin* [41] with this functionality. These considerations are not only theoretically relevant, as recent technological advances such as heat assisted recording [42] can only be simulated correctly with the inclusion of these terms. Although it is possible to investigate domain wall motion in these high-temperature regimes [43], in this thesis we restrict ourselves to temperatures well below the [Curie temperature](#) where the [Landau-Lifshitz-Gilbert equation](#) is still valid.

### 1.3.3 Micromagnetic simulations

As mentioned before, due to the complexity of the micromagnetic equations, only very simple problems can be analysed analytically. Even these problems require specialised methods and great insight. More often than not, even after considerable simplifications, one finds that the analytical solution to a problem simply does not exist or is too impractical to work with.

The logical way to circumvent these challenges is to use a numerical approach, and perform *micromagnetic simulations*. Unfortunately, also in this respect [micromagnetism](#) is a challenging topic. The reason for this is threefold:

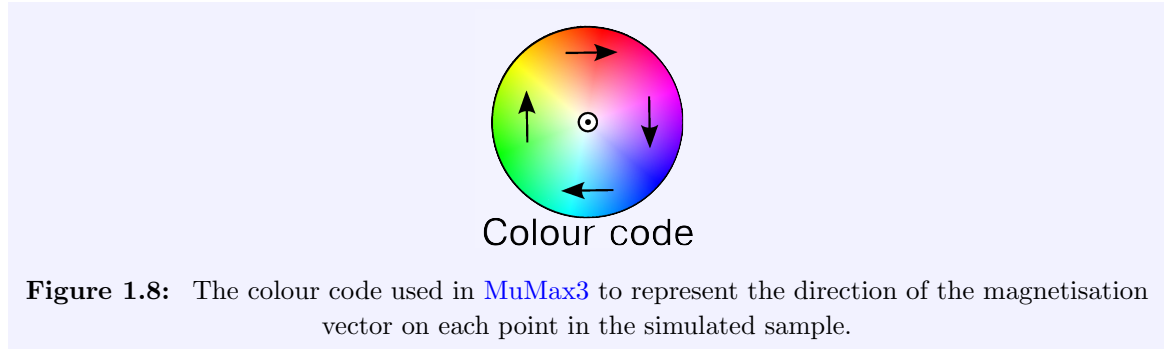
1. The [magnetostatic energy](#) results from a [long-range interaction](#). In contrast to the [anisotropy](#) or [exchange interaction](#) which are local interactions, the magnetostatic energy should be calculated between all magnetic moments.
2. Due to the small length scales on which the magnetisation can vary (typically the [exchange length](#) is a few nm), a tiny spatial discretisation is necessary. To simulate a sample of even a few  $\mu\text{m}$ , already millions of *finite difference cells* are needed. Alternatively, when simulating [magnetic nanoparticles](#), one is interested in averaged-out macroscopic properties of large ensembles and also here large simulations are necessary.

3. Finally, also the timescales on which the magnetisation varies are very small and typically of the order of femto to picoseconds. Thus, even with optimised time integration schemes (cf. Appendix A) simulations require a huge amount of time steps.

Especially the first point makes it hard to perform micromagnetic calculations. For instance, to calculate the demagnetising energy by brute force, an  $\mathcal{O}(N^2)$  algorithm is necessary, as compared to an  $\mathcal{O}(N)$  algorithm required for the local energy terms. With the help of ingenious algorithms, one can reduce this calculation to  $\mathcal{O}(N \log N)$ , but still this is the most expensive calculation in any micromagnetic code. There have been attempts to simplify these calculations by approximating the long-range interactions by “equivalent” (pseudo-)short-range interactions but these attempts proved futile and the conclusion was that it is not possible to cheaply calculate the [demagnetising field](#) while maintaining the correct solution[44].

To be able to perform scientifically relevant simulations, the use of specialised software is necessary. In Chapters 2 and 3 we use *MuMax3*[45] for this purpose. *MuMax3* is a full-blown GPU-accelerated micromagnetic code. It calculates the demagnetising energy by performing a *fast Fourier transform* (FFT) and is one of the fastest codes available.

As referenced, Fig. 1.8 shows the colour code for the direction of the magnetisation used in the figures in the aforementioned chapters, where *MuMax3* is used. The colours represent only the direction of the magnetisation as the size is considered to be constant and equal to 1. The hue represents the in-plane direction of the magnetisation vector, while white and black represent the directions in and out of the plane of the magnet respectively.



In Chapter 4, micromagnetic simulations are performed with the *Vinamax* code. The implementation details and validation of this code are given in Chapter 4.2, and we will limit ourselves here to the purpose of *Vinamax* and the differences between *Vinamax* and *MuMax3*.

As stated before, *MuMax3* is a general purpose micromagnetic code, which uses a [fast Fourier transform](#) (FFT) to calculate the demagnetising energy. This method is suboptimal in sparse geometries. In Chapter 4, the system under study is a diluted ensemble of magnetic nanoparticles. To simulate these in *MuMax3* one would need to calculate an FFT over an almost empty geometry. In contrast, *Vinamax* makes use of a *fast multipole method*, which only calculates the demagnetising energy between particles, and allows for sparse and irregular

---

geometries. As the magnetisation dynamics of these nanoparticles are rather slow and need many averages in time and space to be comparable to experimental data, simulations quickly tend to become extremely long. Its main purpose is therefore to validate higher level models (or approximations) with the numerically calculated exact solutions for some well-chosen problems.

## CHAPTER 2

---

### Domain wall motion

---

*Domains and walls, when they exist,  
should in principle emerge from the theory.*  
— William Fuller Brown Jr.

## 2.1 Introduction

### 2.1.1 Magnetic Domains

As already stated in the [historical overview](#), before the 20th century nobody could explain why ferromagnetic materials sometimes display no net magnetisation. Although not known why, it was known that the individual magnetic moments all lie parallel to their neighbours in such materials. [Weiss](#) [3] resolved this apparent paradox by very carefully stating that the magnetisation could point in opposite directions in different regions of the material, while it is uniform within these regions. This statement was proven true when [Bitter](#) [7] applied a suspension of iron-oxide nanoparticles to the surface of a magnetic material. The particles are attracted to the stray fields at the edges of the different domains and thus visualise the domain structure. Two examples, reproduced from the original paper by [Bitter](#) are shown in Figs. [2.1](#) and [2.2](#).



**Figure 2.1:** Patterns obtained on an iron-silicon alloy in large fields. Reproduced from [7].



**Figure 2.2:** The narrow lines are the deposit obtained on a crystal of nickel. Reproduced from [7].

In their landmark 1935 paper[10] Landau and Lifshitz first discussed a realistic model of domains based on the minimisation of the energy. Similarly, it will be explained how the formation of domains can be energetically favourable[46] with the help of Fig. 2.3.

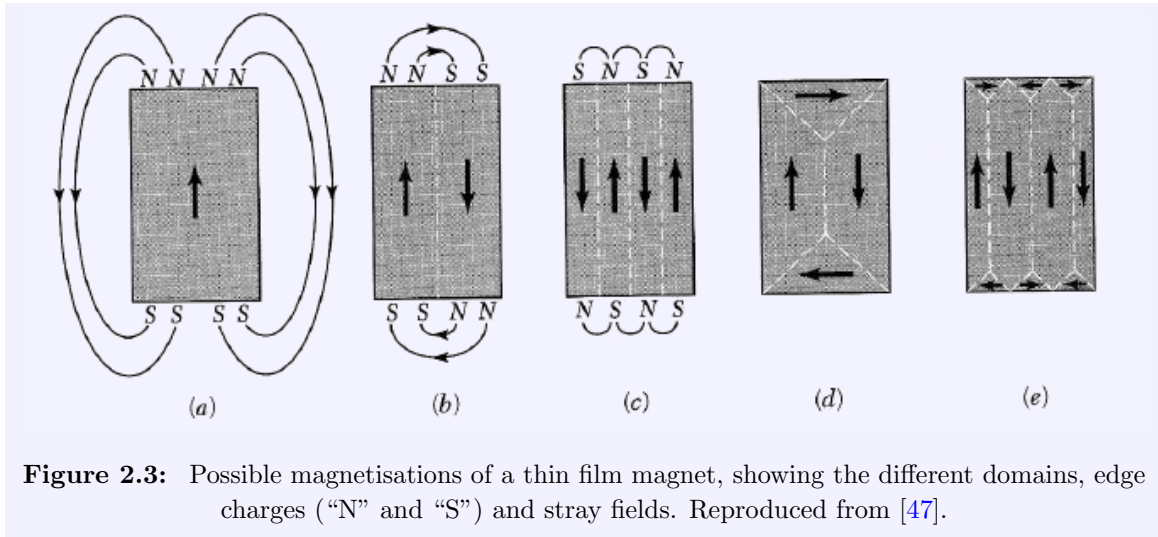


**Figure 2.3:** Possible magnetisations of a thin film magnet, showing the different domains, edge charges (“N” and “S”) and stray fields. Reproduced from [47].

In Fig. 2.3 (a) a uniformly magnetised thin film is shown. One clearly sees that the stray fields (arrows outside the magnet) are very large and must contain a lot of energy. In Fig. 2.3 (b) the magnet is split into two domains, and the energy in the stray field is roughly halved. Subsequently, in Fig. 2.3 (c), the magnet is divided into even smaller domains and the magnetostatic energy is further reduced. Finally, in Figs. 2.3 (d) and (e) small triangular domains magnetised perpendicular to the others are introduced and there are no stray fields left. Such a magnetic configuration is called a *flux-closed magnetisation*. Typical examples of flux-closed states in thin films are the *Landau state* in square shaped samples (Fig. 2.4) and the *vortex state* in disks (Fig. 2.5).



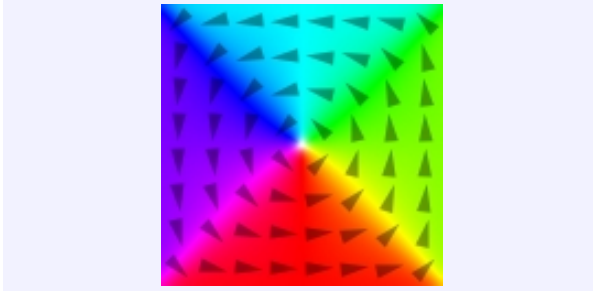


**Figure 2.4:** A Landau state in a  $400 \times 400 \times 20 \text{ nm}^3$  square permalloy film.

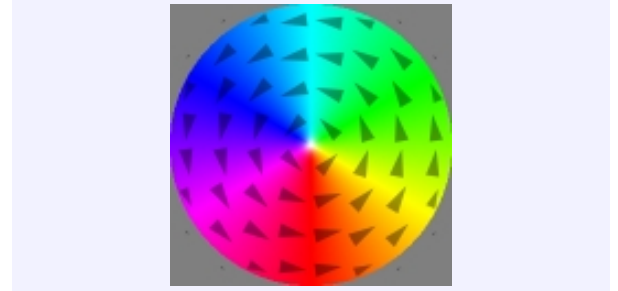


**Figure 2.5:** A magnetic vortex state in a permalloy disk with 400 nm diameter and thickness of 20 nm.

So far, it appears as if it is always favourable to add more and more domains to minimise the energy. This evidently is not true, as we neglected the cost in exchange energy at the boundaries of these domains. These domain walls are regions where the magnetic moments no longer lie parallel to their neighbours. The energy in the stray field scales with the volume of the magnet, while the energy in magnetic domain walls only scales with the surface. This means that in large samples the magnetostatic energy is dominant (e.g. Fig. 2.7), while the domain walls become energetically more expensive in smaller magnets (e.g. Fig. 2.6).

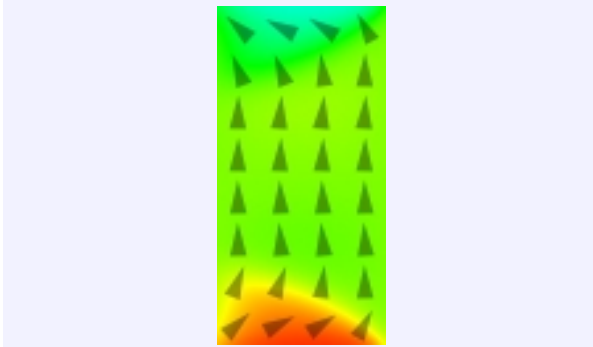


**Figure 2.6:** An equilibrium magnetisation state in a  $200 \times 400 \times 10 \text{ nm}^3$  permalloy nanostructure is uniform, apart from small domains at the edges.

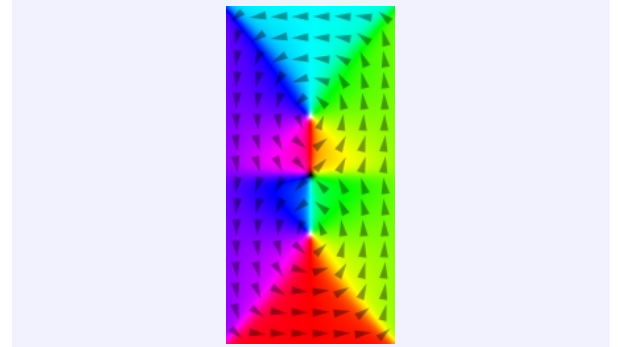


**Figure 2.7:** An equilibrium magnetisation state in a  $400 \times 800 \times 20 \text{ nm}^3$  permalloy nanostructure, consisting of several domains and domain walls.

It can be shown that there exists a critical size under which the formation of domain walls is not energetically favourable and the resulting magnetisation is uniform. In that case we have a *single-domain* or *monodomain* configuration. For spherical magnets (e.g. magnetic nanoparticles), Brown gave an analytical expression for this criterion[2, 48]. Using his expression, we find that the nanoparticles under study in Chapter 4 can be assumed to be monodomain for diameters smaller than approximately 40 nm (but this is a very general number and is of course material dependent).

### 2.1.2 Domain walls

We already established that magnetic domains exist and that their presence can be energetically favourable. Their existence and size are dictated by the [magnetostatic interaction](#). If this were the only energy term, the boundaries between different domains, called *domain walls* would be infinitely thin and the magnetisation would turn 180 degrees from one spin to the next. Contrary, the [exchange interaction](#) prefers to vary the magnetisation as smoothly as possible. The energy is thus minimal when domain walls extend as far as possible, while changing the magnetisation direction very gradually. Finally, due to the [anisotropy](#) (including [shape anisotropy](#)), an energy penalty is induced when the magnetisation is aligned along an unfavourable direction. This results again in smaller domain walls. It is the interplay between all three interactions that determines the size of a domain wall.

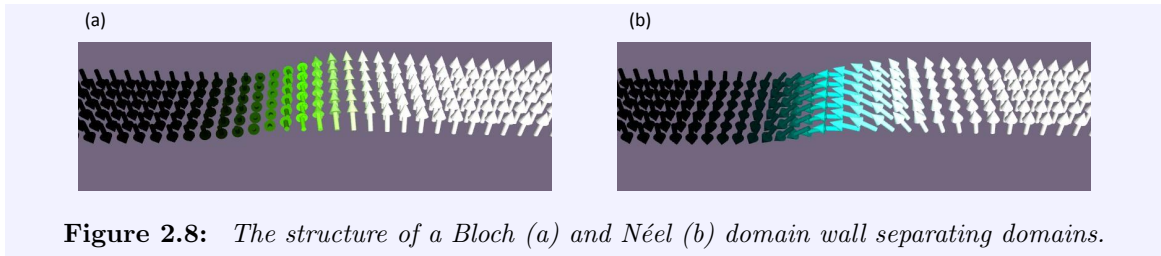
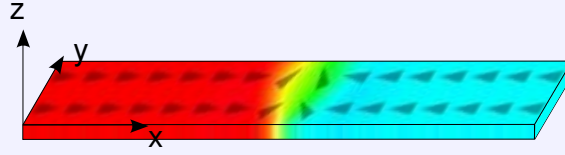


Figure 2.8 (a) illustrates how the magnetisation varies in a *Bloch wall*. This is a wall where the magnetisation turns in the plane of the wall. This kind of wall generates surface charges (or stray fields), which allowed [Bitter](#) to visualise them. However, when the thickness of the film becomes very thin, the energy contained in these stray fields becomes too high compared to the [exchange energy](#) and another kind of wall becomes energetically favourable: the *Néel wall*. In this wall the magnetisation turns in the plane perpendicular to that of the wall, as shown in Fig. 2.8 (b).

### Domain walls in nanowires

Chapters 2 and 3 deal with the motion of domain walls through *nanowires*. These are magnetic structures with a length (x-direction in Fig. 2.9) of several  $\mu\text{m}$  and a cross section of typically 100 to 500 nm (y-direction) by 1 to 10 nm (z-direction). The cross section of these *wires* is rectangular, and the aspect ratio between the width and the thickness can be quite large, making them essentially planar structures with a negligible thickness. This contrasts with the normal meaning of a wire which has a circular cross section[49–51]. Technically, they are *nanostrips*, but we prefer to stay with the term nanowire as it is commonly used throughout literature[52–54] for such structures.



**Figure 2.9:** A domain wall in a nanowire together with the Cartesian axes used throughout this chapter.

Depending on the magnetic properties and geometry of the wire, there exist several possible domain wall structures. This section contains an overview of the domain walls encountered in this thesis. We will classify these domain walls by their *topological charge* (also called *winding number*) [55, 56]. This quantity is defined as the number of times that the magnetisation turns counterclockwise around a point. It is important as it is conserved and can be used to explain what happens in domain wall dynamics [57]. For now, we will have a look at static pictures and leave the dynamics for the next section, Section 2.1.4.

We first make a distinction between in-plane and out-of-plane (PMA) magnetised materials, and begin our description with an in-plane material: [permalloy](#).

In a [permalloy](#) (cf. page 17) nanowire there is no crystal anisotropy and the shape of the wall is determined by the interplay between the [exchange energy](#) and the [magnetostatic energy](#) which gives rise to a [shape anisotropy](#). In nanowires with a small cross section (e.g.  $100 \times 10 \text{ nm}^2$ ) the equilibrium domain wall is a V-shaped *transverse domain wall*.

In Fig. 2.10, such domain walls are shown. The left panels show *tail-to-tail* domain walls, while the right panels depict *head-to-head* domain walls. These names indicate whether the magnetisations outside of the domain wall point towards or away from each other. The “tip” of the V-shaped domain wall contains a half [antivortex core](#) with [topological charge](#)  $-1/2$ , while the other side has [topological charge](#)  $+1/2$ . As shown in the figure, for each configuration, the magnetisation in the domain wall can point up or down. The transverse walls shown in Fig. 2.10 are *symmetric transverse walls*.

There also exist *asymmetric transverse domain walls*, of which an example is shown in Fig. 2.11. There is no fundamental difference between both, in the sense that they can be transformed into each other by a continuous transformation of the magnetisation without having to nucleate or annihilate a topological defect. The difference between both is that they correspond to different minima in the total energy landscape and thus can be distinguished quite clearly from each other. In different geometries, different structures are the minimum energy state, which is why they are also shown separately in the phase diagram in Fig. 2.14.

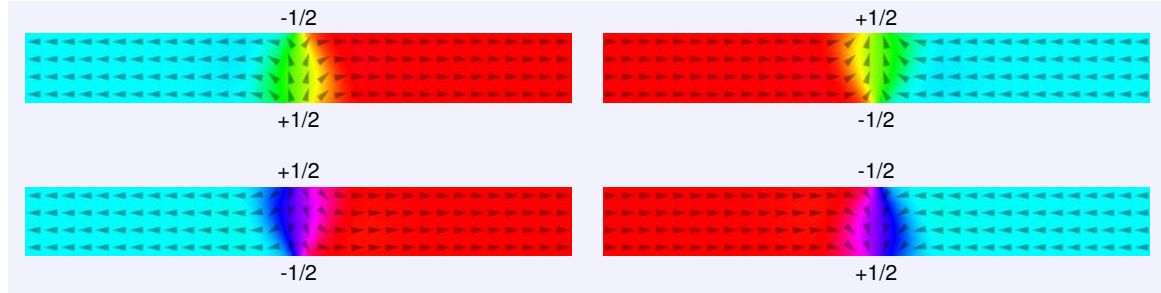


**Figure 2.10:** The possible transverse domain wall configurations in a [permalloy](#) nanowire with cross-sectional area of  $100 \times 10 \text{ nm}^2$ . The numbers denote the [topological charges](#). Notice that we removed the *edge charges* at the left and right sides of the nanowire to simulate an infinitely long wire. This is also the case in all the following figures, but will not be mentioned again.

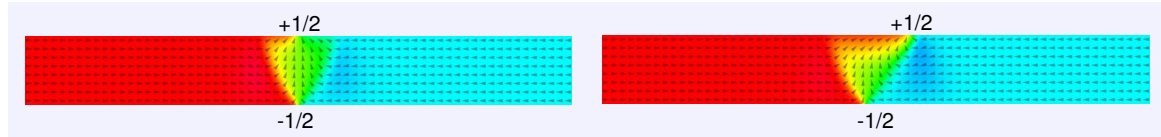


**Figure 2.11:** An example of a symmetric (left) and asymmetric (right) transverse domain wall in a [permalloy](#) nanowire with cross-sectional area of  $400 \times 10 \text{ nm}^2$ . The numbers denote the [topological charges](#). Both domain walls are stable and do not automatically relax into an other state. Note however, that the ground state in this geometry is a vortex domain wall (see below).

A second structure, (which however is not an equilibrium state) is an *antivortex domain wall*. This wall contains an *antivortex core* with [topological charge](#) -1. The possible configurations are shown in Fig. 2.12. Again, we see there are [head-to-head](#) and [tail-to-tail](#) configurations possible. On top of this we also see that antivortex cores have a *polarity*, i.e. the core points either in (black) or out (white) of the plane of the nanowire.

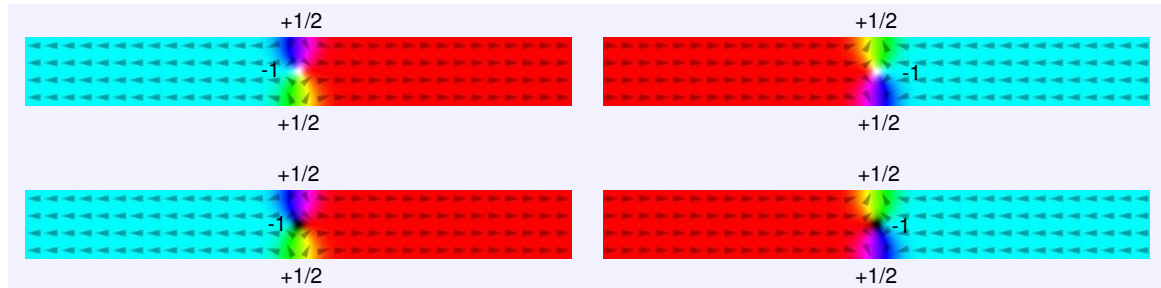
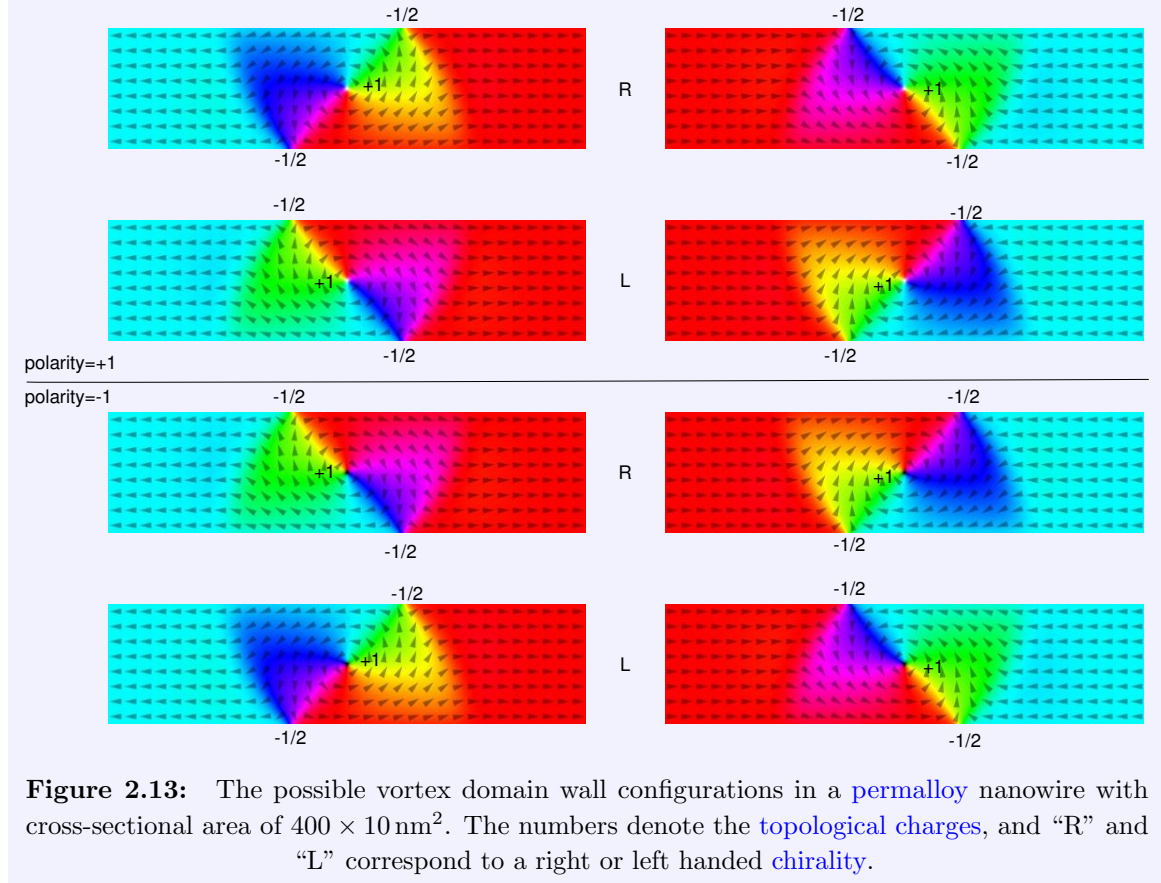


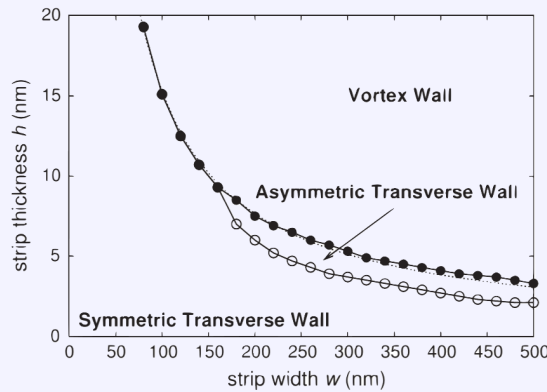
**Figure 2.12:** The possible antivortex domain wall configurations in a [permalloy](#) nanowire with cross-sectional area of  $100 \times 10 \text{ nm}^2$ . The numbers denote the [topological charges](#).

When looking at nanowires with larger cross-sections, we see that the equilibrium shape first becomes an [asymmetric transverse domain wall](#), cf. Fig. 2.11, and for even larger structures (e.g.  $400 \times 10 \text{ nm}^2$ ) the [demagnetising field](#) becomes so strong that the domain wall cannot remain uniformly magnetised and transforms into a *vortex domain wall*. Such walls contain a *vortex core* with topological charge +1. The size of this core is of the order of a few times the [exchange length](#) [58]. Next to the [polarity](#), vortices also have a *circulation*, i.e. the magnetisation can rotate clockwise or counterclockwise around the vortex core. The product

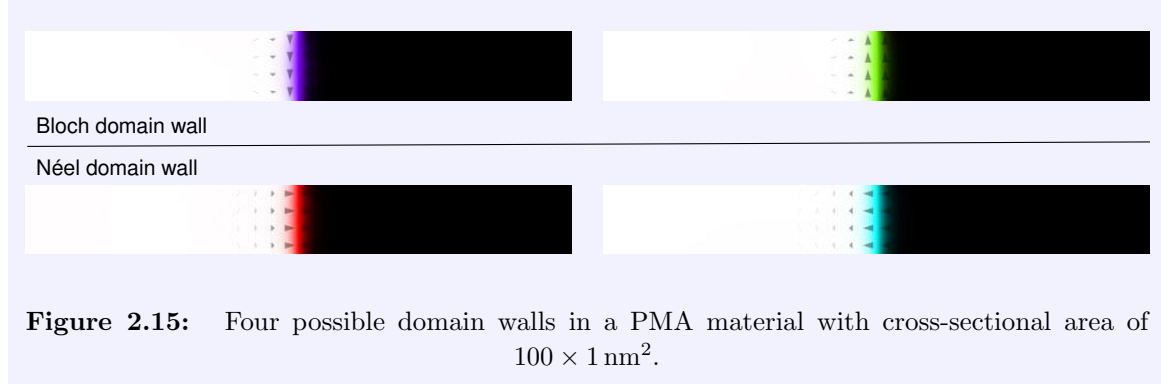
of the [polarity](#) and the [circulation](#) is the *chirality* or *handedness*. All possible configurations are shown in Fig. 2.13. When we will consider the dynamics of vortex domain walls in Section 2.1.4, we will see that the [circulation](#) remains conserved, but the [polarity](#) [59, 60], and thus the [chirality](#) can change sign.



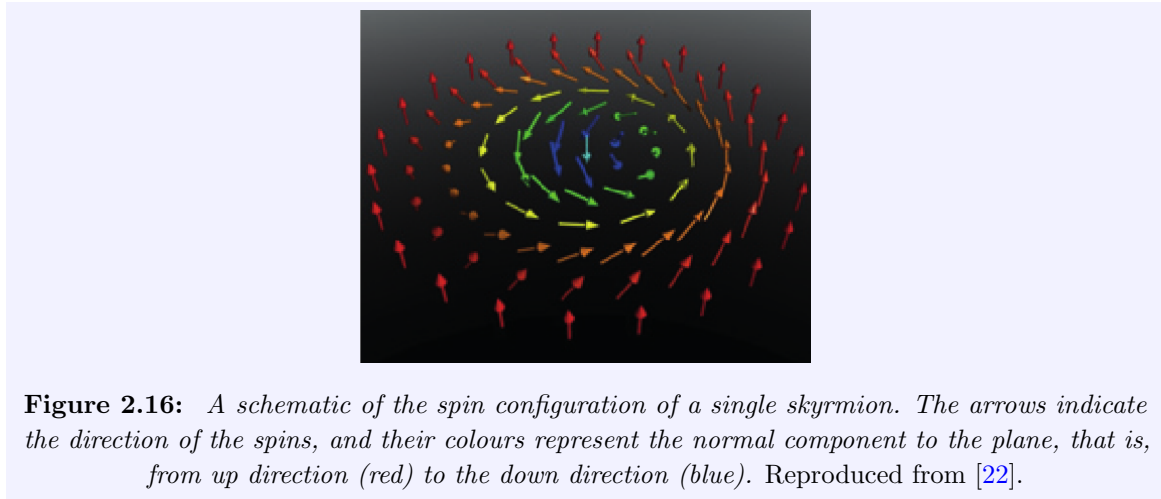
The equilibrium shape of the domain wall depends on the geometry of the nanowire, and is summarised for [permalloy](#) nanowires in the phase diagram shown in Fig. 2.14.



For completeness we show the two possible domain wall configurations encountered in narrow PMA nanowires in Fig. 2.15. They are classified based on whether the domain wall turns in (Bloch wall) or out (Néel wall) of the plane of the wall.



A final structure which can be encountered in PMA materials are *skyrmions* [22]. A skyrmion is a magnetic bubble in which the magnetisation in the centre points in the opposite direction as in its surrounding. A schematic of the spin configuration of a skyrmion is shown in Fig. 2.16. Skyrmions are topologically protected in the sense that they are characterised by a topological integer (its skyrmion number) which cannot be changed by a continuous transformation of the magnetisation. Historically, the first skyrmions encountered were stabilised by the magnetostatic interaction and were of the order of a few  $\mu\text{m}$  large. Recently, also skyrmions stabilised by the Dzyaloshinskii-Moriya interaction were detected. These skyrmions are only a few nm large and can be moved just like domain walls. Therefore they are being investigated as possible alternatives to the domain wall based technologies discussed at the end of this section.



### 2.1.3 1D-model

Before the advent of extensive computational capabilities it was not possible to numerically integrate the Landau-Lifshitz-Gilbert equation. Therefore, early micromagnetic research was



focused on very specific topics where clever simplifications could be made. One successful example was a model of *Schryer and Walker*[15] to describe the motion of [Bloch walls](#), driven by a uniform magnetic field, through a magnetic nanowire.

Their approach made an abstraction of the Bloch domain wall as a zero dimensional (0D) point particle moving through a one dimensional (1D) nanowire, hence the name *1D-model*. Instead of keeping track of the directions of all magnetic moments in the domain walls, the magnetisation within the domain wall is assumed to be uniform and the only remaining parameters are the domain wall position  $x$ , the domain wall width  $\Delta_{1D}$  and the out-of-plane (the plane of the sample) tilting angle  $\Phi_{1D}$  of the magnetisation.

This model was investigated by *Thiaville*[62] when the numerical results of [micromagnetic simulations](#) became available. The new results were compared to the solutions of these equations and the latter turned out to be quite accurate. Surprisingly, they were also valid for [Néel walls](#), and to a certain extent even for [vortex domain walls](#) [52, 63].

The equations, as given by *Thiaville* in Ref. [62], but with the anisotropy limited to the first order term are

$$\dot{\Phi}_{1D} + \alpha \dot{x} / \Delta_{1D} = \gamma_0 H_{\text{ext},x}, \quad (2.1)$$

$$\dot{x} / \Delta_{1D} - \alpha \dot{\Phi}_{1D} = \gamma H_K \sin \Phi_{1D} \cos \Phi_{1D}, \quad (2.2)$$

$$\dot{\Delta}_{1D} = (12\gamma / \alpha M_s \pi^2) [A_{\text{ex}} / \Delta_{1D} - K \Delta_{1D}]. \quad (2.3)$$

Where  $H_K$  denotes the transverse anisotropy field  $2K / \mu_0 M_s$ . The derivation of these equations is given in Refs. [15, 62] but lies beyond the scope of this work.

Later, *Thiaville* also extended this work to include a [spin-polarised current](#) as a driving force[64, 65]. The expressions for the domain wall velocity and the time variation of  $\Phi_{1D}$  due to the combination of an external field  $H_{\text{ext},x}$  and a [spin-polarised current](#)  $J_x$  are given by:

$$\dot{x} = \frac{\gamma_0 \Delta_{1D}}{\alpha} H_{\text{ext},x} - \frac{\beta}{\alpha} b J_x - \frac{\Delta_{1D}}{\alpha} \dot{\Phi}_{1D} \quad (2.4)$$

and

$$\dot{\Phi}_{1D} = \frac{\gamma_0}{1 + \alpha^2} H_{\text{ext},x} - \frac{1}{\Delta_{1D}} \frac{\beta - \alpha}{1 + \alpha^2} b J_x - \frac{\alpha \gamma_0}{1 + \alpha^2} H_K \frac{\sin 2\Phi_{1D}}{2}. \quad (2.5)$$

One difficulty in the use of these equations is that there is no clear correspondence between the quantities one can obtain from [micromagnetic simulations](#) (e.g. the average magnetisation along different axes) and the variables  $x$ ,  $\Phi_{1D}$  and  $\Delta_{1D}$ . Also, the internal structure of the domain wall is assumed to be constant, while this approximation may sometimes prove to be too crude.

In our group, Vandermeulen[66] has developed a [1D-model](#), starting from variables that are easily derived from micromagnetic simulations. By comparing the resulting equations, it is possible to derive their relation to the 1D-parameters,  $x$ ,  $\Phi_{1D}$  and  $\Delta_{1D}$ . In the next section the

derivation of this model is given for domain wall motion in an in-plane material like [permalloy](#). The model is also valid in [PMA](#) materials but requires a coordinate transformation which is not shown here for clarity.

### Derivation of the 1D-model

We define  $\phi$  as the local out-of-plane angle of the magnetisation of a single cell. By using the  $\langle\langle\cdot\rangle\rangle$  operator, which is defined as a spatial average over the entire simulation window we find an average out-of-plane angle of the magnetisation

$$\langle\langle\phi\rangle\rangle = \langle\langle\arctan \frac{m_z}{m_y}\rangle\rangle. \quad (2.6)$$

The idea of the [1D-model](#) is to reduce all information about the domain wall to a few variables. The complete domain wall structure is thus approximated as a single macrospin. From this assumption we can infer that

$$\Phi_{1D} = \arctan \frac{\langle\langle m_z \rangle\rangle}{\langle\langle m_y \rangle\rangle}, \quad (2.7)$$

or

$$\sin \Phi_{1D} = \frac{\langle\langle m_z \rangle\rangle}{\langle\langle \sqrt{m_y^2 + m_z^2} \rangle\rangle}, \quad (2.8)$$

and

$$\cos \Phi_{1D} = \frac{\langle\langle m_y \rangle\rangle}{\langle\langle \sqrt{m_y^2 + m_z^2} \rangle\rangle}. \quad (2.9)$$

Furthermore, instead of using the local [effective field](#) with all its energy terms, we define an average effective field  $\langle\langle \mathbf{H}_{\text{eff}} \rangle\rangle$  containing only the externally applied fields along the unit vectors ( $\mathbf{e}_x$ ,  $\mathbf{e}_y$  and  $\mathbf{e}_z$ ) and the [demagnetising field](#), where  $\mathcal{N}_{\text{eff},x,y,z}$  are the effective [demagnetising factors](#) of the domain wall,

$$\begin{aligned} \langle\langle \mathbf{H}_{\text{eff}} \rangle\rangle &= H_{\text{ext},x} \mathbf{e}_x + H_{\text{ext},y} \mathbf{e}_y + H_{\text{ext},z} \mathbf{e}_z \\ &\quad - \frac{M_s}{\mathcal{D}} (\mathcal{N}_{\text{eff},x} \langle\langle m_x \rangle\rangle \mathbf{e}_x + \mathcal{N}_{\text{eff},y} \langle\langle m_y \rangle\rangle \mathbf{e}_y + \mathcal{N}_{\text{eff},z} \langle\langle m_z \rangle\rangle \mathbf{e}_z) \end{aligned} \quad (2.10)$$

The [demagnetising field](#) is scaled with a geometry dependent factor  $\mathcal{D}$ , which will be determined later when we compare our final equations to Eqs. (2.4) and (2.5).

Another quantity of interest is  $\langle\langle \delta \rangle\rangle$ , which is the amount of magnetisation which does not lie along the axis of the nanowire, and thus is a measure for the size of the domain wall,

$$\langle\langle \delta \rangle\rangle \equiv \frac{\langle\langle m_y^2 + m_z^2 \rangle\rangle}{\langle\langle m_x^2 + m_y^2 + m_z^2 \rangle\rangle} = \langle\langle m_y^2 + m_z^2 \rangle\rangle. \quad (2.11)$$



When we take the average of the derivative of  $\phi$  multiplied with  $\delta$  we find

$$\langle\langle\delta\dot{\phi}\rangle\rangle = \langle\langle m_y \dot{m}_z - m_z \dot{m}_y \rangle\rangle. \quad (2.12)$$

By filling in Eq. (2.10) in the [Landau-Lifshitz-Gilbert equation](#), we can find expressions for  $\dot{m}_z$  and  $\dot{m}_y$ , and by substituting them in Eq. (2.12) we arrive at

$$\begin{aligned} \langle\langle\delta\dot{\phi}\rangle\rangle = & \frac{\gamma_0}{1+\alpha^2} H_{\text{ext},x} \langle\langle\delta\rangle\rangle - \frac{2}{L_x} \frac{\beta-\alpha}{1+\alpha^2} b J_x + \frac{\alpha\gamma_0}{1+\alpha^2} \left[ -H_{\text{ext},y} \langle\langle m_z \rangle\rangle \right. \\ & \left. + H_{\text{ext},z} \langle\langle m_y \rangle\rangle - \frac{M_s}{\mathcal{D}} (\mathcal{N}_{\text{eff},z} - \mathcal{N}_{\text{eff},y}) \langle\langle m_y \rangle\rangle \langle\langle m_z \rangle\rangle \right] \\ & + \text{asymmetric terms.} \end{aligned} \quad (2.13)$$

The explicit form of the asymmetric terms is not shown. These terms originate in asymmetries in the domain wall shape and are negligible in the case of [current-driven domain wall motion](#) and can be taken into account via an [effective wall width](#) in the case of [field-driven domain wall motion](#). This is explained in further detail in Section 3.2, where it will be of importance.

Similarly,  $\langle\langle\dot{m}_x\rangle\rangle$  can be determined to be

$$\begin{aligned} \langle\langle\dot{m}_x\rangle\rangle = & \frac{\gamma_0}{\alpha} H_{\text{ext},x} \langle\langle\delta\rangle\rangle - \frac{1}{\alpha} \langle\langle\delta\dot{\phi}\rangle\rangle \\ & - \frac{2}{L_x} \frac{\beta}{\alpha} b J_x + \text{asymmetric terms.} \end{aligned} \quad (2.14)$$

It is easy to see that the position  $x$  of the domain wall is proportional to the average magnetisation along the nanowire axis,

$$x = \frac{L_x}{2} \langle\langle m_x \rangle\rangle, \quad (2.15)$$

with  $L_x$  the length of the simulation window.

Using this information and Eq. (2.14) we can write the domain wall velocity as

$$\dot{x} = \frac{\gamma_0 L_x \langle\langle\delta\rangle\rangle}{2\alpha} H_{\text{ext},x} - \frac{\beta}{\alpha} b J_x - \frac{L_x \langle\langle\delta\rangle\rangle}{2\alpha} \frac{\langle\langle\delta\dot{\phi}\rangle\rangle}{\langle\langle\delta\rangle\rangle} + \text{asymmetric terms.} \quad (2.16)$$

When comparing Eqs. (2.16) and (2.4) we derive the following relations between  $\Delta_{1D}$ ,  $\dot{\Phi}_{1D}$  and their counterparts which can be extracted from simulations:

$$\Delta_{1D} \equiv \frac{L_x \langle\langle\delta\rangle\rangle}{2} \quad (2.17)$$

and

$$\dot{\Phi}_{1D} = \frac{\langle\langle\delta\dot{\phi}\rangle\rangle}{\langle\langle\delta\rangle\rangle}. \quad (2.18)$$

Similarly, we find

$$\begin{aligned} \frac{\langle\langle \delta \dot{\phi} \rangle\rangle}{\langle\langle \delta \rangle\rangle} = & \frac{\gamma_0}{1+\alpha^2} H_{\text{ext},x} - \frac{2}{L_x \langle\langle \delta \rangle\rangle} \frac{\beta - \alpha}{1+\alpha^2} b J_x + \frac{\alpha \gamma_0}{1+\alpha^2} \left[ -H_{\text{ext},y} \frac{\langle\langle m_z \rangle\rangle}{\langle\langle \delta \rangle\rangle} \right. \\ & \left. + H_{\text{ext},z} \frac{\langle\langle m_y \rangle\rangle}{\langle\langle \delta \rangle\rangle} - \frac{M_s}{\mathcal{D}} (\mathcal{N}_{\text{eff},z} - \mathcal{N}_{\text{eff},y}) \frac{\langle\langle m_y \rangle\rangle \langle\langle m_z \rangle\rangle}{\langle\langle \delta \rangle\rangle} \right] \\ & + \text{asymmetric terms.} \end{aligned} \quad (2.19)$$

When comparing the last terms in Eqs. (2.19) and (2.5) we see the following correspondence:

$$H_K \frac{\sin 2\Phi_{1D}}{2} = \frac{M_s}{\mathcal{D}} (\mathcal{N}_{\text{eff},z} - \mathcal{N}_{\text{eff},y}) \frac{\langle\langle m_y \rangle\rangle \langle\langle m_z \rangle\rangle}{\langle\langle \delta \rangle\rangle}. \quad (2.20)$$

From Eqs. (2.8), (2.9) and (2.11), under the assumptions of the 1D-model, we find that

$$\frac{\sin 2\Phi_{1D}}{2} = \frac{\langle\langle m_y \rangle\rangle \langle\langle m_z \rangle\rangle}{\langle\langle \sqrt{\delta} \rangle\rangle^2}. \quad (2.21)$$

and thus that

$$\mathcal{D} = \frac{\langle\langle \sqrt{\delta} \rangle\rangle^2}{\langle\langle \delta \rangle\rangle} \quad (2.22)$$

and

$$H_K = M_s (\mathcal{N}_{\text{eff},z} - \mathcal{N}_{\text{eff},y}) \quad (2.23)$$

To summarise, the equations equivalent to Eqs. (2.1) and (2.2) are given by:

$$\begin{aligned} \langle\langle \delta \dot{\phi} \rangle\rangle = & \frac{\gamma_0 \langle\langle \delta \rangle\rangle}{1+\alpha^2} H_{\text{ext},x} - \frac{2}{L_x} \frac{\beta - \alpha}{1+\alpha^2} b J_x + \frac{\alpha \gamma_0}{1+\alpha^2} \left[ -H_{\text{ext},y} \langle\langle m_z \rangle\rangle \right. \\ & \left. + H_{\text{ext},z} \langle\langle m_y \rangle\rangle - M_s (\mathcal{N}_{\text{eff},z} - \mathcal{N}_{\text{eff},y}) \frac{\langle\langle m_y \rangle\rangle \langle\langle m_z \rangle\rangle \langle\langle \delta \rangle\rangle}{\langle\langle \sqrt{\delta} \rangle\rangle^2} \right] \\ & + \text{asymmetric terms} \end{aligned} \quad (2.24)$$

and

$$\dot{x} = \frac{\gamma_0 L_x \langle\langle \delta \rangle\rangle}{2\alpha} H_{\text{ext},x} - \frac{\beta}{\alpha} b J_x - \frac{L_x}{2\alpha} \langle\langle \delta \dot{\phi} \rangle\rangle + \text{asymmetric terms} \quad (2.25)$$

where the correspondence between the variables from the 1D-model and the averages obtainable from micromagnetic simulations are given by:

$$\Delta_{1D} \equiv \frac{L_x \langle\langle \delta \rangle\rangle}{2} \quad (2.26)$$

$$\dot{\Phi}_{1D} = \frac{\langle\langle \delta \dot{\phi} \rangle\rangle}{\langle\langle \delta \rangle\rangle} \quad (2.27)$$

$$H_K = M_s (\mathcal{N}_{\text{eff},z} - \mathcal{N}_{\text{eff},y}) \quad (2.28)$$

$$\Phi_{1D} = \arctan \frac{\langle\langle m_z \rangle\rangle}{\langle\langle m_y \rangle\rangle} \quad (2.29)$$

$$\langle\langle \phi \rangle\rangle = \langle\langle \arctan \frac{m_z}{m_y} \rangle\rangle \quad (2.30)$$

### 2.1.4 Domain wall motion

Domain walls can be driven by an externally applied field, a [spin-polarised current](#) or a combination of both[67, 68].

#### Field-driven domain wall motion

Intuitively it is easy to understand how an externally applied field is able to move domain walls. The magnetic domains aligned in the direction of the external field are energetically favourable and tend to grow at the expense of domains aligned in other directions, thus moving the domain walls in between.

We will analyse *field-driven domain wall motion* of a domain wall in a nanowire as depicted in Fig. 2.9 with the help of Eqs. (2.24) and (2.25). In the absence of a [spin-polarised current](#) and when neglecting the asymmetric terms, the out-of-plane tilting of the domain wall (and thus  $\langle\langle m_z \rangle\rangle$ ) will increase until both terms in Eq. (2.24) cancel each other out and  $\dot{\Phi}_{1D} = 0$ .

In this dynamic equilibrium, which only exist for sufficiently small fields, Eq. (2.25) reduces to

$$\dot{x} = v = \frac{\gamma_0 L_x \langle\langle \delta \rangle\rangle}{2\alpha} H_{\text{ext},x}. \quad (2.31)$$

From this equation we learn that once an equilibrium is reached, the velocity remains constant and depends linearly on the external field. Therefore we use the notation for an averaged-out domain wall velocity  $v$  instead of its instantaneous velocity  $\dot{x}$ .

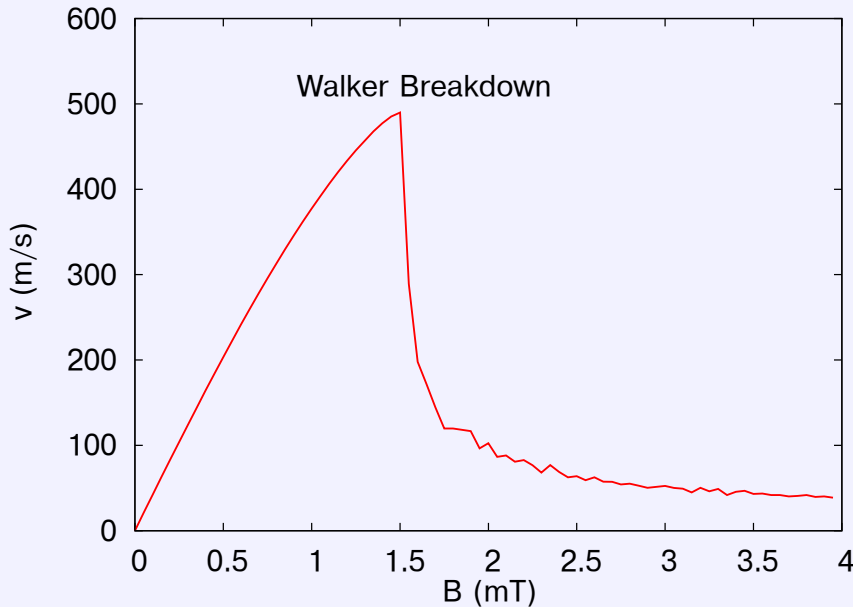


**Figure 2.17:** Mobility curve of a field-driven vortex domain wall in a [permalloy](#) (cf. page 17) nanowire with cross section of  $100 \times 10 \text{ nm}^2$ .

In Fig. 2.17 the results of micromagnetic simulations are shown to illustrate this behaviour. Up to a field of roughly 1.5 mT, the velocity indeed increases with the external field. However, it does not display a perfectly linear dependency. This originates in the fact that the domain wall slightly changes shape at higher velocities and thus  $\langle\langle\delta\rangle\rangle$  is field dependent. The wall also becomes asymmetric and the asymmetric terms in Eq. (2.25) cannot be neglected anymore. A detailed comparison between the extended 1D-model, where we take these effects into account, and the numerical results is given in Section 3.2.

At 1.5 mT, we see a sudden drop in the domain wall velocity, called the *Walker breakdown* [15]. This breakdown corresponds to the field at which it is no longer possible for the torques in Eq. (2.24) to compensate each other and the dynamical equilibrium ( $\dot{\Phi}_{1D} = 0$ ) is never reached. What happens physically in this regime depends on the equilibrium domain wall structure and thus the nanowire size.

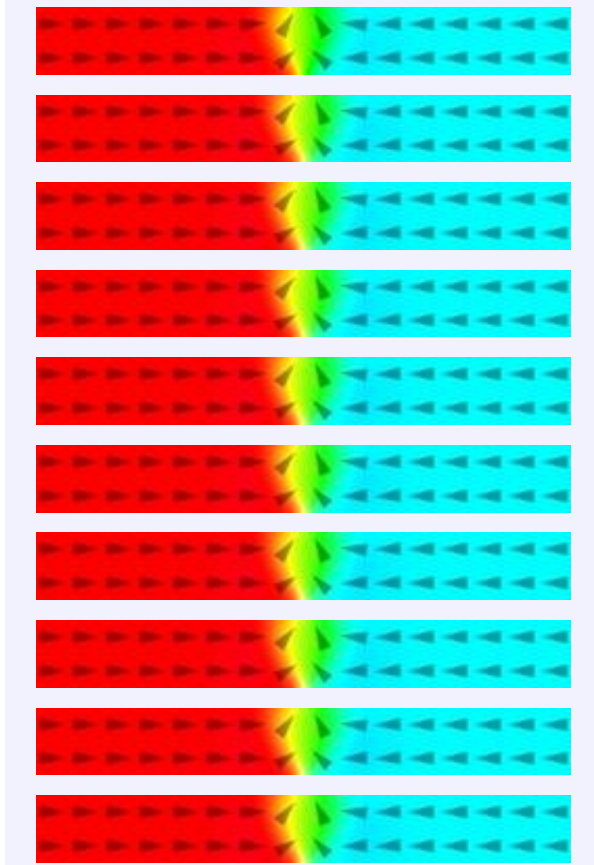


**Figure 2.18:** Snapshots (3 ns apart) of a field-driven (1 mT) transverse domain wall below the Walker breakdown in a permalloy nanowire. The figures are centred around the domain wall during its motion.

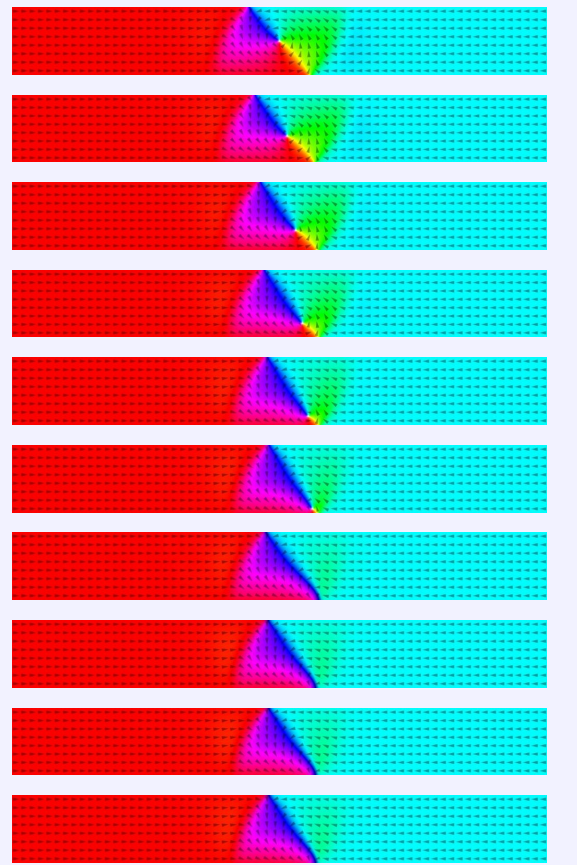


**Figure 2.19:** Snapshots (3 ns apart) of a field-driven (1 mT) vortex domain wall below the Walker breakdown in a permalloy nanowire. The figures are centred around the domain wall during its motion.

We consider domain walls in nanowires with a cross-sectional area of  $100 \times 10 \text{ nm}^2$  and  $400 \times 10 \text{ nm}^2$  where the equilibrium domain wall is a [transverse domain wall](#) and a [vortex domain wall](#) respectively.

Figures [2.18](#) and [2.19](#) show snapshots (3 ns apart) of the domain wall motion driven by a field of 1 mT, in the linear regime below the [Walker breakdown](#). The nanowires on the right are twice as wide as the ones on the left, which is why there are twice as many small arrows in the y-direction denoting the magnetisation direction.

When driven by the external field, the [transverse domain wall](#) (Fig. [2.18](#)) does not transform; only its out of plane component increases (not visible in the figure) but after a while an equilibrium configuration is reached and the domain wall is driven smoothly forward with a constant velocity.

The [vortex domain wall](#) (Fig. [2.19](#)), on the other hand, does change shape. The [vortex core](#) is pushed out of the nanowire and the wall is transformed into a transverse domain wall. This transverse wall then behaves the same as the one shown in Fig. [2.18](#): an equilibrium configuration is reached and the wall is driven forward by the external field.

Above the [Walker breakdown](#) the domain wall cannot adapt its shape to an equilibrium state and Figs. [2.20](#) and [2.21](#) illustrate the dynamics in this regime.

In the 100 nm wide nanowire, an [antivortex core](#) is nucleated at the bottom, which then traverses the nanowire to annihilate at the other side. At this point in time the domain wall again is a [transverse domain wall](#) but with its magnetisation pointing the other direction. Subsequently a new [antivortex core](#) is nucleated, now with the opposite [polarity](#), which again traverses the nanowire to annihilate at the other side. Above the [Walker breakdown](#), the domain wall thus displays periodic transformations between an antivortex and a transverse domain wall configuration while it is driven forward.

In the 400 nm wide nanowire, something similar is observed. But, now the equilibrium domain wall is a [vortex domain wall](#). Similarly to what happens below the [Walker breakdown](#), the [vortex core](#) is pushed out of the nanowire and the domain wall transforms into a [transverse domain wall](#). However, now a new [vortex core](#) (again with the opposite [polarity](#)) nucleates and is pushed to the other side of the domain wall where it is annihilated again. To summarise, the domain wall displays periodic transformations between a vortex domain wall and a transverse domain wall configuration during its forward motion.

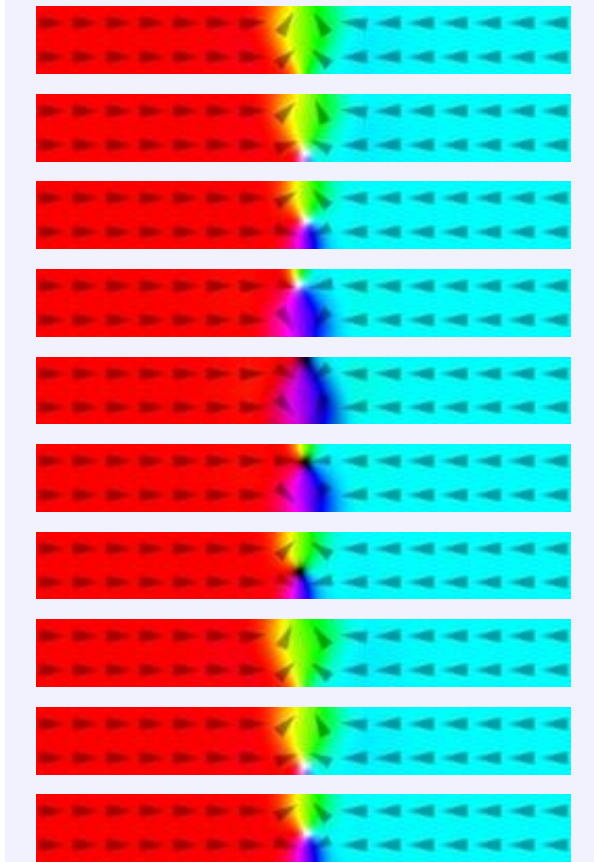


**Figure 2.20:** Snapshots (3 ns apart) of a field-driven (2 mT) transverse domain wall above the Walker breakdown in a permalloy nanowire. The figures are centred around the domain wall during its motion.

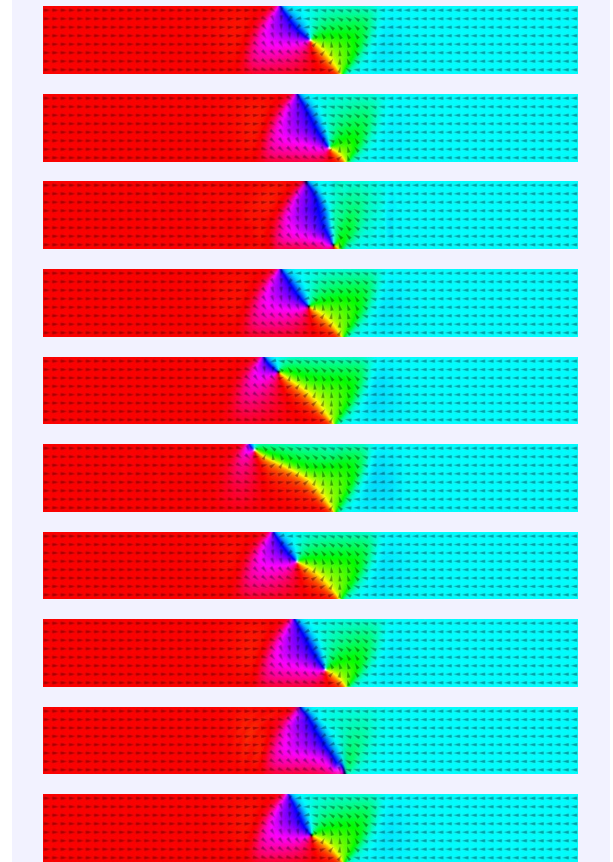


**Figure 2.21:** Snapshots (3 ns apart) of a field-driven (2 mT) vortex domain wall above the Walker breakdown in a permalloy nanowire. The figures are centred around the domain wall during its motion.

### Current-driven domain wall motion

As explained in Section 1.3.2, a [spin-polarised current](#) can transfer angular momentum from the conduction electrons to the local magnetisation. This mechanism can also be used to drive domain walls: *current-driven domain wall motion*. This motion is quite similar to [field-driven domain wall motion](#). To avoid unnecessary repetition, the motion of [transverse domain walls](#) will not be discussed explicitly. The differences between the current and field-driven case are analogous to the changes observed in a [vortex domain wall](#), which we will discuss below.

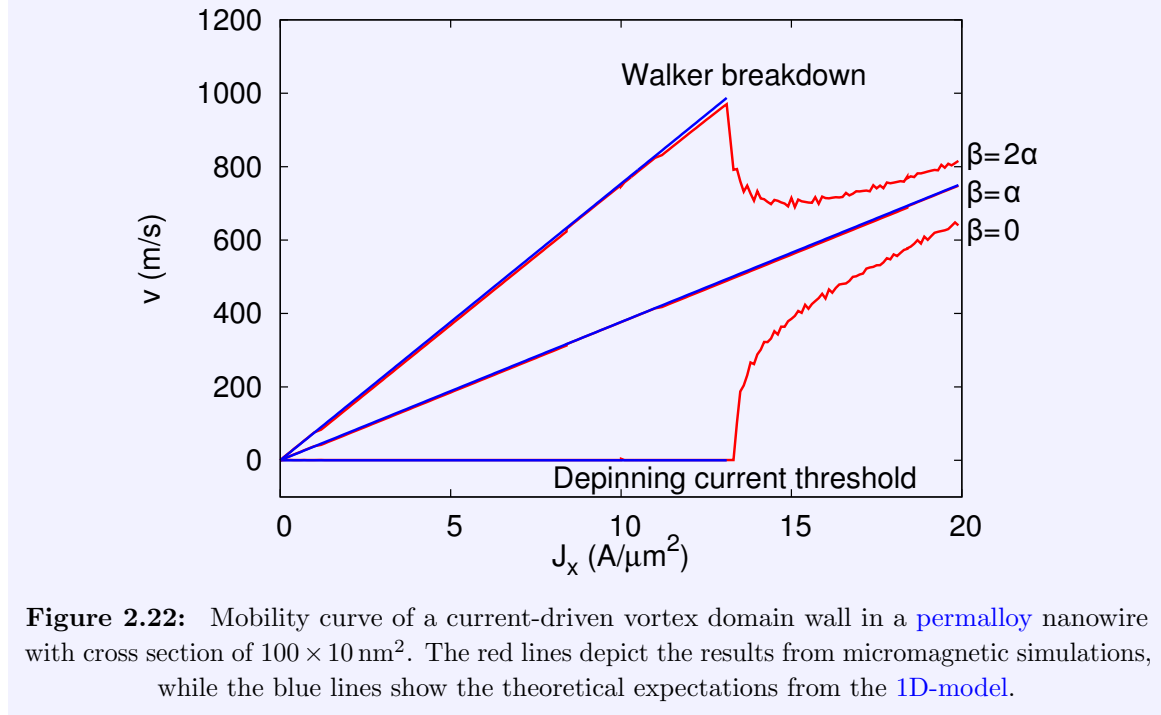
Similar to field-driven domain wall motion, for current densities below the [Walker breakdown](#), Eq. (2.25) reduces to

$$v = -\frac{\beta}{\alpha} b J_x, \quad (2.32)$$

where the notation  $J_x$  signifies a current density applied along the x-axis.



As shown in Fig. 2.22 there is a very good agreement between the simulation results and the theoretical predictions below the Walker breakdown. So, in contrast to field-driven domain wall motion, there is almost no influence of the domain wall asymmetry.



We consider a permalloy (cf. page 17) nanowire with cross-sectional dimensions of  $400 \times 10 \text{ nm}^2$  in which the vortex wall is the stable equilibrium domain wall configuration [61]. The characteristics of the domain wall motion are largely determined by the degree of non-adiabaticity  $\beta$ , see Fig. 2.22. The adiabatic case ( $\beta = 0$ ) shows an intrinsic *depinning current threshold* below which the domain wall is not moving (this pinning mechanism is called *intrinsic pinning*) and above which the domain wall moves at a speed dependent on the applied current. Similarly as in Fig. 2.19, below the *depinning current threshold* the *vortex domain wall* transforms into a *transverse domain wall*. Once the transverse domain wall is formed, the internal structure is such that an equilibrium shape is obtained for which the effective field torques balance the adiabatic spin-transfer torques resulting in zero net torque, and consequently no movement. Also above the *depinning current threshold* (similar as in Fig. 2.21) a transverse domain wall is formed. However, since the adiabatic spin transfer torques are larger, the transverse domain wall can insufficiently adapt its internal structure to balance the spin transfer torques. As a result the transverse domain wall becomes unstable, giving rise to the formation of a vortex wall. Furthermore, the vortex core now has an opposite core *polarity* and travels towards the opposite transverse direction while moving along the wire as shown in Fig. 2.23. This way a periodic movement is observed which is characterised by successive vortex and transverse domain wall formations. The vortex *polarity* determines the transverse direction in which the vortex core moves. A vortex with negative *polarity* moves downwards, while a vortex with positive *polarity* moves upwards.



**Figure 2.23:** The path of a vortex core in a [permalloy](#) nanowire where the vortex domain wall is driven by a spin-polarised current and  $\beta = 0$ .

When a non-adiabatic contribution to the spin transfer torque is taken into account with  $\beta > \alpha$ , two velocity vs. applied current regimes are separated by the [Walker breakdown](#), as shown in Fig. 2.22. Below the [Walker breakdown](#) the vortex domain wall again transforms into a transverse domain wall. However, due to the extra non-adiabatic (field-like) torques this wall is able to move along the wire without changing its shape, resulting in a constant velocity. Above the Walker breakdown, again a periodic movement with a successive formation of vortex and transverse domain wall structures takes place. The extra non-adiabatic contributions to the torque give rise to a larger net velocity along the wire. Contrary to the  $\beta = 0$  case, a vortex with positive [polarity](#) now moves in the downward direction while an oppositely polarised vortex moves in the upward direction (Fig. 2.24).



**Figure 2.24:** The path of a vortex core in a [permalloy](#) nanowire where the vortex domain wall is driven by a spin-polarised current and  $\beta = 2\alpha$ . The differences in the shape of the path of the vortex core between this figure and Fig. 2.23 can be explained by the chirality of the vortex.

When  $\beta = \alpha$  (Fig. 2.25), the net transverse torques (adiabatic and non-adiabatic) acting on the core balance each other, resulting only in a longitudinal vortex movement along the wire axis and consequently in a linear velocity vs. current characteristic.



**Figure 2.25:** The path of a vortex core in a [permalloy](#) nanowire where the vortex domain wall is driven by a spin-polarised current and  $\beta = \alpha$ .

### (Anti)vortex core motion

As seen in the previous sections, the domain wall type, the (anti)vortex core [polarity](#), and the [degree of non-adiabaticity](#) influence the transverse direction in which the core moves while the domain wall as a whole moves forward.

Here, these differences will be explained based on the torques in the [Landau-Lifshitz equation](#). We first look at the difference between a field driven vortex and antivortex domain wall. To this end, we repeat Eq. (1.20), written in its explicit form

$$\dot{\mathbf{m}} = -\frac{\gamma_0}{1 + \alpha^2} \mathbf{m} \times \mathbf{H}_{\text{eff}} - \frac{\alpha\gamma_0}{1 + \alpha^2} \mathbf{m} \times (\mathbf{m} \times \mathbf{H}_{\text{eff}}). \quad (2.33)$$



The torques due to the first term in Eq. (2.33) are shown schematically in Figs. 2.26 and 2.27 for an antivortex and vortex domain wall respectively. The torques due to the damping term all point in the positive x-direction (which is the direction in which the field was applied) and are not depicted. For the antivortex domain wall, these torques result in an upward motion of the antivortex core in the domain wall, in accordance with Fig. 2.20. For the vortex domain wall, the vortex core moves diagonally in the direction of the “yellow region” in the bottom right.

For both domain wall types an opposite core polarity would result in a core motion in the opposite direction. A change in chirality (in the case of a vortex wall) results in a diagonal motion in the opposite x-direction but the same y-direction. Finally, when looking at a tail-to-tail instead of a head-to-head domain wall with the same polarity (and chirality in the case of a vortex wall), the x-direction of the core motion remains the same, but the y-direction is switched.

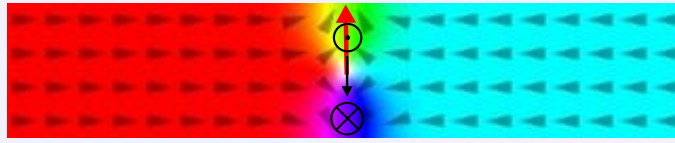


**Figure 2.26:** A schematic overview of the torques (black arrows) corresponding to the first term of Eq. (2.33) acting on the different regions of an antivortex domain wall driven by an externally applied field in the positive x-direction. The direction of the core motion is depicted as a red arrow.

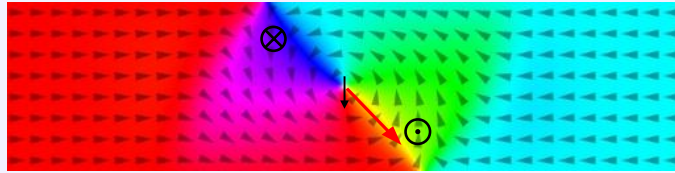


**Figure 2.27:** A schematic overview of the torques (black arrows) corresponding to the first term of Eq. (2.33) acting on the different regions of a vortex domain wall driven by an externally applied field in the positive x-direction. The direction of the core motion is depicted as a red arrow.

Next, we turn our attention to a vortex domain wall driven by a spin-polarised current with the electrons flowing in the positive x-direction. We will not repeat the argument for the case of an antivortex domain wall as the reasoning is similar.

Equation (1.22) can be written in its explicit form as

$$\begin{aligned} \dot{\mathbf{m}} = & -\frac{\gamma_0}{1+\alpha^2} \mathbf{m} \times \mathbf{H}_{\text{eff}} - \frac{\alpha\gamma_0}{1+\alpha^2} \mathbf{m} \times (\mathbf{m} \times \mathbf{H}_{\text{eff}}) \\ & -\frac{1}{1+\alpha^2} [b\mathbf{J} \cdot \nabla] \mathbf{m} + \frac{\beta-\alpha}{1+\alpha^2} \mathbf{m} \times [b\mathbf{J} \cdot \nabla] \mathbf{m}, \end{aligned} \quad (2.34)$$

where the second line contains the [spin-transfer torque](#) terms. The torques represented by the first of these terms are shown schematically in Fig. 2.28 and result in a net motion of the

vortex core in the positive x-direction (independent of its polarity or chirality). This result is also visible in Fig. 2.25.

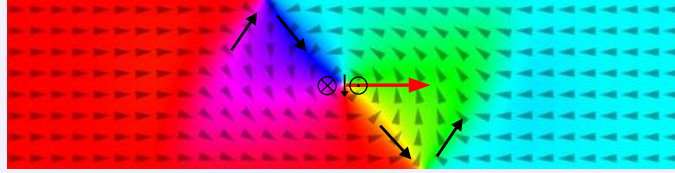


**Figure 2.28:** A schematic overview of the torques (black arrows) corresponding to the first spin-transfer torque term of Eq. (2.34) acting on the different regions of a vortex domain wall driven by an spin-polarised current with the electrons flowing in the positive x-direction. The direction of the core motion is depicted as a red arrow.

The torques due to the term proportional with  $\beta - \alpha$  are shown schematically in Fig. 2.29 for the case  $\beta > \alpha$ . In this case, the vortex core moves diagonally to the bottom right, as also shown in Fig. 2.24. When  $\beta = \alpha$  these torques do not act on the core anymore, and when  $\beta < \alpha$  the core moves in the opposite direction because these torques also point in the opposite direction. This can be verified by comparing the core motion in Figs. 2.23 and 2.24.

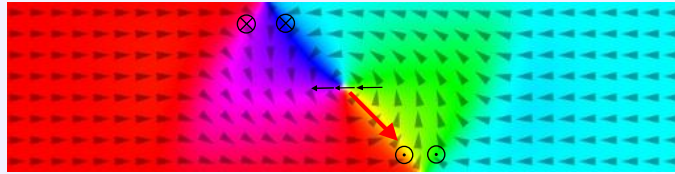


**Figure 2.29:** A schematic overview of the torques (black arrows) corresponding to the second spin-transfer torque term of Eq. (2.34) acting on the different regions of a vortex domain wall driven by an spin-polarised current with the electrons flowing in the positive x-direction with  $\beta > \alpha$ . The direction of the core motion is depicted as a red arrow.

Finally, based on these examples, it should be clear how to predict the core motion for other domain walls e.g. with a different core **polarity** or **chirality**.

### Domain wall based technology

By now, one could start wondering if this domain wall motion could be of any use in *real-world applications*. In conventional *electronics*, where only electrical charges are transported, the use of domain walls is rather limited due to the large external fields necessary to move them. However, there exist practical applications, e.g. Novotechnik [69, 70] has made a spiral-shaped sensor, in which domain walls are generated/annihilated depending on the angle between the sensor and an external magnet. Because the electrical resistance of the nanowires discretely changes with the number of domain walls, one can electrically measure the exact angular position of the sensor. This sensor is for instance used in the automotive industry to determine the position of the steering wheel.

The most promising uses of domain wall technology lie in *spintronics* applications. In these applications, not only the charge but also the spin of the **electron** is used. As shown in Section

2.1.4, a [spin-polarised current](#) can move a domain wall through a nanowire, without the need for large magnetic fields.

An example of a possible memory device is the *racetrack memory*, presented in 2008 by S. Parkin[53, 71]. As shown in Fig. 2.30, in this device the bits are represented by the magnetisation of the domains ((anti)parallel to the longitudinal nanowire axis), see Figs. 2.30 (a) and (b). The position of these bits (domains) can be manipulated by a [spin-polarised current](#), applied along the nanowires length axis, to move them over a read or write head [Fig. 2.30 (c) and (d)]. The read head measures the magnetisation direction with the help of a TMR sensor. The write head applies a current through a conductor perpendicular to the nanowire to generate stray fields which switch the data bit/magnetic domain to the desired direction. By incorporating these nanowires into a 3D structure, high storage densities can be reached, as shown in Fig. 2.30 (e).

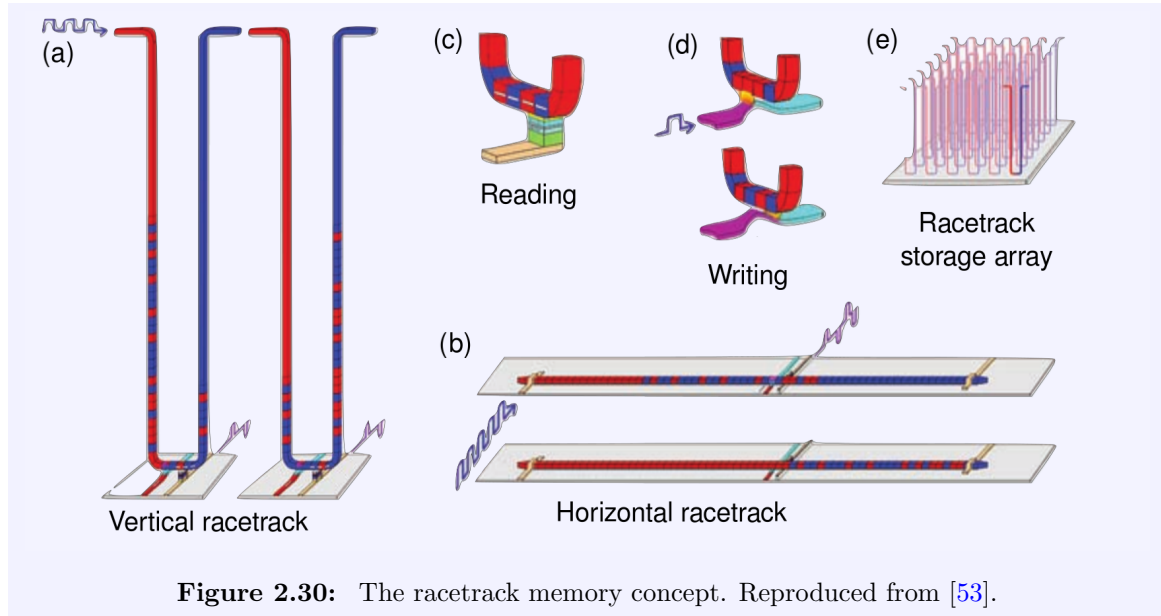


**Figure 2.30:** The racetrack memory concept. Reproduced from [53].

In later versions, the [racetrack memory](#) concept was extended to [PMA](#) materials[72], versions which exploited the [Dzyaloshinskii-Moriya interaction](#) [73] or even antiferromagnetically coupled nanowires[74] to further improve its performance.

Today all computations are performed electronically, while most data storage is magnetic. In an ideal configuration it should be possible to perform calculations as well as store data magnetically. Therefore, an other popular use of domain walls in [spintronics](#) is *domain-wall logic*[75, 76]. There have been developments in this direction, i.e. the concept of domain wall logic gates have been proven to work in simulations, or in some cases even experimentally[75, 77, 78]. In a first implementation these gates were quite bulky and relied on large external fields to operate[75]. Recently however, also [current-driven domain wall motion](#) based logic gates were presented where the magnetic bits were represented by the direction of the domains[77] or

even the walls in between the different domains[79].

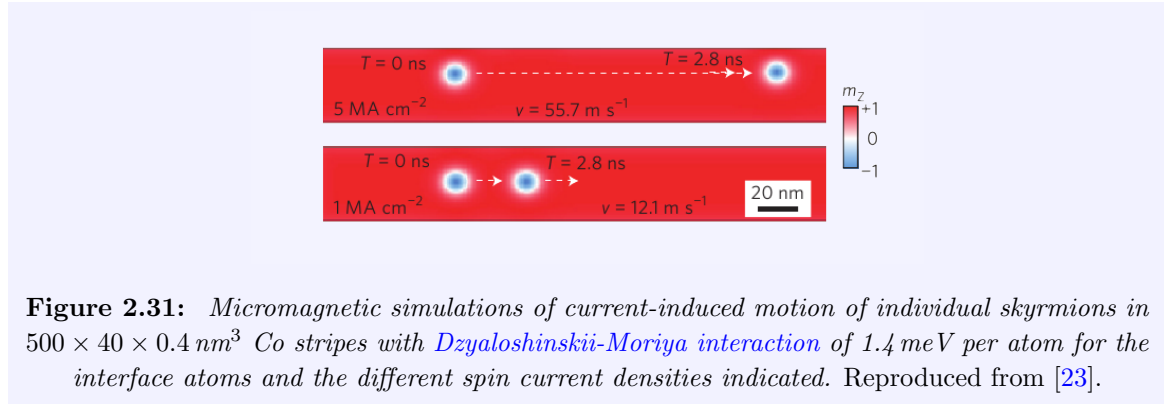


**Figure 2.31:** Micromagnetic simulations of current-induced motion of individual skyrmions in  $500 \times 40 \times 0.4 \text{ nm}^3$  Co stripes with *Dzyaloshinskii-Moriya interaction* of  $1.4 \text{ meV}$  per atom for the interface atoms and the different spin current densities indicated. Reproduced from [23].

Although the *racetrack memory* might be commercially available within a few years for specialised purposes, one should be careful not to oversell these ideas[80]. There is a big difference between laboratory controlled experiments of a proof of concept and a reliable and performant commercially available device. Domain wall based technologies have been in the pipeline for over 10 years now, but just like the now-obsolete *bubble memory*, there are difficulties in achieving the necessary integration densities. However, these difficulties might be overcome in the coming years with the recent realisation of stable skyrmions (only a few nm large) at room temperature[81, 82]. People are already working on simulations of skyrmion racetrack memories[23, 24, 83] (see Fig. 2.31) and even skyrmion-motion based logic[84].

The largest drawback all these devices share is that the required current densities are of the order of  $10^{12} \text{ A/m}^2$ . For comparison, the current density used in copper wires in household appliances is typically of the order of  $10^6 \text{ A/m}^2$ . These huge current densities result in a large *Joule heating* of the nanowires. This effectively limits the use of these current densities to pulses of only a few ns long without risking to destroy the nanowires. However, also in this respect solutions exist. For instance, in electric field driven domain wall motion there is no need for large current densities[85, 86] and finally, as mentioned in the beginning of this section, in domain wall based sensors[87], the domain wall velocity is not critically important.

### 2.1.5 Overview of this chapter

The first part of this section contained an overview of domains, domain walls, and their motion in nanowires. We saw that this motion can be driven by an externally applied magnetic field or a *spin-polarised current* and that a complete understanding of domain wall motion in magnetic nanowires is required to enable future domain-wall based technologies to work reliably. As the production process of these devices dictates that the nanowires contain material defects, it is important that their effects can be taken into account.

In Section 2.2, we will investigate how defects can be implemented in *micromagnetic simula-*

tions. Real defects give rise to a [pinning potential](#) which can be characterised in terms of a depth and an interaction range. We will investigate how individual defects can be included by comparing the numerical properties of simulated pinning potentials to experimental results reported in literature. Alternatively, in [polycrystalline](#) samples, the [grain boundaries](#) are a source of disorder. In the second part of this section a method to include material grains in simulations is presented.

In Section 2.3, the developed methods to include defects will be used in [micromagnetic simulations](#) of [current-driven domain wall motion](#) through disordered nanowires. Their influence on the domain wall mobility will be investigated. We will see that the apparent size of the [degree of non-adiabaticity](#) in current driven domain wall motion, which was a topic of debate at the time we presented this research, can be influenced by disorder. Finally, simulations of [polycrystalline permalloy](#) nanowires will be presented in which we again investigate the domain wall mobility.

The methods and results presented in this chapter have been published in [88], [89] and [90] and were added as features to [MuMax3](#) [45].

## 2.2 Simulating disordered nanowires

We ended Section 2.1.4 with an overview of domain wall based technological devices. In the development of such devices, [micromagnetic simulations](#) play a crucial role. However, to be useful these simulations should be as realistic as possible. For instance, the effects of material imperfections and [thermal fluctuations](#) should be taken into account. In this section we investigate how material defects or polycrystalline materials can be included in the simulations.

### 2.2.1 Defect characterisation

Several experiments to characterise the nature of trapping sites and to quantify their properties have been conducted[91–93]. In these studies, it was found that defects give rise to *potential wells* for [domain walls](#), defined as local minima in the micromagnetic energy profile, which can be characterised in terms of their depth and interaction range. We will numerically investigate the properties of defects implemented in different ways and propose a method to realistically include the influence of intrinsic defects in 2-dimensional (2D) numerical simulations.

Experimentally, the depth of a defect *pinning potential* is determined to be between 1 to 5 eV [91–93], while its interaction range is of the same size as the diameter of the [vortex core](#) used to probe the defect, i.e. approximately 20 nm[91, 93, 94].

In numerical simulations the energy of the system is easily accessible which makes measuring the properties of the [potential well](#) a less challenging task than in experiments, where only macroscopic quantities are measurable. This advantage is exploited to perform a systematic study of different possibilities to include defects in simulations.

To determine the properties of the [potential well](#) in micromagnetic simulations we simulate a disk (diameter: 750 nm, thickness: 10 nm) in which a defect is introduced in the central region, see Fig. 2.32 (a). A magnetic [vortex core](#) is inserted 200 nm from the centre. From that point, the vortex relaxes, following a spiralling trajectory towards the disk centre. During this slow relaxation (over 400 ns) the total energy of the system is probed, see Fig. 2.32.

The depth of the [potential well](#) is extracted from the difference between the energy with and without defect. The interaction range is measured from the centre of the defect and is determined by the radius at 10% of its depth, as shown in Fig. 2.32.

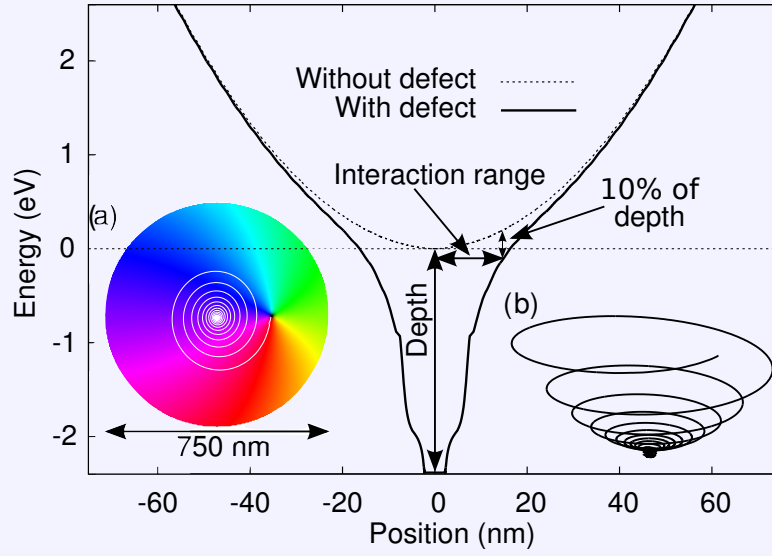


**Figure 2.32:** The magnetic energy of a vortex in a disk with (full line) and without (dotted line) a defect, implemented as a region in the centre of size  $10 \times 10$  nm with the [exchange stiffness constant](#) reduced by 70% at the boundaries. Without the defect the energy profile has a parabolic shape. The defect causes an additional [potential well](#) to this, for which the depth and interaction range are shown. Inset (a) depicts the initial magnetisation in the disk and the trajectory the [vortex core](#) follows while it relaxes into the defect. Inset (b) depicts the energy of the system.

One way to simulate a defect is to focus on its physical size: the thickness of the film is not everywhere the same. We perform 3-dimensional (3D) simulations of a disk in which the thickness of the centre region is reduced to 2.5, 5 or 7.5 nm, corresponding with 1, 2 or 3 [finite difference cells](#). We also investigated if we can replace these simulations by performing an equivalent and faster 2D simulation in which the [saturation magnetisation](#) is reduced. A second way to simulate a defect is to introduce a region with a reduced [exchange stiffness constant](#) at the boundaries.

In the 2D simulations the disks are discretised using cells of  $3.125 \times 3.125 \times 10 \text{ nm}^3$ . In the 3D simulations the thickness of the disk is further discretised using cells with a thickness of 2.5 nm. Simulations were performed for defect regions of different sizes of  $1 \times 1$  up to  $4 \times 4$  [finite difference cells](#) with a reduction in the [saturation magnetisation/exchange stiffness constant](#) at the boundaries ranging from 10 to 100% (see Fig. 2.33). In the simulations in which the [saturation magnetisation](#) is reduced, the [exchange length](#) at the boundary of the defect region is kept to its original value.

The results of the 3D simulations are shown as green points in Fig. 2.33 (a). It is observed that the depth of the [potential well](#) rises as function of thickness reduction in the defect region and is larger for larger defect regions.

An effort is made to investigate if these 3D simulations can be reduced to equivalent 2D



simulations in which defects are simulated as regions with a reduced [saturation magnetisation](#). The depth of the resulting [potential wells](#) is linearly dependent on the reduction in [saturation magnetisation](#) and is larger for larger defects, see Fig. 2.33 (a). To make the 2D simulations equivalent to the 3D ones, it is not sufficient to reduce the [saturation magnetisation](#) as much as the thickness reduction. There are two different approaches possible to make the simulations equivalent. A first approach is to include regions with larger sizes in the 2D simulations. A second approach is to reduce the [saturation magnetisation](#) more than the corresponding reduction in thickness. To estimate the size of this reduction Fig. 2.33 (a) can be used as a guidance.

For sizes larger than  $1 \times 1$  [finite difference cells](#) a jump is observed for defects with the [saturation magnetisation](#) set to 0. This jump is caused by the possible disappearance of the [vortex core](#) in the defect. This phenomenon was also observed in [95] and is energetically favourable as the vortex core (which contains a lot of energy) can disappear together with its energy in the defect region.

The interaction range is weakly dependent on the thickness reduction and at first sight seems to be dependent on the size of the defect. However, this dependency arises mainly because the interaction range is measured from the centre of the defect. If the size of the defect is deducted from the interaction range, it is found that the resulting distance is almost constant and equal to the [vortex core](#) diameter. This observation is supported by Refs. [92] and [93] where it is stated that the measured energy profile is convolved with the energy profile of the [vortex core](#), resulting in an interaction range of approximately the same size as the diameter of the [vortex core](#). The interaction ranges for the 3D simulations are approximately 20 nm, which is a factor two larger than in the 2D simulations. This is consistent with the observation that the [vortex core](#) is also larger in 3D simulations[96].

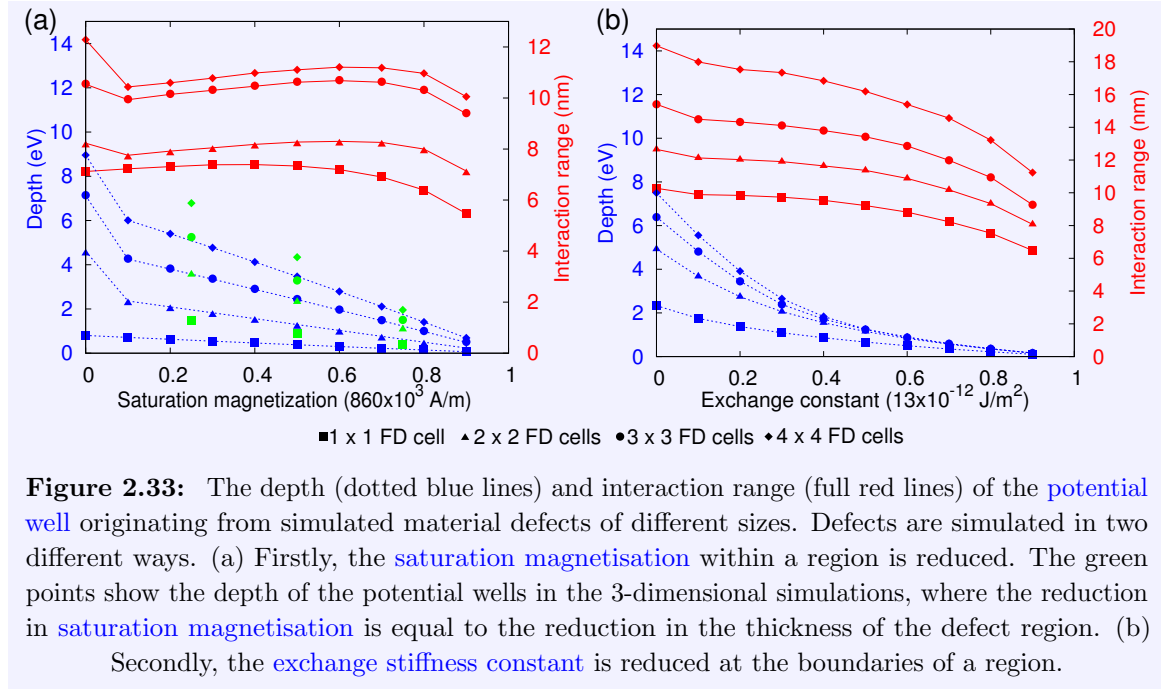
In the simulations where defects are implemented as regions with a reduced [exchange stiffness constant](#), it is found that the depth of the [potential well](#) slowly rises as a function of the reduction in the [exchange stiffness constant](#). It is again observed that larger defects give rise to deeper potential wells. See Fig. 2.33 (b).

The interaction range is weakly dependent on the reduction in the [exchange stiffness constant](#) and rises for larger defects. The seeming size dependency is again caused by the used method, i.e. the interaction range is measured from the centre of the defect region and not from the edge.

Based on these results, the following methods to realistically include defects in micromagnetic simulations are proposed: Firstly, defects can be included as regions with a size of approximately 10 by 10 nm (similar to the film thickness) with their [saturation magnetisation](#) reduced by 50%. Alternatively, defects can be defined as regions with the [exchange stiffness constant](#) reduced by 70% at the boundaries. The [potential well](#) caused by such defects is shown in Fig. 2.32 and has a depth close to the average of the experimentally measured values. For both



approaches the interaction range is approximately the same as the [vortex core](#) diameter.



Although these results are based on a case study on [permalloy](#) nanowires, they can be extended to other materials as we included defects in our simulations based on the physical properties of real defects. For instance, the varying saturation magnetisation is equivalent to a varying thickness and the reduced exchange coupling corresponds to misaligned crystal lattices. These, together with possible variations in the anisotropy strength/direction in [PMA](#) materials, are common defects in nearly all materials.

### 2.2.2 Polycrystalline materials

In contrast to the individual defects characterised above, disorder can also exist on the level of the *material grains*.

*Polycrystalline* materials are crystalline materials without long-range order in the crystal lattice. Typically, when a thin film is grown, a few *seeds* are present around which the other atoms place themselves. In this way, a material grain grows until it finds a neighbouring grain. Grain properties as grain size, thickness, etc. can vary, and there is a mismatch between the crystal lattices at the *grain boundaries*. Numerical[88] as well as experimental[92, 93, 97] investigations show that distributed disorder gives rise to local [pinning potentials](#). For a magnetic vortex in [permalloy](#) (cf. page 17), the potentials have a depth of 1 to 5 eV[91–93], and an interaction range approximately equal to the [vortex core](#) diameter since the measured [potential well](#) is convolved with the [vortex core](#) profile [93, 97]. Because the trapping site density in experiments is correlated with the grain density [97], the grain structure of the material is

suspected as a possible source of disorder[93, 97]. In this section, we present a method to simulate the complete grain structure of **polycrystalline** materials in a computationally efficient way.

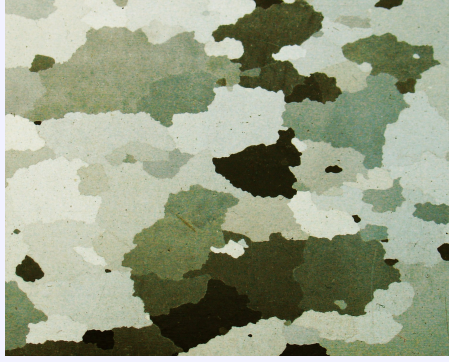


**Figure 2.34:** Uncoated electrical steel is an example of a **polycrystalline** material where the different grains are visible by the naked eye. By Zureks (Own work) [GFDL (<http://www.gnu.org/copyleft/fdl.html>)], via Wikimedia Commons

The grain structure of the **polycrystalline** material is implemented using a *Voronoi tessellation*, in which each **Voronoi cell** represents a grain. This approach enables one to define both edge roughness[98, 99] and material grains [100]. Subdividing the material in grains starts with defining randomly distributed points (*Voronoi centres*) across the simulation geometry. A *Voronoi cell* consists of all points closest to a common **Voronoi centre**. To cover the infinitely long simulation geometry we virtually divide the nanowire into a grid of square tiles, sufficiently large so we can expect at least a few **Voronoi centres** per tile. Poisson statistics are used to determine the number of centres in the tile, while their positions are uniformly distributed over the tile using a random number generator with seed based on the tile index. This way we can map each **finite difference cell** in the moving computational domain to a **Voronoi cell** without explicitly storing the complete tessellation along the wire. Indeed, when shifting the computational domain along the wire axis new grains can be inserted from the sides based on the tile index. Also, as the simulation window might sometimes move backwards, this enables grains that previously left the simulation window to re-enter. This implementation is sketched in Fig. 2.35.

Having subdivided the geometry, one can vary the local material parameters in and between the grains. This way, grain dependent anisotropy directions can represent the different lattice orientations in grains. The other possibilities are a grain dependent **saturation magnetisation** representing thickness variations between grains[101] and a reduced **exchange stiffness constant** at the **grain boundaries** representing a reduced magnetic coupling between neighbouring grains[100].

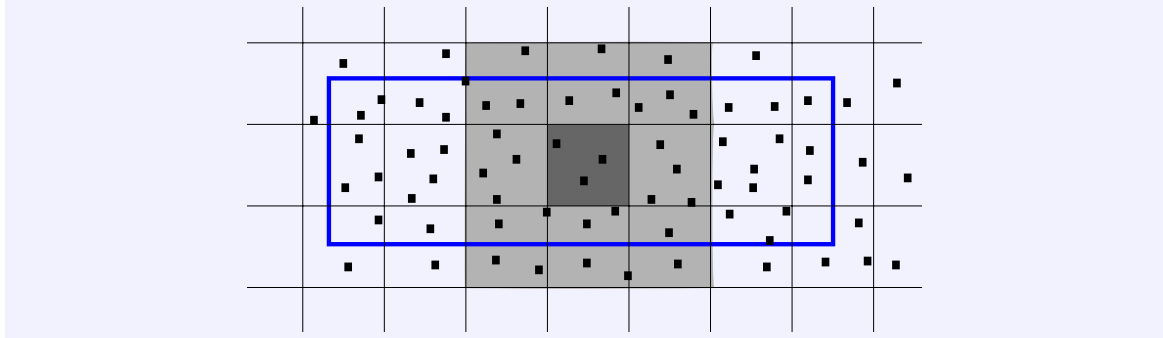


**Figure 2.35:** The different **Voronoi centres** (black cells) are generated within the different tiles, with a random generator that uses the tile indices as a seed. For each **finite difference cell** the **Voronoi cell** to which it belongs is determined by looking for the closest **Voronoi centre** in its own tile (dark grey) and all neighbouring (light grey) tiles. In this way also **Voronoi centres** outside the simulation window (blue) are found.

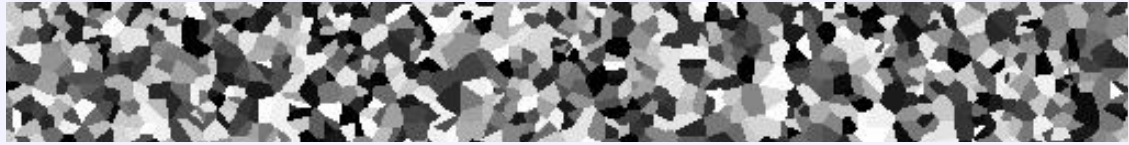


**Figure 2.36:** An example of a nanowire with a surface of  $1600 \times 200 \text{ nm}^2$  subdivided into **Voronoi cells** (gray scale) with an average diameter of 20 nm.

In the next section, we will investigate the influence of disorder on domain wall motion through a nanowire. We will consider **permalloy** (cf. page 17) nanowires of thickness 10 nm and width 200 nm discretised in **finite difference cells** of size  $3.125 \times 3.125 \times 10 \text{ nm}^3$ . In Fig. 2.36 an example of the typical grain structure generated with **Voronoi cells** with an average diameter of 20 nm is shown.

## 2.3 Domain wall motion in disordered nanowires

### 2.3.1 Disordered nanowires with distributed local defects

Having investigated how defects can be included in magnetic nanowires, we will now investigate what the influence of such defects on [current-driven domain wall motion](#) is. We recall from Section 1.3 that it is necessary to add two [spin-transfer torque](#) terms (an adiabatic and a non-adiabatic term)[27] to the [Landau-Lifshitz equation](#) to correctly describe the influence of a [spin-polarised current](#)  $\mathbf{J}$  on the magnetisation dynamics. In the resulting equation,

$$\dot{\mathbf{m}} = \gamma_0 \mathbf{H}_{\text{eff}} \times \mathbf{m} + \alpha \mathbf{m} \times \dot{\mathbf{m}} - [b\mathbf{J} \cdot \nabla] \mathbf{m} + \beta \mathbf{m} \times [b\mathbf{J} \cdot \nabla] \mathbf{m}, \quad (2.35)$$

$\beta$  denotes the [degree of non-adiabaticity](#). Since the introduction of the non-adiabatic term, there has been a lot of debate on the magnitude of  $\beta$ , with theoretically predicted values ranging from  $\beta \approx \alpha$  [27, 102, 103] over  $\beta = 2\alpha$  [65] to  $\beta = 4\alpha$  [104]. Additionally, experiments have been unable to converge to one value. In this section, we clarify some of these results by explaining how disorder can influence these experiments. In Ref. [95] the effects of distributed disorder, implemented as voids, on transverse domain wall dynamics have been studied. Here, this study is extended to wider wires in which the vortex defines the equilibrium domain wall state, and with disorder implemented as defect regions with a reduced [exchange stiffness constant](#) at their boundaries.

We first turn our attention to the different experimental techniques used to quantify  $\beta$ . One way is to measure the depinning field necessary to pull a vortex out of a [pinning potential](#) in the presence of a [spin-polarised current](#) [105–107]. A similar technique consists of investigating the thermal hopping between pinning sites in the presence of a [spin-polarised current](#) [108] where different values for  $\beta$  are estimated for the same material depending on the magnetic structure: a [vortex domain wall](#) or a [transverse domain wall](#). Another approach is to determine local [vortex core](#) displacements due to [spin-polarised currents](#) in the confining potential of e.g. a pinning site [109], a disk [110], or a square geometry [111]. A third set of experiments, only able to extract  $\beta/\alpha$ , is based on measuring the distance a domain wall is able to cover due to a current pulse with known amplitude and duration. Here, resulting time and space averaged velocities are fitted to theoretical and/or simulated values [112–115]. Apart from these methods to directly quantify  $\beta$  or  $\beta/\alpha$ , electrical and magnetic imaging techniques show domain wall transformations when an electric current is applied, indicating  $\beta \neq \alpha$  [63, 116, 117]. Table 2.1 gives an overview of experiments performed to measure  $\beta$ .

**Table 2.1:** Overview of experimentally obtained values for  $\beta$  in [permalloy](#).

Method	$\beta$	$\beta/\alpha$	Ref.
Current-assisted domain wall depinning from a pinning site	$0.040 \pm 0.005$	2*	[105]
	$0.040 \pm 0.005$	2-4*	[106]
	$0.040 \pm 0.0025$	$\approx 5.3$	[107]
Thermal depinning vortex domain wall	$0.073 \pm 0.026$	$\approx 9$	[108]
	$0.01 \pm 0.004$	$\approx 1$	[108]
Local vortex core movements	0.04	8*	[109]
	$0.15 \pm 0.07$	$> 10$	[110]
	$0.15 \pm 0.02$	$> 7$	[111]
Vortex domain wall motion in nanowires	0.01*	$0.96 \pm 0.02$	[115]
	0.008*	1	[114]
	0.007*	0.7	[113]
	not mentioned	1	[112]

\* based on estimated values of  $\alpha$

Even within the broad range of possible values reported, a clear discrepancy between measurements based on domain wall motion and other methods is present, as these consistently report lower values for  $\beta$  compared to the other methods.

Simulations investigating the effect of sample imperfections on the domain wall mobility have mainly concentrated on nanowire *edge roughness* [98, 118, 119]. It is found that this suppresses the [Walker breakdown](#), allowing the domain wall to move faster for higher applied fields or currents compared to the corresponding nanowire with perfect geometry. These studies, however, neglect the influence of disorder distributed within the wire. Nevertheless, real nanowires contain defects in their microstructure, e.g. *surface roughness*, which can act as pinning centres for the domain walls. Here, we will investigate what influence these effects have on domain wall dynamics.

We consider nanowires with dimensions  $3\,200 \times 400 \times 10\,\text{nm}^3$ , discretised using [finite difference cells](#) of  $3.125 \times 3.125 \times 10\,\text{nm}^3$ . In the previous section we developed a method to include defects in [micromagnetic simulations](#). From experiments [92, 93, 97, 120, 121] it is known that these defects are randomly distributed throughout the wire with densities  $\Sigma$  ranging from 690 to  $2000\,\mu\text{m}^{-2}$ . To include distributed defects in our simulations we introduce small regions ( $9.375 \times 9.375\,\text{nm}^2$  in size) with a reduced [exchange length](#) at their boundaries. By reducing the [exchange stiffness constant](#)  $A_{\text{ex}}$  to 30% of its normal value across the region boundaries, a corresponding reduction in  $l_{\text{ex}}$  of roughly 50% was obtained.

In Fig. 2.37 the [pinning potential](#) for such a single region is shown, illustrating the correspondence with experimentally determined depths of 2 eV. In the simulations we included random distributions of these regions with densities ranging from  $\Sigma = 500$  to  $1500\,\mu\text{m}^{-2}$ .

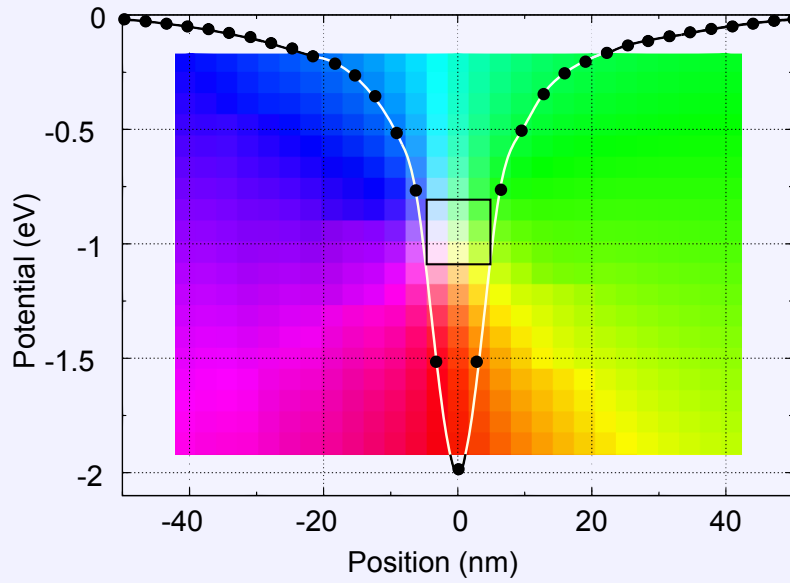


**Figure 2.37:** The potential well of a defect of size  $3 \times 3$  finite difference cells, indicated by the black square, interacting with a vortex core, with the exchange length reduced by roughly 50% at the boundaries. The depth of the potential well is approximately 2 eV and the interaction range is comparable to the size of the vortex core diameter[88].

Averaged velocities are extracted from 25 disorder realisations and for each realisation the domain wall motion is simulated for 20 ns. Figure 2.38 shows averaged velocities  $v$  versus applied current densities  $J_x$ . Comparing the domain wall velocity in the disordered nanowires (coloured lines) to the non-disordered nanowire case (black lines) we observe two main differences:

1. For the adiabatic as well as for the non-adiabatic case a similar depinning threshold appears at much smaller currents than the intrinsic depinning current threshold.
2. In the non-adiabatic case  $\beta = 2\alpha$ , we see a suppression of the Walker breakdown.

The origin of this different behaviour can be found in the interplay between the defects and the vortex domain wall, see Fig. 2.38. In a disordered nanowire (see Fig. 2.39), the vortex core can switch polarity at a defect, implying a change in lateral propagation direction and thus hindering the formation of the transverse domain wall. This polarity switching mechanism, which was not found<sup>1</sup> in Ref. [101], explains the absence of the Walker breakdown and the much smaller depinning current threshold. The pinning mechanism itself is also affected by the disorder: instead of the intrinsic pinning mechanism induced by the internal balancing of the effective field and spin-transfer torques inside the domain wall found in a perfect nanowire, disorder gives rise to an extrinsic pinning mechanism in which the vortex core gets pinned at a defect. In the experimentally accessible current ranges, we observe an average motion of the vortex core in the central region of the wire without the formation of transverse domain walls due to successive core polarity switches at defects (Fig. 2.39). In the event the vortex core

<sup>1</sup>Personal communication with Stiles, M. D.

does reach the edge of the nanowire, we observe that defects at the edges allow the nucleation of a vortex core of opposite **polarity**, as is the case in wires with edge roughness [98]. This resembles the motion of a vortex domain wall in a perfect wire for the case  $\beta = \alpha$  (Fig. 2.25), which explains the values of  $\beta/\alpha$  derived from domain wall motion (cf. Table 2.1). Contrary to these experiments, the other methods quantify  $\beta$  based on non-averaged local magnetisation dynamics and thus are not affected by the **polarity**-switching mechanism described in this section.

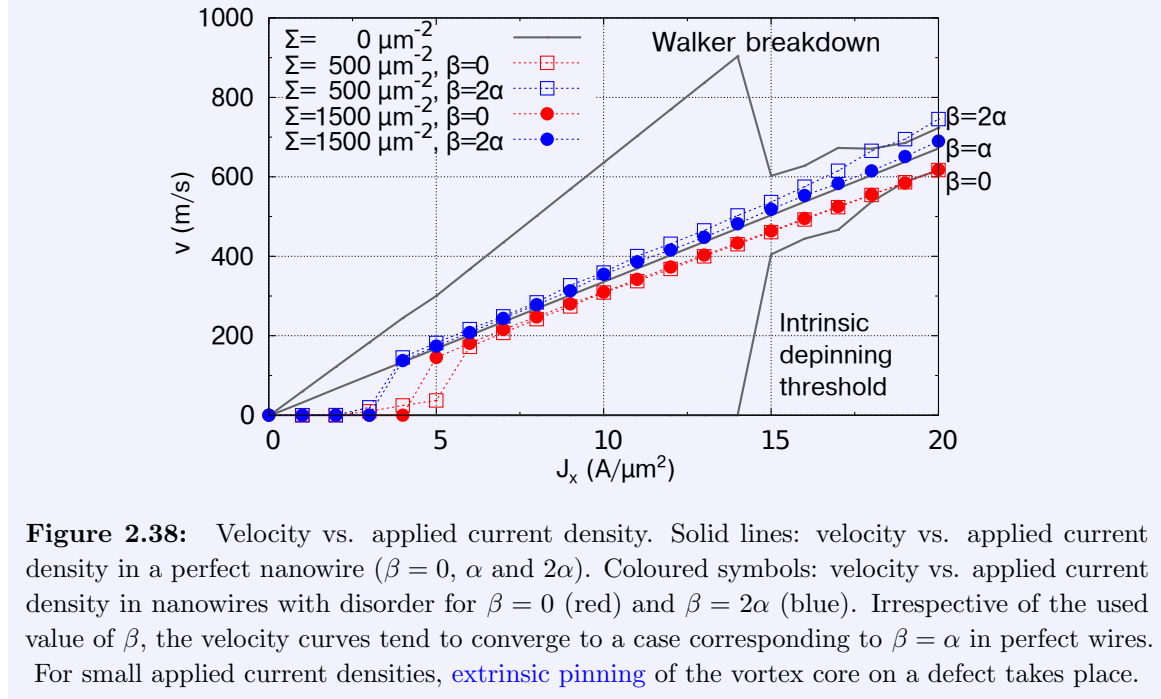


**Figure 2.38:** Velocity vs. applied current density. Solid lines: velocity vs. applied current density in a perfect nanowire ( $\beta = 0$ ,  $\alpha$  and  $2\alpha$ ). Coloured symbols: velocity vs. applied current density in nanowires with disorder for  $\beta = 0$  (red) and  $\beta = 2\alpha$  (blue). Irrespective of the used value of  $\beta$ , the velocity curves tend to converge to a case corresponding to  $\beta = \alpha$  in perfect wires. For small applied current densities, **extrinsic pinning** of the vortex core on a defect takes place.

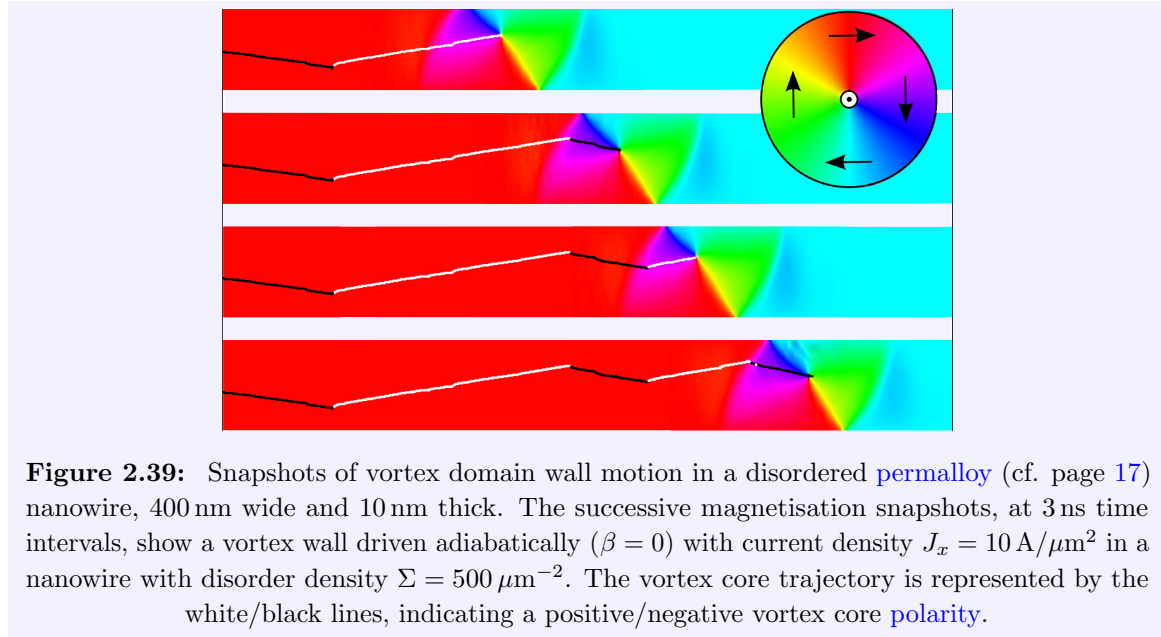


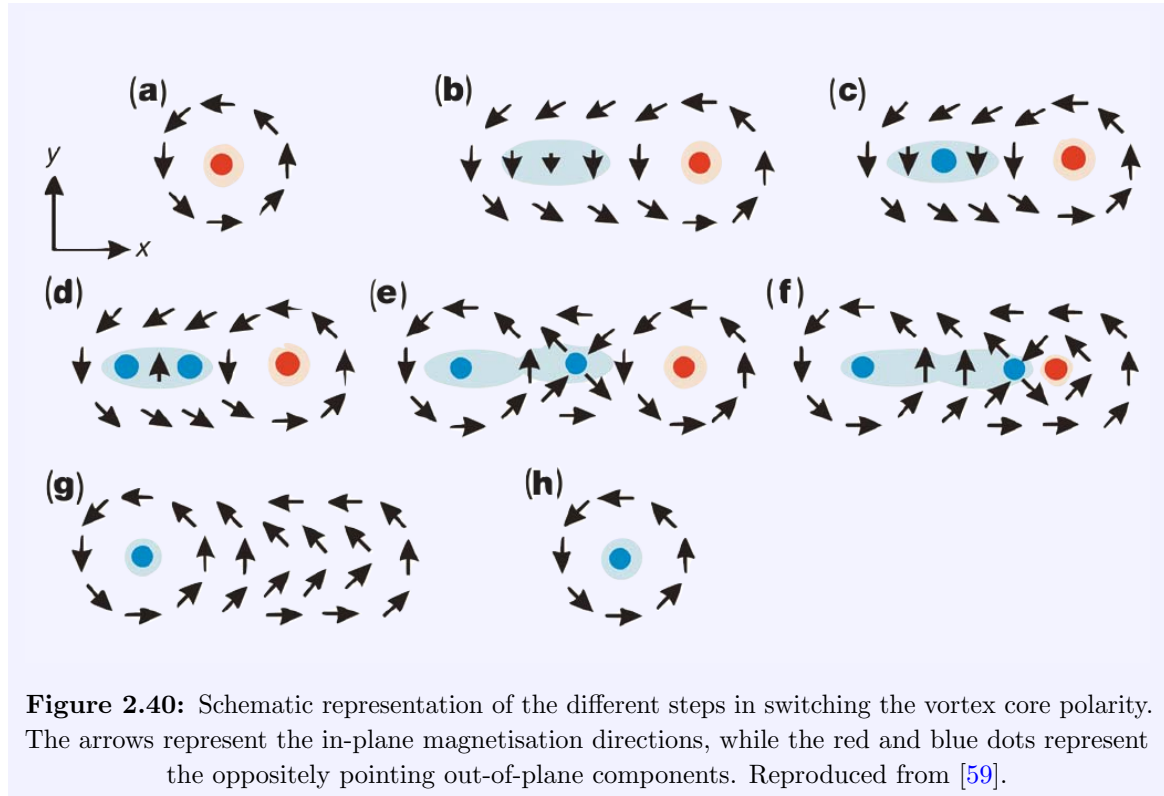
**Figure 2.39:** Snapshots of vortex domain wall motion in a disordered **permalloy** (cf. page 17) nanowire, 400 nm wide and 10 nm thick. The successive magnetisation snapshots, at 3 ns time intervals, show a vortex wall driven adiabatically ( $\beta = 0$ ) with current density  $J_x = 10 \text{ A}/\mu\text{m}^2$  in a nanowire with disorder density  $\Sigma = 500 \mu\text{m}^{-2}$ . The vortex core trajectory is represented by the white/black lines, indicating a positive/negative vortex core **polarity**.



To understand the vortex core polarity switching mechanism, we first look into the switching mechanism as observed in gyrating vortices in nanodisks[59]. There, the switching takes place in different steps, as schematically shown in Fig. 2.40. When a vortex core (a) moves, an area with opposite out-of-plane magnetisation is formed next to it (b),(c). When the vortex core has a sufficiently high velocity, there is enough energy available for the nucleation of a vortex-antivortex pair (d),(e). This pair splits up and the antivortex annihilates with the original vortex (f),(g). This process releases energy as spin-waves and finally, only the new vortex, with opposite polarity, remains (h).

For vortex domain wall motion in a perfect nanowire, this is not observed as the vortex core never reaches the necessary velocity for the antivortex-vortex pair to nucleate. Instead, the vortex core is pushed towards the nanowire edge and annihilates there. Also at the edge, a new vortex core with opposite core polarity nucleates again.

In disordered nanowires, on the other hand, the lower exchange coupling at grain boundaries or defect regions lowers the energy barrier which prevents the vortex-antivortex pair to nucleate. Consequently, the vortex core can switch its core polarity via the mechanism described above at these defects.



Next, we also investigated the effect of voids on the domain wall mobility and found qualitatively the same mobility curves. Although the [pinning potentials](#) caused by realistic defects are less deep[88] than their counterparts caused by voids, they also allow vortex core [polarity](#)



switching. Therefore, they result in the same type of motion. We expect that all types of defects that give rise to [pinning potentials](#) that are sufficiently deep (e.g. voids, [grain boundaries](#), thickness fluctuations, ...) allow vortex core [polarity](#) switching and consequently lead to the same mobility.

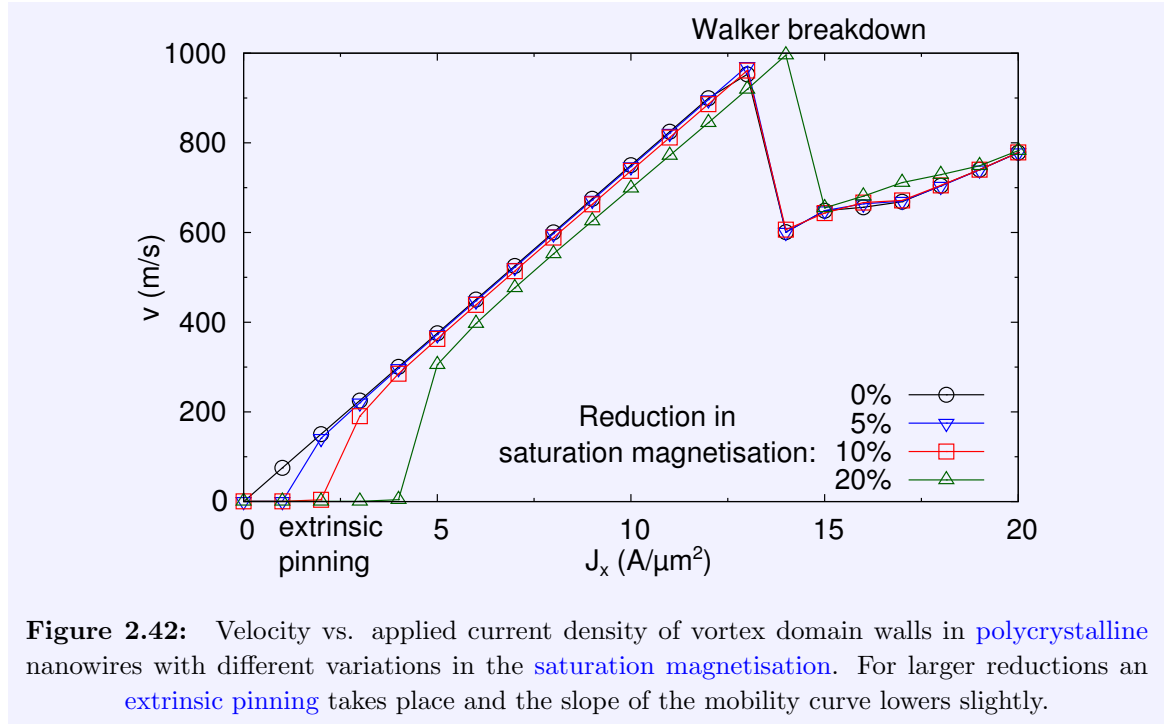
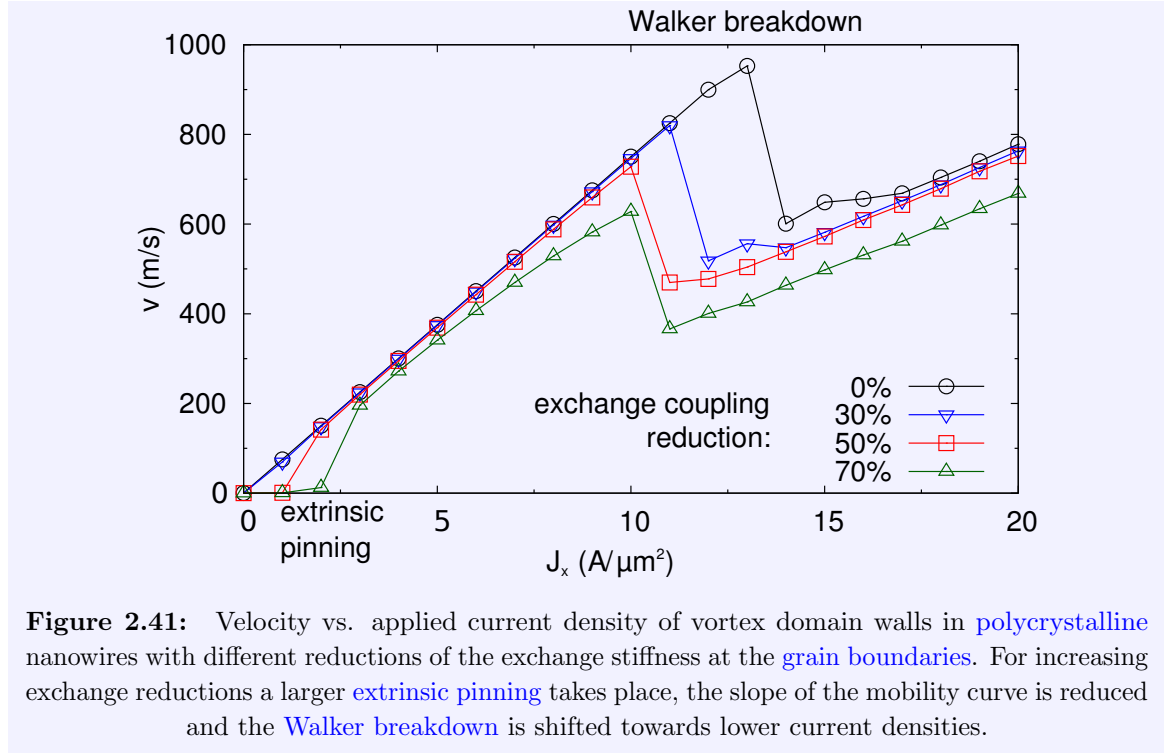
Finally, in contrast to our athermal simulations, a non-zero temperature results in thermally activated depinning and finite but small velocities in a [creep](#) regime [122]. We checked the influence of temperature on the observed phenomena. However, apart from introducing non-zero velocities slightly below the [depinning current threshold](#) (i.e. the [creep](#) regime investigated in detail in Section 3.3), no influence was observed on the domain wall mobility in the flow regime.

### 2.3.2 Polycrystalline nanowires

In this subsection, we investigate the [spin-polarised current](#) driven transverse domain wall motion with  $\beta = 2\alpha$  through the [polycrystalline](#) nanowires described at the end of Section 2.2. Here, we will use an average grain size of 10 nm, corresponding to the thickness of the nanowire. The simulated time frame is 500 ns and the moving window centred around the domain wall is 1200 nm wide.

We initialise the magnetisation as a [transverse domain wall](#), as this is the only stable state in non-disordered nanowires below the [Walker breakdown](#) at non-zero current densities. The mobility of this domain wall is simulated with different material grain parameters. First we will study the influence of the [grain boundaries](#) by reducing the [exchange stiffness constant](#) from 100% to 30% of the original value in steps of 10%. Secondly, the influence of grain thickness fluctuations is studied by varying the [saturation magnetisation](#) within the different grains. A maximum deviation  $\Delta$  of the average [saturation magnetisation](#)  $M_s$  is considered from 0% to 25% in steps of 5%. In a given simulation, the [saturation magnetisation](#) for each grain is taken randomly from the set  $\{M_s - \Delta, M_s - \Delta/2, M_s, M_s + \Delta/2, M_s + \Delta\}$ .

The results of these simulations are shown in Figs. 2.41 and 2.42 and similarly as shown above, show that disorder is able to pin the magnetic domain wall at low current densities. This [extrinsic pinning](#) mechanism[95] gets stronger for larger reductions in the exchange coupling and larger variations in [saturation magnetisation](#) as the depth of the corresponding [pinning potential](#) increases[88].



In Section 2.2 it was shown that a single defect simulated as either a region with reduced saturation magnetisation or exchange coupling can give rise to equivalent potential wells. However, depending on the simulation approach, the influence of the grains on the domain wall dynamics differs: only grains simulated with a reduced mutual exchange coupling have a

large effect at and above the [Walker breakdown](#). Below the [Walker breakdown](#), the domain wall is of the transverse type and at the [Walker breakdown](#) a vortex core is nucleated at the wire edge. As we discussed earlier, a reduction in exchange coupling facilitates the nucleation of the vortex core, explaining the reduction in [Walker breakdown](#) current density in Fig. 2.41. However, the effects are less pronounced than in Fig. 2.38 due to the smaller nanowire width (only 200 nm) which stabilises the transverse domain wall. Compared to the reduced exchange coupling, the effect on the core stability of variations in the [saturation magnetisation](#) is much weaker, but leads to a stronger [extrinsic pinning](#). However, the effect on the [Walker breakdown](#) current density is negligible and we do not observe vortex core switching. Hence also the domain wall velocity above the [Walker breakdown](#) is hardly affected, see Fig. 2.42. In real materials, both effects are present and we conclude that our implementation of [polycrystalline](#) materials gives rise to similar effects on the domain wall mobility as the distributed local defects considered above.

The results presented in these sections show that realistic material defects can have a significant influence on the domain wall mobility. Therefore, defects should be properly considered when evaluating experimental data and when new concepts are introduced to enhance the domain wall mobility[123], e.g. by the *spin-Hall effect* [124, 125] or the *Rashba effect* [126–129].



---

## Domain wall motion at finite temperature

---

*Nothing is more practical  
than a good theory.*  
— Ludwig Boltzmann

### 3.1 Introduction

In Section 2.1.3, we introduced the 1D-model. We discussed how the 1D-model parameters relate to quantities which can be extracted from micromagnetic simulations and showed how it can explain and predict the motion of domain walls through magnetic nanowires. However, the derived equations did not take thermal fluctuations or material imperfections into account, while applications based on an accurate positioning of domain walls are inevitably influenced by these sources of disorder.

In the previous chapter we studied the influence of disorder on domain wall mobility at zero temperature. One of the conclusions was that at low driving forces, below the extrinsic depinning current threshold, domain walls could get trapped in a potential well from which they could never escape. Above the extrinsic depinning current threshold, the driving forces are strong enough to overcome all energy barriers and the domain wall velocity is in good agreement with the predictions from the 1D-model. In this high velocity regime, the domain wall mobility is temperature independent[130].

In contrast, most experiments are performed at low velocities because of the high current densities (of the order of  $1 \text{ A}/\mu\text{m}^2$ ) required to move domain walls. In this regime, where extrinsic pinning takes place, the domain wall mobility is influenced by temperature: due to thermal fluctuations domain walls are able to escape from potential wells and move further until they are trapped again, resulting in a (slow) motion. The aim of this chapter is to study

this thermally driven domain wall motion and extend the [1D-model](#) to capture this complex behaviour.

The chapter is organised as follows. In Section [3.1](#) the derivation is given of an [equation of motion](#) which describes a magnetic domain wall moving along a disordered nanowire driven by a [spin-polarised current](#) and an external field at a finite temperature.

In Section [3.2](#), we will analytically solve the [high-friction limit](#) of the equation of motion in nanowires in the absence of magnetic defects and will validate the resulting predictions for the domain wall mobility (which contains a drift and a [diffusion](#) component) against micromagnetic simulations.

Finally, in Section [3.3](#), we will numerically solve the full [equation of motion](#) in a disordered nanowire, and will validate it again by comparison to micromagnetic simulations. The numerical solution will then be used to investigate the [creep](#) behaviour of transverse domain walls through disordered nanowires.

The results presented in this chapter have been published in [\[131\]](#) and [\[132\]](#).

### 3.1.1 Derivation of the equation of motion

We now extend the [1D-model](#) to take disorder and [thermal fluctuations](#) into account. To this end we will write both sources of disorder as a magnetic field contribution. Therefore, we extend our notation from  $H_{\text{ext},x}$  to  $H_x$ , which contains more fields than only the externally applied field  $H_{\text{ext},x}$ . The starting points for this derivation are Eqs. [\(2.24\)](#) and [\(2.25\)](#), describing the velocity and time derivative of the out-of-plane angle of the magnetisation from the 1D-model, respectively (cf. Section [2.1.3](#)):

$$\dot{x} = \frac{\gamma_0 L_x \langle\langle\delta\rangle\rangle}{2\alpha} H_x - \frac{\beta}{\alpha} b J_x - \frac{L_x}{2\alpha} \langle\langle\delta\dot{\phi}\rangle\rangle + \text{asymmetric terms} \quad (3.1)$$

and

$$\begin{aligned} \langle\langle\delta\dot{\phi}\rangle\rangle &= \frac{\gamma_0 \langle\langle\delta\rangle\rangle}{1 + \alpha^2} H_x - \frac{2}{L_x} \frac{\beta - \alpha}{1 + \alpha^2} b J_x \\ &\quad - \frac{\alpha \gamma_0}{1 + \alpha^2} M_s (\mathcal{N}_{\text{eff},z} - \mathcal{N}_{\text{eff},y}) \frac{\langle\langle m_y \rangle\rangle \langle\langle m_z \rangle\rangle \langle\langle\delta\rangle\rangle}{\langle\langle\sqrt{\delta}\rangle\rangle^2} \\ &\quad + \text{asymmetric terms.} \end{aligned} \quad (3.2)$$

For small angles  $\Phi_{1D}$  [Eq. [\(2.21\)](#)], we can approximate

$$\frac{\langle\langle m_y \rangle\rangle \langle\langle m_z \rangle\rangle}{\langle\langle\sqrt{\delta}\rangle\rangle^2} = \frac{\sin 2\Phi_{1D}}{2} \approx \Phi_{1D}, \quad (3.3)$$

in Eq. [\(3.2\)](#), and using the relation between  $\Phi_{1D}$  and  $\langle\langle\delta\dot{\phi}\rangle\rangle$  [Eq. [\(2.27\)](#)], we can write the domain wall velocity [Eq. [\(3.1\)](#)] as

$$\dot{x} = -\frac{L_x \langle\langle\delta\rangle\rangle}{2\alpha} \dot{\Phi}_{1D} + \frac{L_x \gamma_0 \langle\langle\delta\rangle\rangle}{2\alpha} H_x - \frac{\beta}{\alpha} b J_x + \text{asymmetric terms.} \quad (3.4)$$

In the following we will not further explicitly write the asymmetric terms. We repeat that they are negligible in the case of [current-driven domain wall motion](#) and will be taken into account when necessary in Section 3.2.

Similarly as to Ref. [133], we find that the time-derivative of Eq. (3.4), which is the acceleration of the domain wall, is given by

$$\ddot{x} = -\frac{L_x \langle\langle \delta \rangle\rangle}{2\alpha} \ddot{\Phi}_{1D}. \quad (3.5)$$

Taking the time derivative of Eq. (3.2) and using the small angle approximation [Eq. (3.3)] we find

$$\ddot{\Phi}_{1D} = \frac{-\alpha\gamma_0}{1+\alpha^2} M_s (\mathcal{N}_{\text{eff},z} - \mathcal{N}_{\text{eff},y}) \dot{\Phi}_{1D}. \quad (3.6)$$

When substituting Eq. (3.6) in Eq. (3.5), we find

$$\ddot{x} = \frac{\alpha\gamma_0}{1+\alpha^2} M_s (\mathcal{N}_{\text{eff},z} - \mathcal{N}_{\text{eff},y}) \frac{L_x \langle\langle \delta \rangle\rangle}{2\alpha} \dot{\Phi}_{1D}. \quad (3.7)$$

Substituting  $\dot{\Phi}_{1D}$  from Eq. (3.4) again in Eq. (3.7) finally leads to

$$\ddot{x} = \frac{-\alpha\gamma_0}{1+\alpha^2} M_s (\mathcal{N}_{\text{eff},z} - \mathcal{N}_{\text{eff},y}) \left[ \dot{x} - H_x \frac{L_x}{2\alpha} \gamma_0 \langle\langle \delta \rangle\rangle + \frac{\beta}{\alpha} b J_x \right] \quad (3.8)$$

### 3.1.2 Field contributions

We now take a closer look at the contributions to  $H_x$ . Apart from the contribution due to an externally applied field  $H_{\text{ext},x}$ ,  $H_x$  has two other contributions: one due to the thermal field and one due to the potential [energy profile](#).

#### Thermal field

As we recall from Section 1.3.2, the x-component<sup>1</sup> of the thermal field has the following properties:

$$\langle H_{\text{th},x} \rangle = 0, \quad (3.9)$$

$$\langle H_{\text{th},x}(t) H_{\text{th},x}(t') \rangle = q \delta_D(t - t'), \quad (3.10)$$

$$q = \frac{2k_B T \alpha}{\mu_0 \gamma_0 M_s V}. \quad (3.11)$$

The thermal field  $H_{\text{th},x}$  can thus be written as

$$H_{\text{th},x} = \eta \sqrt{\frac{2k_B T \alpha}{M_s \gamma_0 \mu_0 \langle\langle \delta \rangle\rangle V dt}}, \quad (3.12)$$

with  $\eta$  a Gaussian distributed random variable with mean 0 and standard deviation 1.

---

<sup>1</sup>In Section 3.2 we will prove that only the x-component of the thermal field influences the domain wall motion.

### Potential energy profile

The second contribution to  $H_x$  is due to the potential *energy profile*  $U$ . When this energy profile is not flat, a field will act on the particle to push it towards the (local) energy minimum. The size of this field can be determined as

$$H_U = \frac{-L_x}{2M_s\mu_0 V} \frac{\partial U}{\partial x}. \quad (3.13)$$

To extract the potential *energy profile* from micromagnetic simulations, one can track the micromagnetic energy in the simulation while a domain wall, driven by a *spin-polarised current* large enough to overcome all energy barriers, moves through the disordered nanowires. The *Gilbert damping parameter* should be set sufficiently high so that all excess energy dissipates and the domain wall instantaneously adapts its shape to the disorder. This way the micromagnetic energy (consisting of the sum of all local micromagnetic energy densities) closely follows the potential energy profile of the disordered wire and possible deformations in the domain wall are taken into account.

One example of a system with a periodic *energy profile* is shown in Fig. 3.1 (a). Similarly as in other studies[134, 135], we included periodic defects 50 nm apart in a *permalloy* (cf. page 17) nanowire with cross-sectional dimensions of  $100 \times 10 \text{ nm}^2$ . The defects, shown as black squares, are *finite difference cells*<sup>2</sup> with their exchange coupling reduced by 50%. They give rise to potential wells with a depth of 0.1 eV and the resulting *energy profile*, described by

$$U = 0.05 \text{ eV} \cos\left(\frac{(x - 20 \text{ nm})2\pi}{50 \text{ nm}}\right), \quad (3.14)$$

is shown in Fig. 3.1 (b).

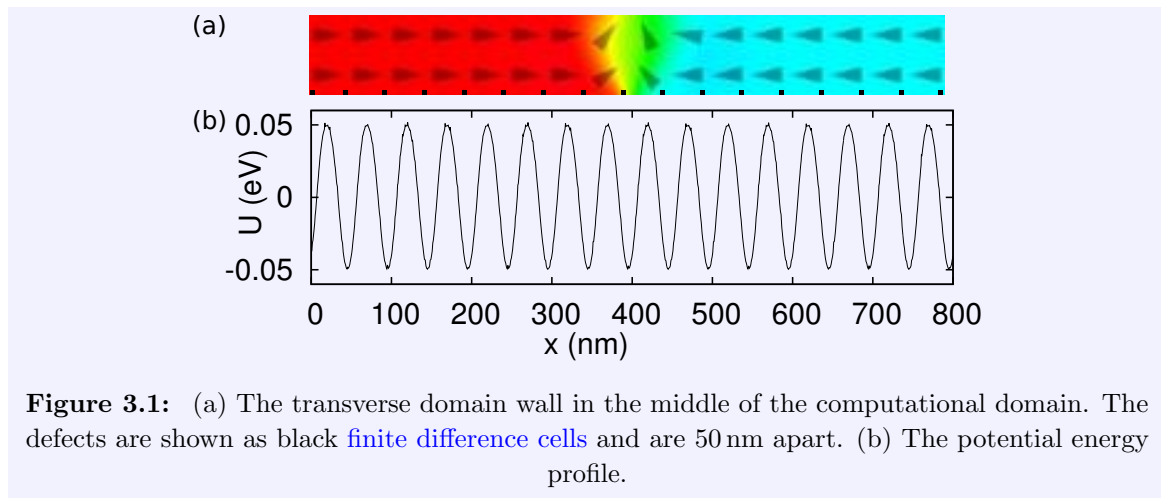


**Figure 3.1:** (a) The transverse domain wall in the middle of the computational domain. The defects are shown as black *finite difference cells* and are 50 nm apart. (b) The potential energy profile.

<sup>2</sup>The nanowire was discretised in *finite difference cells* with size  $3.125 \times 3.125 \times 10 \text{ nm}^3$ .



### 3.1.3 Equation of motion

By substituting the field contributions  $H_x = H_{\text{ext},x} + H_{\text{th},x} + H_U$  described in Eqs. (3.12) and (3.13) in Eq. (3.8) and rearranging the prefactors we obtain the *equation of motion*.

$$m\ddot{x} = -\Gamma\dot{x} - \frac{L_x}{V}\frac{\partial U}{\partial x} + \Theta\eta\sqrt{T/dt} - J_x\Xi + 2\mu_0 M_s H_{\text{ext},x}. \quad (3.15)$$

In this equation,  $m$ ,  $\Gamma$ ,  $\Theta$  and  $\Xi$  are defined as

$$m = \frac{4(1 + \alpha^2)\mu_0}{\gamma_0^2(\mathcal{N}_{\text{eff},z} - \mathcal{N}_{\text{eff},y})\langle\langle\delta\rangle\rangle L_x}, \quad (3.16)$$

$$\Gamma = \frac{4M_s\mu_0\alpha}{\langle\langle\delta\rangle\rangle L_x\gamma_0}, \quad (3.17)$$

$$\Theta = 2\sqrt{\frac{2M_s\mu_0 k_B\alpha}{\gamma_0\langle\langle\delta\rangle\rangle V}}, \quad (3.18)$$

$$\Xi = \frac{b\beta M_s 4\mu_0}{\gamma_0\langle\langle\delta\rangle\rangle L_x}. \quad (3.19)$$

$m$  represents the domain wall mass,  $\Gamma$  is a measure for the friction the domain wall experiences during its motion through the nanowire and  $\Theta$  and  $\Xi$  are prefactors related to the [thermal fluctuations](#) and current density, respectively.

### 3.1.4 Domain wall mass

The *domain wall mass*,  $m$ , is equal to the [Döring](#) mass[11],

$$m_D = \frac{2(1 + \alpha^2)\mu_0 M_s}{\gamma^2 H_K \Delta_{1D}}, \quad (3.20)$$

which can easily be seen when substituting  $H_K = M_s(\mathcal{N}_{\text{eff},z} - \mathcal{N}_{\text{eff},y})$  and  $\Delta_{1D} = L_x\langle\langle\delta\rangle\rangle/2$ .

This domain wall mass, typically expressed in kg/m<sup>2</sup>, was found by Döring from energy considerations: starting from the principle that the energy of the wall should scale as  $\frac{mv^2}{2}$  when the wall is driven with velocity  $v$ , he deduced Eq. (3.20). It is noteworthy that we found the same expression derived in a completely different way.

### 3.1.5 High-friction limit

In the most general case, the equation of motion, Eq. (3.15), is a second order differential equation containing two stochastic terms: one uncorrelated term due to the thermal fluctuations and one autocorrelated term describing the energy profile. The complexity of this equation impedes an analytical solution. However, in its *high-friction limit*[136, 137], it is possible to solve the equation of motion for small and large driving forces. In the high-friction limit, the inertia of the domain wall is negligible and Eq. (3.15) reduces to a first order differential equation

$$\Gamma\dot{x} = -\frac{L_x}{V}\frac{\partial U}{\partial x} + \Theta\eta\sqrt{T/dt} - J_x\Xi + 2\mu_0 M_s H_{\text{ext},x}. \quad (3.21)$$

This equation is equivalent to Eq. (3.1) without asymmetric terms and with

$$H_x = H_{\text{ext},x} + H_{\text{th},x} + H_U \quad (3.22)$$

and

$$\langle\langle \delta \dot{\phi} \rangle\rangle = 0. \quad (3.23)$$

In Ref. [136] a similar equation is analytically solved for small driving forces with a spatially correlated disorder  $U \sim \|x - x'\|^{\gamma_c}$ . As we will see later [see Fig. 3.8 (c)], in our case, the autocorrelation goes to zero on a finite length scale, thus  $\gamma_c < 0$  and the analytical solution for the domain wall velocity at small driving forces is given by [136]

$$v = \frac{-\Xi J_x + 2\mu_0 M_s H_{\text{ext},x}}{\Gamma} \exp\left(-\frac{\varepsilon^2}{k_B^2 T^2}\right), \quad (3.24)$$

where  $\varepsilon$  is the standard deviation of the random potential energy  $U$ .

### 3.2 Domain wall motion in non-disordered nanowires

In this section we will look at the motion of magnetic domain walls at finite temperatures in the absence of magnetic defects. To analyse the motion of the domain wall we employ Eq. (3.1), repeated below:

$$\dot{x} = \frac{\gamma_0 L_x \langle\langle \delta \rangle\rangle}{2\alpha} H_x - \frac{\beta}{\alpha} b J_x - \frac{L_x}{2\alpha} \langle\langle \delta \dot{\phi} \rangle\rangle + \text{asymmetric terms}, \quad (3.25)$$

where  $H_x$  contains an externally applied magnetic field  $H_{\text{ext},x}$  and a thermal field  $H_{\text{th},x}$ , described by Eq. (3.12).

Equation (3.25) shows that in general, the domain wall velocity is not only determined by the direct action of a driving field or current, but is also affected by the time variation of the magnetisation tilting  $\langle\langle \delta \dot{\phi} \rangle\rangle$  and the asymmetry of the domain wall. In this study we will restrict ourselves to the regime below the [Walker breakdown](#), where the domain wall tilting is fixed, resulting in a vanishing third term of Eq. (3.25).

#### 3.2.1 Zero temperature

We aim to quantitatively describe the domain wall motion. To this end, we interpret the results of [micromagnetic simulations](#)<sup>3</sup> of the motion of the [transverse domain wall](#) shown in Fig. 3.2 within the framework of the [1D-model](#).

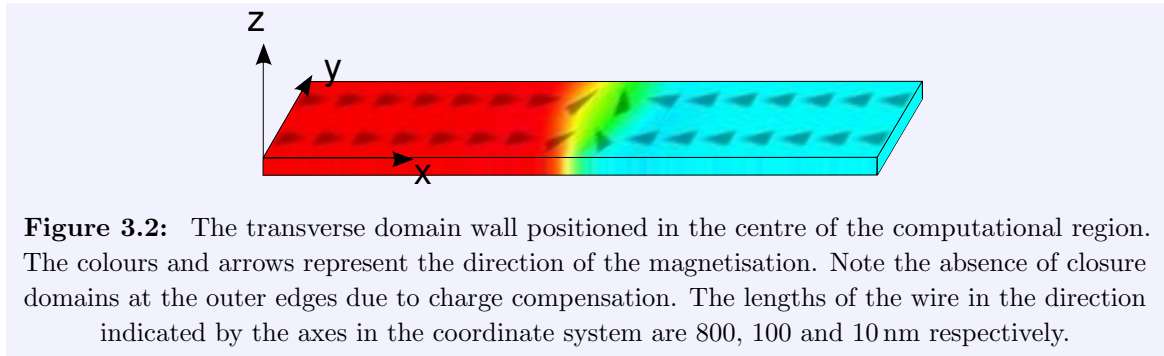
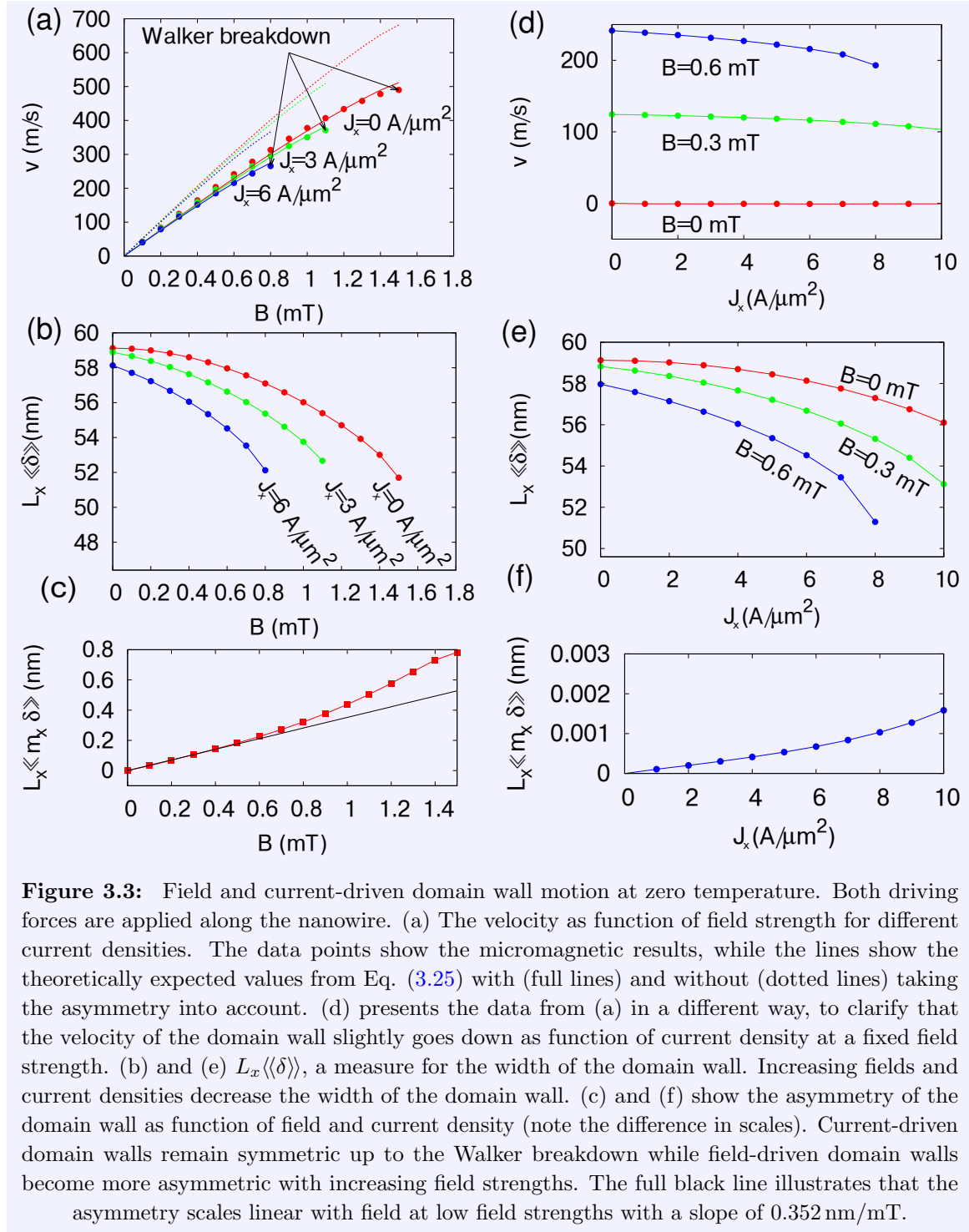


**Figure 3.2:** The transverse domain wall positioned in the centre of the computational region. The colours and arrows represent the direction of the magnetisation. Note the absence of closure domains at the outer edges due to charge compensation. The lengths of the wire in the direction indicated by the axes in the coordinate system are 800, 100 and 10 nm respectively.

Figure 3.3 clarifies the combined action of a constant field along the nanowire and a current on the domain wall at 0 K and with  $\beta = 0$ . Recall from Fig. 2.22 that a [spin-polarised current](#) with  $\beta = 0$  does not result in a net velocity of the domain wall under the intrinsic depinning current threshold. When also an external field is applied, the velocity of the domain wall increases with increasing field strengths up to the [Walker breakdown](#), see Fig. 3.3 (a).

<sup>3</sup>To simulate domain wall motion in an infinite wire, we restrict the computational region to an 800 nm wide window centred around the moving domain wall. Magnetic charges at the window edges are compensated. The cross section of the wire is  $100 \times 10 \text{ nm}^2$ . Typical material parameters for [permalloy](#) (cf. page 17) were used, with  $\alpha = 0.01$ .



Based on Eq. (3.25), we expect for a rigid, symmetric domain wall a linear dependency of the domain wall velocity on the external field. However, the domain wall width  $L_x \langle\langle \delta \rangle\rangle$  decreases with larger fields as shown in Fig. 3.3 (b). Introducing this field dependency in Eq. (3.25) leads to the dotted lines in Fig. 3.3 (a), showing that the reduction in domain wall

alone cannot explain the reduction in velocity. Indeed, the asymmetry of the wall significantly influences the dynamics. In Fig. 3.3 (c)  $L_x \langle m_x \delta \rangle$  vs. applied field is shown. This quantity represents the net magnetisation component along the nanowire axis within the domain wall, and is a measure for the domain wall asymmetry as it is zero for a symmetric domain wall and large for an asymmetric one. Panel (c) clearly shows that the wall gets increasingly asymmetric for larger fields.

To take this asymmetry into account we assume a linear dependency on the field [see Fig. 3.3 (c)] with a slope  $\sim \chi_a$ , which can be interpreted as a susceptibility along the  $x$ -axis. This allows us to include the asymmetry in Eq. (3.25) by defining an *effective wall width*  $\langle \delta_{\text{eff}} \rangle$ ,

$$\langle \delta_{\text{eff}} \rangle \equiv \langle \delta \rangle (1 - \chi_a) \approx 0.74 \langle \delta \rangle. \quad (3.26)$$

This value accommodates for the difference between the dotted lines and simulation data in Fig. 3.3 (a). In other models [52, 64, 65, 68] a similar rescaling is done by adopting different definitions of the domain wall width or by using the width as a fitting parameter, implicitly taking the asymmetry into account. In the following we remove the asymmetric terms from the equations as these effects are now included in  $\langle \delta_{\text{eff}} \rangle$ .

Figures 3.3 (d) to (f) show similar simulation results, now with varying  $J_x$  ( $\beta = 0$ ). In panel (d) the offset in velocity at  $J_x = 0 \text{ A}/\mu\text{m}^2$  is determined by the applied field and  $\langle \delta_{\text{eff}} \rangle$  at this field. With increasing current density the domain wall velocity gradually goes down. This is explained by the reduction in domain wall width for increasing current, as shown in panel (e). Panel (f) shows that currents have a much smaller influence on the domain wall asymmetry and can be neglected.

### 3.2.2 Nonzero temperatures and $\beta = 0$

To isolate the effects of temperature, we performed a set of simulations, applying no external field and only an *adiabatic spin-polarised current* ( $\beta = 0$ ). In the absence of temperature no net motion of the domain wall is expected under the Walker breakdown [63, 89] as is clear from Eq. (3.25). Hence, all domain wall dynamics can be attributed to thermal effects.

In our simulations, we have applied a current density  $J_x = 1 \text{ A}/\mu\text{m}^2$  at 300 K for 100 ns on the transverse domain wall shown in Fig. 3.2. In Fig. 3.4, 1000 paths of the domain wall are shown, each simulated with a different thermal field realisation. The red line highlights one typical path.

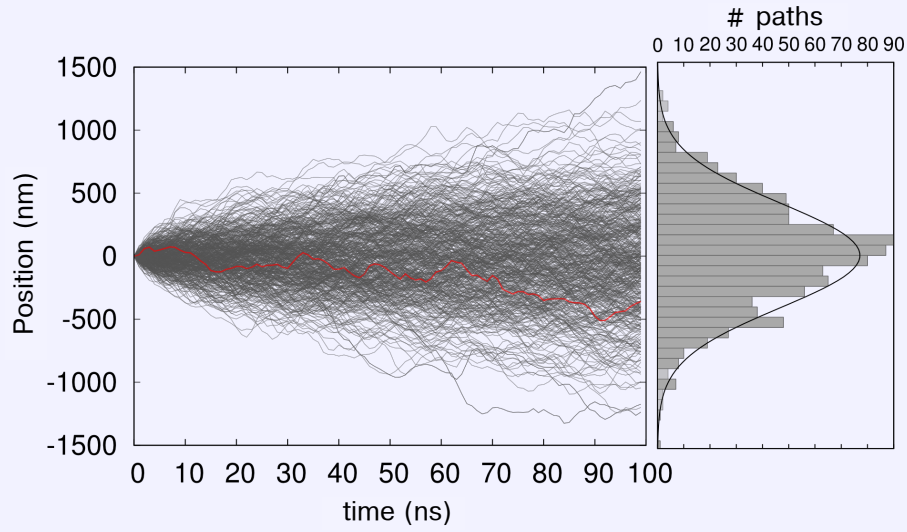


**Figure 3.4:** The left side of the figure shows the positions as function of time for 1000 domain walls in a magnetic nanowire at 300 K, and  $J_x = 1 \text{ A}/\mu\text{m}^2$  ( $\beta = 0$ ). One randomly chosen path is highlighted in red. The right side shows the distribution of their final positions, with a fitted Gaussian curve centred at 0, proving that the motion is [diffusion](#) with no average displacement.

On the right side of Fig. 3.4, the distribution of the final domain wall positions after 100 ns is shown. The combined action of [thermal fluctuations](#) and current does not give rise to an average domain wall motion: the data is described by a Gaussian with zero average. Consequently, the motion can be interpreted as a random walk resulting in *diffusion* and characterised by a mean square displacement  $\langle x^2 \rangle$ .

To investigate the influence of current on the diffusion, we performed similar simulations varying  $J_x$  from 0 to  $10 \text{ A}/\mu\text{m}^2$  (close to the [Walker breakdown](#) current density of  $\pm 14 \text{ A}/\mu\text{m}^2$ ). For each current density, 500 thermal field realisations are simulated. The results are shown in Fig. 3.5 (a), where the red dots represent  $\langle x^2 \rangle/t$ , as this quantity is independent of the simulation time.

As a function of current density almost constant values of  $\langle x^2 \rangle/t$  are found, indicating that, apart from the indirect effect due to a decrease in  $L_x \langle \delta \rangle$  for higher current densities [as shown in Fig. 3.3 (e)], the current density does not influence the [diffusion](#) characteristics.

The domain wall tilts out of the plane of the nanowire until it reaches a tilting determined by the current density. Here, at zero temperature, all torques cancel out and the wall does not move[63]. Thermal fluctuations give rise to an additional field torque responsible for the motion of the domain wall. These [thermal fluctuations](#) are independent of the current density and thus give rise to similar diffusion. Repeating these simulations at different temperatures shows that  $\langle x^2 \rangle/t$  scales linearly with temperature as expected[138] [cf. Fig. 3.5 (b)].

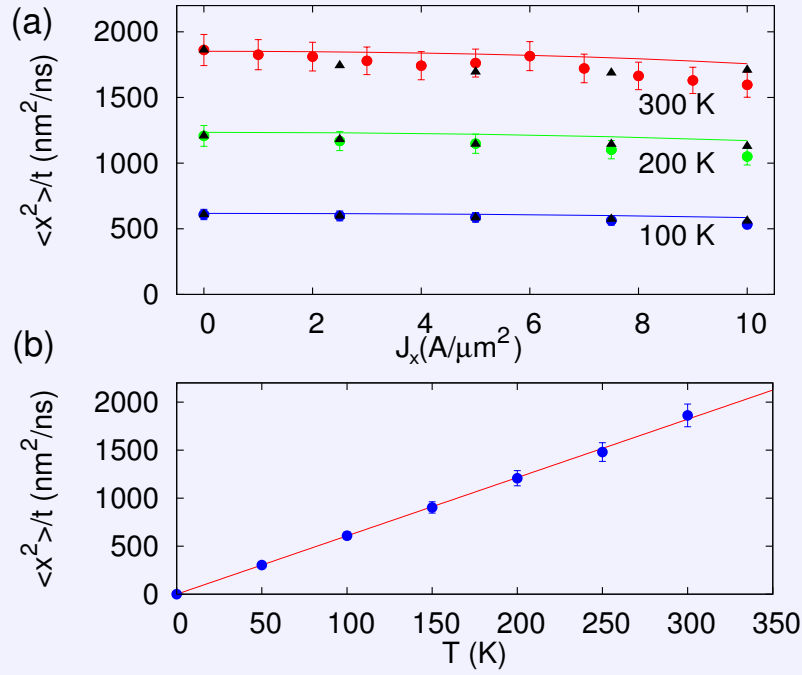


**Figure 3.5:** (a) The domain walls' mean square displacement over time averaged over 500 realisations as function of current density at 3 different temperatures. The coloured dots with error bars show the simulated data with  $\beta = 0$ , while the full lines show the theoretical curves expected by Eq. (3.27). The results represented by the black triangles will be discussed in Section 3.2.3 and show the mean square displacement corrected for the drift velocity for simulations with  $\beta = 2\alpha$ . The error bars on these values are comparable to their counterparts for  $\beta = 0$  but are not shown for clarity. (b) The mean square displacement over time as function of temperature at  $J_x = 0$  A/μm². The full line is a fit to the data and shows that there is a linear temperature dependency.

Now, we will introduce [thermal fluctuations](#) in the [1D-model](#) to explain our observations. Contrary to the fields used in Fig. 3.3, the thermal field acting on the domain wall fluctuates in time, and has no preferential direction. The spread on the domain wall positions[138] is described by  $\langle x^2 \rangle = \left\langle \left( \int_0^t \dot{x} dt' \right)^2 \right\rangle$  which can be quantified by substituting  $\dot{x}$  from Eq. (3.25),

$$\begin{aligned}
 \left\langle \left( \int_0^t \dot{x} dt' \right)^2 \right\rangle &= \left\langle \left( \int_0^t \frac{L_x \gamma_0 \langle \delta_{\text{eff}} \rangle}{2\alpha} H_x dt' \right)^2 \right\rangle \\
 &= \left\langle \frac{L_x^2 \gamma_0^2 \langle \delta_{\text{eff}} \rangle^2}{4\alpha^2} \left( \int_0^t H_{\text{th},x} dt' \right)^2 \right\rangle \\
 &= \frac{L_x^2 \gamma_0^2 \langle \delta_{\text{eff}} \rangle^2}{4\alpha^2} q t = \frac{\gamma_0 k_B L_x \langle \delta_{\text{eff}} \rangle}{2\alpha M_s \mu_0 L_y L_z} T t.
 \end{aligned} \tag{3.27}$$

Here, we assumed that the domain wall tilting follows the thermal fluctuations sufficiently fast to neglect<sup>4</sup>  $\langle \delta_{\text{eff}} \dot{\phi} \rangle$ , corresponding to the [high-friction limit](#) of the [equation of motion](#). The

<sup>4</sup> In Eq. (2.24), we saw that  $H_{\text{ext},y}$  and  $H_{\text{ext},z}$ , and thus also the  $y$  and  $z$  components of the thermal field

volume of the domain wall  $V = \langle\langle\delta_{\text{eff}}\rangle\rangle L_x L_y L_z$ . Note that this volume is dependent on the current density [cf. Fig. 3.3 (e)]. As expected for normal [diffusion](#),  $\langle x^2 \rangle$  grows linearly in time.

To summarise our results for  $\beta = 0$ : the full lines in Fig. 3.5 (a) show  $\langle x^2 \rangle / t$  given by Eq. (3.27). For experimentally relevant (low) current densities there is an almost perfect agreement between theory and simulation. Furthermore, Eq. (3.27) predicts that  $\langle x^2 \rangle$  linearly depends on temperature, which is also confirmed by our simulations. Moreover, the model takes small domain wall deformations into account via  $\langle\langle\delta_{\text{eff}}\rangle\rangle$ . These deformations result in nonlinear deviations for large current densities also found in the simulations shown in Fig. 3.3 (a). The remaining slight difference between the full lines and the data points is explained by the fact that we assumed a linear scaling of the asymmetry with the externally applied field, while Fig. 3.3 (c) shows that this approximation is only valid for small fields. Alternatively, this might indicate that we are operating at the limit of where the [high-friction limit](#) is still valid.

### 3.2.3 Nonzero temperatures and $\beta = 2\alpha$

In a last set of simulations, we applied a [spin-polarised current](#) with [degree of non-adiabaticity](#)  $\beta = 2\alpha$ , and investigated the domain wall motion at different temperatures, again considering 500 realisations per data point. When  $\beta \neq 0$ , we expect a net velocity of the wall for any  $J_x > 0 \text{ A}/\mu\text{m}^2$ .

We have performed micromagnetic simulations at 5 different current densities. For all temperatures ( $T = 100, 200$  and  $300 \text{ K}$ ) these give rise to the same values (shown as data points in Fig. 3.6). These points also coincide with the domain wall velocity at  $0 \text{ K}$  described by Eq. (3.25). The fact that all data coincides confirms that the drift velocity of the domain wall is unaffected by temperature[130].

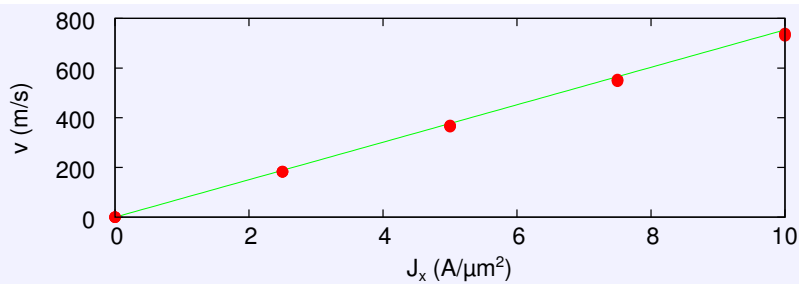


**Figure 3.6:** The drift velocity of current-driven domain walls with  $\beta = 2\alpha$  at different temperatures. The data points (coinciding for all temperatures) are in almost perfect agreement with the theoretically expected velocities from Eq. (3.25), represented by the full line.

At nonzero temperatures, the domain wall motion also has a [diffusion](#) component, next to

---

only contribute to  $\langle\langle\delta\dot{\phi}\rangle\rangle$ . The excellent correspondence between the theory, where we neglect these terms, and the full micromagnetic simulations proves that only the x component of the thermal field gives rise to motion of the domain wall, and that the [high-friction limit](#) is a valid approximation in this system.



a drift component. This diffusion components,  $\langle x^2 \rangle / t$  (corrected for the drift velocity) are shown as black triangles in Fig. 3.5 (a), indicating that the adiabatic and non-adiabatic systems exhibit identical diffusion properties. Hence, we can conclude that the diffusion is solely determined by the domain wall shape and the temperature [cf. Eq. (3.27)] and is not affected by the drift velocity.

To conclude, in this section we have investigated the influence of temperature on transverse domain wall dynamics in magnetic nanowires. Temperature is included in the micromagnetic simulations and the 1D-model as a randomly fluctuating field acting on the finite difference cells and domain wall volume respectively. In general, the domain wall motion contains a drift and a diffusion component. We verified that the drift velocity of the domain wall is unaffected by temperature and found that the domain wall diffusion gives rise to a mean square domain wall displacement which grows linearly with time, indicating normal diffusion. The diffusion is solely determined by temperature and the domain wall shape. The domain wall drift and diffusion do not influence each other and can be quantitatively predicted by the 1D-model, extended with a thermal field.

### 3.3 Domain wall motion in disordered nanowires

#### 3.3.1 Introduction

In this section we will include disorder in our analysis of domain wall motion at nonzero temperatures. Driven extended elastic systems in disordered media, such as domain walls in ferromagnets [122, 139], and periodic systems such as vortex lattices [140] are pinned at zero temperature. At finite temperatures  $T > 0$ , smaller than the depinning temperature  $T_{\text{dep}}$ , and driving forces  $f$ , smaller than the depinning force  $f_{\text{dep}}$ , they exhibit a *creep* [141] regime. This originates in the slow thermally activated motion of the elastic system over large energy barriers, leading to a highly non-linear response of the form

$$v \sim \exp \left[ - \left( \frac{T_{\text{dep}}}{T} \right) \left( \frac{f_{\text{dep}}}{f} \right)^{\mu_{\text{creep}}} \right], \quad (3.28)$$

where  $v$  and  $\mu_{\text{creep}}$  are the velocity and the creep exponent, respectively [141]. In particular, for 1D elastic lines such as domain walls in ferromagnetic thin (PMA) films, compelling evidence for the validity of Eq. (3.28) exists, with  $\mu_{\text{creep}}$  assuming the value 1/4 [122, 139].

Controlling the motion of domain walls (and other magnetic solitons like *skyrmions* [23]) in narrow ferromagnetic structures is currently receiving a lot of attention as possible building blocks of future information and communications technology (ICT) components, including memory devices [53, 73, 142, 143] and logic gates [75, 79]. Disorder, necessarily present in such systems, could hamper the controllability of domain walls in the devices as it introduces a stochastic component in the domain wall dynamics [95, 144], but may in some cases also positively affect the device specifications [98]. In addition to disorder, also temperature adds a stochastic component in the domain wall dynamics. Both stochastic effects complicate the control of the domain wall motion in the creep regime.

Although domain wall based devices are not meant to be used in the *creep* regime, high current densities make it challenging to operate them at high speeds (i.e. in the domain wall flow regime) due to *Joule heating* [53]. Additionally, stray fields originating in the surrounding electronics can exert small forces on the domain walls. Therefore, understanding and controlling the effects of disorder and *thermal fluctuations* on the domain wall dynamics subjected to small driving forces, the creep regime, is important for the design of future domain wall based devices.

In Ref. [145], Kim *et al.* experimentally showed that in PMA materials the creep scaling law, Eq. (3.28), breaks down when the nanowire dimensions are reduced (see Fig. 3.7). In Ta/Pt/Co<sub>90</sub>Fe<sub>10</sub>/Pt nanowires, narrower than about 300 nm, domain walls could no longer be described as elastic lines, as assumed in the derivation of Eq. (3.28); rather, they behaved like compact objects jumping across energy barriers resulting in a creep motion strongly deviating from Eq. (3.28), as illustrated in Fig. 3.7.

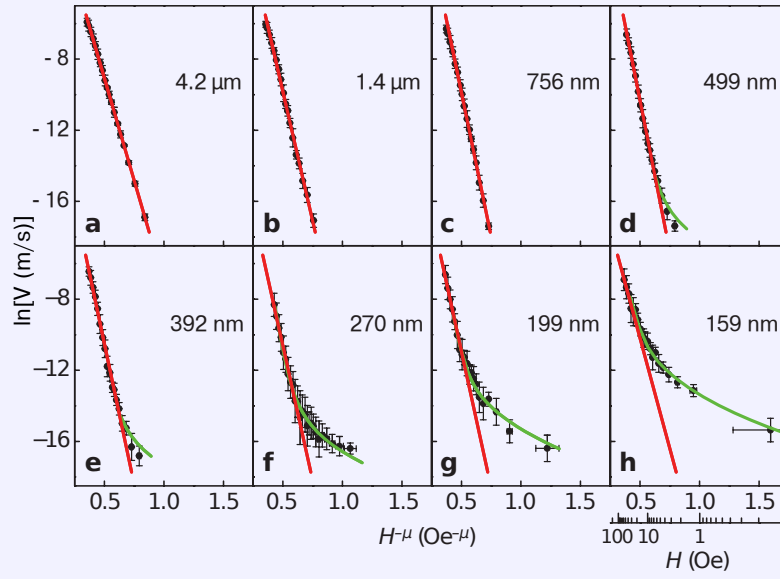


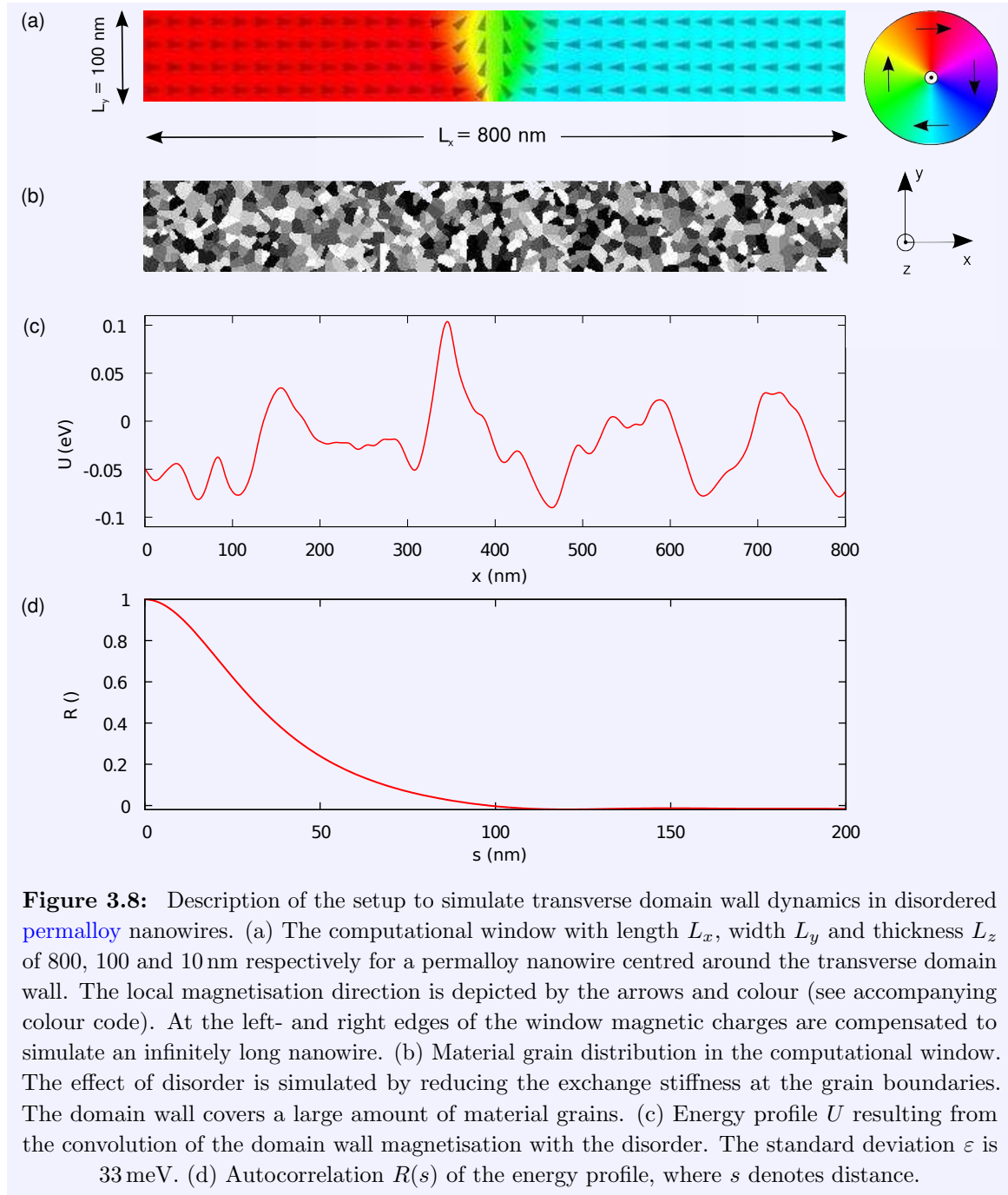
**Figure 3.7:** Non-equilibrium criticality of domain wall speed along ferromagnetic nanowires with different widths. The red lines are the best fit to the creep scaling law [Eq. (3.28)] with  $\mu_{\text{creep}} = 1/4$ . Reproduced from [145].

### 3.3.2 Micromagnetic simulations

Previous micromagnetic studies on domain wall motion have resulted in a deep understanding of the underlying dynamics [63] and a 1D-model, which accurately predicts the domain wall velocity in the absence of disorder or thermal effects[52]. As also shown in the previous sections, these simulations have been extended with thermal fluctuations [131], disorder[89, 98, 100, 101] or a combination of both[119, 146]. However, the extremely low domain wall velocities in the creep regime made a thorough micromagnetic study with proper statistics computationally very challenging. This explains why up to now only phenomenological descriptions proved feasible [146].

In this section, we numerically explore the creep regime of domain walls in an in-plane magnetised system. Based on micromagnetic simulations and the numerical solution of the equation of motion, Eq. (3.15) we are able to collect enough data to properly probe the domain wall dynamics deep in the creep regime.

We analyse the current driven creep motion of domain walls in disordered permalloy (cf. page 17) nanowires, starting with extensive micromagnetic simulations, i.e. numerically solving the Landau-Lifshitz-Gilbert equation extended with spin transfer torque terms [27]. The system is shown in Fig. 3.8: a transverse domain wall in an infinitely long permalloy nanowire with cross-sectional dimensions of  $100 \times 10 \text{ nm}^2$  simulated in a moving window with length 800 nm, centred around the domain wall. Temperature fluctuations are included as a stochastic thermal field  $\mathbf{H}_{\text{th}}$  [Eq. (3.12)], contributing to the effective field  $\mathbf{H}_{\text{eff}}$ .



As discussed in detail in Section 2.2, various ways exist to include disorder in micromagnetic simulations[88, 90, 95, 100, 101, 147]. Although holes in the material have been used previously[95], more sophisticated approaches introduce the influence of material grains by spatially varying the strip thickness[88] or saturation magnetisation [88, 100, 101], or considering a reduced exchange coupling between the grains[88, 100]. In PMA materials, an additional variable anisotropy strength and direction can be used[100]. Alternatively, disorder can also

be taken into account as an effective field term in Eq. (1.21) [147].

Here, we consider a polycrystalline [permalloy](#) (cf. page 17,  $\alpha = 0.01$ ) nanowire, in which the [material grains](#) are generated with a [Voronoi tessellation](#), see Fig. 3.8 (b). At grain boundaries, the [exchange stiffness constant](#) is reduced by 20%. This implementation introduces an [energy profile](#)  $U$  consisting of stochastic potential wells with depths up to 0.1 eV and standard deviation  $\varepsilon = 0.33$  meV, see Fig. 3.8 (c). While the grains have an average size of 10 nm (the strip thickness), the space scale at which the energy varies corresponds to the convolution of the 100 nm wide domain wall with the disorder. This is reflected in the autocorrelation

$$R(s) = \frac{\langle (U_x)(U_{x+s}) \rangle}{\varepsilon^2} \quad (3.29)$$

of  $U$  (with zero mean and standard deviation  $\varepsilon$  [Eq. (3.29)]) which goes to zero on a length scale comparable to the domain wall width [Fig. 3.8 (d)]. Such an [energy profile](#) is in correspondence with experimental data[91–93].

Using [MuMax3](#), we performed extensive simulations of [current-driven domain wall motion](#) through the nanowire described above for current densities ranging from  $0.1 \text{ A}/\mu\text{m}^2$  to  $4 \text{ A}/\mu\text{m}^2$ ,  $\beta = 0.01$  and temperatures of 250 K and 300 K. For each temperature and current density combination we performed 5 simulations with different realisations of the thermal field. Depending on the velocity of the domain wall, the simulation time ranged from  $5 \mu\text{s}$  to  $100 \mu\text{s}$ : at 250 K, for  $J_x \in [0.2, 2.4] \text{ A}/\mu\text{m}^2$  and at 300 K for  $J_x \in [0.14, 2.4] \text{ A}/\mu\text{m}^2$  the simulated time was  $50 \mu\text{s}$ , while it was  $5 \mu\text{s}$  for larger current densities. At 300 K, for the lowest current densities of  $J_x = 0.12 \text{ A}/\mu\text{m}^2$  and  $0.1 \text{ A}/\mu\text{m}^2$ , the corresponding simulation times were  $75 \mu\text{s}$  and  $100 \mu\text{s}$ . The simulations were performed with the second order [Heun's method](#) with a fixed time step of 50 fs. In Fig. 3.9 each data point shows the average domain wall velocity over five simulations with different temperature realisations. The panels at the right show the domain wall paths for some representative current densities. In the flow regime (e.g.  $J_x = 4 \text{ A}/\mu\text{m}^2$ ) the disorder nor the [thermal fluctuations](#) have a noticeable effect on the domain wall motion. At intermediate current densities, in the depinning regime (e.g.  $J_x = 1 \text{ A}/\mu\text{m}^2$ ), only a small number of pinning potential wells are strong enough to temporarily pin the domain wall. This introduces some variance in the domain wall velocities. In the [creep](#) regime (e.g.  $J_x = 0.1 \text{ A}/\mu\text{m}^2$ ), the domain walls repetitively pin for several microseconds, resulting in average domain wall velocities down to 1 m/s. In order to collect enough data (i.e. successive pinning and depinning events) increasingly long time windows are simulated for decreasing current densities (see Fig. 3.9). This way, with a simulation speed of  $5 \mu\text{s}$  per day<sup>5</sup>, the simulation of each one out of the five realisations contributing to the data point at  $J_x = 0.1 \text{ A}/\mu\text{m}^2$  takes 20 days. This definitely puts a computational limit to the full micromagnetic approach and calls for a more simplified description to further probe the low velocity creep regime.

---

<sup>5</sup>Using a GeForce GTX970 GPU.

### 3.3.3 Equation of motion

To address the low current density regime, we employ the [equation of motion](#) derived in Section 3.1, repeated below.

$$m\ddot{x} = -\Gamma\dot{x} - \frac{L_x\partial U}{V\partial x} + \Theta\eta\sqrt{T/dt} - J_x\Xi + 2\mu_0 M_s H_{\text{ext},x} \quad (3.30)$$

Equation (3.30) describes a magnetic domain wall moving along a disordered magnetic nanowire with [energy profile](#)  $U$  as shown in Fig. 3.8 (c). The domain wall is driven by a current density  $J_x$  and an external field  $H_{\text{ext},x}$  at a finite temperature. The domain wall mass  $m$  was found to be  $2.91 \mu\text{g}/\text{m}^2$  for the studied system.  $\Gamma$  is a measure for the friction, while  $\Theta$  and  $\Xi$  are prefactors related to the thermal fluctuations and the current density, respectively. In this equation of motion, all model parameters can be easily extracted from micromagnetic simulations without any fitting. For example,  $\langle\langle\delta\rangle\rangle = \langle\langle m_y^2 + m_z^2 \rangle\rangle = 0.0739$  is a measure for the domain wall volume relative to the volume  $V$  of the computational window and  $\mathcal{N}_{\text{eff},y}$  and  $\mathcal{N}_{\text{eff},z}$  are demagnetizing factors determined by the shape of the domain wall, respectively quantified as 0.88 and 0.08.

This allows us to validate Eq. (3.30) by direct comparison of its solution with the full micromagnetic simulation data shown in Fig. 3.9. The full black lines are obtained from the numerical integration<sup>6</sup> of the equation of motion [Eq. (3.30)] using the [energy profile](#)  $U$  extracted from the micromagnetic simulations and show an excellent agreement with the micromagnetic model.

The now fully validated Eq. (3.30) requires much less computational power to evaluate and thus allows us to investigate current regimes which are inaccessible by full micromagnetic simulations. Figure 3.10 (a) presents the mobility curves, i.e.  $v/J_x$ , for current densities between  $0.01 \text{ A}/\mu\text{m}^2$  and  $10 \text{ A}/\mu\text{m}^2$  and temperatures ranging from 200 K to 500 K. It appears that the domain wall velocity scales linearly with the current density for low and high current densities, with a nonlinear regime in between. In the flow regime at high current densities, the linear scaling of the velocity with current density is expected [62, 63]. We identify the intermediate regime (roughly between  $0.5 \text{ A}/\mu\text{m}^2$  and  $5 \text{ A}/\mu\text{m}^2$ ) as the depinning regime. Although it is nonlinear, it does not follow the [creep](#) scaling law [Eq. (3.28)], see inset Fig. 3.10 (a). The linear regime at low current densities is surprising as it deviates from the creep scaling law found for extended domain walls.

---

<sup>6</sup>The equations were numerically integrated with [Euler's method](#) by time stepping them with a fixed time step of 50 fs until either a distance of 1 nm was covered or 0.01 s of simulated time was reached.

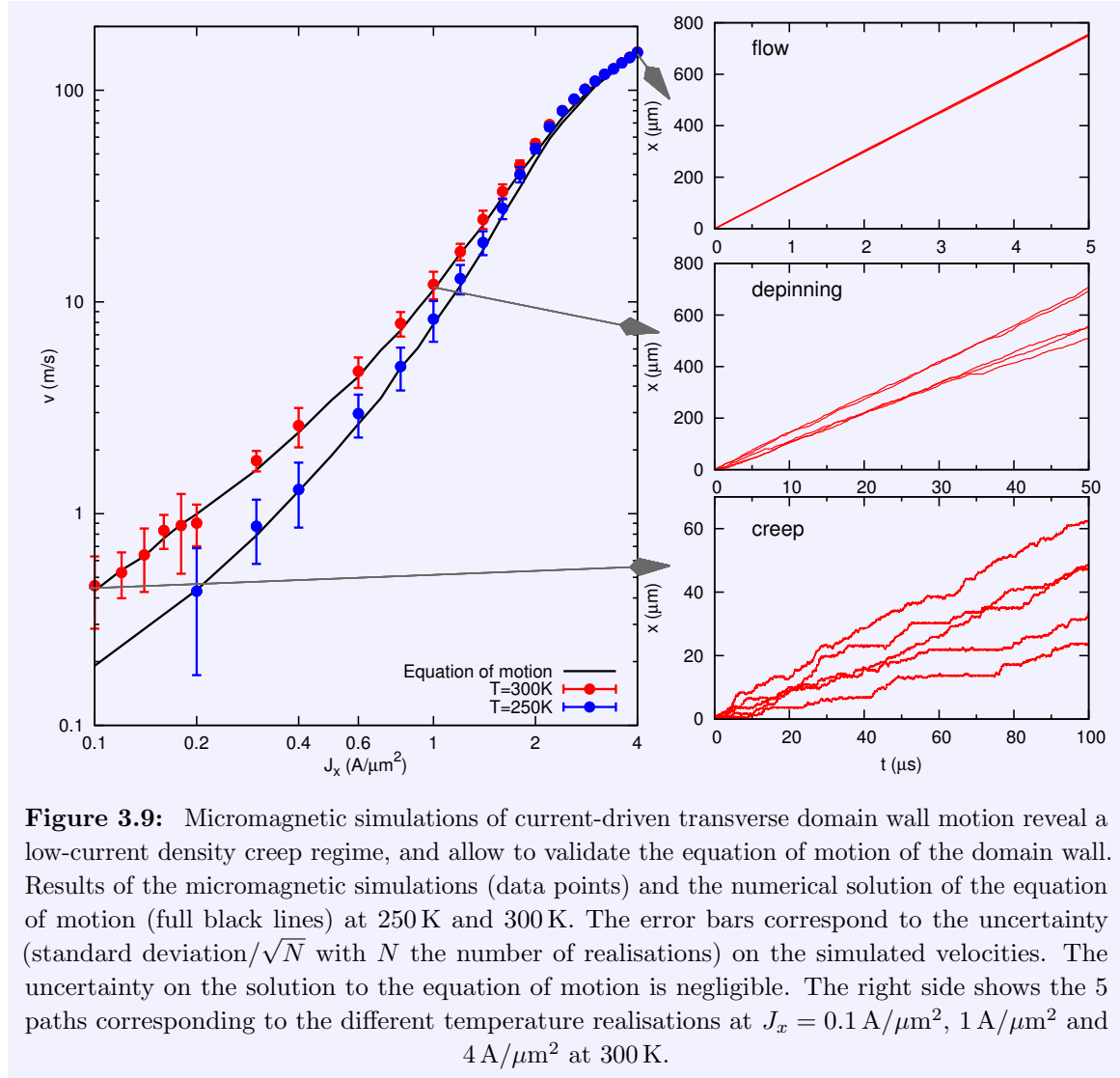


**Figure 3.9:** Micromagnetic simulations of current-driven transverse domain wall motion reveal a low-current density creep regime, and allow to validate the equation of motion of the domain wall. Results of the micromagnetic simulations (data points) and the numerical solution of the equation of motion (full black lines) at 250 K and 300 K. The error bars correspond to the uncertainty (standard deviation/ $\sqrt{N}$  with  $N$  the number of realisations) on the simulated velocities. The uncertainty on the solution to the equation of motion is negligible. The right side shows the 5 paths corresponding to the different temperature realisations at  $J_x = 0.1$  A/μm², 1 A/μm² and 4 A/μm² at 300 K.

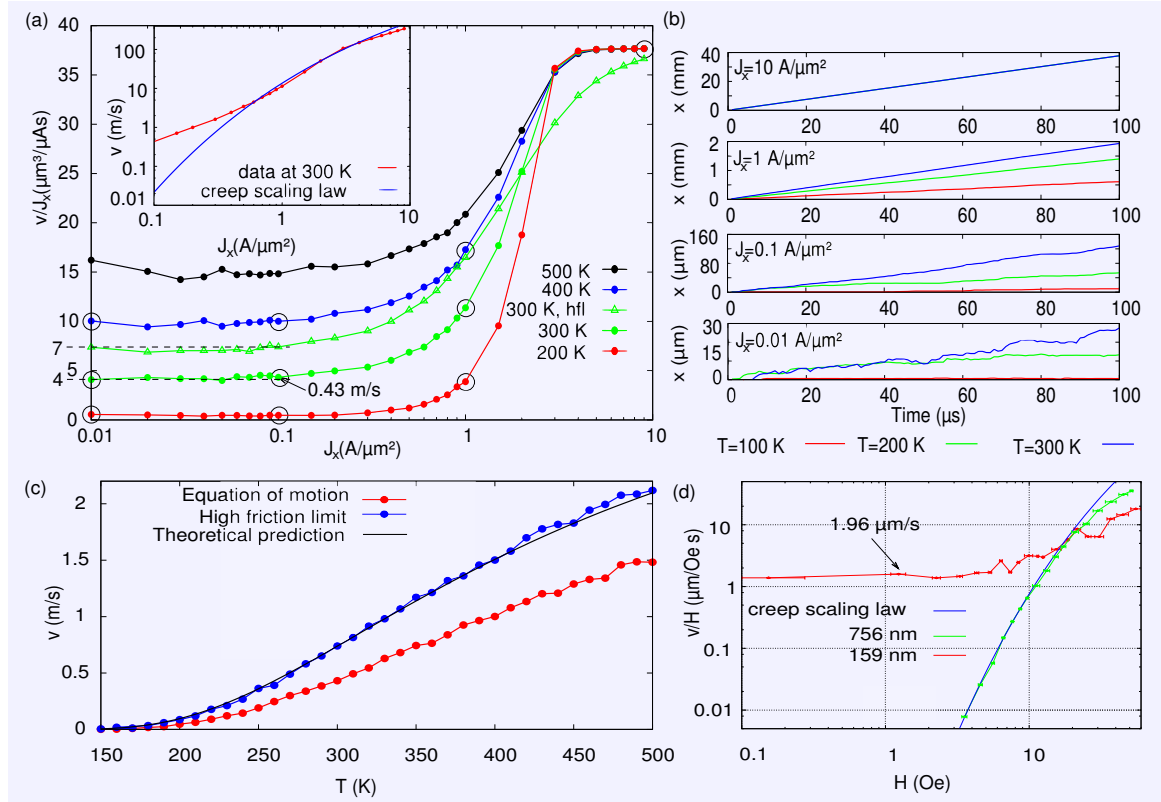


**Figure 3.10:** A linear creep regime emerges for low current densities and applied fields. (a) Numerical evaluation of the equation of motion at different temperatures  $T$ . Note the linear regimes at low and high current densities. The solution in the [high-friction limit](#) (hfl) is shown for  $T = 300$  K (green triangles). The inset shows the velocity as function of current density at 300 K. For the intermediate, non-linear regime a creep scaling law [eq. (3.28)] is fitted to illustrate that it cannot explain our data. (b) domain wall paths corresponding to the circled data points in panel (a) with  $T = 100$  K, 200 K, 300 K. (c) Temperature dependence of the domain wall velocity for  $J_x = 0.1 \text{ A}/\mu\text{m}^2$ . Data points show the numerical evaluation of the equation of motion and its high-friction limit. The solid line shows the theoretical prediction in the high-friction limit, based on Eq. (3.24) i.e.  $v = v_0 \exp(-\varepsilon^2/k_B^2 T^2)$  with  $v_0 = 3.769 \text{ m/s}$  and  $\varepsilon = 33 \text{ meV}$ . (d) Experimental data from Ref. [145]. The red curve proves the linear dependency of  $v$  on the driving force (here, the applied field  $H$ ), measured in a 159 nm wide PMA nanowire. This contrasts the green curve measured for a wider strip (756 nm) where the classical creep scaling law, Eq. (3.28), is recovered at small driving forces. To illustrate the six orders of magnitude difference in domain wall velocities between the in-plane magnetised simulated system [panel (a)] and the experimental PMA-system [panel (d)] representative domain wall velocities in the respective linear creep regimes are indicated.

### 3.3.4 High-friction limit

We repeat from Section 3.1.5 that in the [high-friction limit](#) the domain wall velocity scales linearly with small driving forces ( $J_x$  and  $H_{\text{ext},x}$ ) [148], with the velocity given by Eq. (3.24), repeated below



$$v = \frac{-\Xi J_x + 2\mu_0 M_s H_{\text{ext},x}}{\Gamma} \exp\left(-\frac{\varepsilon^2}{k_B^2 T^2}\right). \quad (3.31)$$

In the [high-friction limit](#),  $v/J_x$  at  $T = 300$  K is  $7 \mu\text{m}^3/\mu\text{As}$  in the linear regime, as indicated in Fig. 3.10 (a). This numerical solution of Eq. (3.21) agrees with the analytically predicted value but clearly differs from the solution of the complete equation of motion where  $v/J_x = 4 \mu\text{m}^3/\mu\text{As}$  at  $T = 300$  K, as also indicated in the same figure. This means that the domain wall mass cannot be neglected in our in-plane magnetised system. However, studies suggest that in [PMA](#) materials the domain wall mass can be neglected[149] due to the combination of a very small domain wall width and a high [Gilbert damping parameter](#)  $\alpha$  [typically an order of magnitude larger than in [permalloy](#) (cf. page 17)]. This makes the high-friction limit valuable in the study of the [creep](#) regime of domain walls moving in narrow nanowires. For completeness, Fig. 3.10 (c) shows the temperature dependency of the domain wall velocity in the high-friction limit for  $J_x = 0.1 \text{ A}/\mu\text{m}^2$  predicted by Eq. (3.24) (full black line) and numerically obtained by solving Eq. (3.21) (blue dotted line).

### 3.3.5 PMA materials

Most experimental data on domain wall creep in [PMA](#) materials is obtained in wide strips where the description as an elastic line moving through a two-dimensional landscape is valid, and generally a good agreement with the creep scaling law [Eq. (3.28)] is found[122, 139, 150–154]. However, for sufficiently narrow nanowires, a deviation from the creep scaling law is experimentally observed[145]. In Fig. 3.10 (d), we plot the original field driven data for the 159 nm and 756 nm wide Ta/Pt/Co<sub>90</sub>Fe<sub>10</sub>/Pt nanowire reported in Ref. [145]. For the 756 nm wide nanowire, the creep scaling law fits the data very well. This is in sharp contrast with the 159 nm wide nanowire where  $v$  depends linearly on the applied field for low fields, in agreement with Eq. (3.24). This provides experimental evidence for the existence of the linear creep regime at small driving forces in case of compact domain walls, behaving like point particles in a one dimensional random energy profile.

We now compare the velocities of the domain wall at comparable driving forces in the linear regime for the experimental field-driven and numerical current-driven systems, respectively and see that they differ about 6 orders of magnitude, as shown in panels (a) and (d) in Fig. 3.10. This mainly originates from the small domain wall widths in [PMA](#) materials, resulting in significantly stronger pinning than in [permalloy](#) (cf. page 17) nanowires [155]. Although it is possible to perform micromagnetic simulations to investigate the [energy profile](#) [100], the low domain wall velocities prohibit full micromagnetic simulations in the creep regime of PMA systems. Even on the timescales made accessible by numerically solving the equation of motion [Eq. (3.30)] it is impossible to collect enough data on thermally assisted domain wall motion. Based on the small driving force and the high friction limit of the equation of motion [Eq. (3.24)] we can however estimate a lower limit of 90 meV for the variation  $\varepsilon$  of the [energy profile](#) in the experimental [PMA](#) system of Ref. [145].

### 3.3.6 Periodic potential energy profile

Until now, we investigated [polycrystalline](#) nanowires with random disorder. Here we will look at the system with a periodic [energy profile](#) presented in Section 3.1.2. The domain wall has a tendency to get pinned in the energy minima, and in absence of any driving forces relaxes towards these positions.

Such systems are useful in e.g. the [racetrack memory](#) [53, 73], where the domain wall magnetisation represents bits and thus contains the information to be stored. In order to reliably read and manipulate this information it is crucial that the domain walls can be positioned accurately on a read or write head. A second concern is to maintain enough distance between the different domain walls in order to keep them from collapsing due to thermal [diffusion](#) (see Section 3.2) and corrupting the data. It has been shown [135] that periodic imperfections in the nanowire, like notches [156] can be used to achieve these goals, as the domain walls get pinned to these minima in the [energy profile](#).

We will use Eq. (3.30) to study the motion of current driven transverse domain walls in a periodic [energy profile](#). We compare micromagnetic simulations with numerical solutions to the equation of motion and a general theoretical result for the [Brownian motion](#) of particles in a periodic potential[148]. At zero temperature there are two qualitatively different solutions to Eq. (3.30)[148] with a periodic [energy profile](#)  $U$ .

Firstly, there exists a *locked state*, in which the driving force is too low to let the domain wall escape from the [potential wells](#). In this case the wall will come to rest in an equilibrium position where the driving force and the force due to the potential well are balanced, and the average velocity is zero.

Secondly, a *running state* exists in which the wall gains enough speed to overcome the barriers in between the potential wells and keeps moving along the nanowire. In this state, the velocity will oscillate depending on the position in the periodic [energy profile](#) but will be nonzero on average[134, 148]. The threshold current density between these two regimes depends on the initial velocity and position of the domain wall, giving rise to a hysteresis effect in the velocity as function of current density. This is illustrated in Fig. 3.11, where the results of micromagnetic simulations of current driven domain wall motion through the periodic [energy profile](#) presented in Section 3.1.2 are shown.

In this figure, the red curve corresponds to the velocity of the domain wall initialised at rest in the bottom of a potential well. The green curve is generated by first letting the domain wall get into a [running state](#) by driving it with a high current density ( $J_x = 6 \text{ A}/\mu\text{m}^2$ ), and then bringing the current density down to the value shown on the x-axis. The blue line corresponds to the numerical solution of Eq. (3.30). The numerical solution is only shown for the domain walls initialised in the [running state](#) because, when it is initialised at rest and the current density is switched on, the internal magnetisation of the domain wall changes. In this case,

the domain wall is not a rigid object, and not suited to be described by a 1D-model. Although the qualitative picture remains the same, the depinning current threshold does not correspond with the one determined from micromagnetic simulations. Therefore, we have not shown the numerical solution to Eq. (3.30) for the case where the domain wall is initialised at rest.

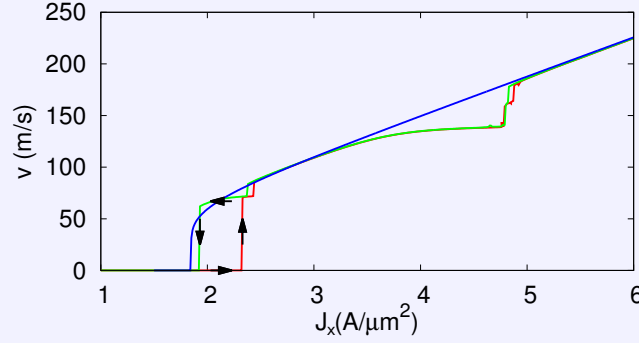


**Figure 3.11:** Velocity as function of current density for current driven domain wall motion in a periodic potential energy profile described by Eq. (3.14). The results from micromagnetic simulations are shown in red for a domain wall initialised at rest in a potential well and green for a domain wall initialised in a running state. The blue line corresponds to the numerical solution of Eq. (3.30) for a domain wall initialised in the running state.

A second difference between the micromagnetic simulations and the numerical solution to Eq. (3.30) is seen around  $2 \text{ A}/\mu\text{m}^2$  and from  $4$  to  $5 \text{ A}/\mu\text{m}^2$ . As shown in Fig. 3.11, at these current densities, there is no linear relation between the velocity and the current density. Instead, we see that the velocity remains almost constant. These plateaus in the velocity correspond to internal resonances in the magnetisation of the wall: As the domain wall moves through the potential energy profile, the magnetisation within the wall tilts forward and backward. One period of this oscillation corresponds to the time it takes to move one notch further forward. This is shown schematically in Fig. 3.12. These internal magnetisation changes are only accounted for in the full micromagnetic simulations and are not taken into account in Eq. (3.30).

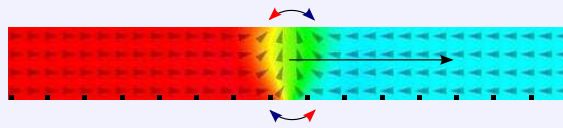


**Figure 3.12:** Schematic representation of the domain wall magnetisation fluctuations while the wall moves forward through the periodic potential profile.

At nonzero temperatures, next to the locked and running states, a third state, called the *bistable regime*, exists [148]. Here, a domain wall, initially in a *locked state*, can overcome an energy barrier with the help of *thermal fluctuations*. It then has enough potential energy to keep on moving, just as in the *running state* until the thermal fluctuations randomly trap the domain wall again in a potential well. Because the domain wall randomly switches between both states, this is called the *bistable regime*. In this regime, finite velocities are found for all

current densities. However, due to the large number of realisations necessary to determine the average velocity in such a system, it was not possible to perform full micromagnetic simulations and only the numerical solutions<sup>7</sup> of Eq. (3.30) are shown in Fig. 3.13 (a). At high current densities, the expected linear dependency between the domain wall velocity and the current density is recovered. At lower current densities, a clear transition is seen to the **bistable regime** which at the lowest current densities also shows a linear  $v$  vs  $J_x$  dependency, in correspondence with the behaviour in random potentials[132, 145]. Panels (b) to (d) show a typical domain wall path at different current densities. For the system under study the height of the energy barriers was 100 meV. This is four times higher than the thermal energy  $k_B T$  at room temperature ( $\approx 25$  meV). Therefore the transitions between the locked and running state follow each other rapidly and are difficult to see. In Fig. 3.13 (e) to (g), we show the results of the same calculation, repeated at 75 K. Now, there are much less transitions and all regimes are clearly discernible. Finally in panel (a), at 300 K, also the result of our calculation in a random potential **energy profile** from Fig. 3.10 is repeated. There,  $\varepsilon = 33$  meV, while it is 35 meV for the periodic potential energy profile. Although, the average velocities in the linear regimes are comparable, we see that the nonlinear transition between them is much steeper in the periodic energy profile.

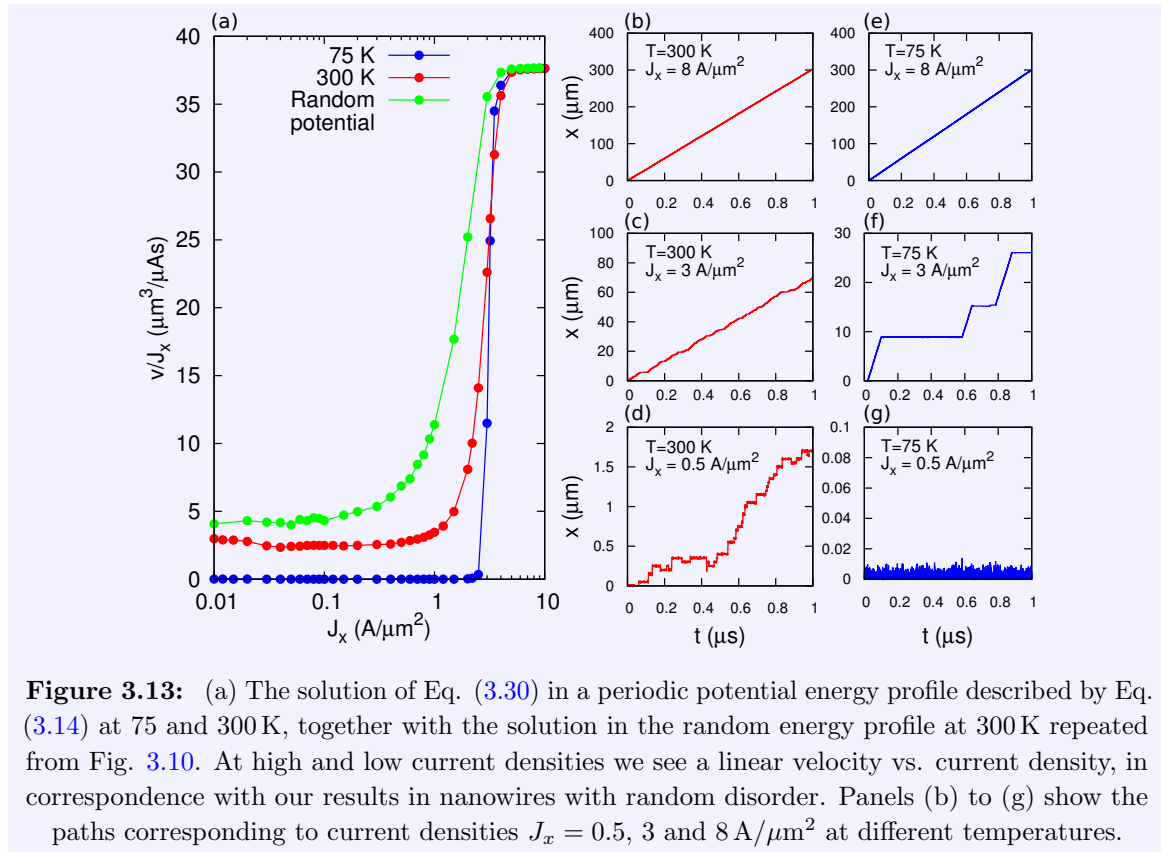


**Figure 3.13:** (a) The solution of Eq. (3.30) in a periodic potential energy profile described by Eq. (3.14) at 75 and 300 K, together with the solution in the random energy profile at 300 K repeated from Fig. 3.10. At high and low current densities we see a linear velocity vs. current density, in correspondence with our results in nanowires with random disorder. Panels (b) to (g) show the paths corresponding to current densities  $J_x = 0.5, 3$  and  $8 \text{ A}/\mu\text{m}^2$  at different temperatures.

<sup>7</sup>The equation of motion [Eq. (3.30)] was numerically solved with Euler's method by time stepping it with a fixed time step of 50 fs for 1  $\mu\text{s}$ . Extra realisations were performed until the uncertainty on the average velocity was smaller than 1%, with a maximum of 10 000 realisations.

### 3.3.7 Conclusion

The creep motion of rough 1D lines in large geometries displays a highly non-linear behaviour. In smaller geometries, this scaling law is expected to break down. We have shown that the velocity of compact domain walls displays a simple linear dependence on the driving force. To this end, we compared full micromagnetic simulations, which make no a-priori assumptions about the domain walls, to the solutions of an equation of motion which assumes the domain wall can be described by a point particle. The results of both approaches are consistent, proving that the motion of the domain walls can indeed be described as a point particle moving through a disordered [energy profile](#). This allowed us to investigate domain wall motion in regimes inaccessible to full micromagnetic simulations, where we could compare our results with existing experimental data. In periodic potential energy profiles, the domain wall motion is described well by our equation of motion when the domain wall is rigid. However, in such energy profiles the domain wall magnetisation sometimes exhibits internal resonances which are only accounted for in the micromagnetic simulations. Maybe this limitation of the current [1D-model](#) can be overcome by extending it with an extra parameter proportional to the tilting of the domain wall in the plane of the nanowire.



## CHAPTER 4

---

### Magnetic nanoparticles

---

*One person's data is another person's noise*  
— K. C. Cole

#### 4.1 Introduction

In this chapter we turn our attention to the magnetisation dynamics of *magnetic nanoparticles*. As the name suggests these are magnetic structures a few (10-100) nanometer in size. They consist of a single magnetic core covered by a non-magnetic shell (*single core particles*) or, alternatively, of several cores encapsulated by the same shell (*multicore particles*). Typically, iron oxides like magnetite or maghemite[1] are used for the cores, while the shells are made of biocompatible coatings like dextran. The latter allows for the safe use of the particles in [biomedical applications](#).

The nanoparticles are assumed to be small enough for the magnetisation to point in the same direction throughout the whole particle, i.e. they are *single-domain particles*. This contrasts the topic from the previous chapters where we investigated the motion of the walls between different magnetic domains. At first, both topics seem unrelated. However, on closer inspection they have a lot in common. For instance, the description of [thermal fluctuations](#) in micromagnetism, as used in Chapter 3, historically originated in the work of Brown [13, 30] who developed this theory to explain the thermal switching of [magnetic nanoparticles](#).

The central concept throughout this thesis is disorder. In the previous chapters, we investigated different possible sources of disorder. In Chapter 2, the effect of material imperfections was investigated and in Chapter 3, we added a stochastic thermal field as a second source of disorder. In this chapter we will further investigate these [thermal fluctuations](#). Due to the extremely small geometries in nanoparticles these fluctuations play an important role in the

magnetisation dynamics.

The introduction of this chapter contains an overview of the historical and theoretical background of [magnetic nanoparticles](#) and an introduction to [magnetorelaxometry](#).

In Section 4.2, the implementation and validation of [Vinamax](#) will be presented. [Vinamax](#) is a simulation tool for nanoparticles and has been published in [157].

In the next section [Vinamax](#) is used to investigate the concentration dependence of the iron oxide [magnetic nanoparticles](#) on the [Néel relaxation time](#) constant  $\tau_N$ . The results presented in this section have been published in [158].

In the last section of this chapter, Section (4.4), we present a new technique to characterise [magnetic nanoparticles](#). Typically, the dynamic behaviour of [magnetic nanoparticles](#) is investigated by measuring their response to externally applied magnetic fields. In contrast, we present a study of the magnetic fluctuations in an ensemble of [magnetic nanoparticles](#) recorded in the absence of any external excitation. Several samples of [magnetic nanoparticles](#) with varying particle size, composition and environment were investigated. We interpret the thermal magnetic [noise spectrum](#) to estimate particle size distributions and compare these to the distributions derived from [magnetorelaxometry](#) measurements of the same samples. The results presented in this section have been published in [159].

#### 4.1.1 Historical background

We begin our discussion with a historical and theoretical background of [magnetic nanoparticles](#). The longstanding fascination with magnetic nanoparticles was summarised by Temple *et al.* in Ref. [160]: *Almost uniquely, micro and nanoscale magnetic particles have held cross-disciplinary interest for leading physicists, chemists and biologists alike for more than half a century*[161–163]. In fact, as early as 1930, “Fine ferromagnetic particles” were already a topic of interest. In that year, *Frenkel and Dorfman* stated that sufficiently small particles should be uniformly magnetised[164]. Indeed, when the size of a magnet is very small, the [magnetostatic energy](#) is not large enough to compete with the [exchange energy](#) or [anisotropy energy](#). As explained in Section 2.1, only above a certain size is it energetically favourable to form domains.

This idea could have been proven already in 1935 when [Landau and Lifshitz](#) calculated the energy of a non-uniform state in spherical particles. However, they neglected to compare this energy to the one of a uniformly magnetised state. In 1940, [Brown](#) [165] noticed that domain theory fails to describe the magnetisation in long thin samples but did not see the implications of this result. Only around the fifties did *Guillaud*[166], *Kittel*[167], *Néel*[168] and *Stoner and Wolfarth*[169, 170] more or less independently introduce the concept of a [single-domain particle](#). This is commonly defined as a particle which is in a state of uniform magnetisation at any field[161]. Finally, in 1968 [Brown](#) [171] proved that *the state of lowest free energy is one of uniform magnetisation if  $r < r_{c0}$  and one of nonuniform magnetisation if  $r > r'_c$ , where*



$r_{c0}$  and  $r'_c$  are certain definite values of the radius  $r$ , and where  $r_{c0} < r'_c$ . This means that there exist a critical size under which the uniform magnetisation is always the lowest energy state and another size above which it never is. For sizes in between these limits it is possible that the ground state in the absence of an external field is a state of uniform magnetisation while it is not in the presence of an externally applied field. This theorem is also subject to some limitations:

1. The theorem only deals with the ground state. However, the system might be in some metastable state at higher energies. In fact, without this possibility, we would never observe hysteresis. The transition between different states at different energies is not trivial and will be discussed later.
2. This theorem was deduced without taking into account any possible [surface anisotropy](#). However, in some particles this extra energy term can alter the energy landscape and thus change the results significantly.

The increased knowledge (in part catalysed by the advent of [micromagnetic simulations](#)) about [magnetic nanoparticles](#) opened the door to use them in practical applications[19, 172]. Starting from the nineties, but especially in recent years[173], [magnetic nanoparticles](#) have gained a lot of interest due to their appealing properties for (mostly biomedical) applications. For instance, when exposed to an alternating magnetic field, they generate heat which can be used in the destruction of cancer cells [174]. Furthermore, when equipped with a suitable coating, they can be ideal drug carriers [175] or disease detectors [176]. Finally, the combination of the small sizes enabling virtually full body coverage and the large magnetic moment enabling non-invasive detection, makes them excellent candidates for use in imaging applications[177–181]. However, for these applications to work reliably, the magnetic behaviour of the nanoparticles should be fully understood. Before looking more closely at some of these applications, we will discuss the theoretical background of nanoparticle magnetisation.

### 4.1.2 Theoretical background

The key to understanding the magnetisation dynamics of [magnetic nanoparticles](#) lies in the energy landscape of these particles. Figure 4.1 illustrates the notations adopted in this chapter.

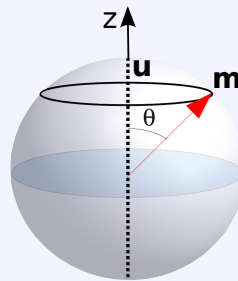


**Figure 4.1:** Schematic overview of a magnetic nanoparticle discussed in this section. The uniaxial anisotropy axis  $\mathbf{u}$  and the angle  $\theta$  between the  $z$ -axis and the magnetisation  $\mathbf{m}$  are shown.

As mentioned in Chapter 1, we will consider several energy terms which together dictate the magnetisation of these particles: the uniaxial **anisotropy energy** and the **Zeeman energy**. Here, we consider an ensemble of non-interacting nanoparticles, so that the **magnetostatic energy** can be neglected. For simplicity, the anisotropy axes  $\mathbf{u}$  lie along the same direction as the direction in which the external field is applied and the magnetisation is measured: the z-axis.

We thus remain with the anisotropy energy

$$E_{\text{anisotropy}} = KV \sin^2(\theta) \quad (4.1)$$

and the Zeeman energy

$$E_{\text{Zeeman}} = -VH_{\text{ext}}M_s \cos(\theta). \quad (4.2)$$

Figure 4.2 shows the energy of a nanoparticle in an external field for 5 different anisotropy strengths.

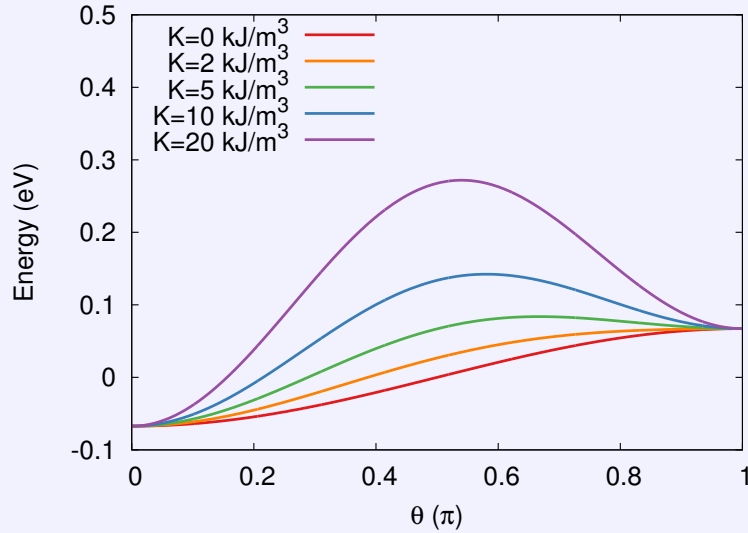


**Figure 4.2:** The energy for uniaxially anisotropic nanoparticles ( $r = 8 \text{ nm}$ ) in an external field of 12.5 mT for various anisotropy strengths.

For perfectly isotropic particles (red line), the Zeeman energy is the only relevant energy term. We see that there is only one minimum in the energy landscape, which lies in the direction in which the external field is applied. For increasing anisotropy strengths we see that the energy orthogonal to the uniaxial anisotropy axis goes up, and starting from roughly  $5 \text{ kJ/m}^3$  a local minimum at  $\theta = \pi$  appears. There exist simple analytical models[182] which predict the equilibrium magnetisation. Here, we will discuss two of them as they will be useful in the next sections.

First we will look at the energy landscape of an ensemble of isotropic nanoparticles. This energy landscape is determined completely by the external field  $H_{\text{ext}}$  and thus the Zeeman energy [Eq. (4.2)].

The equilibrium magnetisation in the presence of an external field was determined in 1905 by *Langevin*. His argument went as follows[1]: the probability that the magnetisation points in a certain direction is the product of a Boltzmann factor,

$$\exp\left(\frac{-\mu_0 V H_{\text{ext}} M_s \cos(\theta)}{k_B T}\right), \quad (4.3)$$

which takes the ratio between the thermal and Zeeman energy into account, and a geometric factor

$$2\pi \sin(\theta). \quad (4.4)$$

The ensemble average magnetisation along the z-axis is given by

$$\langle m_z \rangle = \frac{\int_0^\pi \cos(\theta) \exp\left(\frac{-\mu_0 V H_{\text{ext}} M_s \cos(\theta)}{k_B T}\right) 2\pi \sin(\theta) d\theta}{\int_0^\pi \exp\left(\frac{-\mu_0 V H_{\text{ext}} M_s \cos(\theta)}{k_B T}\right) 2\pi \sin(\theta) d\theta}. \quad (4.5)$$

If we substitute

$$\xi = \frac{\mu_0 M_s V H_{\text{ext}}}{k_B T} \quad (4.6)$$

and solve the integrals [Eq. (4.5)] the resulting magnetisation  $\langle m_z \rangle$  is given by the *Langevin function*  $\mathcal{L}(\xi)$ ,

$$\mathcal{L}(\xi) = \coth(\xi) - \frac{1}{\xi}. \quad (4.7)$$

When we consider anisotropic particles (with [uniaxial anisotropy](#)), the energy landscape is changed by the inclusion of the anisotropy energy term, and thus also the equilibrium magnetisation is influenced. In the limit of infinitely strong anisotropy, the only two occupied states will be the ones parallel and antiparallel to the anisotropy axis (the “up” and “down” directions respectively), which is why this is called the *two-state approximation*, corresponding to the *Brillouin* theory for spin 1/2.

The partition function of this system reads

$$\mathcal{Z} = \exp\left(\frac{-M_s V H_{\text{ext}}}{k_B T}\right) + \exp\left(\frac{M_s V H_{\text{ext}}}{k_B T}\right). \quad (4.8)$$

The probabilities to find a moment in the up and down direction then are

$$P_u = \frac{\exp(-\xi)}{\mathcal{Z}} \quad (4.9)$$

and

$$P_d = \frac{\exp(\xi)}{\mathcal{Z}} \quad (4.10)$$

respectively, where we used the same definition for  $\xi$  as above [Eq. (4.6)]. The equilibrium magnetisation, defined as  $P_u - P_d$  then is

$$\langle m_z \rangle = \tanh(\xi) \quad (4.11)$$

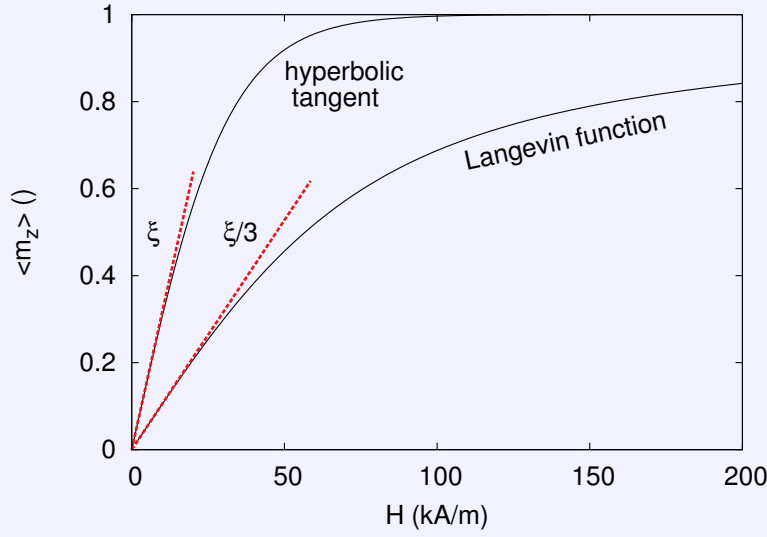


**Figure 4.3:**  $M(H)$  curves of two idealised systems. The Langevin function describes the magnetisation of isotropic particles while the hyperbolic tangent describes the magnetisation for anisotropic particles in the [two-state approximation](#). In the limit of small fields, the susceptibility for isotropic particles is  $\xi/3$  [with  $\xi$  as defined in Eq. (4.6)] and gradually goes to  $\xi$  in the limit of large anisotropy.

As one can see, the equilibrium state of these particles is unmagnetised in the absence of an external field ( $\xi = 0$ , and magnetised in the presence of an external field. The magnetisation thus displays a type of [paramagnetism](#). However in contrast to atomic paramagnetism, the magnetic moment of [magnetic nanoparticles](#) can easily be as large as  $10^5$  [Bohr magnetons](#) coupled by the [exchange interaction](#). Therefore this type of [paramagnetism](#) is called *superparamagnetism*, a term introduced by *Bean* in 1955[183].

We have discussed the equilibrium magnetisation of a superparamagnet. However, we are also interested in how (and how fast) a sample relaxes towards its equilibrium magnetisation. There are two different relaxation processes. In the first process, the particle itself rotates. This is called *Brownian relaxation* as it is based on the random thermal motion of the nanoparticle. This rotation randomises the magnetisation direction of the nanoparticles and thus demagnetises a sample in the absence of an external field. This happens on a timescale called the *Brownian relaxation time*  $\tau_B$ :

$$\tau_B = \frac{3pV_h}{k_B T} \quad (4.12)$$

In this equation,  $p$  denotes the viscosity of the fluid containing the nanoparticles, and  $V_h$  is the hydrodynamic volume of the nanoparticles. If the nanoparticles consist of (a) magnetic core(s) and a non-magnetic shell, the hydrodynamic volume is the total volume of the core(s) and shell together. Note that this *Brownian motion* was first discovered by R. *Brown* in 1827 and later modeled by *Einstein*[138] and has nothing to do with W. F. [Brown](#) who developed the theory behind the [thermal fluctuations](#) driving the next relaxation mechanism.

The second relaxation mechanism is called *Néel relaxation* [184] and originates in the random [thermal fluctuations](#) of the magnetic moment of the particle itself. The typical timescale at which this happens in the absence of an external field is called the *Néel relaxation time*  $\tau_N$

$$\tau_N = \tau_0 \exp\left(\frac{KV_c}{k_B T}\right) \quad (4.13)$$

In this equation,  $V_c$  denotes the volume of the nanoparticle core and  $\tau_0$  stands for the inverse of twice the attempt frequency and is typically taken as a constant in the range of  $10^{-8}$  to  $10^{-12}$  s. Although  $\tau_0$  is considered fixed, it is actually dependent on the properties of the nanoparticles. [Néel](#) tried to explain [184] the relation between  $\tau_0$  and the (material) properties of the nanoparticles, and [Brown](#) refined Néel's work to arrive at [30]

$$\tau_0 = \frac{1 + \alpha^2}{2\alpha\gamma_0} \sqrt{\frac{2\pi k_B T}{\mu_0 H_K^3 M_s V}} \quad (4.14)$$

with  $H_K = 2K/\mu_0 M_s$ . We will return to this attempt frequency in Section 4.3, where we will determine  $\tau_0$  for a specific nanoparticle sample based on [magnetorelaxometry](#) data.

The ratio between the energy barrier and the thermal energy in the system in Eq. (4.13) relates the relaxation time to the anisotropy strength. If the thermal energy is too low to overcome the energy barrier within the time frame of the experiment, the magnetisation of the nanoparticle is considered *blocked*. Due to the exponential temperature dependency, there exist a transition temperature under which the magnetisation is blocked and above which it is able to freely rotate within the timescale of the experiment. The temperature at which this transition takes place is called the *blocking temperature*.

We finish this theoretical background by stating that the dipolar interactions between particles were neglected so far. Taking these into account considerably complicates the picture as also the position of each individual particle influences the magnetisation. In Section 4.3, these effects will be numerically investigated.

### 4.1.3 Applications

In recent years, many *biomedical applications* based on nanotechnology [185] in general and [magnetic nanoparticles](#) [19, 173] specifically have emerged. Examples of applications under development are:

- *Targeted drug delivery* [186, 187]. Medicines attached to nanoparticles are administered locally by guiding them towards the desired regions with external fields.
- *Disease detection* [188, 189]. When nanoparticles are coated with a biochemical marker which attaches them to certain cell types, e.g. cancer cells, the magnetic field of the particles allows to monitor the position of these cells.

- *Hyperthermia*[190–192]. Once magnetic nanoparticles are attached to e.g. cancer cells, they can be heated in an oscillating field and destroy the cells.

Most applications require an accurate knowledge of the spatial distribution of the magnetic particles [193, 194] and thus require a nanoparticle imaging technique [195, 196]. Some promising imaging techniques are *Magnetic Particle Imaging* [181], *magnetorelaxometry* [20] and *Electron Paramagnetic Resonance*[197] (which in the context of ferromagnetic materials is often called *ferromagnetic resonance*[198]). While each method has its distinct advantages, none of them is able to quantitatively reconstruct the spatial particle distribution *in vivo*. While magnetic particle imaging has a sub-millimeter resolution[199], its field of view still is quite small and it has a large power consumption. Electron paramagnetic resonance can accurately determine the total *magnetic nanoparticle* concentration in the sample, but currently only allows to recover the 1D spatial distribution [197]<sup>1</sup>. Inadequate knowledge of the distribution of the nanoparticles results in suboptimal applications and even a decrease in patient safety and comfort. The development of an adequate technique for nanoparticle imaging is challenging, in part, due to an insufficient understanding of the collective magnetic behaviour of the particles.

Next to these *biomedical applications*, magnetic nanoparticles are currently also investigated for data storage[200]. Over the last 50 years, hard drives essentially stayed the same: data is written on platters of a magnetic material. During these 50 years, the size of the regions which represented a bit became smaller and smaller. We recently approached the point, called the *superparamagnetic limit*, where the integrity of the data is no longer safe against *thermal fluctuations*. Introducing *PMA* materials in the platter allowed to make the surface of the bits smaller, but also these will eventually (and quite soon) hit the superparamagnetic limit. As an alternative, research is conducted on extremely small (<4 nm) *single-domain particles* made from materials (e.g. FePt, CoPt) with an extremely high anisotropy of up to 10 MJ/m<sup>3</sup> or more exotic rare-earth transition metals like SmCo with anisotropies of up to 20 MJ/m<sup>3</sup>, corresponding to a bit size of 2.2 nm [201]. There still remain some challenges, mostly of chemical nature, which need to be addressed, but it is clear that these nanoparticles are also regarded as a promising system to solve problems outside of biomedicine.

#### 4.1.4 Magnetorelaxometry

Now we will have a closer look at magnetorelaxometry, as this application will return in later sections. *Magnetorelaxometry* is an established measurement technique which can be used for the quantitative imaging of *magnetic nanoparticles* [178, 193, 195, 202, 203]. It assists the aforementioned *biomedical applications* of disease detection, drug targeting and hyperthermia. Furthermore, binding processes of *magnetic nanoparticle*-based biochemical reactions can be analysed [204–206] and it is actively utilised to investigate the physical properties of *magnetic nanoparticle* suspensions[207–210].

---

<sup>1</sup>In simulations this was recently extended towards 2D and 3D [177].

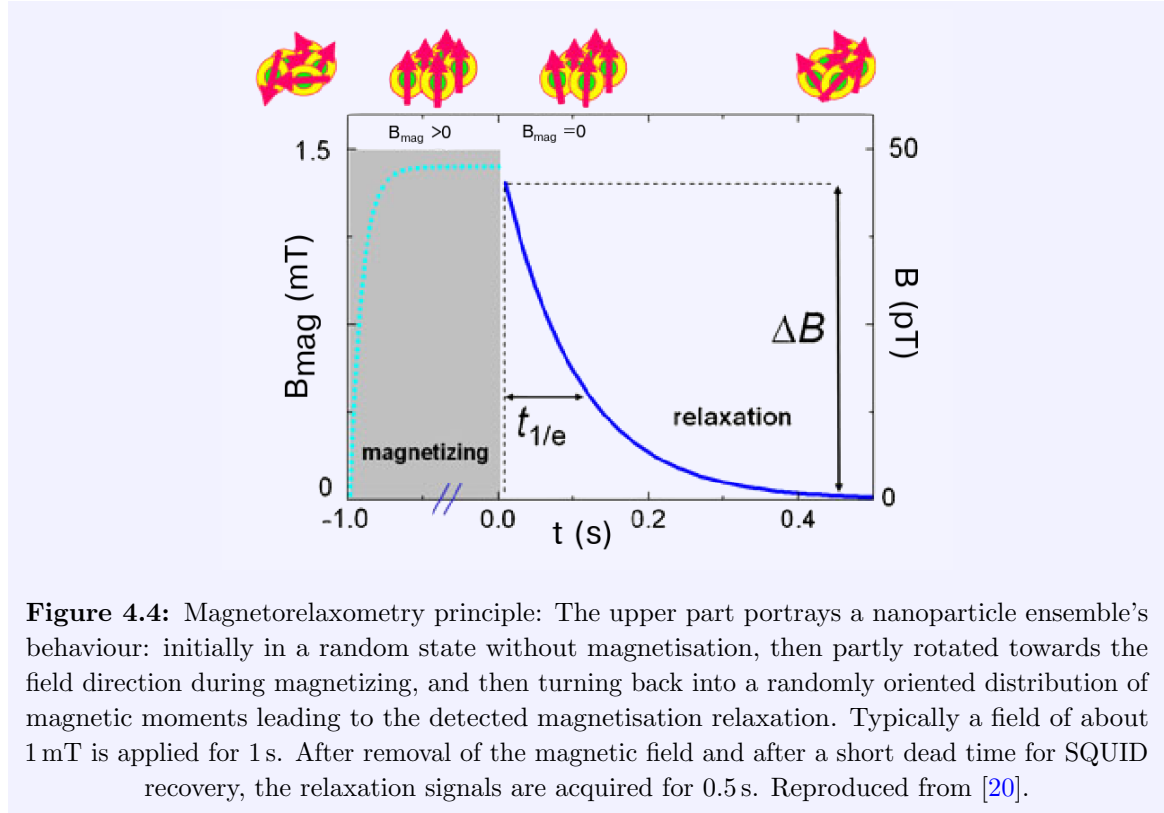


**Figure 4.4:** Magnetorelaxometry principle: The upper part portrays a nanoparticle ensemble's behaviour: initially in a random state without magnetisation, then partly rotated towards the field direction during magnetizing, and then turning back into a randomly oriented distribution of magnetic moments leading to the detected magnetisation relaxation. Typically a field of about 1 mT is applied for 1 s. After removal of the magnetic field and after a short dead time for SQUID recovery, the relaxation signals are acquired for 0.5 s. Reproduced from [20].

A [magnetorelaxometry](#) measurement starts with the application of a magnetising field of typically 1 mT to a superparamagnetic nanoparticle sample. After a certain time (typically 1 second) this field is switched off and the sample relaxes back towards its demagnetised state [20]. The magnetisation  $\langle m_z \rangle$  of a sample of [magnetic nanoparticles](#) with size distribution  $P(V)$  relaxes from  $\langle m_z \rangle_0$  towards 0 with a characteristic time constant  $\tau_N$ , called the [Néel relaxation time](#) constant[184] according to

$$\langle m_z \rangle = \int_V \langle m_z \rangle_0 \exp\left(-\frac{t}{\tau_N(V)}\right) P(V) dV. \quad (4.15)$$

Note that the magnetisation decays exponentially when all particles have the same volume. Otherwise the decaying signal is characterised by the size distribution of the particles, i.e. a sum of exponentials. During the relaxation time of typically 0.5 s, the magnetic field can be measured with sensitive magnetometers such as SQUIDs or Fluxgates[189, 211–214].

To obtain quantitative information from these measurements, a comparison with a reference sample of known [magnetic nanoparticle](#) concentration measured under equal conditions is needed [20]. This reference sample must have the same physical properties because these have a large impact on the [magnetorelaxometry](#) signal. When assuming that dipolar interactions between the [magnetic nanoparticles](#) are negligible, the concentration of the sample can be obtained by the ratio of the two [magnetorelaxometry](#) measurement amplitudes (reference and investigation), as this scales linearly with the concentration.

## 4.2 Vinamax

To optimise [biomedical applications](#) based on [magnetic nanoparticles](#), a complete understanding of the magnetisation dynamics is necessary. Especially understanding the collective behaviour of ensembles of particles remains challenging to this day. Numerically investigating these particles from first principles (i.e. micromagnetically [2]) can lead to an understanding of this collective behaviour and consequently an improved performance of aforementioned applications. There was no simulation software available that is both accurate on the smallest timescales at which the micromagnetic dynamics take place, and still is able to simulate the long timescales involved in experiments. Therefore, we have developed *Vinamax*: a simulation tool in which individual nanoparticles are represented by single macrospins. *Vinamax* numerically simulates the magnetic dynamics by solving the [Landau-Lifshitz equation](#) [10]. It considers demagnetising and anisotropy fields, and takes into account externally applied fields that can be space and time-dependent. To be able to simulate large ensembles of nanoparticles the demagnetising interaction is calculated efficiently using a [dipole approximation method](#) [215]. This contrasts with approaches in which the demagnetising interaction is not taken into account [216] or cut off after a short distance, e.g. when considering aggregates of nanoparticles [217]. Additionally, thermal effects [13, 39] can be taken into account by two different approaches: a stochastic field term can be added to the effective field or the [magnetic nanoparticles](#) are switched at stochastic time intervals, equivalent to the first approach. *Vinamax* is a useful tool to validate higher-level models and/or investigate their limitations and has been published in [157].

This section focuses on the implementation and validation of *Vinamax* and is organised as follows. First the [Landau-Lifshitz equation](#) with the additional stochastic term is described in detail together with the algorithm used to calculate the [dipole-dipole interaction](#). Section 4.2.2 demonstrates the validity of the software by comparing simulation results to *MuMax3* [66]. The largest differences between both softwares are that *MuMax3* calculates the [magnetostatic field](#) using a [fast Fourier transform](#) method on a grid of cubic cells. This approach has the drawback in nanoparticle simulations that also the empty space between the nanoparticles (which can be more than 99% of the simulated volume) is taken into this calculation. This limits the number of nanoparticles that can be simulated. We were able to validate the *Vinamax* implementation on simple problems, with only a few nanoparticles, by comparing the results with *MuMax3*. Also in Section 4.2.2 the equivalency of the two different approaches to include thermal effects is demonstrated and a [magnetorelaxometry](#) simulation is considered and compared to the [moment superposition model](#) [208, 218], which is typically used to describe a magnetorelaxometry experiment[189]. Hereby we illustrate the usefulness of *Vinamax* in this field. Finally, some concluding remarks about *Vinamax* are given at the end of this section.

### 4.2.1 Methods

In Chapter 1 we introduced the theory of [micromagnetism](#), and in this section we focus on its implementation in *Vinamax*. However, it is not possible to fully separate both, which is why this section contains some repetitions of concepts already introduced earlier.



### Micromagnetic theory

We repeat that in the micromagnetic framework the reduced magnetisation is described as a continuum vector field  $\mathbf{m}(\mathbf{r}, t)$ . In the following the space and time dependence of the magnetisation vector field is no longer explicitly shown in the equations. The nanoparticles under consideration are assumed to be uniformly magnetised[219] (i.e. their size is sufficiently small to be [single-domain particles](#)). The [exchange interactions](#) do not have to be evaluated because all spins within each particle lie parallel to each other. Therefore, [Vinamax](#) can further simplify the continuum approximation by describing every nanoparticle as one single macrospin. [Vinamax](#) provides the user with a wide range of different methods, discussed in appendix A, to numerically integrate the [Landau-Lifshitz equation](#), which describes the magnetic dynamics of the nanoparticles.

The different terms contributing to the effective field are described in more detail below.

### External field

$\mathbf{H}_{\text{ext}}$  is an externally applied field which can be both space and time-dependent.

### Anisotropy field

In [Vinamax](#) the nanoparticles are assumed to have [uniaxial anisotropy](#) which is the case for the iron-oxide nanoparticles used in [biomedical applications](#) [19]. The field, Eq. (4.16), affecting a particle due to this anisotropy is the derivative to  $\mathbf{m}$  of the micromagnetic anisotropy energy term[1], Eq. (4.17).

$$\mathbf{H}_{\text{anisotropy}} = \frac{2K}{M_s \mu_0} (\mathbf{m} \cdot \mathbf{u}) \mathbf{u} \quad (4.16)$$

$$E_{\text{anisotropy}} = KV \left[ 1 - (\mathbf{m} \cdot \mathbf{u})^2 \right] \quad (4.17)$$

The anisotropy constant  $K$  and the anisotropy axis  $\mathbf{u}$  can be chosen freely.  $\mathbf{u}$  can be set to a predefined direction or to uniformly distributed random directions for all nanoparticles. To this end, two random spherical coordinates  $\phi$  and  $\theta$  are generated with the following distributions:

$$\phi = 2\pi v_1 \quad (4.18)$$

$$\theta = 2 \arcsin(\sqrt{v_2}) \quad (4.19)$$

where  $v_{1,2}$  denote two uncorrelated, uniformly distributed random numbers in the interval  $[0.0, 1.0)$ . These spherical coordinates are then mapped to their Cartesian counterparts using the well-known relations below:

$$x = \sin(\theta) \cos(\phi) \quad (4.20)$$

$$y = \sin(\theta) \sin(\phi) \quad (4.21)$$

$$z = \cos(\theta) \quad (4.22)$$

### Magnetostatic field and dipole approximation method

The magnetostatic or [demagnetising field](#) originates in the [dipole-dipole interaction](#) between the different particles. Its contribution to the effective field is given by[1]

$$\mathbf{H}_{\text{demag}} = \sum_i V_i M_{s,i} \left[ 3 \frac{(\mathbf{m}_i \cdot \mathbf{r}_i) \mathbf{r}_i}{r_i^5} - \frac{\mathbf{m}_i}{r_i^3} \right], \quad (4.23)$$

where  $i$  loops over all particles.  $\mathbf{r}_i$  denotes the distance from each particle to the point at which the magnetostatic field is evaluated, and  $V_i$  is the volume of each particle. Although it is uncommon to use the term “[demagnetising field](#)” in the context of nanoparticles, we will use the notation  $\mathbf{H}_{\text{demag}}$  for the magnetostatic field in order to keep the notation consistent throughout the whole thesis.

To evaluate Eq. (4.23) by a direct pairwise calculation of the [demagnetising field](#) between all particles (called the *brute force method*) would take a lot of time. To speed up the evaluation of the demagnetising field, we have implemented a *dipole approximation method*. This method is based on a multipole approximation described by Tan[215]. We will briefly describe our adapted implementation, but for a detailed explanation we refer to Ref. [215].

In [Vinamax](#), the user has to define a *world*, which is a cube that encloses all the particles in the simulation. This cube is then subdivided into 8 subnodes, which are further subdivided until every node contains at most one particle. Within this tree, we then calculate the *centre of magnetisation* once for every node. The centre of magnetisation ( $\mathbf{R}_{\text{CM}}$ ) is the position of the particles in the node weighted with the magnetic moment of each particle. This is shown in Eq. (4.24), where  $\sum_i$  denotes a sum over all particles in the node, and  $\mathbf{r}_i$  is the position of particle  $i$ .

$$\mathbf{R}_{\text{CM}} = \frac{1}{\sum_i V_i M_{s,i}} \sum_i \mathbf{r}_i V_i M_{s,i} \quad (4.24)$$

If  $\rho$ , a length which takes the distance between two nodes and their size into account, is smaller than a threshold<sup>2</sup>  $r^*$ , then we take the contribution of this node to the total demagnetising field into account as if all the particles in that node were compressed into one dipole in the centre of magnetisation of that node. In that case we evaluate

$$\mathbf{H}_{\text{demag}} = \frac{3(\mathbf{M} \cdot \mathbf{r})\mathbf{r}}{r^5} - \frac{\mathbf{M}}{r^3}, \quad (4.25)$$

where  $\mathbf{r}$  denotes the distance between the centre of magnetisation of the node and the point at which the field is evaluated. Before every time step, the magnetisation  $\mathbf{M} = \sum_i V_i M_{s,i} \mathbf{m}_i$  of each node is updated based on the magnetisation of every particle within the nodes.

---

<sup>2</sup>The size of this threshold is a trade-off between accuracy and speed, where  $r^* = 0$  implies an infinite accuracy and corresponds to the brute force method mentioned above.

For every particle, the demagnetising field is evaluated with the algorithm described in Fig. 4.5, copied from Tan [215] with minor adaptations to our implementation.

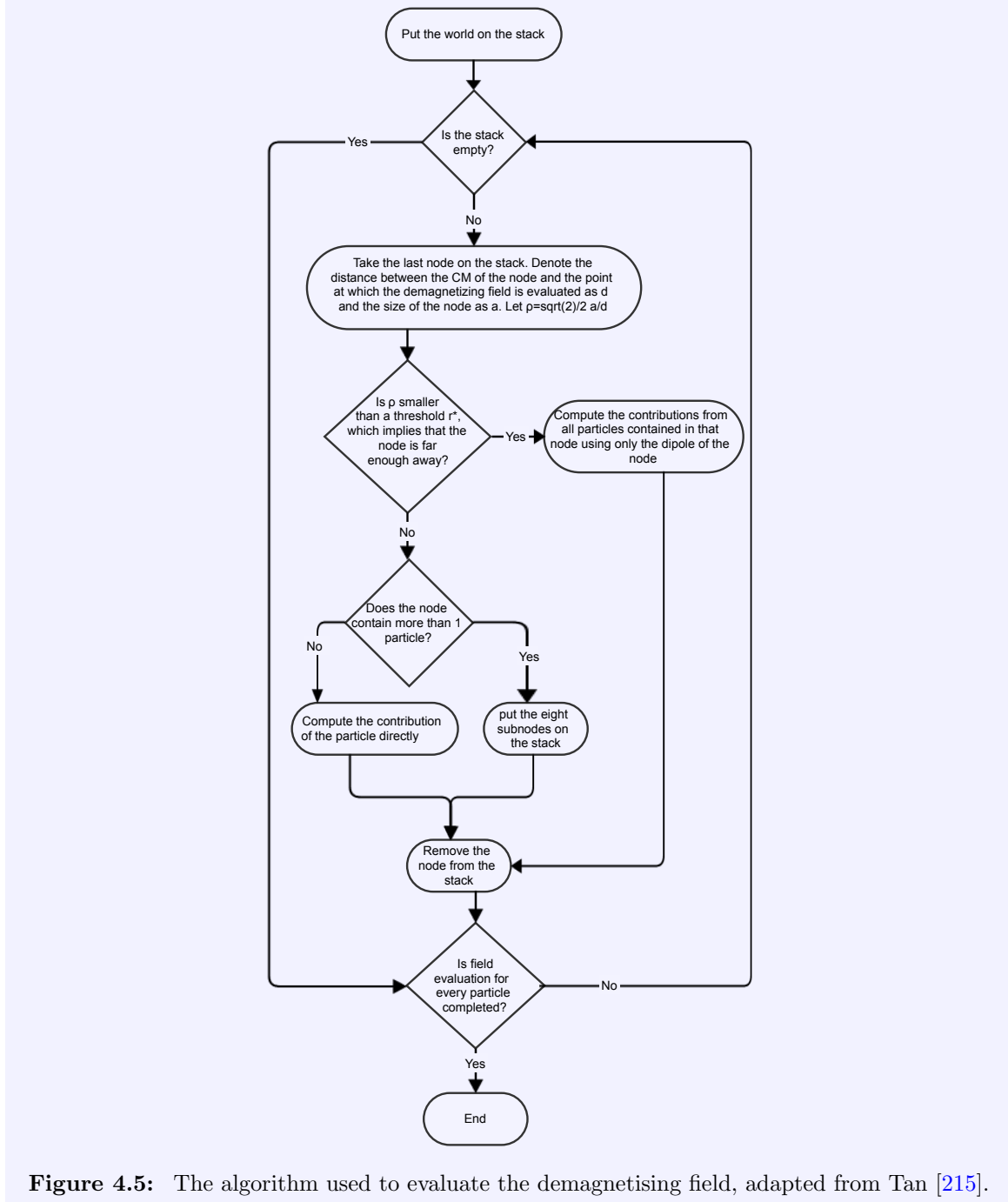


**Figure 4.5:** The algorithm used to evaluate the demagnetising field, adapted from Tan [215].

This algorithm only requires computational time of  $\mathcal{O}(N \log(N))$ , while the direct pairwise evaluation of the demagnetising field ([brute force method](#)) between  $N$  particles [Eq. (4.23)] scales as  $\mathcal{O}(N^2)$ . These statements are validated in Section 4.2.2.

### Thermal fluctuations

In this subsection we describe the two implementations of thermal fluctuations, and afterwards compare their properties

- **Stochastic thermal field**

The effective field  $\mathbf{H}_{\text{eff}}$  includes a stochastic term  $\mathbf{H}_{\text{th}}$  to take [thermal fluctuations](#) [14] into account. [Brown](#) [13] has worked out the detailed properties of this *stochastic field* for a [single-domain particle](#) with the use of the [fluctuation-dissipation theorem](#), which led to Eq. (4.26). Because in [Vinamax](#) each particle is approximated by one single macrospin, it is particularly suitable to use Brown's theory. The equation we implemented reads

$$\mathbf{H}_{\text{th}}(t) = \eta(t) \sqrt{\frac{2k_{\text{B}}T\alpha}{\mu_0\gamma_0M_sV\Delta t}} \quad (4.26)$$

where  $\eta(t)$  denotes a random vector whose components  $\eta(t)$  are normal distributed random numbers with mean 0 and standard deviation 1 which are uncorrelated in space and time and  $\Delta t$  is the time step.

- **Stochastic switching**

The approach described above (stochastic thermal field) has a large computational cost. Therefore, also a faster implementation based on the *stochastic switching* of the nanoparticle magnetisation (a [jump noise process](#)) is presented. This approach, however has the drawback that it is only valid in the absence of an external field<sup>3</sup>, as the implemented equation was derived only for this case.

For a [single-domain particle](#) with [uniaxial anisotropy](#), Eq. (4.26) leads to switching between two states with minimal energy, separated by an energy barrier of height  $\Delta E = KV$  with a switching rate  $f$ :

$$f = f_0 \exp\left(\frac{-\Delta E}{k_{\text{B}}T}\right) \quad (4.27)$$

In the high barrier limit ( $\Delta E \gg k_{\text{B}}T$ )  $f_0$  is equal to [13, 220, 221]

$$f_0 = \frac{\alpha\gamma_0}{1 + \alpha^2} \sqrt{\frac{\mu_0 H_K^3 M_s V}{2\pi k_{\text{B}}T}} \quad (4.28)$$

with  $H_K = 2K/\mu_0 M_s$  equal to the coercive field.

The probability that a particle does not switch during a certain time  $\Delta t$  is given by [220]

$$\frac{dP_{\text{not}}}{dt} = -fP_{\text{not}}. \quad (4.29)$$

---

<sup>3</sup>Here, by “external field”, we mean all fields which do not originate in the nanoparticle itself, like externally applied magnetic fields or the demagnetising field from other nanoparticles

This leads to

$$\ln P_{\text{not}} = \int_0^{\Delta t} f dt \quad (4.30)$$

or

$$P_{\text{switch}} = 1 - \exp(-f\Delta t). \quad (4.31)$$

The next switching time for a particle can thus be generated with

$$t = -\frac{1}{f} \ln(1 - P_{\text{switch}}) \quad (4.32)$$

by substituting  $P_{\text{switch}}$  with a random number, uniformly distributed in the interval (0,1)[36]. When the simulation reaches this time, the magnetisation of the particle is switched to its opposite direction and a new switching time is generated.

The different properties of the two implementations for thermal effects are given in Table 4.1.

**Table 4.1:** The different properties of the methods implemented to simulate thermal effects.

	Stochastic field	Stochastic switching
External field	yes	no
Simulation speed	slow	faster
Adaptive time step	no	yes
Validity	always	approximation for high barrier particles

### Particle size distribution

As the distribution of nanoparticle diameters  $D$  is often described by a *lognormal distribution*[20, 222], the diameter of the particles in [Vinamax](#) can also be drawn from such a distribution. Equation (4.33) shows the probability density function  $P(D)$  for a lognormal distribution, and implies that the logarithm of  $D$  is normally distributed with mean  $\ln \mu$  and standard deviation  $\sigma$ .

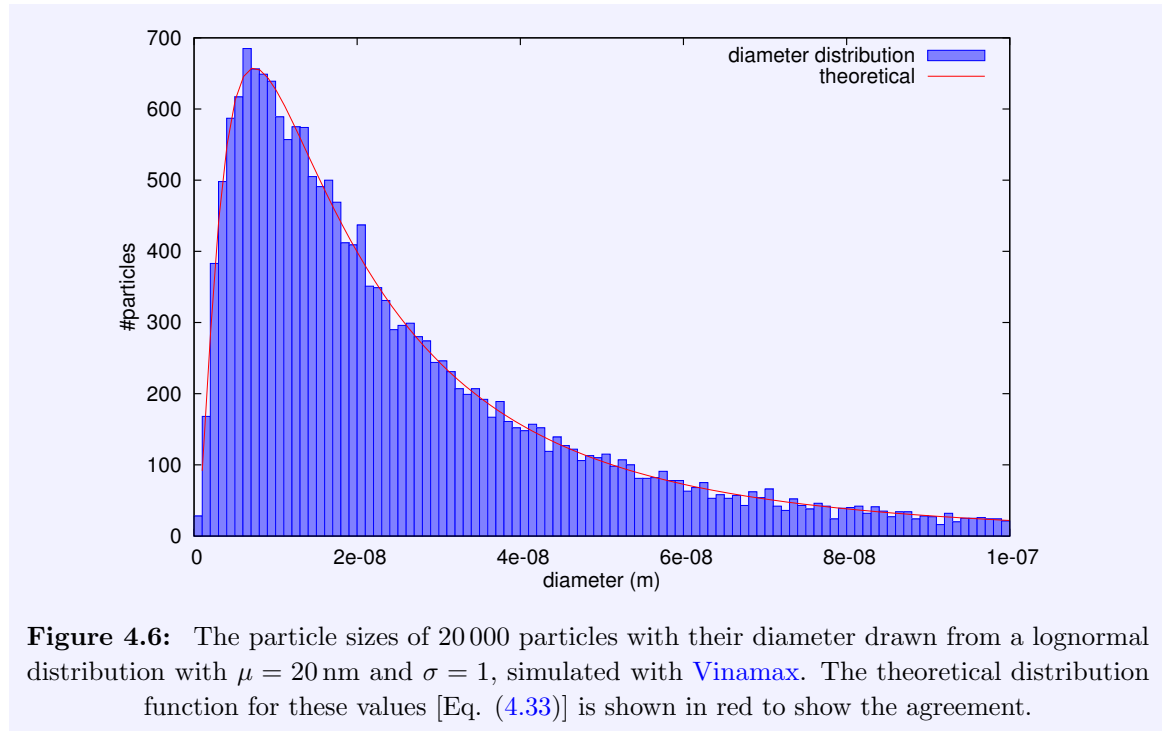
$$P(D) = \frac{1}{\sqrt{2\pi}\sigma D} \exp\left(-\frac{\ln^2(D/\mu)}{2\sigma^2}\right) \quad (4.33)$$

#### 4.2.2 Validation

The use of the macrospin approximation in [Vinamax](#) has the advantage that [exchange interactions](#) do not have to be evaluated. However, this has the drawback that the micromagnetic standard problems[223], which do incorporate exchange interactions, cannot be solved by [Vinamax](#). In this section we therefore simulate some simple, yet general, problems and compare their solution to solutions of the same problems, generated with the micromagnetic simulation software [MuMax3](#) [66]. In [MuMax3](#), a nanoparticle is simulated as a single [finite difference cell](#) with the same size and material parameters as the corresponding nanoparticle in [Vinamax](#).

### Lognormal size distribution

Before validating the implementation of the magnetic dynamics in **Vinamax**, we first verify if the **lognormal distribution** is implemented correctly. Figure 4.6 shows the agreement between the theoretical lognormal size distribution, given by Eq. (4.33), and the one generated with **Vinamax** of 20 000 magnetic nanoparticles with  $\mu = 20$  nm and  $\sigma = 1$ .



### Problem one: Precession and damping

In this first problem a single isotropic particle<sup>4</sup> is considered at 0 K. It is initialised with the magnetisation along the x-axis and a constant external field of 10 mT is applied along the z-axis. The magnetisation gyrates around this axis with a frequency of 28 GHz/T and slowly damps towards the z-axis.

In Fig. 4.7 the result of this simulation is shown. The oscillations in the x- and y-components of the magnetisation have a frequency of 0.28 GHz, which is in agreement with both the theoretically expected value and the result obtained with **MuMax3**. The steady increase of the z-component of the magnetisation corresponds with the damping towards the z-axis ( $\alpha = 0.02$ ).

<sup>4</sup>The nanoparticle has a radius of 10 nm and  $M_s = 860$  kA/m.

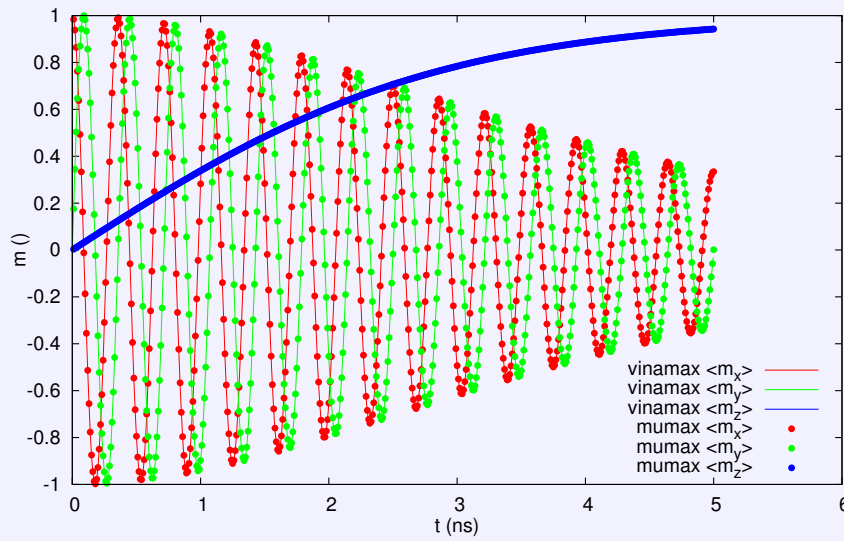


**Figure 4.7:** The average magnetisation components as a function of time for simulation problem one. The magnetisation precesses around the z-axis with a frequency of 0.28 GHz and slowly damps towards this axis. The different colours denote the different magnetisation components. The full lines denote the results obtained with [Vinamax](#), while the dots correspond to the results obtained with [MuMax3](#).

### Problem two: Demagnetising field

The aim of the second problem is to show that the [brute force method](#) to calculate the [demagnetising field](#) is implemented correctly. To this end, at 0 K, two isotropic nanoparticles<sup>5</sup>, initialised with their magnetisation along the y-axis, 129 nm apart, relax in the presence of an external field of 1 mT along the x-axis. The same simulation is repeated without calculating the demagnetising field to see whether this problem is suited to validate the implementation; i.e. to see if the demagnetising field has an influence.

Again, the results are validated by comparing the results from [Vinamax](#) with those from [MuMax3](#). In Fig. 4.8 it can be seen that the demagnetising field is of significant importance in this problem and that the simulation results agree well with each other.

<sup>5</sup>The nanoparticles have a diameter of 32 nm and a [saturation magnetisation](#) of 860 kA/m. The [Gilbert damping parameter](#)  $\alpha$  was set to 0.1.

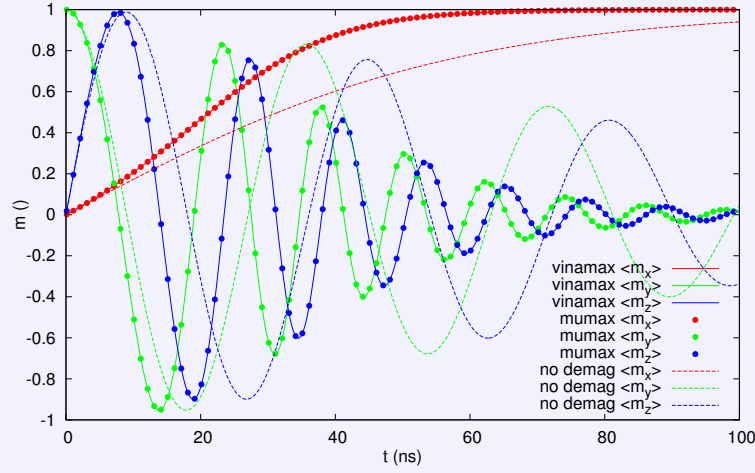


**Figure 4.8:** The average magnetisation components (different colours) as a function of time for simulation problem two. The dashed lines show the dynamics for the case in which the demagnetising field is not included in the simulation. The full lines and big dots show the simulation results (with the demagnetising field) obtained with [Vinamax](#) and [MuMax3](#) respectively. Both results are in agreement with each other.

### Problem three: Dipole approximation method

This example shows the agreement between the dipole approximation implementation and the brute force implementation. The same problem is also solved without calculating the demagnetising field to illustrate that it is of importance in this system.

In this problem 256 isotropic nanoparticles with a diameter of 32 nm and [saturation magnetisation](#) 860 kA/m are created with a spatially uniform distribution in a cube with a side of  $2\ \mu\text{m}$  with their magnetisation along the z-axis. They relax at 0 K in the presence of an external field of 1 mT along the x-axis ( $\alpha = 0.1$ ). In [Fig. 4.9](#) the results of these simulations are visualised, and we can conclude that there is a good agreement between the results obtained with the [dipole approximation method](#) and the [brute force method](#).

We have also investigated the performance of the different methods for evaluating the demagnetising field in [Vinamax](#). [Fig. 4.10](#) shows the scaling behaviour of the time it takes to calculate one time step with the brute force evaluation of the demagnetising field versus the [dipole approximation method](#). All simulations were performed on an Intel Core i7-3770 CPU @ 3.40GHz. The [brute force method](#) scales as  $\mathcal{O}(N^2)$ . The dipole approximation method used an  $r^*$  of 0.7 as this was determined to be a sufficiently low value[224]. This method is slower for smaller numbers of particles, but scales as  $\mathcal{O}(N \log(N))$ . From 512 particles on, the dipole approximation method is faster than the brute force calculation and for large numbers of particles this results in a large speedup of the simulation. Note that we adapted the volume of the simulation to the number of particles to keep the concentration of the particles constant.



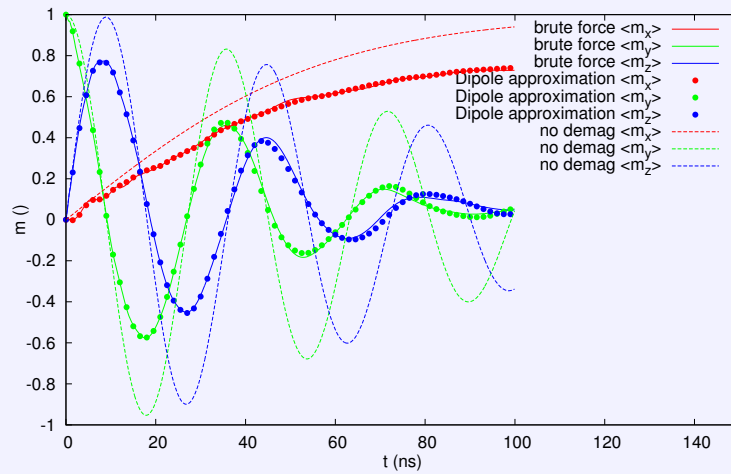


**Figure 4.9:** The average magnetisation components (different colours) as a function of time for simulation problem three. The dashed lines illustrate that the demagnetising field has an influence in this problem. The full lines and the dots correspond with the results obtained using the brute force or [dipole approximation method](#) (with  $r^* = 0.7$ ) respectively in [Vinamax](#), and are in agreement with each other.

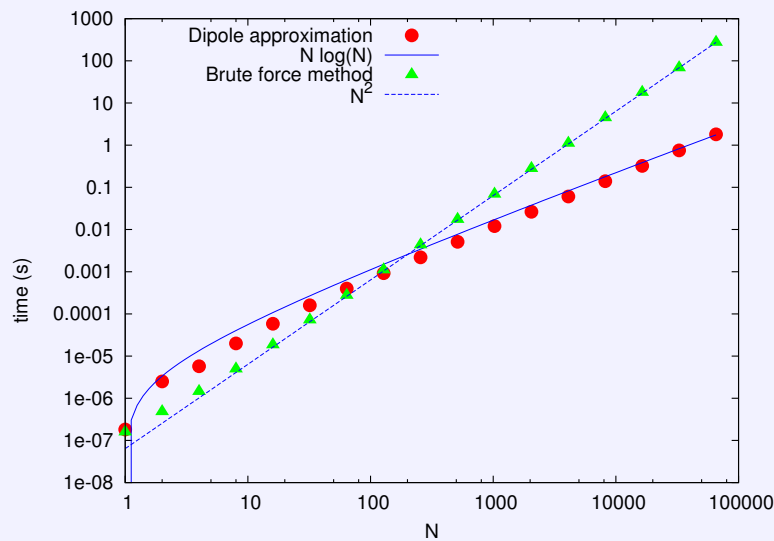


**Figure 4.10:** The time necessary to calculate one time step, with [Heun's method](#), as function of  $N$ , the number of particles in the system. The green triangles correspond with the brute force evaluation of the dipole-dipole interactions, while the red dots correspond with the [dipole approximation method](#) with  $r^* = 0.7$ . To visualise the scaling behaviour of both algorithms, a fit to a function  $\sim N^2$  (blue dots) and  $\sim N \log(N)$  (blue line) is shown.

#### Problem four: Equilibrium magnetisation

In the introduction of this chapter we discussed two models for the equilibrium magnetisation of isotropic particles and anisotropic particles in the [two-state approximation](#) with their

anisotropy axis along the z-axis. Here we will simulate ensembles of nanoparticles with different anisotropy strengths and compare the resulting magnetisation curves with the theoretical expectations.

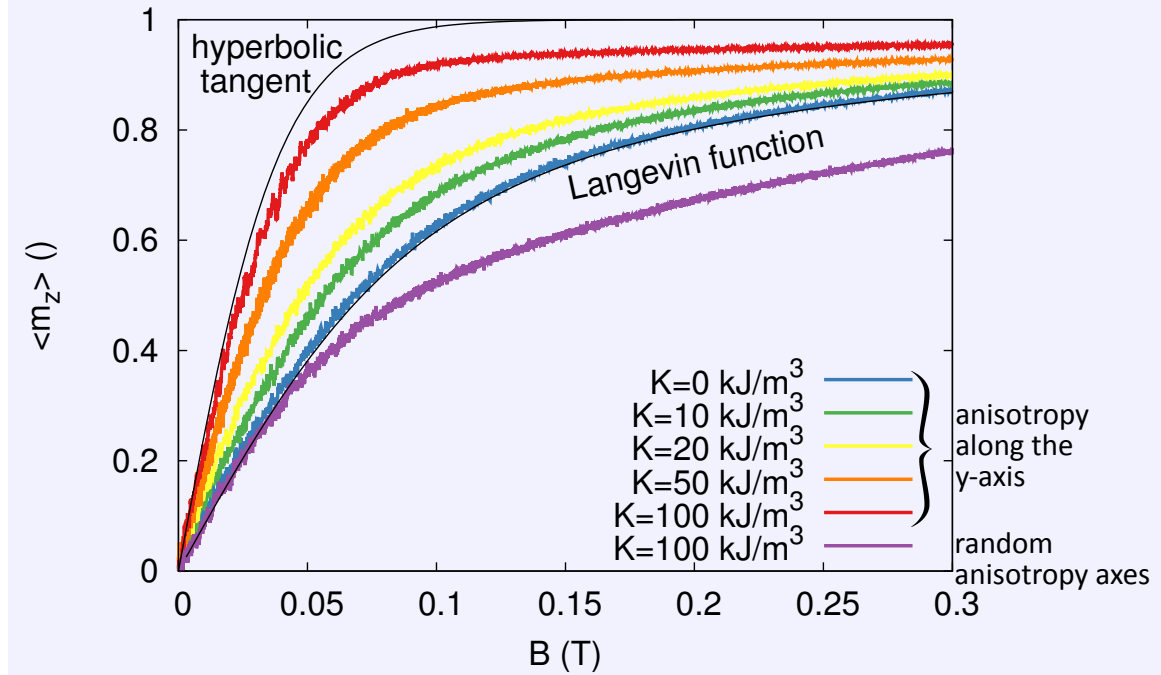


**Figure 4.11:** The average magnetisation along the z-axis as function of applied field for ensembles of particles with different anisotropy strengths. For all coloured lines (except the purple line) the anisotropy axis lies along the z-axis. The black lines correspond to theoretically expected results in the limit of low and high anisotropies. The purple line corresponds to the magnetisation of an ensemble of anisotropic particles with random anisotropy axes.

The magnetisation as function of field is shown in Fig. 4.11. As expected, the blue curve, corresponding with isotropic particles coincides with the [Langevin function](#) [Eq. (4.7)]. For increasing anisotropy strengths (green, yellow, orange and red lines) the curves lie closer and closer to the hyperbolic tangent [Eq. (4.11)] deduced in the [two-state approximation](#) corresponding to an infinite anisotropy.

As shown earlier in Fig. 4.3, at low fields, the susceptibility of the [Langevin function](#) equals  $\frac{\xi}{3}$  with

$$\xi = \frac{\mu_0 M_s V H_{\text{ext}}}{k_B T}, \quad (4.34)$$

as defined earlier in Eq. (4.6). The susceptibility increases for higher anisotropies towards  $\xi$ . Interestingly, in the limit of large anisotropy but with randomly oriented anisotropy axes, this is again equal to  $\frac{\xi}{3}$ , as illustrated by the purple curve.

### Problem five: Thermal switching time distribution and magnetisation relaxation

In an ensemble of [single-domain particles](#) with large uniaxial anisotropy, there exist two ground states, along the anisotropy axis, for every particle. Due to [thermal fluctuations](#), the magnetisation of each particle will switch between these two directions at random intervals. To illustrate this switching behaviour, the magnetisation as function of time for a single particle, simulated with a stochastic field, is shown in Fig. 4.12.

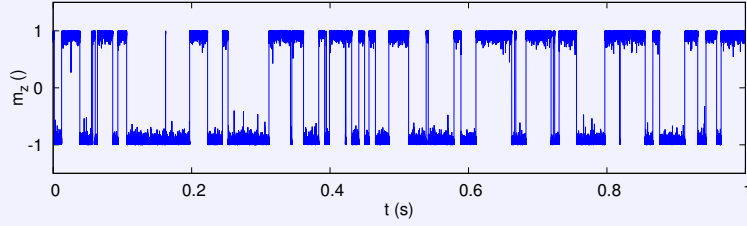


**Figure 4.12:** The magnetisation switching of a single nanoparticle with radius 9 nm at 300 K. The anisotropy constant is 10 kJ/m<sup>3</sup> and the anisotropy axis lies along the z-axis.  $M_s$  was 400 kA/m, and  $\alpha = 0.01$ .

We test our implementation of the stochastic thermal field by looking at the switching rate of uniaxially anisotropic particles at different temperatures. In the high barrier limit, this rate can be calculated analytically with Eqs. (4.27) and (4.28). Figure 4.13 shows that there is an excellent agreement between the theoretically expected and the simulated result.

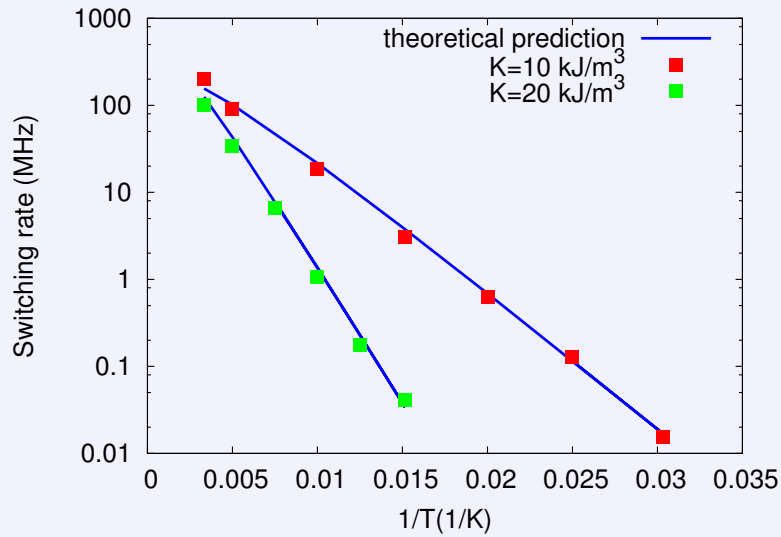


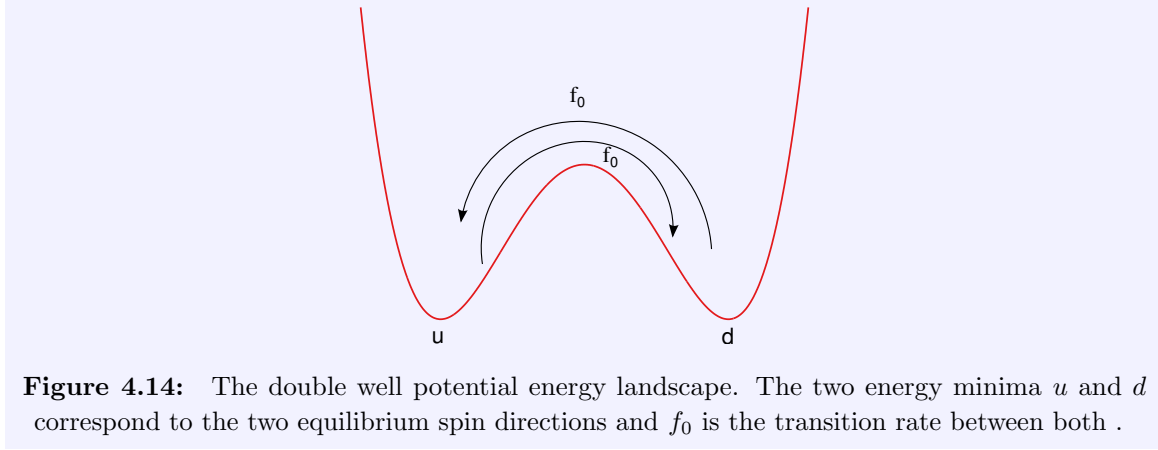
**Figure 4.13:** Arrhenius plot of the thermal switching rate of a particle with radius 5 nm, with  $M_s = 400$  kA/m,  $\alpha = 0.1$ ,  $K = 10$  or  $20$  kJ/m<sup>3</sup>. The blue lines show the theoretically expected switching rate from Eqs. (4.27) and (4.28).

The averaged switching of the individual nanoparticles slowly relaxes the magnetisation of an ensemble towards 0. The rate of this relaxation is given by the [Néel relaxation time](#)<sup>[184]</sup>  $\tau_N$ ,

Eq. (4.35).

$$\tau_N = \tau_0 \exp\left(\frac{KV}{k_B T}\right) \quad (4.35)$$

In this equation,  $\tau_0$  is related to  $f_0$  [Eq. (4.28)] by  $\tau_0 = \frac{1}{2f_0}$ , as explained with Fig. 4.14.



In this figure  $u$  and  $d$  correspond to the up and downwards direction along the  $z$ -axis, respectively. The time-derivative of  $u$ ,  $\dot{u}$  is given by

$$\dot{u} = f_0 d - f_0 u \quad (4.36)$$

and similarly,  $\dot{d}$  is given by

$$\dot{d} = -f_0 d + f_0 u. \quad (4.37)$$

The average magnetisation along the  $z$ -axis is  $\langle m_z \rangle = u - d$ , and its derivative is

$$\langle \dot{m}_z \rangle = 2f_0(d - u) = -2f_0\langle m_z \rangle. \quad (4.38)$$

If we solve this differential equation with the initial condition  $\langle m_z \rangle = 1$ , we find

$$\langle m_z \rangle = \exp(-2f_0 t), \quad (4.39)$$

explaining why  $\tau_0 = \frac{1}{2f_0}$ .

We now look at the distribution of switching times of particles with [uniaxial anisotropy](#). As can be seen in Fig. 4.15, both approaches to include thermal effects (a [stochastic field](#) or [stochastic switching](#)) show good agreement in the distribution of switching times. Therefore we use the stochastic switching implementation to look at the result of many of these switches on the magnetisation.

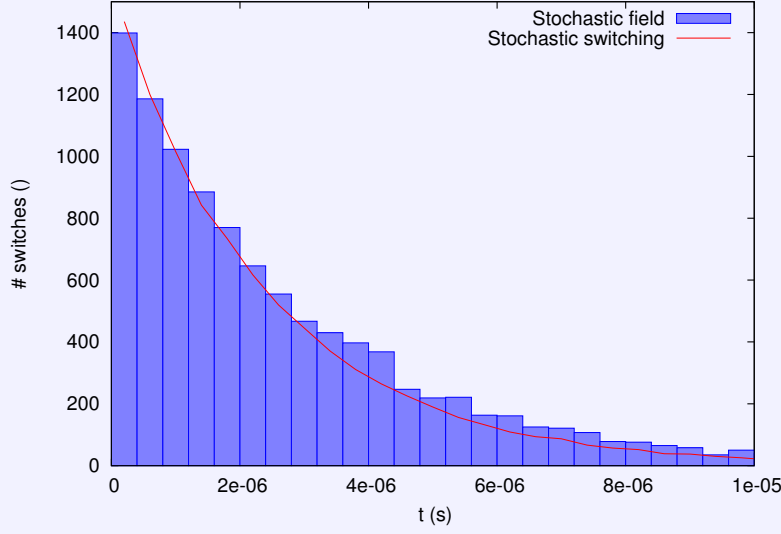


**Figure 4.15:** The switching time distribution for a particle with a diameter of 18 nm for two approaches to take thermal effects into account. The particle was simulated with the stochastic field until it switched 10 000 times (blue bars) and with the stochastic switching (red line) until 100 000 switching events were recorded (rescaled to 10 000, to be able to compare both distributions). The simulated nanoparticle had a [saturation magnetisation](#) of 400 kA/m and uniaxial anisotropy of 10 kJ/m<sup>3</sup>, along the z-axis. It was simulated at a temperature of 300 K and  $\alpha = 0.05$ . Both approaches show good agreement on the switching time distribution.

The magnetisation of an ensemble of nanoparticles with a size distribution  $P(V)$  is described by the *moment superposition model* [208, 218] [repeated from Eq. (4.15)].

$$\langle m_z \rangle = \int_V \langle m_z \rangle_0 \exp\left(-\frac{t}{\tau_N(V)}\right) P(V) dV \quad (4.40)$$

which equals  $\langle m_z \rangle = \langle m_z \rangle_0 \exp\left(-\frac{t}{\tau_N}\right)$  for particles of equal size. In this model, the magnetisation at the start of the relaxation is determined by Eq. (4.41) which describes a magnetisation process of time  $t_{\text{mag}}$  in a constant external magnetic field with size  $H_{\text{ext}}$ , with  $\mathcal{L}(\xi)$  the [Langevin function](#) [Eq. (4.7)].

$$\langle m_z \rangle_0 = \mathcal{L}(\xi) \left[ 1 - \exp\left(-\frac{t_{\text{mag}}}{\tau_N(H_{\text{ext}})}\right) \right] \quad (4.41)$$

Furthermore, during the magnetisation of the ensemble,  $\tau_N(H)$  differs from  $\tau_N$  in the absence of an external field, and is approximated by Eq. (4.42), where the factor 0.82 results from the random orientation of the anisotropy axes[218].

$$\tau_N(H_{\text{ext}}) = \tau_0 \exp\left(\frac{KV}{k_B T} \left(1 - \frac{0.82\mu_0 H_{\text{ext}} M_s}{K}\right)\right) \quad (4.42)$$

We have simulated 3 ensembles of nanoparticles with different size distributions, as shown in Fig. 4.16 (a). Each ensemble was magnetised for 1 second in a magnetic field of 1600 A/m as described by the [moment superposition model](#) [Eq. (4.41)]. The magnetic relaxation of the

sample was then calculated by the moment superposition model [Eq. (4.41)] [black lines in Fig. 4.16 (b)] and was compared to a **Vinamax** simulation. The particles had a **saturation magnetisation** of 400 kA/m, a uniaxial anisotropy of 10 kJ/m<sup>3</sup> and were simulated at 300 K with  $\alpha = 0.05$ . The results are shown in Fig. 4.16 (b) and show that there is in general a good agreement between **Vinamax** and the moment superposition model. The two curves coincide exactly for the ensembles with an infinitely sharp diameter distribution. There is a small deviation between both models for wider diameter distributions. This results from the fact that in **Vinamax**  $\tau_0$  has a particle volume dependency [Eq. (4.28)] while this is not accounted for in the moment superposition model.

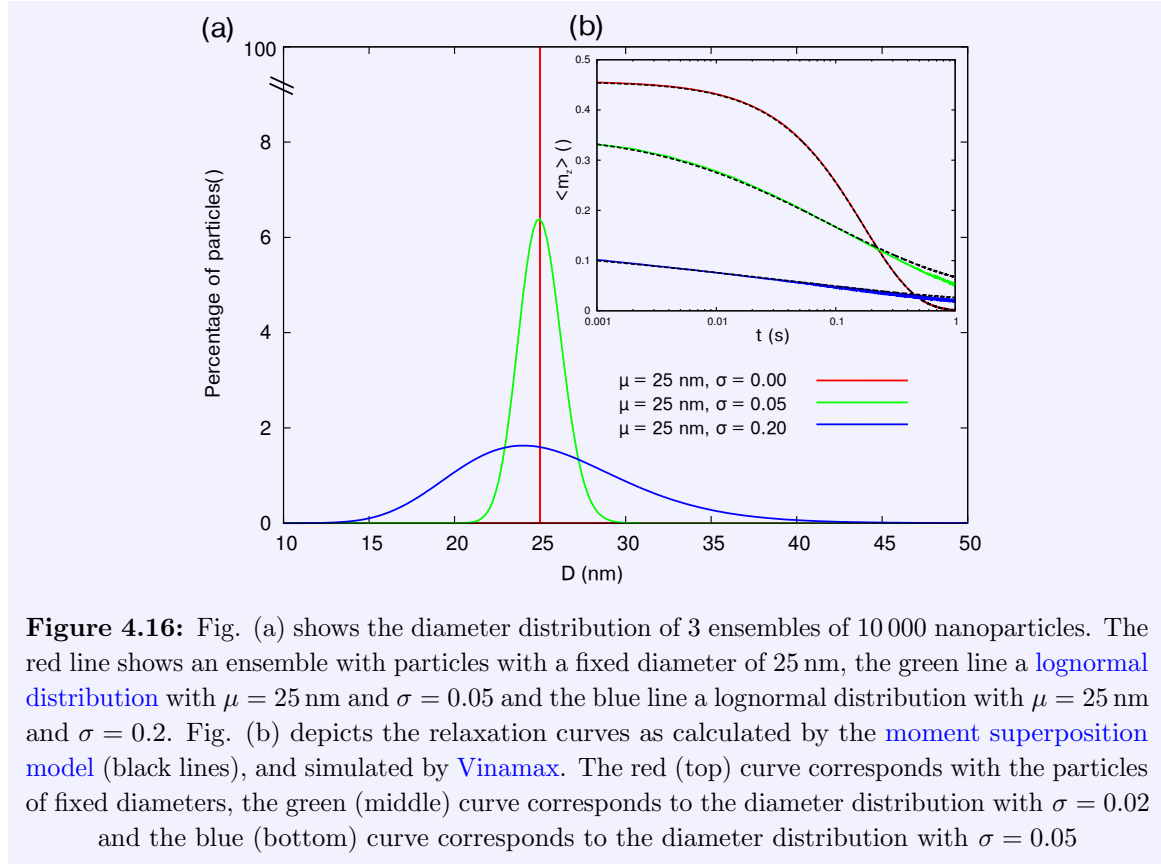


**Figure 4.16:** Fig. (a) shows the diameter distribution of 3 ensembles of 10 000 nanoparticles. The red line shows an ensemble with particles with a fixed diameter of 25 nm, the green line a **lognormal distribution** with  $\mu = 25$  nm and  $\sigma = 0.05$  and the blue line a lognormal distribution with  $\mu = 25$  nm and  $\sigma = 0.2$ . Fig. (b) depicts the relaxation curves as calculated by the **moment superposition model** (black lines), and simulated by **Vinamax**. The red (top) curve corresponds with the particles of fixed diameters, the green (middle) curve corresponds to the diameter distribution with  $\sigma = 0.05$  and the blue (bottom) curve corresponds to the diameter distribution with  $\sigma = 0.2$

### Problem six: Magnetisation response to an alternating field

In this final problem the implementation of a time-varying external magnetic field is validated. To this end we simulate an ensemble of 65536 **magnetic nanoparticles** ( $r = 6.66$  nm,  $M_s = 300$  kA/m,  $\alpha = 0.001$ ,  $K = 10$  kJ/m<sup>3</sup> and  $\mathbf{u}$  is the z-axis) at 300 K in a sinusoidal magnetic field with an amplitude of 2.387 kA/m and a frequency of 200 kHz. Again, this problem is simulated both with **MuMax3** and **Vinamax** and an excellent agreement is seen. In Fig. 4.17 the magnetisation as function of time is shown (left axis) together with the external magnetic field (right axis). The parameters in this problem were chosen such that the magnetisation could not overcome all energy barriers sufficiently fast to instantaneously follow the field. As a result we see that the magnetisation lags behind the field. This gives

rise to a *hysteresis loop*, as shown in Fig. 4.18.

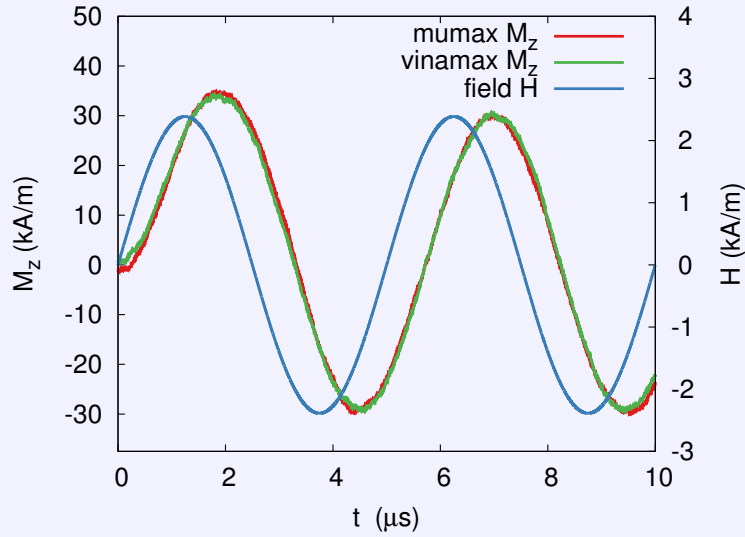


**Figure 4.17:** The magnetisation along the z-axis (left axis) of the ensemble of nanoparticles, simulated with **MuMax3** (red line) and **Vinamax** (green line) as function of time. The externally applied magnetic field (blue line, right axis) leads the magnetisation.

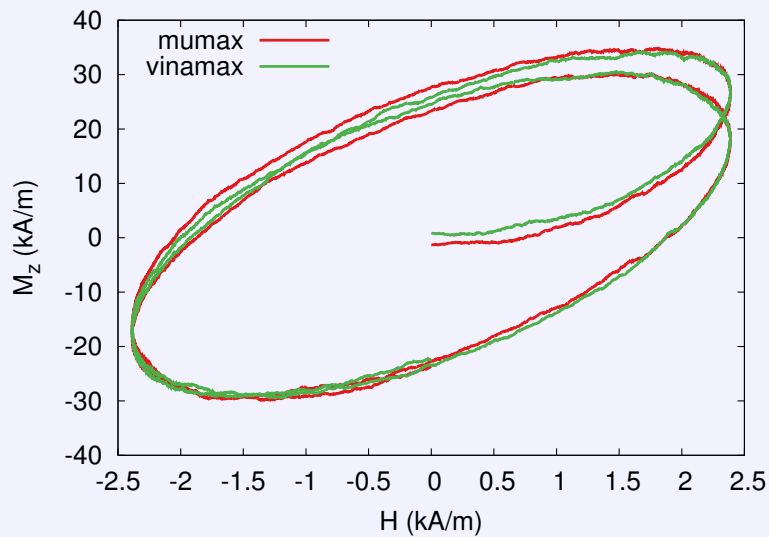


**Figure 4.18:** The magnetisation along the z-axis as function of external field strength, simulated with **MuMax3** and **Vinamax**. Because the thermal fluctuations are not large enough to overcome the energy barriers, the magnetisation is not in its equilibrium position and lags behind the magnetic field, giving rise to a hysteresis loop.

### 4.2.3 Conclusion

The aim of this section was to present **Vinamax**: a numerical software package which performs micromagnetic simulations of **magnetic nanoparticles**, approximated by macrospins. We validated **Vinamax** in various problems against other micromagnetic software (**MuMax3**) and analytical results. Each problem shows that a different part of **Vinamax** is implemented correctly and the results agree with the expected ones. **Vinamax** was also used to simulate a **magnetorelaxometry** experiment and the resulting magnetisation curve corresponds with the one obtained with the **moment superposition model**, which is typically used to describe these experiments[208, 218]. A small deviation was seen in the case of a broad distribution of nanoparticles which is due to the fact that in **Vinamax** the attempt frequency is volume dependent while this is considered constant in the moment superposition model.

Thanks to the **dipole approximation method** which scales as  $\mathcal{O}(N \log(N))$  with  $N$  the number of particles, it is possible to simulate systems with large amounts of particles, and on large timescales, which we will use in the next section. We emphasise that **Vinamax** can be used as a research tool in **biomedical applications**, where we especially aim at nanoparticle imaging techniques, such as **magnetorelaxometry**, where the collective effect of nanoparticles still is not completely understood. For instance, in the next section, **Vinamax** will be used to investigate the effect of dipolar interactions on the relaxation curve.



### 4.3 The Néel relaxation time constant

In the previous section we presented [Vinamax](#) [157]. Here, we will use this software package to investigate different aspects of the [Néel relaxation time](#) constant  $\tau_N$  in [magnetorelaxometry](#).

There exist different theoretical models which describe the relation between the physical properties of the [magnetic nanoparticles](#) and the [magnetorelaxometry](#) signal. Examples of such models are the [moment superposition model](#) [208, 225] and the *cluster moment superposition model* [20, 208]. However, compared to full [micromagnetic simulations](#), they have a less detailed level of modeling and do not take into account possible dipolar interactions between the [magnetic nanoparticles](#).

#### 4.3.1 Dipolar interaction in magnetorelaxometry

In the first part of this section, our aim is to investigate the influence of the [dipole-dipole interactions](#) between [magnetic nanoparticles](#) in [magnetorelaxometry](#) experiments. As reference samples in some cases [203, 208, 211, 226] contain [magnetic nanoparticle](#) amounts which differ to a great extent with respect to the sample, it might be possible that the comparison between the reference and sample [magnetorelaxometry](#) curves is not valid.

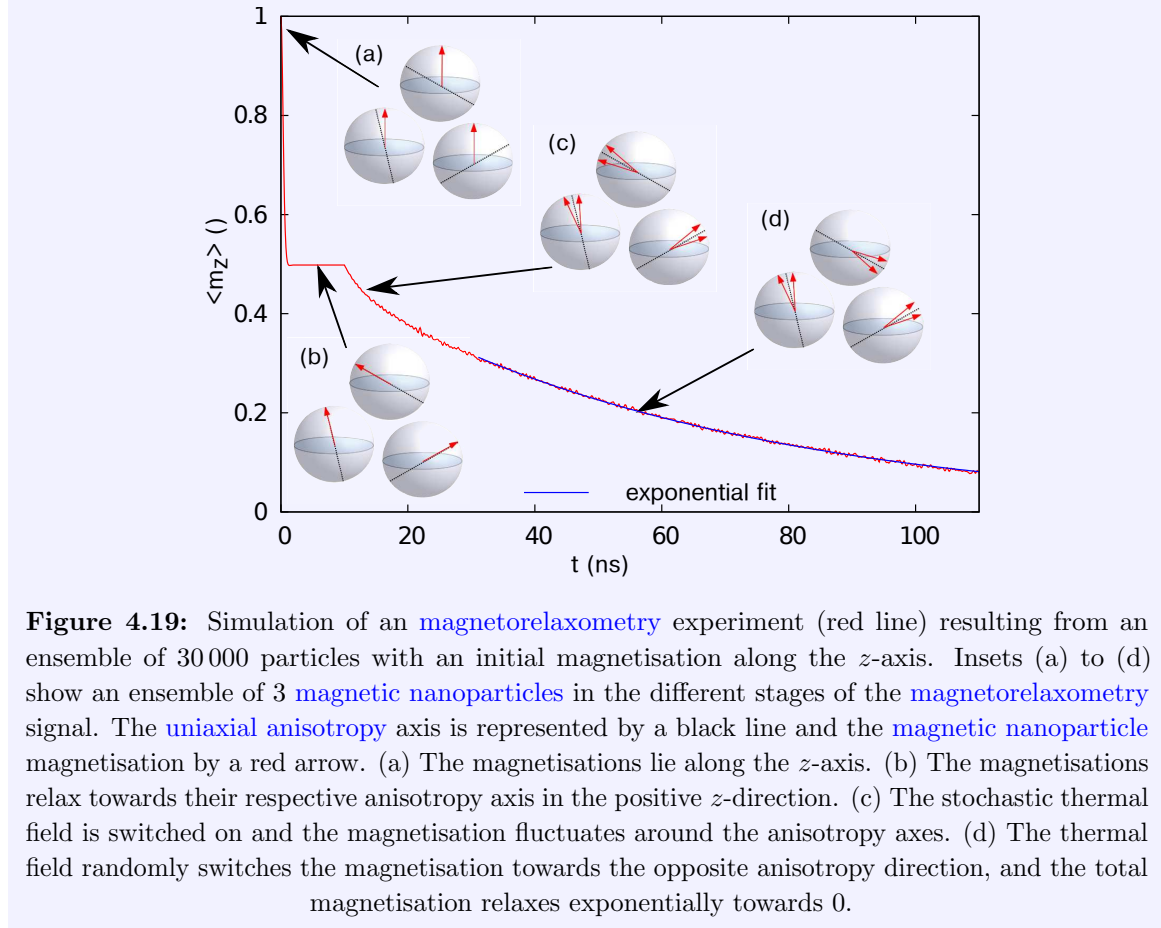
We start by performing a simulation in which these interactions are not taken into account, corresponding with an infinitely diluted sample. Figure 4.19 shows the simulated [magnetorelaxometry](#) signal of an ensemble of 30 000 nanoparticles having identical diameters of 11 nm, a random, but constant, [uniaxial anisotropy](#) axis and typical material parameters for magnetite: a [saturation magnetisation](#) of 400 kA/m and an anisotropy constant of 14.4 kJ/m<sup>3</sup>.

Insets (a) to (d) in Fig. 4.19 show a reduced [magnetic nanoparticle](#) ensemble of 3 particles to explain their magnetic states at the different stages in the [magnetorelaxometry](#) simulation. The magnetisation of the [magnetic nanoparticles](#) is represented by a red arrow and the anisotropy axis by a black line.

As [dipole-dipole interactions](#) equally affect the magnetising and demagnetising phase of a [magnetorelaxometry](#) experiment, we only simulate the demagnetising phase for practical purposes. To be able to accurately determine the [Néel relaxation time](#) constant  $\tau_N$ , we initialise the [magnetic nanoparticles](#) in a fully magnetised state along the  $z$ -axis. The normalised net magnetic moment along the  $z$ -axis of the particles is represented by  $\langle m_z \rangle$  and equals 1 in this stage [Fig. 4.19 (a)].

In the next stage [Fig. 4.19 (b)] the [magnetic nanoparticles](#) relax (with the thermal field still switched off) towards one of the energetic ground states, i.e. the magnetisation parallel with the uniaxial anisotropy axis in the positive  $z$  direction (due to the initialisation along the  $z$ -axis). The theoretical prediction of  $\langle m_z \rangle$  for randomly orientated anisotropy axes is

$$\int_0^{\pi/2} \sin(\theta) \cos(\theta) d\theta = 0.5.$$



In the subsequent stage [Fig. 4.19 (c)], the thermal field is switched on corresponding to a temperature of 300 K and the magnetisation fluctuates around the anisotropy axis. Due to these thermal fluctuations the magnetisation can switch between the two anisotropy directions at random intervals. Consequently,  $\langle m_z \rangle$  decays towards zero at a rate given by the Néel relaxation time constant  $\tau_N$  [Eqs. (4.15) and (4.35)] as shown in Fig. 4.19 (d). By fitting an exponential curve to the simulated magnetorelaxometry curve,  $\tau_N$  can be determined. In this simulation this was equal to 60 ns, and the fitted curve is shown in Fig. 4.19.

We investigate the effect of dipole-dipole interactions on the Néel relaxation time constant. Due to the large computational cost of evaluating the dipolar interactions, the simulations are limited to relaxation constants of the order of microseconds. We used the magnetic nanoparticle ensemble of the previous simulation as this ensemble had a relaxation constant of 60 ns (without dipolar interactions). The Gilbert damping parameter  $\alpha$  equals 0.01 in this simulation (note that the dipolar interactions are independent of the value of  $\alpha$ , which we verified numerically). We repeated the magnetorelaxometry simulation for increasing magnetic nanoparticle concentrations, taking into account the dipolar interactions on each

particle. Because the dipolar field only significantly changes after a switching event, and thus much more slowly than the other effective field terms, it was only updated every 10 ps. This approximation drastically speeds up the computations and it was verified that this does not affect the results. The [magnetic nanoparticles](#) in the simulations are fixed in space at uniformly distributed positions. As [magnetic nanoparticles](#) in [biomedical applications](#) are typically iron oxides, the [magnetic nanoparticle](#) amount is represented by an iron concentration. Fig. 4.20 shows the relaxation constant for increasing iron concentrations relative to the one obtained from the simulation without dipolar interactions (Fig. 4.19). Starting from an iron concentration of approximately 100 mmol/l (corresponding with a particle volume fraction of 0.0007 or 5.5 mg/cm<sup>3</sup> iron) we observe a steady decrease in the relaxation constant.

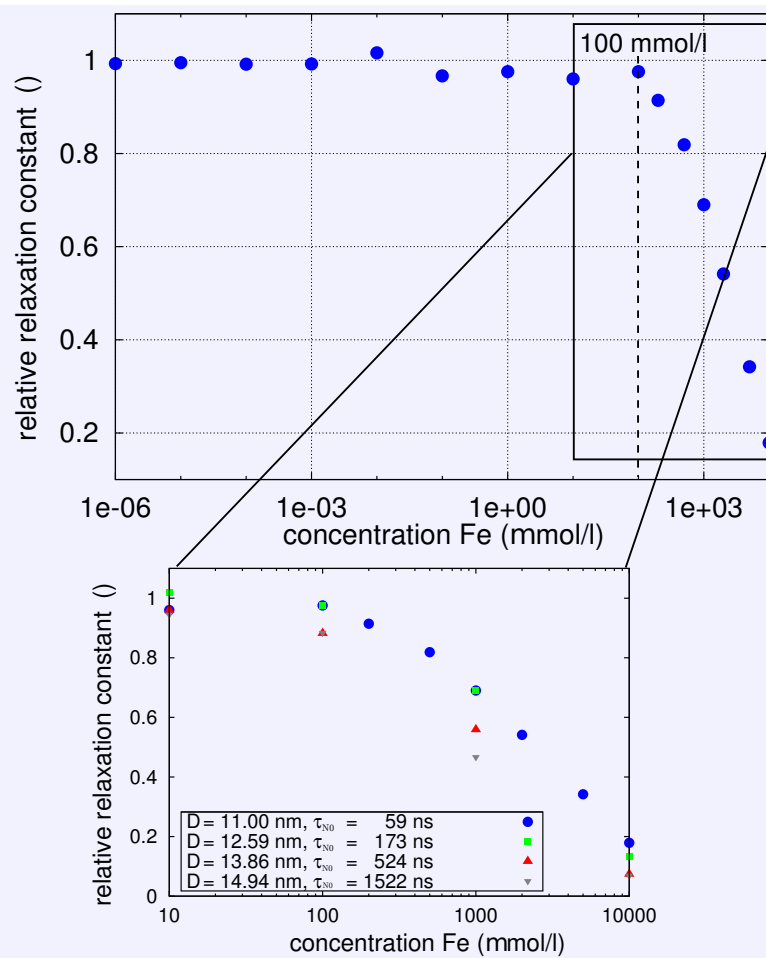


**Figure 4.20:** The relative relaxation time constant ( $\tau_N/\tau_{N0}$ , with  $\tau_{N0}$  the relaxation time constant without interactions) for increasing iron concentrations. When the iron concentration of 100 mmol/l is exceeded a decrease of the relaxation constant is observed. Inset: For [magnetic nanoparticles](#) of larger volumes the dipolar interactions start to influence the relaxation time constant from the same concentration (100 mmol/l iron).

A simple theoretical argument that only takes into account the interaction due to the nearest neighbours shows that the concentration from which on the dipolar interaction starts to affect

the relaxation time is independent of the size of the particles: the size of the demagnetising field of a nearest neighbour on a particle scales as  $V/r^3$  with  $V$  the volume of the particle and  $r$  the distance to its nearest neighbour. When considering a sample with the same iron concentration, but with larger particles, the net effect on the dipolar field is independent of the volume of the particles. Nonetheless, we have performed additional simulations of [magnetic nanoparticles](#) with a volume of 1.5, 2 and 2.5 times the volume of the [magnetic nanoparticles](#) with  $D = 11$  nm. The results imply that dipolar interactions start to affect particles of different sizes at a concentration of around 100 mmol/l iron. At higher concentrations, the particles are too close together to only take their nearest neighbours into account and the data points do not coincide anymore. We therefore emphasize that during experiments caution should be taken when using samples with high iron concentrations. This is especially important in experiments where particles are bound to cells or tissues, because these can induce local areas of high [magnetic nanoparticle](#) concentrations. One way of reducing particle aggregation is to employ particles with a sufficiently thick non-magnetic coating, such as dextran.

#### 4.3.2 The Gilbert damping parameter in magnetic nanoparticles

A second topic of interest when discussing  $\tau_N$  is the inverse of the attempt frequency:  $\tau_0$  [Eq. (4.35)]. The size of this parameter is determined by the value of the [Gilbert damping parameter](#),  $\alpha$ , which is not accurately known for [magnetic nanoparticles](#). We repeat that [Brown](#) [13] determined that in the high barrier limit ( $KV \gg k_B T$ ), and in the absence of an external field,  $\tau_0$  is given analytically by Eq. (4.14) with  $H_K = 2K/\mu_0 M_s$ :

$$\tau_0 = \frac{1 + \alpha^2}{2\alpha\gamma_0} \sqrt{\frac{2\pi k_B T}{\mu_0 H_K^3 M_s V}}. \quad (4.43)$$

Except for the [Gilbert damping parameter](#)  $\alpha$ , every quantity in this equation is known for [magnetic nanoparticles](#). There are indications[227–229] that this value can be significantly lower in nanoscale magnets than in bulk materials. Therefore we compare our numerical model to an actual [magnetorelaxometry](#) experiment to determine  $\alpha$ . Typically,  $\tau_0$  takes values between  $10^{-8}$  and  $10^{-12}$  s [20]. A good estimate of  $\alpha$  together with Eq. (4.43) could lead to a more accurate value of  $\tau_0$ . For iron oxide [magnetic nanoparticles](#) there is no data available for  $\alpha$ . There is however a value of 0.07 determined for the bulk material [230]. For thin films there is a clear trend visible for  $\alpha$  to increase with size[227–229], with an upper limit for  $\alpha$  of 0.0365[228]. We argue that in [magnetic nanoparticles](#) this value is expected to be even significantly smaller because of the nanoscale dimensions in every direction. Similar to the results on CoZr nanoparticles[229], we expect a size dependency of  $\alpha$ . However, as the [magnetic nanoparticles](#) used in practical applications have a limited range this dependency may safely be neglected.

We compare our numerical model to an [magnetorelaxometry](#) experiment performed at the Physikalisch-Technische Bundesanstalt in Berlin [210] to determine the [Gilbert damping parameter](#)  $\alpha$ . The [magnetic nanoparticles](#) are large single magnetite core SHP-20 particles

(Ocean Nanotech, USA) coated by oleic acid combined with an amphiphilic polymer. The size distribution was obtained by TEM[210] and showed a [lognormal distribution](#), which is identified by 2 parameters: a mean and the standard deviation of the logarithm of the distribution. These were determined to be 19 nm and 0.11 respectively. The [saturation magnetisation](#) was determined to be 250 kA/m and  $K = 14.5 \text{ kJ/m}^3$ . The [magnetic nanoparticles](#) are freeze dried in a sugar matrix so only [Néel relaxation](#) occurs allowing to simulate the [magnetorelaxometry](#) signal using our numerical model. The iron concentration is 4.85 mmol/l, which is sufficiently low to neglect [dipole-dipole interactions](#) (see Fig. 4.20). The experiment was performed at 295 K. The magnetising field was applied for 1 second and had an amplitude of 1600 A/m. In contrast to the numerical method described earlier in this section (Fig. 4.19), we now consider an experiment in which the particles are not fully magnetised. Consequently, the magnetising stage of the experiment also has to be simulated. After this stage, the [magnetorelaxometry](#) signal is recorded as the sample is allowed to relax for 0.4 seconds.

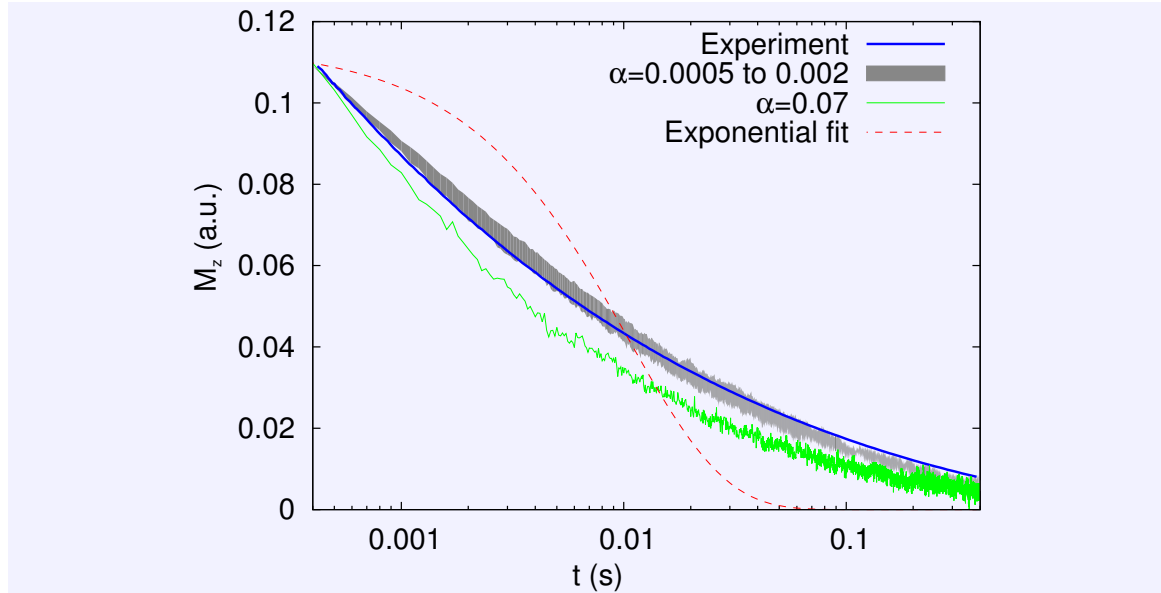


**Figure 4.21:** Comparison of [magnetorelaxometry](#) simulations for a range of different  $\alpha$  with a [magnetorelaxometry](#) measurement (smooth full blue line). The gray region, with  $\alpha$  between 0.0005 and 0.002 agrees well with the measurement. The simulation for the bulk  $\alpha = 0.07$  (green line) differs significantly from this measurement. The signature shape of the [magnetorelaxometry](#) curve, which closely matches the experimental one, proves that the size distribution of the particles is simulated correctly. For reference purposes a purely exponential function is fit to the data, corresponding to a sample of [magnetic nanoparticles](#) with equal diameters.

Figure 4.21 shows the result of [magnetorelaxometry](#) simulations of 10 000 000 particles with stochastic switching for a range of different  $\alpha$  values. The full blue line shows the measurement data from the [magnetorelaxometry](#) experiment. The green line shows a simulation with  $\alpha = 0.07$ , for which we observe a large discrepancy between the simulated and measured [magnetorelaxometry](#) curve. The gray region shows the simulation results for  $\alpha$  ranging from 0.0005 to 0.002, in close agreement to the [magnetorelaxometry](#) measurement data. Therefore we

suggest  $\alpha = 0.001$  for these type of particles, which is indeed significantly lower compared to the bulk value of 0.07. The signature shape of the [magnetorelaxometry](#) measurement curve agrees well with our simulations. As a reference, a purely exponential fit to the measurement data is also shown (red dashed line), which could only result from a sample consisting of particles with equal diameters, as was the case in Figs. 4.19 and 4.20. We report  $\tau_0 = \frac{4.64 \times 10^{-20}}{\sqrt{V}} \text{ s} \sqrt{\text{m}^3}$  which leads to a value of 8.65 ns for the average diameter of 19 nm in this experiment, well within the previously reported range of  $10^{-8}$  to  $10^{-12}$ . Note that we assumed an anisotropy constant of  $14.5 \text{ kJ/m}^3$ , as determined earlier [210]. However, this value has some uncertainty, and the exact value used influences our calculation of  $\alpha$ . We emphasise that our determined value for  $\alpha$  is not exact, but rather an estimate of the order of magnitude.

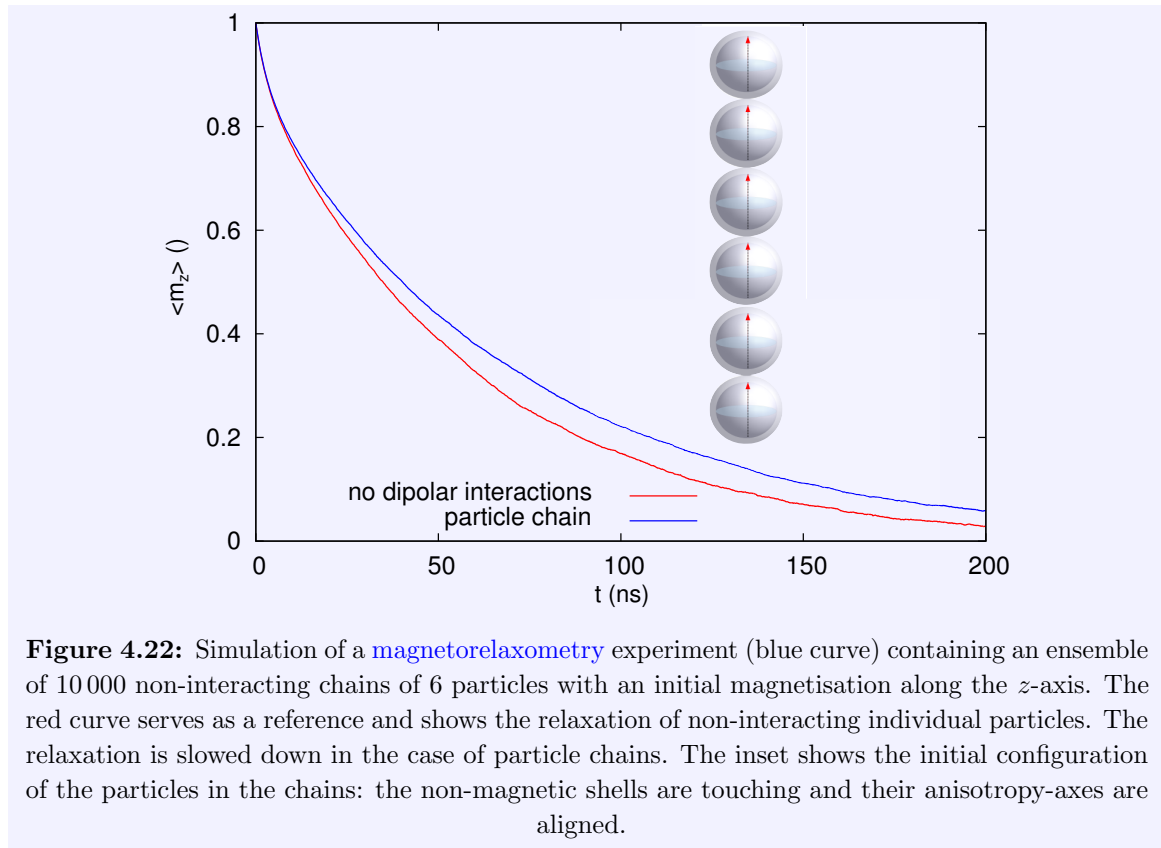


**Figure 4.22:** Simulation of a [magnetorelaxometry](#) experiment (blue curve) containing an ensemble of 10 000 non-interacting chains of 6 particles with an initial magnetisation along the  $z$ -axis. The red curve serves as a reference and shows the relaxation of non-interacting individual particles. The relaxation is slowed down in the case of particle chains. The inset shows the initial configuration of the particles in the chains: the non-magnetic shells are touching and their anisotropy-axes are aligned.

In this section we have investigated the effect of dipolar interactions between [magnetic nanoparticles](#) which are fixed in space on uniformly distributed positions. This is realistic in e.g. freeze-dried samples or samples containing nanoparticles with a thick non-magnetic coating which prevents aggregation. However, when the particles are able to move freely, the minimisation of the free energy might lead to chain formation[231]. This chain formation starts already at very low concentrations but is more distinct in samples with high concentrations[222]. In contrast to the previously discussed samples with uniform particle distributions, the presence of these structures decreases the relaxation time[232–234]. There is a plethora of possible configurations of particle chains, where possible parameters are the length of the chains, possible ring formation, the proximity of different chains,... A full study of such samples

is beyond the scope of this thesis, but we performed one simulation where we consider a sample consisting of 10 000 chains of 6 particles. The particles have the same properties as the ones described in the previous section, except we now consider particles with a non-magnetic coating of 10 nm on top of their 11 nm diameter. The particle chains are initialised as depicted in the inset of Fig. 4.22, i.e. with their anisotropy axes and magnetisation aligned with the magnetising field, leading to a magnetisation of 1 along the z-axis. The results of these simulations are shown in Fig. 4.22, and confirm that dipolar interactions between the particles help to stabilise the magnetisation of the particles, and hence slow down the thermal relaxation.

In conclusion, in this section we employed a numerical model starting from first principles to simulate [magnetorelaxometry](#) experiments taking into account anisotropy, thermal effects and dipolar interactions. We determined that for iron concentrations higher than 100 mmol/l the dipolar interactions affect the [magnetorelaxometry](#) curve and decrease the relaxation time constant. Furthermore, an estimate of the [Gilbert damping parameter](#)  $\alpha$  was obtained by comparison to an [magnetorelaxometry](#) measurement of iron oxide [magnetic nanoparticles](#). We determined  $\alpha \approx 0.001$  for SHP-20 magnetite nanoparticles, a value considerably lower than the bulk value of 0.07. This leads to an inverse attempt frequency  $\tau_0$  of 8.65 ns for 19 nm diameter [magnetic nanoparticles](#) and scales as  $1/\sqrt{V}$  for [magnetic nanoparticles](#) of other sizes.

## 4.4 Thermal magnetic noise spectra of nanoparticle ensembles<sup>6</sup>

Many techniques are able to investigate the magnetic moment of an ensemble of nanoparticles but most of these measurements require the use of an external magnetic field. Examples thereof are static magnetisation measurements such as magnetisation versus magnetic field ( $M(H)$ ) curves or dynamic magnetisation measurements such as AC susceptometry, magnetic particle spectroscopy and magnetic particle rotation [235–237]. Alternatively, one can investigate the relaxation of the magnetic moment of the nanoparticle sample after the magnetic field is switched off (*magnetorelaxometry*) [20, 189, 238]. Using aforementioned measurement techniques, particle characteristics such as the size distribution or aggregation can be determined by fitting a theoretical model to the measurement data [208, 239]. Recently, also the impact of particle interactions was taken into account [158, 240, 241]. A third approach, in the absence of an external field, is to measure the noise signal resulting from the thermal switching of the nanoparticles. This switching has already been the topic of many theoretical studies [13, 14, 184]. Experimentally, it is possible to investigate the switching rate of individual superparamagnetic structures by scanning electron or magnetic force microscopy [242, 243]. Although this resulted in a better understanding of the switching rate of individual particles, the averaged spectrum of an ensemble of particles, as is used in *biomedical applications*, remains elusive. With the help of SQUIDS, an increased *noise spectrum* as a result of *magnetic nanoparticle* has been observed [244], but the shape of the spectrum and its relation to the properties of the nanoparticle ensemble remains unexplored.

In this section we present the measured *noise spectrum* of several *magnetic nanoparticle* samples. We present a model to estimate the size distribution of the particles from the *noise spectrum* and compare it to those from *magnetorelaxometry* data of the same samples.

The fluctuations in the magnetic moment of nanoparticles can be the result of two distinct processes: one is the spatial rotation of the nanoparticle as a whole, and another in which only the magnetic moment of the nanoparticle changes direction. Both processes give rise to a characteristic fluctuation rate,  $\nu_N$  and  $\nu_B$  respectively [Eq. (4.44)], which depend on the size, the material parameters and the environment of the particle:

$$\nu_N = \nu_0 \exp\left(\frac{-KV_c}{k_B T}\right) \quad \text{and} \quad \nu_B = \frac{k_B T}{6pV_h}. \quad (4.44)$$

In these equations,  $V_c$  and  $V_h$  are the core and hydrodynamic volumes, respectively and  $\nu_0$  is an attempt frequency of 0.1 GHz.

Each nanoparticle is characterised by an effective rate

$$\nu_{\text{eff}} = \nu_N + \nu_B. \quad (4.45)$$

---

<sup>6</sup>The research presented in this section was performed during a 3-month stay as a guest scientist at the Physikalisch-Technische Bundesanstalt in Berlin.



However, due to the exponential dependence of  $\nu_N$  on the core volume [Eq. (4.44)], the range of particle sizes for which both mechanisms are relevant is very small as  $\nu_N$  is either much smaller or much larger than  $\nu_B$ . Consequently,  $\nu_{\text{eff}}$  is approximately equal to either  $\nu_N$  or  $\nu_B$ .

Both the [noise spectrum](#) and the [magnetorelaxometry](#) data of the samples are determined by these size dependent rates, so the particle sizes can be estimated by fitting the experimental data. Typically, the [lognormal distribution](#) [20], as defined in Eq. (4.33), is used to describe the diameter distribution of [magnetic nanoparticles](#).

In the following, a subscript c or h will be added to  $\mu$  and  $\sigma$  to indicate the parameters of the core or hydrodynamic diameter distribution. We will assume the nanoparticles have size distributions  $P(V_c)$  and  $P(V_h)$ , with  $V_{c,h} = \frac{\pi D_{c,h}^3}{6}$ , the core or hydrodynamic volume of a particle with diameter  $D_{c,h}$ . Because the relation between the core and shell sizes is unknown, we assume the core and hydrodynamic diameter distributions to be independent and use the fraction of each ensemble that fluctuates by the Néel mechanism as a fitting parameter  $\phi_N$ . This is inspired on the [cluster moment superposition model](#) [208] and takes the possibility for particles to cluster into account. With this approach, the relaxing magnetic moment  $V_c M = V_c \|\mathbf{M}\|$  of an ensemble of nanoparticles can be described by

$$\begin{aligned} V_c M(t) = & \phi_N \int_{V_c} M_0 V_c \exp(-\nu_N(V_c)t) P(V_c) dV_c \\ & + (1 - \phi_N) \int_{V_h} M_0 V_h R \exp(-\nu_B(V_h)t) P(V_h) dV_h, \end{aligned} \quad (4.46)$$

where  $M_0$  denotes the magnetisation of the nanoparticle at time 0 and  $R$  is the ratio between the total core and hydrodynamic volumes in the distributions. Note that  $2\nu_N$  and  $2\nu_B$  are the inverse of the [Néel relaxation time](#) and the [Brownian relaxation time](#),  $\tau_N$  and  $\tau_B$ , normally used in the description of [magnetorelaxometry](#) [20].

It is well-known that the noise power spectrum from the random switching of a magnetic moment has a *Lorentzian* shape[245],

$$S(f) = \frac{\nu/2}{\nu^2 + (\pi f)^2}. \quad (4.47)$$

The [noise spectrum](#) of an ensemble of [magnetic nanoparticles](#) with all the same sizes will also have this shape. The bottom curve in Fig. 4.23 is characterised by a flat white noise part up to the cutoff frequency  $\nu$ , after which the noise power rapidly decreases as  $1/f^2$ . In reality however, the nanoparticles have a size distribution, which also affects the [noise spectrum](#). The middle and upper curve of Fig. 4.23 show the [noise spectra](#) for lognormal diameter distributions [Eq. (4.33)] with  $\mu = 18$  nm and  $\sigma = 0.05$  and  $0.2$ , respectively. This spectrum can then be described as

$$S(f) = \int_0^\infty \frac{g(\nu)\nu/2}{\nu^2 + (\pi f)^2} d\nu \quad (4.48)$$

where  $g(\nu)$  depends on the size distribution of the particle sizes as

$$g(\nu) = \phi_N P(\nu_N(V_c)) + (1 - \phi_N) P(\nu_B(V_h)). \quad (4.49)$$

The superposition of these noise processes, each with a different cutoff frequency, changes the shape of the power spectrum and is responsible for the  $1/f$  noise shape[246] [cf. Fig. 4.25 (d)] as can also be seen in the data presented in Ref. [244].

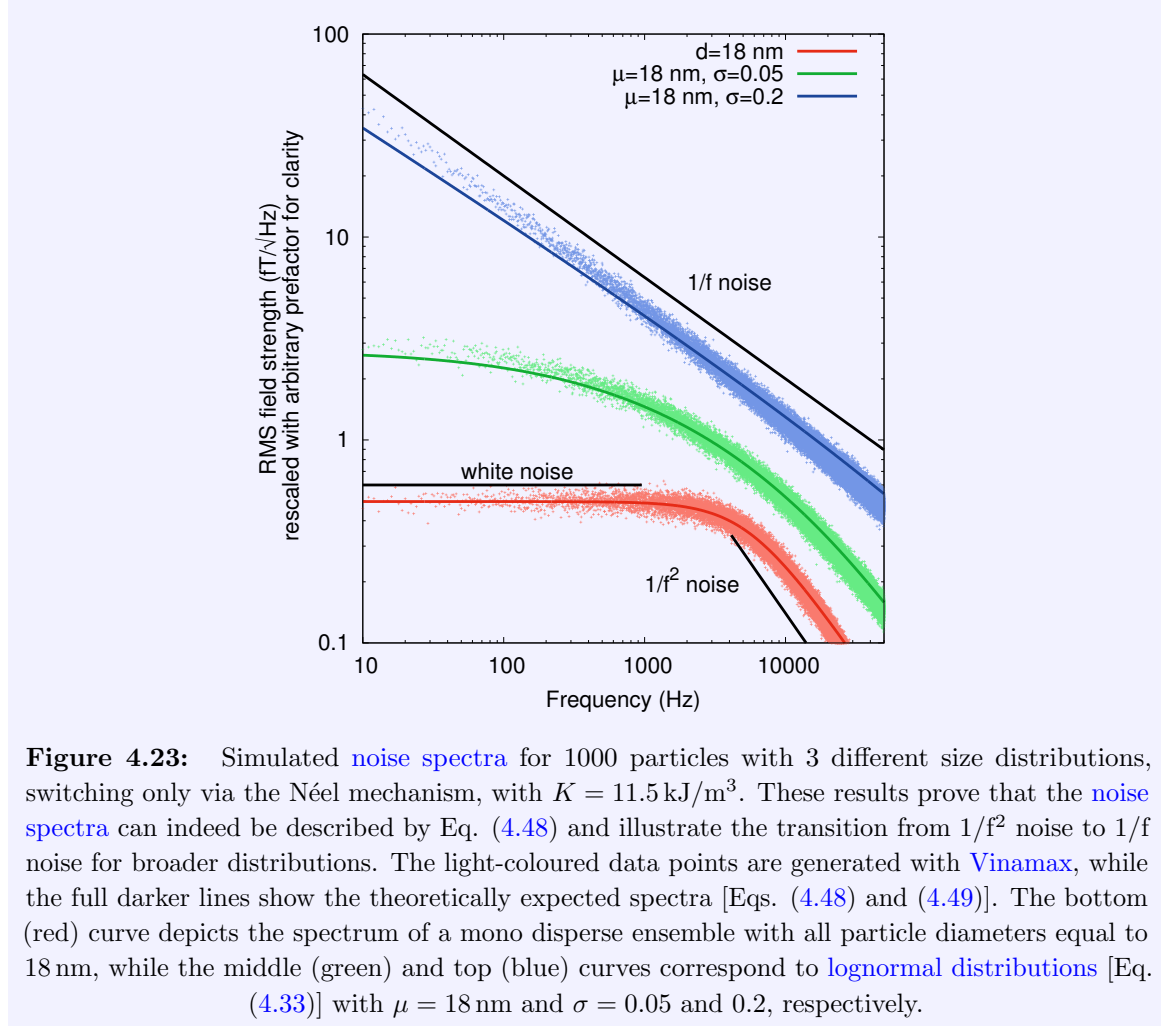


**Figure 4.23:** Simulated noise spectra for 1000 particles with 3 different size distributions, switching only via the Néel mechanism, with  $K = 11.5 \text{ kJ/m}^3$ . These results prove that the noise spectra can indeed be described by Eq. (4.48) and illustrate the transition from  $1/f^2$  noise to  $1/f$  noise for broader distributions. The light-coloured data points are generated with Vinamax, while the full darker lines show the theoretically expected spectra [Eqs. (4.48) and (4.49)]. The bottom (red) curve depicts the spectrum of a mono disperse ensemble with all particle diameters equal to 18 nm, while the middle (green) and top (blue) curves correspond to lognormal distributions [Eq. (4.33)] with  $\mu = 18 \text{ nm}$  and  $\sigma = 0.05$  and  $0.2$ , respectively.

Noise and magnetorelaxometry data of 5 different samples were taken in the 8-layered magnetically shielded room at Physikalisch-Technische Bundesanstalt (PTB) in Berlin [247]. A single channel magnetorelaxometry system [20] was used for both the noise measurements and magnetorelaxometry measurements. It contains a low  $T_c$  SQUID in a dewar. The sample is placed outside the dewar in a  $150 \mu\text{l}$  cuvette, 12 mm below the SQUID. Magnetorelaxometry measurements at  $T = 295 \text{ K}$  are taken by applying a magnetic field of 1 mT to the sample for 1 s. After a dead time of  $200 \mu\text{s}$  the magnetorelaxometry signal is recorded for 0.5 s. The coil system generating the magnetic field for the magnetorelaxometry measurements is removed during noise measurements to avoid the related background noise. The noise spectra of the samples is recorded by a spectrum analyzer (HP 35670A Dynamic Signal Analyzer) in units<sup>7</sup> of  $\text{fT}/\sqrt{\text{Hz}}$ .

<sup>7</sup>Noise is always proportional to the square of the detection bandwidth. If we average over longer periods (i.e. lower bandwidth) the noise will average out. Therefore noise is always specified as the noise spectral density,

The measurements were taken in 4 frequency windows (10 Hz to 110 Hz, 100 Hz to 1.7 kHz, 1.6 kHz to 14.4 kHz and 12.8 kHz to 50 kHz), which were logarithmically divided into 800 points. Due to time limitations only 50 averages were taken in the first window, while 500 averages were taken in the other windows. Using the same setting, the background [noise spectrum](#) was recorded using an empty sample holder.

The samples used in this study are iron oxide particles dispersed in water from Berlin Heart GmbH with an iron concentration of 55.7 mg/ml which were 1:1 diluted with water [BH11], 1:1 diluted with glycerol [BHGL] and immobilised in gypsum [BHIM]. We also used a cobalt ferrite sample (SiMAG/CF-Carboxyl) acquired from Chemicell GmbH [COFE] and cobalt ferrite nanoparticles with a silica shell [CODS]. For the latter one the magnetic core was prepared via a co-precipitation method [249] and afterwards covered via a silica shell by a modified Stoeber process [250].

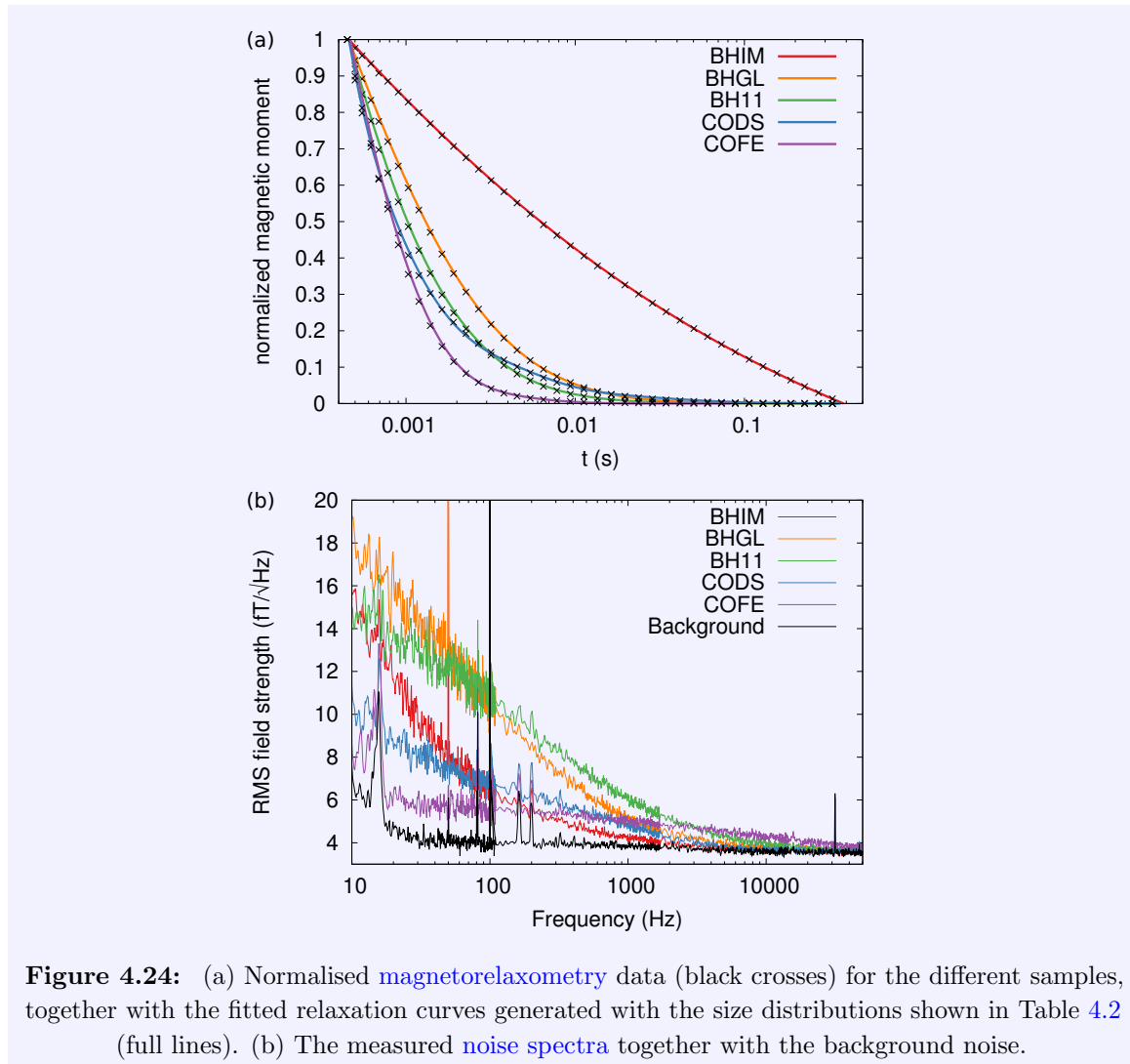


**Figure 4.24:** (a) Normalised [magnetorelaxometry](#) data (black crosses) for the different samples, together with the fitted relaxation curves generated with the size distributions shown in Table 4.2 (full lines). (b) The measured [noise spectra](#) together with the background noise.

*e.g.  $fT/\sqrt{\text{Hz}}$ , which removes this dependency on bandwidth.*[248]

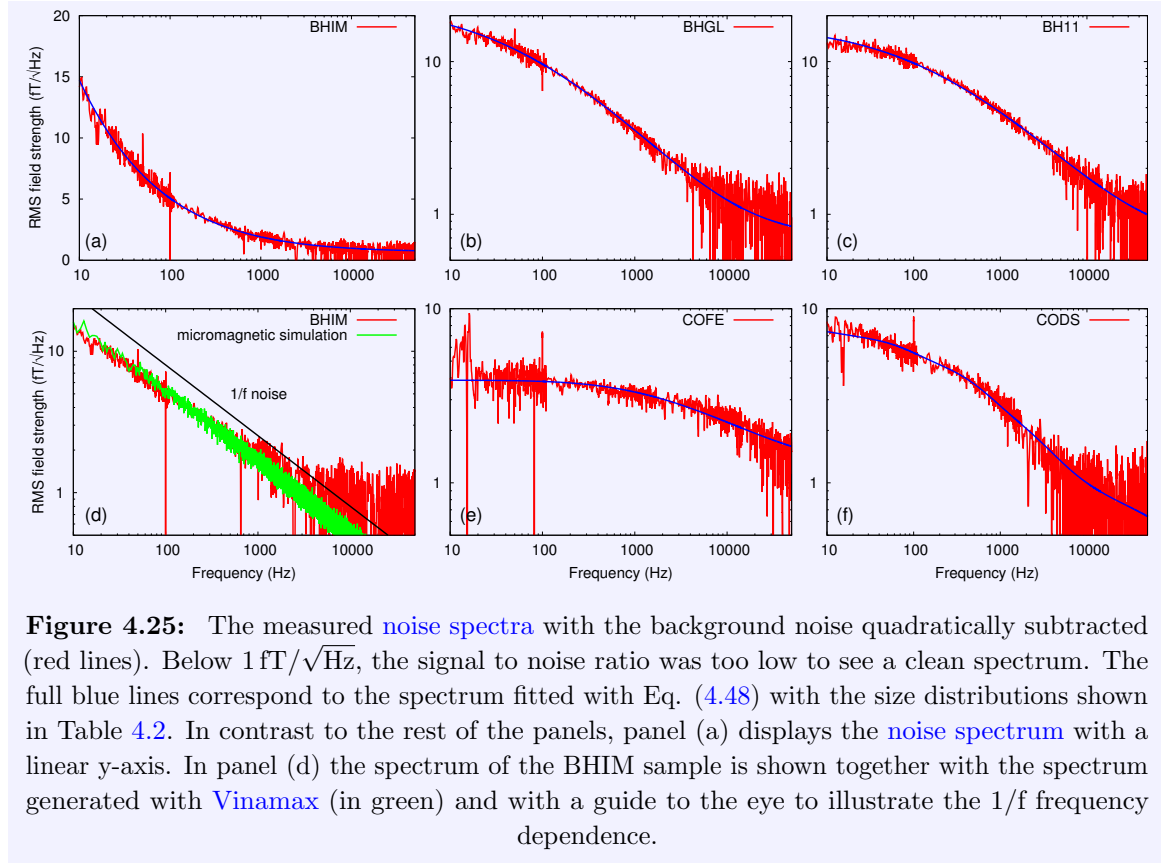
The measured relaxation curves and [noise spectra](#) from the samples described above are shown in Fig. 4.24. The relaxation curves (black crosses), shown in Fig. 4.24 (a) were normalised to allow an easy comparison. To estimate the size distributions, we fitted<sup>8</sup> Eq. (4.46) to this data. As can be seen in Fig. 4.24 (a) (full lines) there is an excellent correspondence and the fit parameters are shown in Table 4.2.

Fig. 4.24 (b) shows the raw [noise spectra](#). For all samples, the noise amplitude is significantly larger than the background noise. The shape clearly depends on the size distributions and environment of the particles. The noise amplitude of the immobilised particles [BHIM] goes down faster than those of the liquid samples. This is attributed to the predominance of slow [Néel relaxation](#) processes, in good agreement with the slow relaxation observed in [magnetorelaxometry](#). The [noise spectra](#) of the liquid samples remain higher up to larger frequencies by the additional contribution of the faster [Brownian relaxation](#). In line with the difference in viscosity, the spectrum of the BH particles remains higher up to larger frequencies for the suspension in water [BH11] than in Glycerol [BHGL]. The higher viscosity in glycerol gives rise to a smaller contribution of rates at higher frequencies [cf. Eq. (4.44)], thus explaining the steeper slope observed for the [BHGL] sample. In line with the fast relaxation, the noise amplitude in the [COFE] sample remains large up to very high frequencies.

**Table 4.2:** The parameters for the size distributions of the different samples estimated from their [magnetorelaxometry](#) signal and their noise signal.  $\mu$  has units of nm, the others are unitless. We used a saturation magnetisation of 400 kA/m for all samples. The BH- samples were fitted with  $K = 11.5 \text{ kJ/m}^3$  while the CO- samples were fitted with  $K = 100 \text{ kJ/m}^3$ , as determined from [magnetorelaxometry](#) data. All liquid samples had a viscosity of 1 mPas, except for the water/glycerol sample where we used a viscosity of 5.6 mPas, in agreement with tabulated values.

Sample	MRX					Noise spectrum				
	$\mu_c$	$\sigma_c$	$\mu_h$	$\sigma_h$	$\phi_N$	$\mu_c$	$\sigma_c$	$\mu_h$	$\sigma_h$	$\phi_N$
BHIM	18	0.15	–	–	1.00	21	0.13	–	–	1.00
BHGL	–	–	29	0.49	0.00	–	–	27	0.59	0.00
BH11	–	–	35	0.50	0.00	–	–	27	0.64	0.00
CODS	7.5	0.09	25	0.33	0.45	9.2	0.04	16	0.27	0.39
COFE	9.6	0.01	28	0.43	0.09	6.6	0.01	20	0.47	0.02

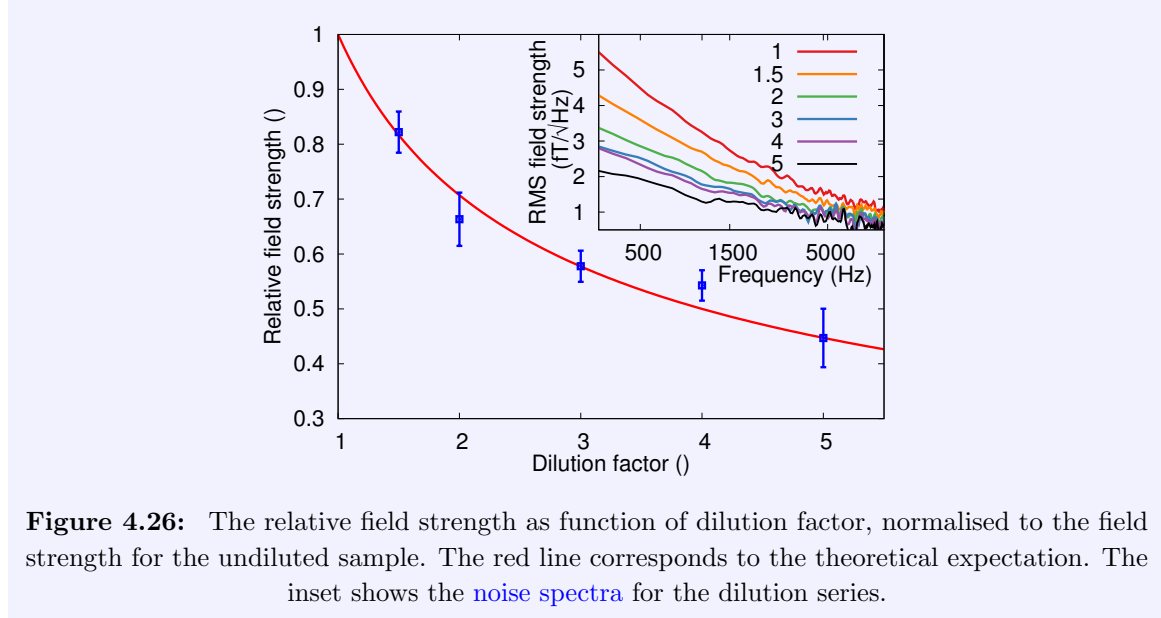
<sup>8</sup>As  $M_0$  and the offset on the final magnetisation were not experimentally determined, we took these into account by linearly rescaling our fitted curve to match the first and last data point. The fit itself was performed by simulated annealing.



In Fig. 4.25, the noise spectra (red lines) are shown for each sample, but this time with the background noise subtracted. The full blue lines depict the fitted shape of the spectrum using Eqs. (4.48) and (4.49) and the size distribution estimates shown in Table 4.2. The noise spectra of the immobilised samples can also be simulated with the Vinamax [157] code, as only the  $\nu_N$  mechanism is relevant. We averaged over 50 ensembles consisting of 1000 nanoparticles with a lognormal distribution. The thermal switching of the nanoparticles, implemented as a jump noise process [36], was simulated for 1 s for each ensemble. In Fig. 4.25 (d) the result of this simulation is shown in green.

When looking at Table 4.2, a rough agreement between the parameter estimations from both datasets can be seen. However, a trend in the differences can be observed: typically the hydrodynamic diameter distribution is estimated a little smaller from the noise spectrum than from the magnetorelaxometry data. This might originate in the fact that the equilibrium configuration of the particles, and thus also their relaxation, is influenced by external fields[222, 240]. The noise spectrum is measured in the absence of an external field while the magnetorelaxometry data are recorded after the samples were magnetised for 1 s by a magnetic field of 1 mT. During this time, clustering by chain formation may occur. The resulting interactions can decrease the relaxation rate[240]. This process is not taken into account in the model and will result in overestimation of the particle sizes. This clustering will also depend on the particle concentration. For instance, the relaxation measured in an 1:6 diluted BH sample

was faster than in the 1:1 diluted [BH11] sample. However, these data are not shown in Fig. 4.24 because the corresponding noise spectrum was too small compared to the background noise.



Finally, also a dilution series of Berlin Heart particles in water was investigated. The used dilution factors ( $DF$ ) were 1 (undiluted), 1.5, 2, 3, 4 and 5 (corresponding to a 1 in 5 dilution). For these samples we were only interested in the scaling of the noise amplitude. To this end, 5000 spectra between 100 and 12.9 kHz, logarithmically divided into 200 points, were averaged. To obtain the scaling factor, we performed a pointwise division between the spectrum of the undiluted sample and all other spectra between 400 Hz and 2 kHz. This range was chosen as it had the best signal to noise ratio. For each dilution factor, the resulting ratios were then averaged and their standard deviations determined.

The averaged noise spectra are shown in the inset of Fig. 4.26. The relative strengths of these spectra were extracted and normalised to the strength of the undiluted sample and confirm that the strength decays as  $1/\sqrt{DF}$ , as expected from the model. Indeed, the measured spectra can be seen as the square root of the sum of the power spectra of the individual particles (in  $\text{fT}^2/\text{Hz}$ ), and the number of particles (proportional to the power spectrum) decreases linearly with  $DF$ .

To conclude, in this section we demonstrated that the magnetic noise spectral density of nanoparticles ensembles, of only a few  $\text{fT}/\sqrt{\text{Hz}}$ , can be measured with SQUIDs in a magnetically shielded environment. A model was constructed to interpret these noise spectra in terms of the relaxation rates of the particles and their size distribution could be estimated. These results were consistent with the size distributions obtained from magnetorelaxometry data of the same samples. In the future such noise measurements might be used at different offset fields to investigate cluster formation and its influence on the relaxation rates.

---

## Conclusions and Outlook

---

*[...]Now, endings normally happen at the end.  
But as we all know, endings are just beginnings.  
You know, once these things really get started,  
it's jolly hard to stop them again.  
However, as we have all come this far,  
I think, under the circumstances  
the best solution is that we all just keep going [...]*  
— Mike Oldfield, *Amarok*

### 5.1 Conclusions

Throughout this thesis, we have investigated several realisations of disorder like single defects, polycrystalline materials, thermal fluctuations and randomly positioned magnetic nanoparticles. To investigate these very different disorder realisations, we focused on two systems. In Chapters 2 and 3, we investigated domain wall motion through magnetic nanowires, and in Chapter 4 we shifted our focus to the magnetisation dynamics of magnetic nanoparticles.

Within these systems, we studied different aspects of disorder. In magnetic nanowires, we first investigated how individual defects could be included in micromagnetic simulations in a way that their effect on the magnetisation was comparable to experimental observations. Next, we extended this study to the implementation of polycrystalline materials. After developing these techniques we used them to investigate their influence on current-driven domain wall motion.

As expected, at low current densities, domain walls get pinned to the minima in the energy profile due to the defects. Above the depinning current threshold we noticed that vortex cores

can switch [polarity](#) at defects. This qualitatively alters their motion as the vortex cores do not reach the edges of the nanowire anymore and behave as if the [degree of non-adiabaticity](#), equals the [Gilbert damping parameter](#), irrespective of its real value. The size of the former was still a topic of debate at the time this research was conducted and our observation explained some contradictory experimental data.

Next, we included the effects of nonzero temperatures in our investigation of domain wall motion. In a first step we performed micromagnetic simulations in ideal nanowires without defects and showed that the [thermal fluctuations](#) give rise to [diffusion](#) on top of the drift velocity due to the driving force. We also included the stochastic thermal field in the [1D-model](#), solved the resulting stochastic [equation of motion](#) analytically and saw a good agreement between both results.

We then performed large-scale [micromagnetic simulations](#) (over 5 GPU-years in total) of the [creep](#) domain wall motion through disordered nanowires and used these results to validate the solution of the [equation of motion](#). We found that the nonlinear creep scaling law is not valid in small nanowires. Instead, we find a linear relation between the velocity of the wall and the driving force. The agreement between the results of the equation of motion and the micromagnetic simulations proves that the motion of the domain wall can be described as a zero dimensional object moving through a one dimensional energy profile. We also investigated domain wall motion through a nanowire with periodic defects and found a good agreement between theory and simulation, except at some current densities where the domain wall displayed internal resonances as it moved through the periodic energy profile. This illustrates one of the limitations of the [1D-model](#): it is only valid when the domain wall under study is a rigid object.

In Chapter 4 we investigated an entirely different system, i.e. ensembles of [superparamagnetic magnetic nanoparticles](#). In these systems, material defects do not influence the magnetisation. Contrary, the strongest disorder is due to the [thermal fluctuations](#). In these superparamagnetic particles, the magnetisation switches randomly between a few equilibrium directions, and only in the presence of an external field, one direction is favoured and a net magnetic moment is present. As the interactions between the different particles influence their magnetisation, a second source of disorder can be identified in the location of the particles.

To model [magnetic nanoparticles](#), we developed a specific micromagnetic software package [Vinamax](#), which we then used to look at different aspects of the [Néel relaxation](#). We also used [Vinamax](#) to compare simulated [magnetorelaxometry](#) measurements to experimental data and be the first to report an estimate of the [Gilbert damping parameter](#) in [magnetic nanoparticles](#). We found a value of approximately 1/1000, which is an order of magnitude smaller than in thin films or bulk materials.

Finally, we performed measurements of the thermal magnetic [noise spectra](#) of an ensemble of nanoparticles. This new technique to investigate magnetic nanoparticles allowed us to measure



the characteristic timescales of the thermal switching of the magnetisation in its thermodynamic equilibrium. This contrasts the usual [magnetic nanoparticle](#) measurement techniques which measure the response to an external excitation. We interpreted these measurements in the same framework used to characterise [magnetic nanoparticles](#) in [magnetorelaxometry](#) measurements and found that both resulting particles characteristics agree with each other. However, a trend in the small differences between both was visible, indicating that the particles are less clustered in their thermal equilibrium than after an exposure to a magnetic field.

Although we studied very different magnetic systems, the effects of disorder actually are very similar. Generally, disorder gives rise to local minima in the energy landscape. This can range from a single [potential well](#) due to a single defect, over an entire [energy profile](#) in a [polycrystalline](#) nanowire to preferential directions in the magnetisation due to dipolar interactions between [magnetic nanoparticles](#). Additionally, [thermal fluctuations](#) play a similar role in all these different systems, and allow the system to overcome the energy barriers due to the disorder. This effect is stronger in smaller systems like [magnetic nanoparticles](#), and in [domain walls](#), which have a comparable size. In equilibrium, the net magnetisation does not change apart from the thermal magnetic noise, or the [diffusion](#) of a magnetic domain wall through an ideal nanowire which both are different manifestations of the same phenomenon. Out of equilibrium, the thermally assisted motion of the domain wall results in a [creep](#) velocity, just like the thermally assisted relaxation of the magnetic moment in a [magnetorelaxometry](#) experiment can be interpreted as a motion towards the equilibrium magnetisation.

## 5.2 Outlook

### 5.2.1 Domain wall motion

In this thesis we focused on the current-driven motion of transverse and vortex domain walls through [permalloy](#) nanowires. However, domain wall motion through nanowires is a very rich topic and a very similar thesis could for example have been written on field driven domain wall motion[251] or domain wall motion through [PMA](#) nanowires[119], or other domain wall configurations stabilised by the [Dzyaloshinskii-Moriya interaction](#) [252] or even [skyrmion](#) motion[23].

Each of these systems has a lot of potential for future research. In [PMA](#) nanowires, for instance, a very large damping is measured ( $\alpha_{\text{eff}} = 0.15$  in Ref. [253]). It would be interesting to see if this can be explained as an extrinsic damping originating in the [polycrystalline](#) structure of the samples. Another interesting topic is [skyrmion](#) motion. There, typically a much lower [depinning current threshold](#) is measured[23]. This indicates that the interaction with material defects is different than in domain wall motion.

When we look back at results presented in this thesis, we see that the most interesting results were obtained in systems where the dynamic behaviour is determined by the interplay between the disorder and the [thermal fluctuations](#).

An interesting extension of our [creep](#) simulations would be to investigate wider nanowires where the creep scaling law is still valid. Recently, it has been shown in experiments that field-driven and current-driven creep motion gives rise to different creep exponents[134]. With an in-depth numerical study we might gain more insight in this surprising result. Unfortunately, these simulations are not yet possible due to the current computational limits.

### 5.2.2 Magnetic nanoparticle ensembles

The latest efforts in magnetic nanoparticle imaging are aimed at imaging different kinds of particles at the same time[254]. In these *multi-colour* approaches the different particles are identified based on subtle differences in their response to an external field. However, this response also depends on the possible interactions between the particles, making it challenging to correctly distinguish the different particles.

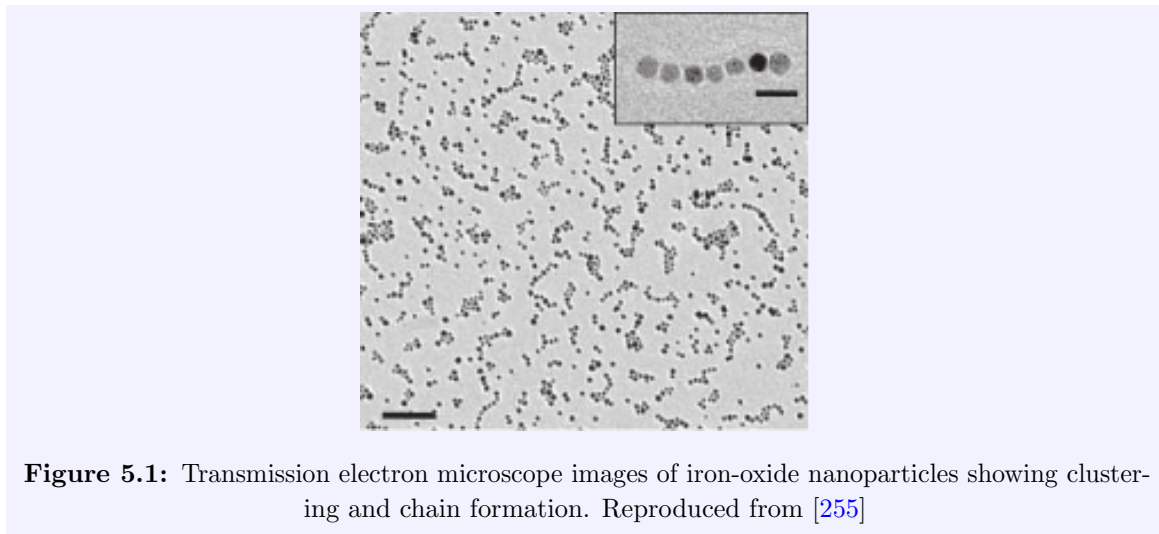


**Figure 5.1:** Transmission electron microscope images of iron-oxide nanoparticles showing clustering and chain formation. Reproduced from [255]

To learn more about these interactions, it would be interesting to extend the interpretation of [magnetorelaxometry](#) results to also include their effect on the [magnetorelaxometry](#) signal. The particles interact with each other via their [dipole-dipole interaction](#), causing clustering or chain formation, see Fig. 5.1. As we already showed in Section 4.3, these configurations are more stable against [thermal fluctuations](#) than free particles, which reflects in the relaxometry signal. When this signal is interpreted in a model which does not take this into account, the size of the particles is overestimated. Our modelling approach offers a controlled environment which allows us to isolate the influence of interactions and to develop a practical model which accurately relates the relaxation signal to the real properties of the particles.

### 5.2.3 Thermal magnetic noise

Next, further research should be performed on the thermal magnetic [noise spectrum](#) of the [magnetic nanoparticles](#), presented in Chapter 4. This method allows for the first time to make sure that any clustering induced by the magnetisation phase of the particles can be excluded when investigating the magnetisation dynamics. We would like to perform extra measurements at offset fields and also include inter-particle interactions in the analysis. We suspect that, in the presence of an externally applied field, the nanoparticle magnetisation will align and the particles will cluster, which will influence their energy and thus the characteristic timescale of the thermal switching.

Finally, this technique could also be extended to artificial *spin ices*. These are ordered arrays of nano magnets, e.g. a square lattice of rectangular magnets, each having only two equilibrium magnetisation directions. In this system, the ground state is a configuration where 2 spins point in and 2 out of each vertex. However, even in this ground state the energy of only 4 of the 6 spin pairs in each vertex is minimised, and not all local interactions are satisfied at the same time, a property called *frustration*. Because of its similarity to water ice, where each oxygen atom is bonded to four hydrogen atoms with two strong and two much weaker bonds, the frustrated magnetic system described above is called artificial [spin ice](#). In such systems, the distances between the nano magnets, and thus the strength of their interaction dictates the average time between the thermal switching of the magnets. Due to the ordered geometries, only a few different energy barriers will be present in the system and we expect to find a very clear spectrum. In simulations it is possible to simply take the Fourier transform of a sufficiently long simulation of the magnetisation, which we already accomplished with magnetic nanoparticles in Section 4.3. These simulation results could then be used to interpret the spectrum, by relating it to the local switching of the magnets. Experimentally, the thermal [noise spectrum](#) of an artificial [spin ice](#) sample might even be recorded with the unique *magneto-optical spectrum analyser* setup[256], developed in our group.



# APPENDIX A

---

## Solvers

---

*Physicists like to think that all you have to do is say,  
these are the conditions, now what happens next?*

— Richard Feynman

Parts of this appendix have been published in [45] and [157]

### A.1 Introduction

As both [MuMax3](#) and [Vinamax](#) numerically solve *Ordinary Differential Equations* (ODE's), a lot of time was spent on the implementation and testing of *solvers*. In this appendix a short introduction to solvers is given together with a list of all solvers implemented in [MuMax3](#) and [Vinamax](#) (with their [Butcher tableaux](#)). Subsequently, the derivation of our own third order solver is given and finally the implementation of all solvers is validated and their performance is compared. For further information about solvers we refer to Ref. [257].

Given the differential equation,

$$\frac{dy}{dt} = f(t, y), \tag{A.1}$$

we are looking for a method to approximate its value  $y_{n+1}$  on time  $t + h$ , given its value  $y_n$  on time  $t$ , where  $h$  is the time step. To approximate  $y_{n+1}(t + h)$  we use a *solver*. In the following we will no longer explicitly write the time dependency of  $y$ .

We start by describing the easiest of solvers, which was already invented by *Euler* as early as 1770 [258] and is appropriately named *Euler's method*. Using this solver we approximate  $y_{n+1}$  as

$$y_{n+1} = y_n + hf(t, y_n). \tag{A.2}$$

This solver is a solver of order 1 ( $\mathcal{O}(1)$ ). This means that our solution only approximates the real solution of the ODE up to first order. Practically, this means that when the time step is made twice as large, the size of the error also doubles. This is a very useful property to test one's implementation of a solver, as this property is very sensitive to even the smallest of programming errors.

All solvers can be subdivided into two classes based on whether they are implicit or explicit. [Euler's method](#) is an *explicit solver* because it approximates the solution of the ODE on a later time only by using information about the ODE at the current time. Therefore this method is also called *Euler forward*. There also exists a class of solvers, called *implicit solvers*, which approximate the solution of the ODE on a later time, also using information about the solution at times later than the current time. The easiest example of such a solver is called *Euler backward* and looks like this:

$$y_{n+1} = y_n + hf(t + h, y_{n+1}). \quad (\text{A.3})$$

A second property we would like to discuss is whether the solver needs a fixed time step or can use an *adaptive time step*. When a solver contains not only a solution of order  $N$  but also a solution of  $\mathcal{O}(N - 1)$ , we can use the difference between both solutions as an approximation of the error size  $\epsilon$  on the solution. This error, as discussed earlier, depends on the size of the time step  $h$ , and given a certain error tolerance  $\tau$ , it is possible, using Eq. (A.4), to suggest a  $h$  for the next time step which is as large as possible, while still maintaining the level of accuracy required[224]. In systems governed by dynamics whose speed changes in time, this can boost the performance of a solver tremendously.

$$h_{\text{optimal}} = h_{\text{current}} \left( \frac{\epsilon}{h_{\text{current}} \tau} \right)^{(1/N)} \quad (\text{A.4})$$

An example of such a solver is *Heun's method*. The first order accurate solution is found using [Euler's method](#):

$$\tilde{y}_{n+1} = y_n + hf(t, y_n). \quad (\text{A.5})$$

Afterwards, the second order solution is found:

$$y_{n+1} = y_n + \frac{h}{2} \left( f(t, y_n) + f(t + h, \tilde{y}_{n+1}) \right). \quad (\text{A.6})$$

The difference between both solutions is an estimate of the error.

A third property our code greatly benefits from is the *first-same-as-last* (FSAL) property. When we have a closer look at [Heun's method](#) [Eqs. (A.5) and (A.6)] we see that we need two evaluations per time step. Similarly, for the *Bogacki-Shampine method*, which is a third order method with embedded second order solution, we need 4 evaluations per step.<sup>1</sup> However,

---

<sup>1</sup>A full description of this method will not be given here, but its [Butcher tableau](#) (see Section A.2) can be found in Table A.6.

contrary to [Heun's method](#), in the [Bogacki-Shampine method](#) the last evaluation of step  $n$  corresponds with the first evaluation of step  $n + 1$ , thus reducing the number of evaluations per step to 3. This property makes this solver  $4/3$  times faster as compared to the case when it didn't have the FSAL property.

Our introduction is continued with a side note on stochastic differential equations. As discussed in Section 1.3.2, we apply a stochastic thermal field to simulate nonzero temperatures. The size of this thermal field was determined by [Brown \[13\]](#), using the [fluctuation-dissipation theorem](#) as:

$$\mathbf{H}_{\text{th}} = \boldsymbol{\eta} \sqrt{\frac{2\alpha k_{\text{B}} T}{\mu_0 M_s \gamma_0 V h}} \quad (\text{A.7})$$

For this discussion, the most important variables in Eq. (A.7) are  $\boldsymbol{\eta}$ , a vector containing 3 Gaussian random variables with average 0 and standard deviation 1 and  $h$ , which denotes the time step.

It is not possible to perform simulations at nonzero temperatures with an adaptive time step. A naive reason for this would be that the size of the thermal field is determined by  $1/\sqrt{h}$ . This implies that, when a large thermal field is generated, the adaptive time step algorithm would decrease the time step, thus further increasing the size of the field, until the solver crashes. However, on closer inspection, we learn that the  $1/\sqrt{h}$  dependency makes the time step smaller at a slower rate than that the error is reduced ( $h^N$  with  $N \geq 1$ ) at smaller time steps [cf. Eq. (A.4)].

The real reason why it is not possible to solve stochastic differential equations with an adaptive time step is more subtle. To give the correct solution, the time average of the random numbers  $\eta$  should be 0, and their standard deviation 1. However, if we would adapt our time step in such a way that small thermal fields (small  $\eta$ ) are applied during longer time steps and large thermal fields (large  $\eta$ ) during shorter time steps, we virtually change the distribution of the random numbers and thus no longer correctly solve the differential equations.

There do exist solvers which take this effect into account[259] and are able to use an adaptive time step algorithm to solve stochastic differential equations. Unfortunately, these solvers are very difficult to implement and the performance gains are not spectacular. The reason for this is twofold. First, these solvers require a lot of overhead in comparison with their fixed-time step counterparts. Second, in simulations where the random field is calculated for a lot of different cells, there will always be one cell, somewhere, where the thermal field is quite large. Consequently, the time step will only vary a little, and will, for practical purposes, be quite constant anyway.

In [MuMax3](#), it used to be impossible to use the solvers with the FSAL property to simulate nonzero temperatures, because the stochastic field changes in between time steps and the first evaluation of the next time step is no longer equal to the last evaluation of the current time step. This was fixed by separately performing the first and last evaluations steps in these schemes and

not using the FSAL property for these solvers when nonzero temperatures are required.[66, 260]

We finish our introduction by listing all solvers implemented in [MuMax3](#) and [Vinamax](#).

- All solvers implemented in [MuMax3](#)
  - [Euler forward](#) (RK1)  
The easiest first order solver, provided for academic purposes.
  - [Euler backward](#)  
The easiest implicit solver, useful for the relaxation of magnetisation towards its ground state.
  - [Heun's method](#) (RK12)  
Offers 2nd order convergence and a 1st order error estimate.
  - [Bogacki-Shampine method](#) (RK23)  
Offers 3th order convergence and a 2nd order error estimate used for adaptive time step control. This method is used when relaxing the magnetisation to its ground state in which case it performs better than the Dormand-Prince method.
  - *Fourth order Runge-Kutta method* (RK4)  
The classic fourth order Runge-Kutta scheme, does not allow for adaptive time steps, but can be used as a fourth order solver. It became rather obsolete when it became possible to use the Bogacki-Shampine and Dormand-Prince solvers at nonzero temperatures.
  - *Dormand-Prince method* (RK45)  
Offers 5th order convergence and a 4th order error estimate used for adaptive time step control. This is the default for dynamical simulations.
- All solvers implemented in [Vinamax](#)
  - [Euler forward](#) (RK1)  
See above
  - [Heun's method](#) (RK12)  
See above
  - *Third order Runge-Kutta method* (RK3)  
The classic third order Runge-Kutta scheme, offers no adaptive time step.
  - Our own third order method  
Our very own third order method, which we derive in Section [A.3](#)
  - [Fourth order Runge-Kutta method](#) (RK4)  
See above
  - [Dormand-Prince method](#) (RK45)  
See above
  - *Sixth order Fehlberg method*  
A 6th order method with embedded 5th order error estimate for adaptive time step control.



– *Seventh order Fehlberg method*

A 7th order method with embedded 6th order error estimate for adaptive time step control.

## A.2 Butcher Tableaus

As is clear from Eqs. (A.5) and (A.6), the notation to describe these solvers quickly becomes quite dense and difficult to read. *Butcher*[257] invented a method to write down all necessary information to understand and implement a solver in a very elegant way: *Butcher tableaus*.

In general, the approximate solution of the ODE

$$\frac{dy}{dt} = f(t, y) \quad (\text{A.8})$$

at time  $t + h$ , given its value  $y$  on time  $t$ , is obtained by taking  $s$  intermediate evaluations of  $f$  at times  $c_i$ ,

$$k_i = f \left( t + c_i h, y_n + h \sum_{j=1}^s a_{ij} k_j \right), \quad (\text{A.9})$$

and then adding them to  $y_n$  with the correct weights  $b_i$ :

$$y_{n+1} = y_n + h \sum_{i=1}^s b_i k_i. \quad (\text{A.10})$$

These formulas can compactly be represented by a [Butcher tableau](#) as follows:

**Table A.1:** General Butcher tableau

$c_1$	$a_{11}$	$a_{12}$	$\dots$	$a_{1s}$
$c_2$	$a_{21}$	$a_{22}$	$\dots$	$a_{2s}$
$\vdots$	$\vdots$	$\vdots$	$\ddots$	$\vdots$
$c_s$	$a_{s1}$	$a_{s2}$	$\dots$	$a_{ss}$
	$b_1$	$b_2$	$\dots$	$b_s$

Below, the [Butcher tableaus](#) of all solvers mentioned in the list above are given. For the methods which have a lower order solution embedded, the lower order solution is shown as an extra row below the higher order solution, and for the highest-order methods, another extra row is added which is the difference between both solutions and approximates the error.

**Table A.2:** [Euler forward](#) (RK1)

0
1

**Table A.3:** Euler backward

1	1
1	1

**Table A.4:** Heun's method (RK12)

0	1	
1	$\frac{1}{2}$	$\frac{1}{2}$
	1	0

**Table A.5:** Third order Runge-Kutta method (RK3)

0	$\frac{1}{2}$		
$\frac{1}{2}$	$\frac{1}{2}$		
1	-1	2	
	$\frac{1}{6}$	$\frac{2}{3}$	$\frac{1}{6}$

**Table A.6:** Bogacki-Shampine method (RK23)

0	$\frac{1}{2}$			
$\frac{1}{2}$	0	$\frac{3}{4}$		
$\frac{3}{4}$	$\frac{2}{9}$	$\frac{1}{3}$	$\frac{4}{9}$	
1	$\frac{2}{9}$	$\frac{1}{3}$	$\frac{4}{9}$	0
	$\frac{7}{24}$	$\frac{1}{4}$	$\frac{1}{3}$	$\frac{1}{3}$

**Table A.7:** Fourth order Runge-Kutta method (RK4)

0	$\frac{1}{2}$			
$\frac{1}{2}$	0	$\frac{1}{2}$		
$\frac{1}{2}$	0	0	1	
1	$\frac{1}{6}$	$\frac{1}{3}$	$\frac{1}{3}$	$\frac{1}{6}$

**Table A.8:** Dormand-Prince method (RK45)

0							
$\frac{1}{5}$	$\frac{1}{5}$						
$\frac{3}{10}$	$\frac{3}{40}$	$\frac{9}{40}$					
$\frac{4}{5}$	$\frac{44}{45}$	$-\frac{56}{15}$	$\frac{32}{9}$				
$\frac{8}{9}$	$\frac{19372}{6561}$	$-\frac{25360}{2187}$	$\frac{64448}{6561}$	$-\frac{212}{729}$			
1	$\frac{9017}{3168}$	$-\frac{355}{33}$	$\frac{46732}{5247}$	$\frac{49}{176}$	$-\frac{5103}{18656}$		
1	$\frac{35}{384}$	0	$\frac{500}{1113}$	$\frac{125}{192}$	$-\frac{2187}{6784}$	$\frac{11}{84}$	
	$\frac{35}{384}$	0	$\frac{500}{1113}$	$\frac{125}{192}$	$-\frac{2187}{6784}$	$\frac{11}{84}$	0
	$\frac{5179}{57600}$	0	$\frac{7571}{16695}$	$\frac{393}{640}$	$-\frac{9209}{339200}$	$\frac{187}{2100}$	$\frac{1}{40}$

**Table A.9:** Sixth order Fehlberg method (Fehlberg56)

0								
$\frac{1}{6}$	$\frac{1}{6}$							
$\frac{4}{15}$	$\frac{4}{75}$	$\frac{16}{75}$						
$\frac{2}{3}$	$\frac{5}{6}$	$-\frac{8}{3}$	$\frac{5}{2}$					
$\frac{4}{5}$	$-\frac{8}{5}$	$\frac{144}{25}$	-4	$\frac{16}{25}$				
1	$\frac{361}{320}$	$-\frac{18}{5}$	$\frac{407}{128}$	$-\frac{11}{80}$	$\frac{55}{128}$			
0	$-\frac{11}{640}$	0	$\frac{11}{256}$	$-\frac{11}{160}$	$\frac{11}{256}$	0		
1	$\frac{93}{640}$	$-\frac{18}{5}$	$\frac{803}{256}$	$-\frac{11}{160}$	$\frac{99}{256}$	0	1	
	$\frac{31}{384}$	0	$\frac{1125}{2816}$	$\frac{9}{32}$	$\frac{125}{768}$	$\frac{5}{66}$	0	0
	$\frac{7}{1408}$	0	$\frac{1125}{2816}$	$\frac{9}{32}$	$\frac{125}{768}$	0	$\frac{5}{66}$	$\frac{5}{66}$
	$-\frac{5}{66}$	0	0	0	0	$-\frac{5}{66}$	$\frac{5}{66}$	$\frac{5}{66}$

Table A.10: Seventh order Fehlberg method (Fehlberg67)

[illegible]

### A.3 Derivation and example

To illustrate how the seemingly random numbers found in the [Butcher tableaux](#) are generated, we will derive our very own explicit third order solver.

We are trying to solve a first order differential equation

$$\frac{dy}{dt} = f(t, y) \quad (\text{A.11})$$

with third order accuracy.

The [Butcher tableau](#) we are trying to fill in looks like this:

**Table A.11:** General three stage Runge-Kutta type method

0		
a	c	
b	d	e
	F	G H

As already mentioned previously, the notation quickly becomes very dense. Therefore we will introduce some notational shortcuts:

- Whenever we evaluate  $f$  at  $(t, y)$ , we no longer write its argument:  $f(t, y) = f$
- Partial derivatives are written as a subscript:  
 $\frac{\partial f}{\partial t} = f_t$   
 $\frac{\partial f}{\partial y} = f_y$

Using Eq. (A.9) and taking the second order Taylor expansion we can find  $k_1, k_2$  and  $k_3$  up to order  $h^2$  (after substituting  $k_1$  and  $k_2$  in  $k_2$  and  $k_3$  where necessary):

$$k_1 = f(t, y_n) = f \quad (\text{A.12})$$

$$\begin{aligned} k_2 &= f(t + ah, y_n + hck_1) \\ &= f + ahf_t + chff_y + a^2\frac{h^2}{2}f_{tt} + ach^2ff_{ty} + c^2\frac{h^2}{2}f^2f_{yy} \end{aligned} \quad (\text{A.13})$$

$$\begin{aligned} k_3 &= f(t + bh, y_n + hdk_1 + hek_2) \\ &= f + bhf_t + dhff_y + ehff_y + aeh^2f_yf_t + ceh^2ff_y^2 \\ &\quad + b^2\frac{h^2}{2}f_{tt} + bdh^2ff_{ty} + beh^2ff_{ty} + d^2\frac{h^2}{2}f^2f_{yy} \\ &\quad + e^2\frac{h^2}{2}f^2f_{yy} + deh^2f^2f_{yy} \end{aligned} \quad (\text{A.14})$$

$$(\text{A.15})$$

inserting this in Eq. (A.10) gives

$$\begin{aligned}
y_{n+1} = & y_n + Fhf + Ghf + Gah^2f_t + Gch^2ff_y + Ga^2\frac{h^3}{2}f_{tt} \\
& + Gach^3f_{ty} + Gc^2\frac{h^3}{2}f^2f_{yy} + Hhf + Hbh^2f_t + Hdh^2ff_y \\
& + Heh^2ff_y + Hae h^3f_yf_t + Hce h^3ff_y^2 + Hb^2\frac{h^3}{2}f_{tt} \\
& + Hbdh^3ff_{ty} + Hbe h^3ff_{ty} + Hd^2\frac{h^3}{2}f^2f_{yy} \\
& + He^2\frac{h^3}{2}f^2f_{yy} + Hde h^3f^2f_{yy},
\end{aligned} \tag{A.16}$$

which we can compare with the Taylor expansion up to order 3:

$$y_{n+1} = y_n + hf + \frac{h^2}{2}(f_t + f_yf) + \frac{h^3}{6}(f_{tt} + 2f_{ty}f + f_tf_y + f^2f_{yy} + f_y^2f), \tag{A.17}$$

to find the following set of equations to determine the unknowns  $a$  up to  $G$ :

$$F + G + H = 1 \tag{A.18}$$

$$aG + bH = 1/2 \tag{A.19}$$

$$cG + H(d + e) = 1/2 \tag{A.20}$$

$$Ga^2 + Hb^2 = 1/3 \tag{A.21}$$

$$Gac + Hb(d + e) = 1/3 \tag{A.22}$$

$$Hea = 1/6 \tag{A.23}$$

$$Ga^2 + H(d + e)^2 = 1/3 \tag{A.24}$$

$$Hec = 1/6 \tag{A.25}$$

$$\tag{A.26}$$

When defining  $a$  and  $b$  ourselves, this can be written as:

$$a = a \tag{A.27}$$

$$b = b \tag{A.28}$$

$$c = a \tag{A.29}$$

$$d = \frac{b(3a^2 - 3a + b)}{a(3a - 2)} \tag{A.30}$$

$$e = b - d \tag{A.31}$$

$$F = \frac{6ab - 3a - 3b + 2}{6ab} \tag{A.32}$$

$$G = \frac{3b - 2}{6a(a - b)} \tag{A.33}$$

$$H = \frac{3a - 2}{6b(a - b)} \tag{A.34}$$

$$\tag{A.35}$$

When  $a = 1/2$  and  $b = 1$ , we obtain the [third order Runge-Kutta method](#) (see Table A.5). We would like to find our own solver and choose  $a = 1/10$  and  $b = 11/26$ <sup>2</sup>. This gives us the following [Butcher tableau](#):

**Table A.12:** Our own third order method

0			
$\frac{1}{10}$	$\frac{1}{10}$		
$\frac{11}{26}$	$-\frac{2189}{5746}$	$\frac{2310}{2873}$	
	$\frac{89}{33}$	$-\frac{475}{126}$	$\frac{2873}{1386}$

## A.4 Performance comparison

In this section we will validate the implementation of the different solvers by investigating the error on the solution as function of the time step. If the solvers are implemented correctly, this error should go down to the level of numerical noise at low time steps and increase as  $h^N$  for increasing  $h$ .

We first consider the different solvers implemented in [MuMax3](#). We have chosen a simple problem for which we know the analytical solution: The magnetisation of a single spin after one precession in an external field of 0.1 T. In Fig. A.1 the error after one precession is shown as function of time step together with a fitted function with the same order as the solver. As the magnetisation is a unitless vector quantity, the absolute error is defined as the norm of the difference between the analytically and numerically calculated magnetisation. From this figure we conclude that all solvers are correctly implemented.

<sup>2</sup>two dates (in month/day notation) of special importance.

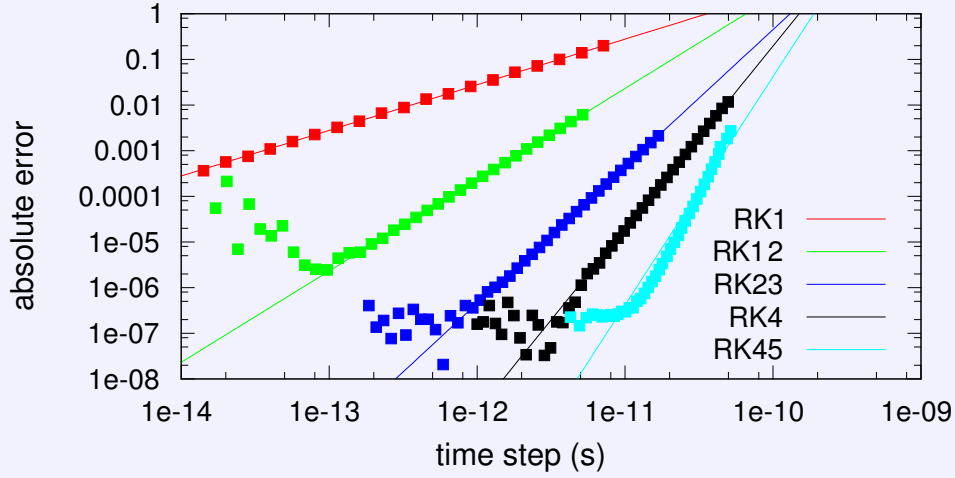


**Figure A.1:** Absolute error on a single spin after precessing without damping for one period in a 0.1 T field, as function of different solvers' time steps, implemented in [MuMax3](#). The errors follow 1st, 2nd, 3rd, 4th or 5th order convergence (solid lines) for the respective solvers down to a limit set by the single precision arithmetic.

For the solvers which are able to use an adaptive time step, we also checked if the actual error indeed scales linearly with the tolerated maximum error (see Fig. [A.2](#)). This error tolerance is only for one time step, so depending on the problem and the simulated time, the actual error will build up to a higher level, but should scale linearly with the error tolerance.

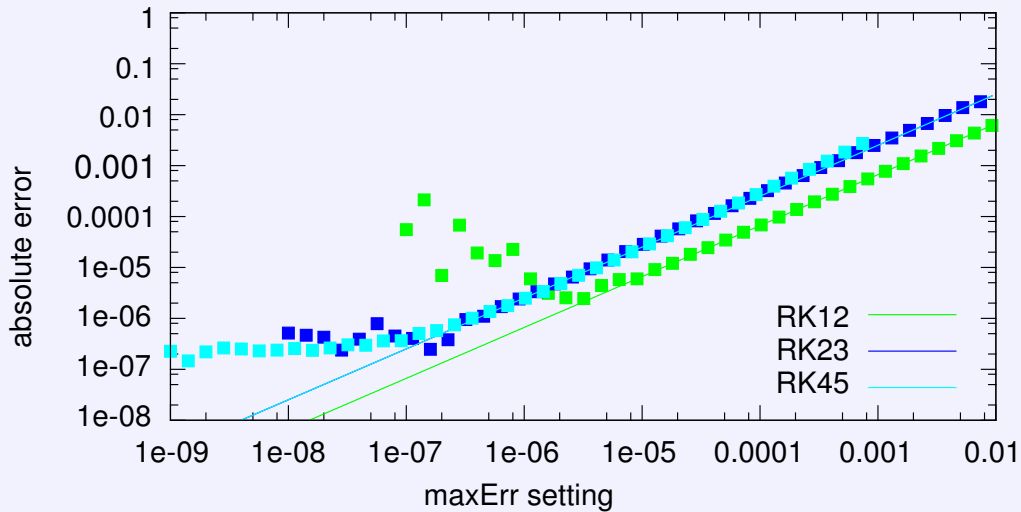


**Figure A.2:** Absolute error on a single spin after precessing without damping for one period in a 0.1 T field, as a function of different solvers' MaxErr settings. Solid lines represent linear fits. The same lower bound as in Fig. [A.1](#) is visible.

For [Vinamax](#), we performed a similar test, but instead of evaluating the error after one precession, we evaluated the error after 100 precessions. To be able to compare these results with the results of Fig. [A.1](#), one should divide the errors by 100.



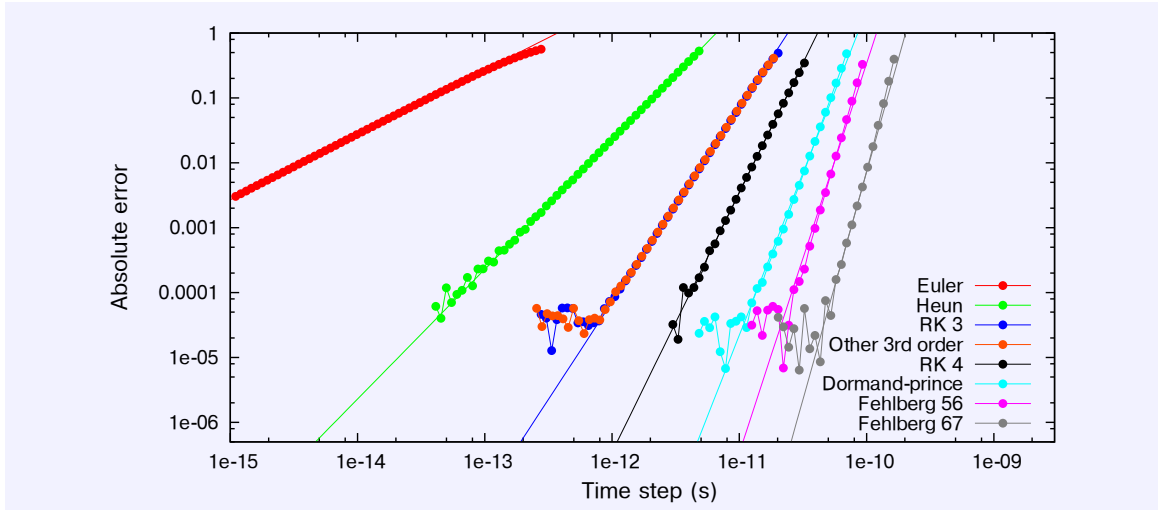


**Figure A.3:** Absolute error on a single spin after precessing without damping for 100 periods in a 0.1 T field, as function of different solvers' time steps. The errors follow 1st, 2nd, 3rd, 4th, 5th, 6th or 7th order convergence (solid lines) for the respective solvers down to a limit set by the single precision arithmetic.

Figure (A.3) shows the error as function of time step and proves that all solvers indeed converge with the correct order (even up to  $\mathcal{O}(7)$  for the Fehlberg method).

From Fig. A.3 it seems that it pays off to implement increasingly complex and higher-order solvers. However, for each additional order, a number of extra evaluations per step are necessary. Table A.13 gives an overview of how many evaluations per step are necessary for each solver. There also exists a theoretical limit which order can be achieved by a certain number of evaluations per step[257]. This limit is given in Table A.14. Note that the Fehlberg methods appear to be suboptimal, but this stems from the fact that they also have a lower order solution embedded, which further increases the number of conditions their numbers in the Butcher tableau have to fulfill, and consequently require more variables and thus more evaluations per step.

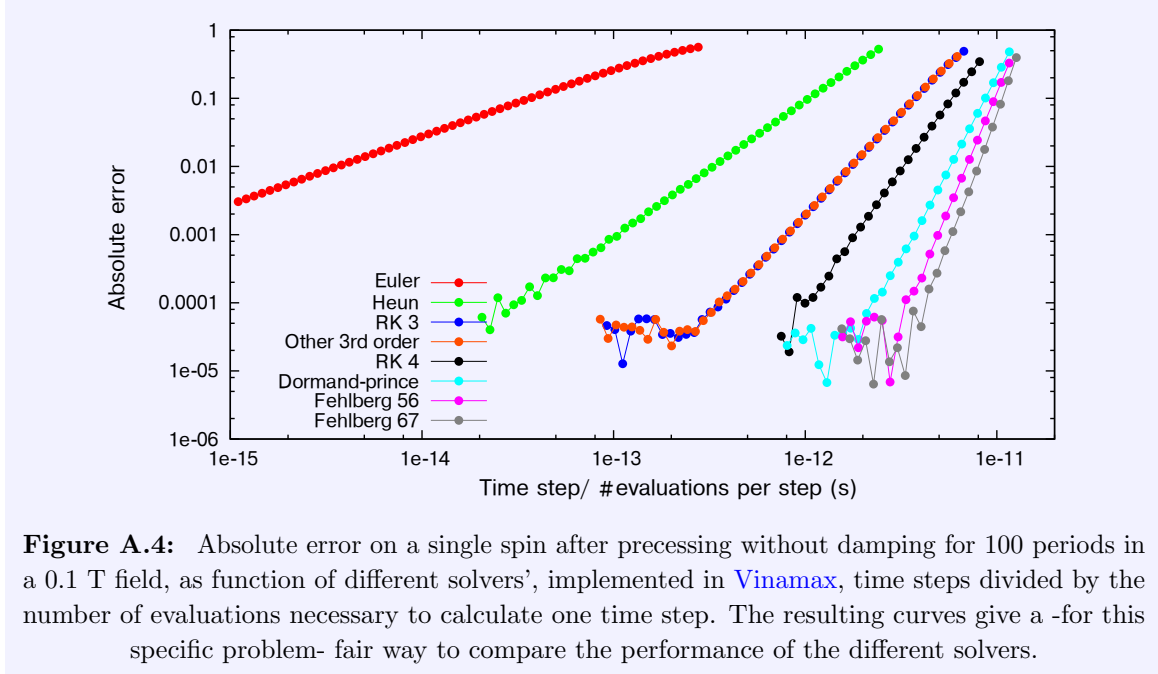
**Table A.13:** Number of evaluations per step for each solver implemented in [Vinamax](#)

solver	Euler	Heun	RK3	RK4	Dormand-Prince	Fehl-berg56	Fehl-berg67
$\frac{\# \text{evaluations}}{\text{step}}$	1	2	3	4	6	8	13

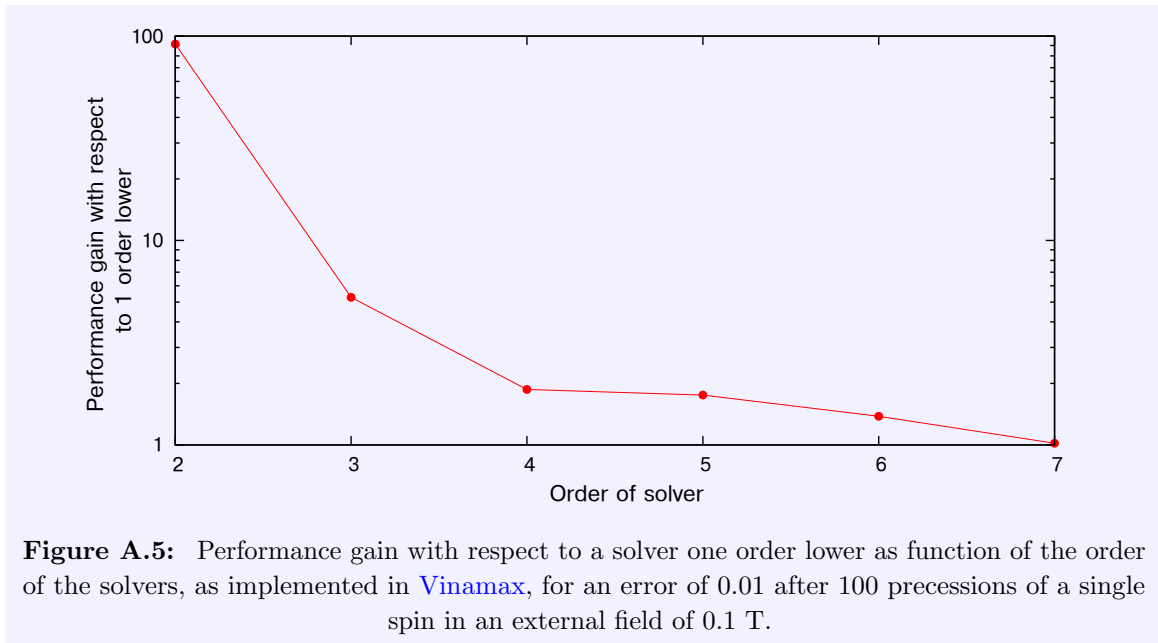
**Table A.14:** The theoretical lower limit of the number of evaluations/step required to obtain a solver of a certain order[257].

$\mathcal{O}(\text{solver})$	1	2	3	4	5	6	7	8
$\frac{\# \text{evaluations}}{\text{step}}$	1	2	3	4	6	7	9	11

To compare the performance of these solvers in a fair way, we divide the time step by the number of evaluations per step. The results are shown in Fig. A.4, from which we conclude that -for this specific problem- the highest order methods are also the most performant ones.



For an error (after 100) precessions of 0.01, the performance gain per extra order used in the solvers is shown in Fig. A.5. We see that the biggest gains are realised by implementing solvers up to fifth order. Especially changing from [Euler forward](#) to [Heun's method](#) is extremely useful and gained almost a factor 100 in speed in this specific problem.



A second point to take into account is the memory usage of these solvers. The [Seventh order Fehlberg method](#) is only slightly faster than the [Sixth order Fehlberg method](#), but uses 13 evaluations per step, as compared to 8. It thus requires almost twice the amount of memory. Especially in [MuMax3](#), where the amount of memory is limited to be able to perform very large simulations, this is not acceptable.

We conclude this appendix by stressing that the biggest performance gain can be found by substituting a first order method for a second order one and that in general we believe the [Dormand-Prince method](#) with [adaptive time step](#) to be the most efficient one in terms of speed and memory usage.



---

## Bibliography

---

- [1] J. M. D. Coey. *Magnetism and magnetic materials*. Cambridge Univ. Press, New York, NY, 2010.
- [2] W. F. Brown. *Micromagnetics*. Interscience Publishers New York, 1963.
- [3] P. Weiss. L’hypothèse du champ moléculaire et la propriété ferromagnétique. *J. Phys. Théor. Appl.*, 6(1):661–690, 1907.
- [4] P. Langevin. Magnétisme et théorie des électrons. 5(8):70–127, 1905.
- [5] W. Heisenberg. Zur Theorie des Ferromagnetismus. *Z. Phys.*, 49(9-10):619–636, 1928.
- [6] H. Barkhausen. Zwei mit Hilfe der neuen Verstärker entdeckte Erscheinungen. *Phys. Z.*, 20:401, 1919.
- [7] F. Bitter. On inhomogeneities in the magnetization of ferromagnetic materials. *Phys. Rev.*, 38:1903–1905, 1931.
- [8] K. J. Sixtus and L. Tonks. Propagation of large Barkhausen discontinuities. *Phys. Rev.*, 37:930–958, 1931.
- [9] F. Bloch. Zur Theorie des Austauschproblems und der Remanenzerscheinung der Ferromagnetika. *Z. Phys.*, 74(5-6):295–335, 1932.
- [10] L. Landau and E. Lifshitz. Theory of the dispersion of magnetic permeability in ferromagnetic bodies. *Phys. Z. Sowietunion*, 8:153, 1935.
- [11] W. Döring. Über die Trägheit der Wände zwischen Weißschen Bezirken. *Z. Naturforsch. A*, 3:373, 1948.
- [12] T. Gilbert. A phenomenological theory of damping in ferromagnetic materials. *IEEE Trans. Magn.*, 40(6):3443–3449, 2004.

- [13] W. F. Brown. Thermal fluctuations of a single-domain particle. *Phys. Rev.*, 130: 1677–1686, 1963.
- [14] W. T. Coffey and Y. P. Kalmykov. Thermal fluctuations of magnetic nanoparticles: Fifty years after Brown. *J. Appl. Phys.*, 112(12):121301, 2012.
- [15] N. L. Schryer and L. R. Walker. The motion of  $180^\circ$  domain walls in uniform DC magnetic fields. *J. Appl. Phys.*, 45(12):5406–5421, 1974.
- [16] A. Vansteenkiste and B. Van de Wiele. Mumax: A new high-performance micromagnetic simulation tool. *J. Magn. Magn. Mat.*, 323(21):2585–2591, 2011.
- [17] A. Vansteenkiste. *Dynamics of magnetic vortices in nanodots: experiment and simulation*. PhD thesis, Ghent University, 2009.
- [18] L. Berger, Y. Labaye, M. Tamine, and J. M. D. Coey. Ferromagnetic nanoparticles with strong surface anisotropy: Spin structures and magnetization processes. *Phys. Rev. B*, 77:104431, 2008.
- [19] Q. A. Pankhurst, J. Connolly, S. K. Jones, and J. Dobson. Applications of magnetic nanoparticles in biomedicine. *J. Phys. D: Appl. Phys.*, 36(13):R167, 2003.
- [20] F. Wiekhorst, U. Steinhoff, D. Eberbeck, and L. Trahms. Magnetorelaxometry assisting biomedical applications of magnetic nanoparticles. *Pharm. Res.*, 29:1189–1202, 2012.
- [21] T. Moriya. Anisotropic superexchange interaction and weak ferromagnetism. *Phys. Rev.*, 120:91–98, 1960.
- [22] N. Nagaosa and Y. Tokura. Topological properties and dynamics of magnetic skyrmions. *Nat. Nanotechnol.*, 8(12):899–911, 2013.
- [23] A. Fert, V. Cros, and J. Sampaio. Skyrmions on the track. *Nat. Nanotechnol.*, 8(3): 152–156, 2013.
- [24] R. Tomasello, E. Martinez, R. Zivieri, L. Torres, M. Carpentieri, and G. Finocchio. A strategy for the design of skyrmion racetrack memories. *Sci. Rep.*, 4, 2014.
- [25] J. Slonczewski. Current-driven excitation of magnetic multilayers. *J. Magn. Magn. Mat.*, 159(1-2):L1–L7, 1996.
- [26] M. N. Baibich, J. M. Broto, A. Fert, F. N. Van Dau, F. Petroff, P. Etienne, G. Creuzet, A. Friederich, and J. Chazelas. Giant magnetoresistance of (001)Fe/(001)Cr magnetic superlattices. *Phys. Rev. Lett.*, 61(21):2472–2475, 1988.
- [27] S. Zhang and Z. Li. Roles of nonequilibrium conduction electrons on the magnetization dynamics of ferromagnets. *Phys. Rev. Lett.*, 93(12):127204, 2004.
- [28] A. Brataas, A. D. Kent, and H. Ohno. Current-induced torques in magnetic materials. *Nat. Mater.*, 11(5):372–381, 2012.

- [29] C. Burrowes, A. P. Mihai, D. Ravelosona, J.-V. Kim, C. Chappert, L. Vila, A. Marty, Y. Samson, F. Garcia-Sanchez, L. D. Buda-Prejbeanu, I. Tudosa, E. E. Fullerton, and J.-P. Attane. Non-adiabatic spin-torques in narrow magnetic domain walls. *Nat. Phys.*, 6(1):17–21, 2010.
- [30] W. F. Brown. Relaxational behavior of fine magnetic particles. *J. Appl. Phys.*, 30(4):S130–S132, 1959.
- [31] A. Lyberatos, D. Berkov, and R. W. Chantrell. A method for the numerical simulation of the thermal magnetization fluctuations in micromagnetics. *J. Phys.: Condens. Matter*, 5(47):8911, 1993.
- [32] L. Lopez-Diaz, D. Aurelio, L. Torres, E. Martinez, M. A. Hernandez-Lopez, J. Gomez, O. Alejos, M. Carpentieri, G. Finocchio, and G. Consolo. Micromagnetic simulations using graphics processing units. *J. Phys. D: Appl. Phys.*, 45(32):323001, 2012.
- [33] I. Mayergoyz, G. Bertotti, and C. Serpico. Landau-Lifshitz magnetization dynamics driven by a random jump-noise process (invited). *J. Appl. Phys.*, 109(7):07D312, 2011.
- [34] I. Mayergoyz, G. Bertotti, C. Serpico, Z. Liu, and A. Lee. Random magnetization dynamics at elevated temperatures. *J. Appl. Phys.*, 111(7):07D501, 2012.
- [35] G. Bertotti, C. Serpico, and I. D. Mayergoyz. Probabilistic aspects of magnetization relaxation in single-domain nanomagnets. *Phys. Rev. Lett.*, 110:147205, 2013.
- [36] A. Lee, Z. Liu, G. Bertotti, C. Serpico, and I. Mayergoyz. Analysis of random magnetization switching using monte carlo simulations. *Physica B*, 435(0):100 – 104, 2014. 9th International Symposium on Hysteresis Modeling and Micromagnetics (HMM 2013).
- [37] D. A. Garanin. Fokker-Planck and Landau-Lifshitz-Bloch equations for classical ferromagnets. *Phys. Rev. B*, 55:3050–3057, 1997.
- [38] V. Baryakhtar. Phenomenological description of relaxation processes in magnets. *Zh. Eksp. Teor. Fiz.*, 87(4):1501–1508, 1984.
- [39] R. F. L. Evans, D. Hinzke, U. Atxitia, U. Nowak, R. W. Chantrell, and O. Chubykalo-Fesenko. Stochastic form of the Landau-Lifshitz-Bloch equation. *Phys. Rev. B*, 85:014433, 2012.
- [40] M. Dvornik, A. Vansteenkiste, and B. Van Waeyenberge. Micromagnetic modeling of anisotropic damping in magnetic nanoelements. *Phys. Rev. B*, 88:054427, 2013.
- [41] <https://github.com/godsic/hotspin>.
- [42] H. F. Hamann, Y. C. Martin, and H. K. Wickramasinghe. Thermally assisted recording beyond traditional limits. *Appl. Phys. Lett.*, 84(5):810–812, 2004.

- [43] C. Schieback, D. Hinzke, M. Kläui, U. Nowak, and P. Nielaba. Temperature dependence of the current-induced domain wall motion from a modified Landau-Lifshitz-Bloch equation. *Phys. Rev. B*, 80(21):214403, 2009.
- [44] W. F. Brown. Domains, micromagnetics, and beyond: Reminiscences and assessments. *J. Appl. Phys.*, 49(3):1937–1942, 1978.
- [45] A. Vansteenkiste, J. Leliaert, M. Dvornik, M. Helsen, F. Garcia-Sanchez, and B. Van Waeyenberge. The design and verification of MuMax3. *AIP Adv.*, 4(10):107133, 2014.
- [46] R. P. Feynman, R. B. Leighton, and M. L. Sands. *The Feynman lectures on physics*. 1963–1965. Three volumes.
- [47] C. Kittel. *Introduction to Solid State Physics*. John Wiley & Sons, Inc., New York, 8th edition, 1986.
- [48] W. F. Brown. Virtues and weaknesses of the domain concept. *Rev. Mod. Phys.*, 17:15–19, 1945.
- [49] M. Yan, A. Kákay, S. Gliga, and R. Hertel. Beating the Walker limit with massless domain walls in cylindrical nanowires. *Phys. Rev. Lett.*, 104(5):057201, 2010.
- [50] P. Klein, R. Varga, and M. Vazquez. Stable and fast domain wall dynamics in nanocrystalline magnetic microwire. *J. Alloys Compd.*, 550:31–34, 2013.
- [51] V. O. Dolocan. Domain wall pinning and interaction in rough cylindrical nanowires. *Appl. Phys. Lett.*, 105(16):162401, 2014.
- [52] A. Thiaville and Y. Nakatani. *Spin Dynamics in Confined Magnetic Structures III*, volume 101/2006 of *Topics Appl. Phys.*, chapter Domain-Wall Dynamics in Nanowires and Nanostrips, pages 161–205. Springer, Berlin–Heidelberg, 2006.
- [53] S. Parkin, M. Hayashi, and L. Thomas. Magnetic domain-wall racetrack memory. *Science*, 320(5873):190–194, 2008.
- [54] L. Thomas, R. Moriya, C. Rettner, and S. Parkin. Dynamics of magnetic domain walls under their own inertia. *Science*, 330(6012):1810–1813, 2010.
- [55] O. Tchernyshyov and G.-W. Chern. Fractional vortices and composite domain walls in flat nanomagnets. *Phys. Rev. Lett.*, 95:197204, 2005.
- [56] G.-W. Chern, H. Youk, and O. Tchernyshyov. Topological defects in flat nanomagnets: The magnetostatic limit. *J. Appl. Phys.*, 99(8), 2006.
- [57] J.-Y. Lee, K.-S. Lee, S. Choi, K. Y. Guslienko, and S.-K. Kim. Dynamic transformations of the internal structure of a moving domain wall in magnetic nanostrips. *Phys. Rev. B*, 76(18):184408, 2007.



- [58] A. Wachowiak, J. Wiebe, M. Bode, O. Pietzsch, M. Morgenstern, and R. Wiesendanger. Direct observation of internal spin structure of magnetic vortex cores. *Science*, 298(5593):577–580, 2002.
- [59] B. Van Waeyenberge, A. Puzic, H. Stoll, K. Chou, T. Tyliczszak, R. Hertel, M. Fähnle, H. Brückl, K. Rott, G. Reiss, I. Neudecker, D. Weiss, C. H. Back, and G. Schütz. Magnetic vortex core reversal by excitation with short bursts of an alternating field. *Nature*, 444(7118):461–464, 2006.
- [60] K. Y. Guslienko, K.-S. Lee, and S.-K. Kim. Dynamic origin of vortex core switching in soft magnetic nanodots. *Phys. Rev. Lett.*, 100:027203, 2008.
- [61] Y. Nakatani, A. Thiaville, and J. Miltat. Head-to-head domain walls in soft nano-strips: a refined phase diagram. *J. Magn. Magn. Mat.*, 290-291:750–753, 2005.
- [62] A. Thiaville, J. M. Garcia, and J. Miltat. Domain wall dynamics in nanowires. *J. Magn. Magn. Mat.*, 242-245(Part 2):1061–1063, 2002.
- [63] O. Boulle, G. Malinowski, and M. Kläui. Current-induced domain wall motion in nanoscale ferromagnetic elements. *Mater. Sci. Eng., R*, 72(9):159 – 187, 2011.
- [64] A. Thiaville, Y. Nakatani, J. Miltat, and N. Vernier. Domain wall motion by spin-polarized current: a micromagnetic study. *J. Appl. Phys.*, 95(11):7049–7051, 2004.
- [65] A. Thiaville, Y. Nakatani, J. Miltat, and Y. Suzuki. Micromagnetic understanding of current-driven domain wall motion in patterned nanowires. *Europhys. Lett.*, 69:990–996, 2005.
- [66] J. Vandermeulen, B. Van de Wiele, A. Vansteenkiste, B. Van Waeyenberge, and L. Dupré. A collective coordinate approach to describe magnetic domain wall dynamics applied to nanowires with high perpendicular anisotropy. *J. Phys. D: Appl. Phys.*, 48(3):035001, 2015.
- [67] G. S. D. Beach, C. Knutson, M. Tsoi, and J. L. Erskine. Field- and current-driven domain wall dynamics: An experimental picture. *J. Magn. Magn. Mat.*, 310(2):2038–2040, 2007.
- [68] A. Mougin, M. Cormier, J. P. Adam, P. J. Metaxas, and J. Ferré. Domain wall mobility, stability and Walker breakdown in magnetic nanowires. *Europhys. Lett.*, 78(5):57007, 2007.
- [69] Novotechnik. How to substantially reduce encoder cost while gaining functionality with multi-turn rotary position sensors. *White Paper*.
- [70] <http://www.novotechnik.de/>.
- [71] M. Hayashi, L. Thomas, R. Moriya, C. Rettner, and S. S. P. Parkin. Current-controlled magnetic domain-wall nanowire shift register. *Science*, 320(5873):209–211, 2008.

- [72] D. Chiba, G. Yamada, T. Koyama, K. Ueda, H. Tanigawa, S. Fukami, T. Suzuki, N. Ohshima, N. Ishiwata, Y. Nakatani, and T. Ono. Control of multiple magnetic domain walls by current in a Co/Ni nano-wire. *Appl. Phys. Expr.*, 3(7):073004, 2010.
- [73] S. Parkin and S.-H. Yang. Memory on the racetrack. *Nat. Nanotechnol.*, 10(3):195–198, 2015.
- [74] S.-H. Yang, K.-S. Ryu, and S. Parkin. Domain-wall velocities of up to 750 m/s driven by exchange-coupling torque in synthetic antiferromagnets. *Nat. Nanotechnol.*, 2015.
- [75] D. A. Allwood, G. Xiong, C. C. Faulkner, D. Atkinson, D. Petit, and R. P. Cowburn. Magnetic domain-wall logic. *Science*, 309:16881692, 2005.
- [76] S. E. Barnes, J. Ieda, and S. Maekawa. Magnetic memory and current amplification devices using moving domain walls. *Appl. Phys. Lett.*, 89(12):122507, 2006.
- [77] K. A. Omari and T. J. Hayward. Chirality-based vortex domain-wall logic gates. *Phys. Rev. Appl.*, 2:044001, 2014.
- [78] S. Goolaup, M. Ramu, C. Murapaka, and W. Lew. Transverse domain wall profile for spin logic applications. *Sci. Rep.*, 5, 2015.
- [79] J. Vandermeulen, B. Van de Wiele, L. Dupré, and B. Van Waeyenberge. Logic and memory concepts for all-magnetic computing based on transverse domain walls. *J. Phys. D: Appl. Phys.*, 48(27):275003, 2015.
- [80] A. Cho. At mixed odds, racetrack memory charges from gate. *Science*, 320(5873):166, 2008.
- [81] C. Moreau-Luchaire, C. Moutafis, N. Reyren, J. Sampaio, C. Vaz, N. Van Horne, K. Bouzehouane, K. Garcia, C. Deranlot, P. Warnicke, P. Wohlhüter, J.-M. George, M. Weigand, J. Raabe, V. Cros, and A. Fert. Additive interfacial chiral interaction in multilayers for stabilization of small individual skyrmions at room temperature. *Nat. Nanotechnol.*, 2016.
- [82] S. Woo, K. Litzius, B. Krüger, M.-Y. Im, L. Caretta, K. Richter, M. Mann, A. Krone, R. M. Reeve, M. Weigand, P. Agrawal, I. Lemesh, M.-A. Mawass, P. Fischer, M. Klaui, and G. S. D. Beach. Observation of room-temperature magnetic skyrmions and their current-driven dynamics in ultrathin metallic ferromagnets. *Nat. Mater.*, 2016.
- [83] A. Rosch. Skyrmions: Moving with the current. *Nat. Nanotechnol.*, 8(3):160–161, 2013.
- [84] X. Zhang, M. Ezawa, and Y. Zhou. Magnetic skyrmion logic gates: conversion, duplication and merging of skyrmions. *Sci. Rep.*, 5, 2015.
- [85] K. J. A. Franke, B. Van de Wiele, Y. Shirahata, S. J. Hämmäläinen, T. Taniyama, and S. van Dijken. Reversible electric-field-driven magnetic domain-wall motion. *Phys. Rev. X*, 5:011010, 2015.

- [86] B. Van de Wiele, J. Leliaert, K. J. A. Franke, and S. van Dijken. Electric-field-driven dynamics of magnetic domain walls in magnetic nanowires patterned on ferroelectric domains. *New J. Phys.*, 18(3):033027, 2016.
- [87] H. Corte-León, P. Krzysteczko, H. W. Schumacher, A. Manzin, D. Cox, V. Antonov, and O. Kazakova. Magnetic bead detection using domain wall-based nanosensor. *J. Appl. Phys.*, 117(17):17E313, 2015.
- [88] J. Leliaert, B. Van de Wiele, A. Vansteenkiste, L. Laurson, G. Durin, L. Dupré, and B. Van Waeyenberge. A numerical approach to incorporate intrinsic material defects in micromagnetic simulations. *J. Appl. Phys.*, 115(17):17D102, 2014.
- [89] J. Leliaert, B. Van de Wiele, A. Vansteenkiste, L. Laurson, G. Durin, L. Dupré, and B. Van Waeyenberge. Influence of material defects on current-driven vortex domain wall mobility. *Phys. Rev. B*, 89:064419, 2014.
- [90] J. Leliaert, B. Van de Wiele, A. Vansteenkiste, L. Laurson, G. Durin, L. Dupré, and B. Van Waeyenberge. Current-driven domain wall mobility in polycrystalline permalloy nanowires: A numerical study. *J. Appl. Phys.*, 115(23):233903, 2014.
- [91] J.-S. Kim, O. Boulle, S. Verstoep, L. Heyne, J. Rhensius, M. Kläui, L. J. Heyderman, F. Kronast, R. Mattheis, C. Ulysse, and G. Faini. Current-induced vortex dynamics and pinning potentials probed by homodyne detection. *Phys. Rev. B*, 82(10):104427, 2010.
- [92] J. A. J. Burgess, A. E. Fraser, F. Fani Sani, D. Vick, B. D. Hauer, J. P. Davis, and M. R. Freeman. Quantitative magneto-mechanical detection and control of the Barkhausen effect. *Science*, 339(6123):1051–1054, 2013.
- [93] T. Y. Chen, M. J. Erickson, P. A. Crowell, and C. Leighton. Surface roughness dominated pinning mechanism of magnetic vortices in soft ferromagnetic films. *Phys. Rev. Lett.*, 109:097202, 2012.
- [94] J. Miltat and A. Thiaville. Vortex cores—smaller than small. *Science*, 298(5593):555, 2002.
- [95] B. Van de Wiele, L. Laurson, and G. Durin. Effect of disorder on transverse domain wall dynamics in magnetic nanostrips. *Phys. Rev. B*, 86:144415, 2012.
- [96] J.-H. Moon, K.-J. Lee, D.-H. Kim, and H.-G. Piao. Three-dimensional dynamics of magnetic vortex core in a nanodisk. *J. Korean. Magn. Soc.*, 22(6):195–199, 2012.
- [97] R. L. Compton, T. Y. Chen, and P. A. Crowell. Magnetic vortex dynamics in the presence of pinning. *Phys. Rev. B*, 81:144412, 2010.
- [98] Y. Nakatani, A. Thiaville, and J. Miltat. Faster magnetic walls in rough wires. *Nat. Mater.*, 2:521–523, 2003.

- [99] H. Tanigawa, T. Koyama, M. Bartkowiak, S. Kasai, K. Kobayashi, T. Ono, and Y. Nakatani. Dynamical pinning of a domain wall in a magnetic nanowire induced by Walker breakdown. *Phys. Rev. Lett.*, 101(20):207203, 2008.
- [100] J. Lau, R. McMichael, and M. Donahue. Implementation of two-dimensional polycrystalline grains in object oriented micromagnetic framework. *J. Res. Natl. Inst. Stand. Technol.*, 114(1), 2009.
- [101] H. Min, R. D. McMichael, M. J. Donahue, J. Miltat, and M. D. Stiles. Effects of disorder and internal dynamics on vortex wall propagation. *Phys. Rev. Lett.*, 104:217201, 2010.
- [102] Y. Tserkovnyak, H. J. Skadsem, A. Brataas, and G. E. W. Bauer. Current-induced magnetization dynamics in disordered itinerant ferromagnets. *Phys. Rev. B*, 74(14):144405, 2006.
- [103] D. Berkov and J. Miltat. Spin-torque driven magnetization dynamics: Micromagnetic modeling. *J. Magn. Magn. Mat.*, 320(7):1238–1259, 2008.
- [104] Y. Ban and G. Tatara. Spin-transfer torque in disordered weak ferromagnets. *Phys. Rev. B*, 80(18):184406, 2009.
- [105] S. Lepadatu, A. Vanhaverbeke, D. Atkinson, R. Allenspach, and C. H. Marrows. Dependence of domain-wall depinning threshold current on pinning profile. *Phys. Rev. Lett.*, 102(12):127203, 2009.
- [106] S. Lepadatu, M. C. Hickey, A. Potenza, H. Marchetto, T. R. Charlton, S. Langridge, S. S. Dhesi, and C. H. Marrows. Experimental determination of spin-transfer torque nonadiabaticity parameter and spin polarization in permalloy. *Phys. Rev. B*, 79(9):094402, 2009.
- [107] S. Lepadatu, J. S. Claydon, C. J. Kinane, T. R. Charlton, S. Langridge, A. Potenza, S. S. Dhesi, P. S. Keatley, R. J. Hicken, B. J. Hickey, and C. H. Marrows. Domain-wall pinning, nonadiabatic spin-transfer torque, and spin-current polarization in permalloy wires doped with vanadium. *Phys. Rev. B*, 81(2):020413, 2010.
- [108] M. Eltschka, M. Wötzl, J. Rhensius, S. Krzyk, U. Nowak, M. Kläui, T. Kasama, R. E. Dunin-Borkowski, L. J. Heyderman, H. J. van Driel, and R. A. Duine. Nonadiabatic spin torque investigated using thermally activated magnetic domain wall dynamics. *Phys. Rev. Lett.*, 105(5):056601, 2010.
- [109] L. Thomas, M. Hayashi, X. Jiang, R. Moriya, C. Rettner, and S. P. Parkin. Oscillatory dependence of current-driven magnetic domain wall motion on current pulse length. *Nature*, 443(7108):197–200, 2006.
- [110] L. Heyne, J. Rhensius, D. Ilgaz, A. Bisig, U. Rüdiger, M. Kläui, L. Joly, F. Nolting, L. J. Heyderman, J. U. Thiele, and F. Kronast. Direct determination of large spin-torque nonadiabaticity in vortex core dynamics. *Phys. Rev. Lett.*, 105(18):187203, 2010.

- [111] S. D. Pollard, L. Huang, K. S. Buchanan, D. A. Arena, and Y. Zhu. Direct dynamic imaging of non-adiabatic spin torque effects. *Nat. Commun.*, 3:1028, 2012.
- [112] L. Heyne, J. Rhensius, A. Bisig, S. Krzyk, P. Punke, M. Kläui, L. J. Heyderman, L. L. Guyader, and F. Nolting. Direct observation of high velocity current induced domain wall motion. *Appl. Phys. Lett.*, 96(3):032504, 2010.
- [113] G. S. D. Beach, C. Knutson, C. Nistor, M. Tsoi, and J. L. Erskine. Nonlinear domain-wall velocity enhancement by spin-polarized electric current. *Phys. Rev. Lett.*, 97(5):057203, 2006.
- [114] M. Hayashi, L. Thomas, Y. B. Bazaliy, C. Rettner, R. Moriya, X. Jiang, and S. P. Parkin. Influence of current on field-driven domain wall motion in permalloy nanowires from time resolved measurements of anisotropic magnetoresistance. *Phys. Rev. Lett.*, 96(19):197207, 2006.
- [115] G. Meier, M. Bolte, R. Eiselt, B. Krüger, D.-H. Kim, and P. Fischer. Direct imaging of stochastic domain-wall motion driven by nanosecond current pulses. *Phys. Rev. Lett.*, 98(18):187202, 2007.
- [116] M. Kläui, P.-O. Jubert, R. Allenspach, A. Bischof, J. A. C. Bland, G. Faini, U. Rudiger, C. A. F. Vaz, L. Vila, and C. Vouille. Direct observation of domain-wall configurations transformed by spin currents. *Phys. Rev. Lett.*, 95(2):026601, 2005.
- [117] L. Heyne, M. Kläui, D. Backes, T. A. Moore, S. Krzyk, U. Rudiger, L. J. Heyderman, A. F. Rodriguez, F. Nolting, T. O. Montes, M. A. Nino, A. Locatelli, K. Kirsch, and R. Mattheis. Relationship between nonadiabaticity and damping in permalloy studied by current induced spin structure transformations. *Phys. Rev. Lett.*, 100(6):066603, 2008.
- [118] E. Martinez. The stochastic nature of the domain wall motion along high perpendicular anisotropy strips with surface roughness. *J. Phys.: Condens. Matter*, 24(2):024206, 2012.
- [119] E. Martinez. Micromagnetic analysis of current-driven DW dynamics along rough strips with high perpendicular anisotropy at room temperature. *J. Magn. Magn. Mater.*, 324(21):3542 – 3547, 2012.
- [120] R. L. Compton and P. A. Crowell. Dynamics of a pinned magnetic vortex. *Phys. Rev. Lett.*, 97:137202, 2006.
- [121] J.-S. Kim, O. Boulle, S. Verstoep, L. Heyne, J. Rhensius, M. Kläui, L. J. Heyderman, F. Kronast, R. Mattheis, C. Ulysse, and G. Faini. Current-induced vortex dynamics and pinning potentials probed by homodyne detection. *Phys. Rev. B*, 82:104427, 2010.
- [122] P. J. Metaxas, J. P. Jamet, A. Mougin, M. Cormier, J. Ferré, V. Baltz, B. Rodmacq, B. Dieny, and R. L. Stamps. Creep and flow regimes of magnetic domain-wall motion in ultrathin Pt/Co/Pt films with perpendicular anisotropy. *Phys. Rev. Lett.*, 99(21):217208, 2007.

- [123] A. V. Khvalkovskiy, V. Cros, D. Apalkov, V. Nikitin, M. Krounbi, K. A. Zvezdin, A. Anane, J. Grollier, and A. Fert. Matching domain-wall configuration and spin-orbit torques for efficient domain-wall motion. *Phys. Rev. B*, 87:020402, 2013.
- [124] M. Dyakonov and V. Perel. Current-induced spin orientation of electrons in semiconductors. *Phys. Lett. A*, 35(6):459 – 460, 1971.
- [125] P. P. J. Haazen, E. Murè, J. H. Franken, R. Lavrijsen, H. J. M. Swagten, and B. Koopmans. Domain wall depinning governed by the spin Hall effect. *Nat. Mater.*, 12(4): 299–303, 2013.
- [126] G. Dresselhaus. Spin-orbit coupling effects in zinc blende structures. *Phys. Rev.*, 100: 580–586, 1955.
- [127] E. Martinez. Micromagnetic analysis of the Rashba field on current-induced domain wall propagation. *J. Appl. Phys.*, 111(3):033901, 2012.
- [128] I. Mihai Miron, G. Gaudin, S. Auffret, B. Rodmacq, A. Schuhl, S. Pizzini, J. Vogel, and P. Gambardella. Current-driven spin torque induced by the Rashba effect in a ferromagnetic metal layer. *Nat. Mater.*, 9(3):230–234, 2010.
- [129] M. Stier, R. Egger, and M. Thorwart. Nonequilibrium Rashba field driven domain wall motion in ferromagnetic nanowires. *Phys. Rev. B*, 87:184415, 2013.
- [130] E. Martinez, L. Lopez-Diaz, L. Torres, C. Tristan, and O. Alejos. Thermal effects in domain wall motion: Micromagnetic simulations and analytical model. *Phys. Rev. B*, 75:174409, 2007.
- [131] J. Leliaert, B. Van de Wiele, J. Vandermeulen, A. Coene, A. Vansteenkiste, L. Laurson, G. Durin, B. Van Waeyenberge, and L. Dupré. Thermal effects on transverse domain wall dynamics in magnetic nanowires. *Appl. Phys. Lett.*, 106(20):202401, 2015.
- [132] J. Leliaert, B. Van de Wiele, A. Vansteenkiste, L. Laurson, G. Durin, L. Dupré, and B. Van Waeyenberge. Creep turns linear in narrow ferromagnetic nanostrips. *Sci. Rep.*, 6:20472, 2016.
- [133] Y. Li and B.-G. Liu. Current controlled spin reversal of nanomagnets with giant uniaxial anisotropy. *Phys. Rev. Lett.*, 96(21):217201, 2006.
- [134] S. Dutta, S. A. Siddiqui, J. A. Currivan-Incorvia, C. A. Ross, and M. A. Baldo. Micromagnetic modeling of domain wall motion in sub-100-nm-wide wires with individual and periodic edge defects. *AIP Adv.*, 5(12):127206, 2015.
- [135] J.-S. Kim, M.-A. Mawass, A. Bisig, B. Krüger, R. M. Reeve, T. Schulz, F. Büttner, J. Yoon, C.-Y. You, M. Weigand, H. Stoll, G. Schütz, H. J. M. Swagten, B. Koopmans, S. Eisebitt, and M. Kläui. Synchronous precessional motion of multiple domain walls in a ferromagnetic nanowire by perpendicular field pulses. *Nat. Commun.*, 5:3429, 2014.

- [136] P. Le Doussal and V. M. Vinokur. Creep in one dimension and phenomenological theory of glass dynamics. *Physica C*, 254(1):63–68, 1995.
- [137] H. Risken. *Fokker-Planck Equation*, volume 18 of *Springer Series in Synergetics*. Springer Berlin Heidelberg, 1996.
- [138] A. Einstein. *Investigations on the Theory of the Brownian Movement*. Courier Dover Publications, 1956.
- [139] S. Lemerle, J. Ferré, C. Chappert, V. Mathet, T. Giamarchi, and P. Le Doussal. Domain wall creep in an Ising ultrathin magnetic film. *Phys. Rev. Lett.*, 80(4):849–852, 1998.
- [140] G. Blatter, M. V. Feigel'man, V. B. Geshkenbein, A. I. Larkin, and V. M. Vinokur. Vortices in high-temperature superconductors. *Rev. Mod. Phys.*, 66:1125–1388, 1994.
- [141] P. Chauve, T. Giamarchi, and P. Le Doussal. Creep and depinning in disordered media. *Phys. Rev. B*, 62:6241–6267, 2000.
- [142] J. Franken, H. Swagten, and B. Koopmans. Shift registers based on magnetic domain wall ratchets with perpendicular anisotropy. *Nat. Nanotechnol.*, 7(8):499–503, 2012.
- [143] K.-W. Moon, D.-H. Kim, S.-C. Yoo, S.-G. Je, B. S. Chun, W. Kim, B.-C. Min, C. Hwang, and S.-B. Choe. Magnetic bubblecade memory based on chiral domain walls. *Sci. Rep.*, 5, 2015.
- [144] J. Kim, S.-G. Je, and S.-B. Choe. Universality of stochasticity in magnetic domain-wall motion. *Appl. Phys. Expr.*, 8(6):063001, 2015.
- [145] K.-J. Kim, J.-C. Lee, S.-M. Ahn, K.-S. Lee, C.-W. Lee, Y. J. Cho, S. Seo, K.-H. Shin, S.-B. Choe, and H.-W. Lee. Interdimensional universality of dynamic interfaces. *Nature*, 458(7239):740–742, 2009.
- [146] T. Hayward. Intrinsic nature of stochastic domain wall pinning phenomena in magnetic nanowire devices. *Sci. Rep.*, 5:13279, 2015.
- [147] S. Lepadatu. Effective field model of roughness in magnetic nano-structures. *J. Appl. Phys.*, 118(24):243908, 2015.
- [148] H. Vollmer and H. Risken. Distribution functions for the Brownian motion of particles in a periodic potential driven by an external force. *Z. Phys. B: Condens. Matter*, 34(3):313–322, 1979.
- [149] J. Vogel, M. Bonfim, N. Rougemaille, O. Boulle, I. M. Miron, S. Auffret, B. Rodmacq, G. Gaudin, J. C. Cezar, F. Sirotti, and S. Pizzini. Direct observation of massless domain wall dynamics in nanostripes with perpendicular magnetic anisotropy. *Phys. Rev. Lett.*, 108:247202, 2012.

- [150] M. Yamanouchi, J. Ieda, F. Matsukura, S. E. Barnes, S. Maekawa, and H. Ohno. Universality classes for domain wall motion in the ferromagnetic semiconductor (Ga,Mn)As. *Science*, 317(5845):1726–1729, 2007.
- [151] J.-C. Lee, K.-J. Kim, J. Ryu, K.-W. Moon, S.-J. Yun, G.-H. Gim, K.-S. Lee, K.-H. Shin, H.-W. Lee, and S.-B. Choe. Universality classes of magnetic domain wall motion. *Phys. Rev. Lett.*, 107(6):067201, 2011.
- [152] K.-J. Kim, J.-C. Lee, K.-H. Shin, H.-W. Lee, and S.-B. Choe. Universal classes of magnetic-field- and electric-current-induced magnetic domain-wall dynamics in one and two dimensional regimes. *Curr. Appl. Phys.*, 13(1):228 – 236, 2013.
- [153] J. Ryu, S.-B. Choe, and H.-W. Lee. Magnetic domain-wall motion in a nanowire: Depinning and creep. *Phys. Rev. B*, 84:075469, 2011.
- [154] J. Ferré, P. J. Metaxas, A. Mougin, J.-P. Jamet, J. Gorchon, and V. Jeudy. Universal magnetic domain wall dynamics in the presence of weak disorder. *C. R. Phys.*, 14(8): 651–666, 2013.
- [155] J. Gorchon, S. Bustingorry, J. Ferré, V. Jeudy, A. Kolton, and T. Giamarchi. Pinning-dependent field-driven domain wall dynamics and thermal scaling in an ultrathin Pt/-Co/Pt magnetic film. *Phys. Rev. Lett.*, 113(2):027205, 2014.
- [156] E. Martinez, L. Lopez-Diaz, O. Alejos, L. Torres, and C. Tristan. Thermal effects on domain wall depinning from a single notch. *Phys. Rev. Lett.*, 98(26):267202, 2007.
- [157] J. Leliaert, A. Vansteenkiste, A. Coene, L. Dupré, and B. Van Waeyenberge. Vinamax: a macrospin simulation tool for magnetic nanoparticles. *Med. Biol. Eng. Comput.*, 53(4):309–317, 2015.
- [158] J. Leliaert, A. Coene, G. Crevecoeur, A. Vansteenkiste, D. Eberbeck, F. Wiekhorst, B. Van Waeyenberge, and L. Dupré. Regarding the Néel relaxation time constant in magnetorelaxometry. *J. Appl. Phys.*, 116(16):163914, 2014.
- [159] J. Leliaert, A. Coene, M. Liebl, D. Eberbeck, U. Steinhoff, F. Wiekhorst, B. Fischer, L. Dupré, and B. Van Waeyenberge. Thermal magnetic noise spectra of nanoparticle ensembles. *Appl. Phys. Lett.*, 107(22):222401, 2015.
- [160] R. C. Temple, A. P. Mihai, D. A. Arena, and C. H. Marrows. Ensemble magnetic behaviour of interacting CoFe nanoparticles. *Front. Phys.*, 3(52), 2015.
- [161] C. P. Bean and J. D. Livingston. Superparamagnetism. *J. Appl. Phys.*, 30(4):S120–S129, 1959.
- [162] A. v.d. Giessen. Magnetic properties of ultra-fine iron(III)oxide-hydrate particles prepared from iron(III)oxide-hydrate gels. *J. Phys. Chem. Solids.*, 28(2):343 – 346, 1967.



- [163] F. Crick and A. Hughes. The physical properties of cytoplasm: A study by means of the magnetic particle method Part I. experimental. *Exp. Cell Res.*, 1(1):37–80, 1950.
- [164] J. Frenkel and J. Dorfman. Spontaneous and induced magnetisation in ferromagnetic bodies. *Nature*, 126(3173):274–275, 1930.
- [165] W. F. Brown. Ferromagnetic domains and the magnetization curve. *J. Appl. Phys.*, 11(3):160–172, 1940.
- [166] C. Guillaud and M. Roux. Quelques propriétés ferromagnétiques des ferrites mixtes de nickel et de zinc. *C. R. Acad. Sci.*, 229(22):1133–1135, 1949.
- [167] C. Kittel. Theory of the structure of ferromagnetic domains in films and small particles. *Phys. Rev.*, 70(11-12):965, 1946.
- [168] L. Néel. Magnetisme-propriétés d’un ferromagnétique cubique en grains fins. *C. R. Acad. Sci.*, 224(21):1488–1490, 1947.
- [169] E. Stoner and E. Wohlfarth. Interpretation of high coercivity in ferromagnetic materials. *Nature*, 160(650):98–99, 1947.
- [170] E. Stoner and E. Wohlfarth. A mechanism of magnetic hysteresis in heterogeneous alloys. *Phil. Trans. R. Soc. A*, 240(826):599–642, 1948.
- [171] W. F. Brown Jr. The fundamental theorem of fine-ferromagnetic-particle theory. *J. Appl. Phys.*, 39(2):993–994, 1968.
- [172] K. M. Krishnan. Biomedical nanomagnetism: a spin through possibilities in imaging, diagnostics, and therapy. *IEEE Trans. Magn.*, 46(7):2523–2558, 2010.
- [173] Q. Pankhurst, N. Thanh, S. Jones, and J. Dobson. Progress in applications of magnetic nanoparticles in biomedicine. *J. Phys. D: Appl. Phys.*, 42(22):224001, 2009.
- [174] B. Mehdaoui, A. Meffre, J. Carrey, S. Lachaize, L.-M. Lacroix, M. Gougeon, B. Chaudret, and M. Respaud. Optimal size of nanoparticles for magnetic hyperthermia: A combined theoretical and experimental study. *Adv. Funct. Mater.*, 21(23):4573–4581, 2011.
- [175] M. Arruebo, R. Fernández-Pacheco, M. R. Ibarra, and J. Santamaría. Magnetic nanoparticles for drug delivery. *Nano today*, 2(3):22–32, 2007.
- [176] D. J. Bharali and S. A. Mousa. Emerging nanomedicines for early cancer detection and improved treatment: current perspective and future promise. *Pharmacol. Ther.*, 128(2):324–335, 2010.
- [177] A. Coene, G. Crevecoeur, J. Leliaert, and L. Dupré. Toward 2D and 3D imaging of magnetic nanoparticles using EPR measurements. *Med. Phys.*, 42(9):5007–5014, 2015.
- [178] A. Coene, G. Crevecoeur, M. Liebl, F. Wiekhorst, L. Dupré, and U. Steinhoff. Uncertainty of reconstructions of spatially distributed magnetic nanoparticles under realistic noise conditions. *J. Appl. Phys.*, 115(17):17B509, 2014.

- [179] M. Liebl, U. Steinhoff, F. Wiekhorst, J. Haueisen, and L. Trahms. Quantitative imaging of magnetic nanoparticles by magnetorelaxometry with multiple excitation coils. *Phys. Med. Biol.*, 59(21):6607, 2014.
- [180] B. W. Ficko, P. M. Nadar, P. J. Hoopes, and S. G. Diamond. Development of a magnetic nanoparticle susceptibility magnitude imaging array. *Phys. Med. Biol.*, 59(4):1047, 2014.
- [181] B. Gleich and R. Weizenecker. Tomographic imaging using the nonlinear response of magnetic particles. *Nature*, 435(7046):1214–1217, 2005.
- [182] J. Carrey, B. Mehdaoui, and M. Respaud. Simple models for dynamic hysteresis loop calculations of magnetic single-domain nanoparticles: Application to magnetic hyperthermia optimization. *J. Appl. Phys.*, 109(8):083921, 2011.
- [183] C. P. Bean. Hysteresis loops of mixtures of ferromagnetic micropowders. *J. Appl. Phys.*, 26(11):1381–1383, 1955.
- [184] L. Néel. Théorie du traînage magnétique des ferromagnétiques en grains fins avec applications aux terres cuites. *Ann. géophys.*, 5(2):99–136, 1949.
- [185] C. T. Lim, J. Han, J. Guck, and H. Espinosa. Micro and nanotechnology for biological and biomedical applications. *Med. Biol. Eng. Comput.*, 48(10):941–943, 2010.
- [186] C. Alexiou, W. Arnold, R. Klein, F. Parak, P. Hulin, C. Bergemann, W. Erhardt, S. Wagenpfeil, and A. Lübke. Locoregional cancer treatment with magnetic drug targeting. *Cancer Res.*, 60(23):6641–6648, 2000.
- [187] F. Wiekhorst, M. Liebl, U. Steinhoff, L. Trahms, S. Lyer, S. Dürr, and C. Alexiou. Magnetorelaxometry for in-vivo quantification of magnetic nanoparticle distributions after magnetic drug targeting in a rabbit carcinoma model. In *Magnetic Particle Imaging*, volume 140 of *Springer Proceedings in Physics*, pages 301–305. Springer Berlin Heidelberg, 2012.
- [188] M. Kircher, U. Mahmood, R. King, R. Weissleder, and L. Josephson. A multimodal nanoparticle for preoperative magnetic resonance imaging and intraoperative optical brain tumor delineation. *Cancer Res.*, 63(23):8122–8125, 2003.
- [189] E. Flynn and H. Bryant. A biomagnetic system for *in vivo* cancer imaging. *Phys. Med. Biol.*, 50(6):1273–1293, 2005.
- [190] M. Johannsen, U. Gneveckow, B. Thiesen, K. Taymoorian, C. Cho, N. Waldöfner, R. Scholz, A. Jordan, S. Loening, and P. Wust. Thermotherapy of prostate cancer using magnetic nanoparticles: feasibility, imaging, and three-dimensional temperature distribution. *Eur. Urol.*, 52(6):1653–1662, 2007.
- [191] H. Richter, M. Kettering, F. Wiekhorst, U. Steinhoff, I. Hilger, and L. Trahms. Magnetorelaxometry for localization and quantification of magnetic nanoparticles for thermal ablation studies. *Phys. Med. Biol.*, 55(3):623, 2010.

- [192] E. A. Périgo, G. Hemery, O. Sandre, D. Ortega, E. Garaio, F. Plazaola, and F. J. Teran. Fundamentals and advances in magnetic hyperthermia. *Appl. Phys. Rev.*, 2(4):041302, 2015.
- [193] A. Coene, G. Crevecoeur, and L. Dupré. Adaptive control of excitation coil arrays for targeted magnetic nanoparticle reconstruction using magnetorelaxometry. *IEEE Trans. Magn.*, 48(11):2842–2845, 2012.
- [194] R. Eichardt, D. Baumgarten, B. Petković, F. Wiekhorst, L. Trahms, and J. Haueisen. Adapting source grid parameters to improve the condition of the magnetostatic linear inverse problem of estimating nanoparticle distributions. *Med. Biol. Eng. Comput.*, 50(10):1081–1089, 2012.
- [195] D. Baumgarten, M. Liehr, F. Wiekhorst, U. Steinhoff, P. Münster, P. Miethe, L. Trahms, and J. Haueisen. Magnetic nanoparticle imaging by means of minimum norm estimates from remanence measurements. *Med. Biol. Eng. Comput.*, 46(12):1177–1185, 2008.
- [196] J. Llandro, J. Palfreyman, A. Ionescu, and C. Barnes. Magnetic biosensor technologies for medical applications: a review. *Med. Biol. Eng. Comput.*, 48(10):977–998, 2010.
- [197] A. Coene, G. Crevecoeur, L. Dupré, and P. Vaes. Quantitative estimation of magnetic nanoparticle distributions in one dimension using low-frequency continuous wave electron paramagnetic resonance. *J. Phys. D: Appl. Phys.*, 46(24):245002, 2013.
- [198] I. S. Poperechny and Y. L. Raikher. Ferromagnetic resonance in uniaxial superparamagnetic particles. *Phys. Rev. B*, 93:014441, 2016.
- [199] J. Weizenecker, J. Borgert, and B. Gleich. A simulation study on the resolution and sensitivity of magnetic particle imaging. *Phys. Med. Biol.*, 52(21):6363, 2007.
- [200] N. Frey and S. Sun. chapter Magnetic Nanoparticle for Information Storage Applications, pages 33–68. *Nanomaterials and their Applications*. CRC Press, 2010.
- [201] E. Kirkpatrick, S. Majetich, and M. McHenry. Magnetic properties of single domain samarium cobalt nanoparticles. *IEEE Trans. Magn.*, 32(5):4502–4504, 1996.
- [202] G. Crevecoeur, D. Baumgarten, U. Steinhoff, J. Haueisen, L. Thrams, and L. Dupré. Advancements in magnetic nanoparticle reconstruction using sequential activation of excitation coil arrays using magnetorelaxometry. *IEEE Trans. Magn.*, 48(4):1313 – 1316, 2012.
- [203] M. Liebl, U. Steinhoff, F. Wiekhorst, A. Coene, J. Haueisen, and L. Trahms. Quantitative reconstruction of a magnetic nanoparticle distribution using a non-negativity constraint. *Biomed. Tech.*, 58:2, 2013.
- [204] R. Kötz, T. Bunte, W. Weitschies, and L. Trahms. Superconducting quantum interference device-based magnetic nanoparticle relaxation measurement as a novel tool for

- the binding specific detection of biological binding reactions. *J. Appl. Phys.*, 81(8): 4317–4317, 1997.
- [205] D. Eberbeck, C. Bergemann, F. Wiekhorst, U. Steinhoff, and L. Trahms. Quantification of specific bindings of biomolecules by magnetorelaxometry. *Journal of Nano biotechnology*, 6, 2008.
- [206] D. Eberbeck, F. Wiekhorst, U. Steinhoff, K. O. Schwarz, A. Kummrow, M. Kammel, J. Neukammer, and L. Trahms. Specific binding of magnetic nanoparticle probes to platelets in whole blood detected by magnetorelaxometry. *J. Magn. Magn. Mater.*, 321(10):1617 – 1620, 2009. Proceedings of the Seventh International Conference on the Scientific and Clinical Applications of Magnetic Carriers.
- [207] D. Eberbeck, F. Wiekhorst, U. Steinhoff, and L. Trahms. Quantification of biomolecule agglutination by magnetorelaxometry. *Appl. Phys. Lett.*, 95(21):213701, 2009.
- [208] D. Eberbeck, F. Wiekhorst, U. Steinhoff, and L. Trahms. Aggregation behaviour of magnetic nanoparticle suspensions investigated by magnetorelaxometry. *J. Phys.: Condens. Matter*, 18:S2829–S2847, 2006.
- [209] F. Ludwig, E. Heim, M. Schilling, and K. Enpuku. Characterization of superparamagnetic FeO nanoparticles by fluxgate magnetorelaxometry for use in biomedical applications. *J. Appl. Phys.*, 103:07A314, 2008.
- [210] D. Eberbeck, F. Wiekhorst, S. Wagner, and L. Trahms. How the size distribution of magnetic nanoparticles determines their magnetic particle imaging performance. *Appl. Phys. Lett.*, 98(18):182502, 2011.
- [211] F. Ludwig, S. Mäuselein, E. Heim, and M. Schilling. Magnetorelaxometry of magnetic nanoparticles in magnetically unshielded environment utilizing a differential fluxgate arrangement. *Rev. Sci. Instrum.*, 76:106102, 2005.
- [212] F. Ludwig, E. Heim, S. Mäuselein, D. Eberbeck, and M. Schilling. Magnetorelaxometry of magnetic nanoparticles with fluxgate magnetometers for the analysis of biological targets. *J. Magn. Magn. Mater.*, 293(1):690–695, 2005.
- [213] N. L. Adolphi, D. L. Huber, H. C. Bryant, T. C. Monson, D. L. Fegan, J. Lim, J. E. Trujillo, T. E. Tessier, D. M. Lovato, K. S. Butler, P. P. Provencio, H. J. Hathaway, S. A. Majetich, R. S. Larson, and E. R. Flynn. Characterization of single-core magnetite nanoparticles for magnetic imaging by SQUID relaxometry. *Phys. Med. Biol.*, 55(19): 5985, 2010.
- [214] H. Bryant, N. L. Adolphi, D. L. Huber, D. L. Fegan, T. C. Monson, T. E. Tessier, and E. R. Flynn. Magnetic properties of nanoparticles useful for SQUID relaxometry in biomedical applications. *J. Magn. Magn. Mater.*, 323(6):767 – 774, 2011.

- [215] X. Tan, J. S. Baras, and P. S. Krishnaprasad. Fast evaluation of demagnetizing field in three-dimensional micromagnetics using multipole approximation. In *SPIE's 7th Annual International Symposium on Smart Structures and Materials*, pages 195–201. International Society for Optics and Photonics, 2000.
- [216] P. Babinec, A. Krafčík, M. Babincová, and J. Rosenecker. Dynamics of magnetic particles in cylindrical Halbach array: implications for magnetic cell separation and drug targeting. *Med. Biol. Eng. Comput.*, 48(8):745–753, 2010.
- [217] J. S. Andreu, C. Calero, J. Camacho, and J. Faraudo. On-the-fly coarse-graining methodology for the simulation of chain formation of superparamagnetic colloids in strong magnetic fields. *Phys. Rev. E*, 85:036709, 2012.
- [218] D. Eberbeck, S. Hartwig, U. Steinhoff, and L. Trahms. Description of the magnetisation decay in ferrofluids with a narrow particle size distribution. *Magnetohydrodyn.*, 39:77–83, 2003.
- [219] U. Nowak, O. N. Mryasov, R. Wieser, K. Guslienko, and R. W. Chantrell. Spin dynamics of magnetic nanoparticles: Beyond Brown's theory. *Phys. Rev. B*, 72:172410, 2005.
- [220] L. Breth, D. Suess, C. Vogler, B. Bergmair, M. Fuger, R. Heer, and H. Brueckl. Thermal switching field distribution of a single domain particle for field-dependent attempt frequency. *J. Appl. Phys.*, 112(2):023903, 2012.
- [221] T. Taniguchi and H. Imamura. Thermal switching rate of a ferromagnetic material with uniaxial anisotropy. *Phys. Rev. B*, 85:184403, 2012.
- [222] L. C. Branquinho, M. S. Carrião, A. S. Costa, N. Zufelato, M. H. Sousa, R. Miotto, R. Ivkov, and A. F. Bakuzis. Effect of magnetic dipolar interactions on nanoparticle heating efficiency: Implications for cancer hyperthermia. *Sci. Rep.*, 3, 2013.
- [223] <http://www.ctcms.nist.gov/mumag/mumag.org.html>.
- [224] K. Gustafsson. *Control of error and convergence in ODE solvers*. PhD thesis, University of Lund, 1992.
- [225] F. Ludwig, E. Heim, D. Eberbeck, K. Schwarz, L. Trahms, and M. Schilling. Comparison and calibration of Fluxgate and SQUID magnetorelaxometry techniques for the characterization of magnetic core-shell nanoparticles. *IEEE Trans. Magn.*, 45(10):4857–4860, 2009.
- [226] J. Weizenecker, B. Gleich, J. Rahmer, H. Dahnke, and J. Borgert. Three-dimensional real-time in vivo magnetic particle imaging. *Phys. Med. Biol.*, 54:L1, 2009.
- [227] N. Inaba, H. Asanuma, S. Igarashi, S. Mori, F. Kirino, K. Koike, and H. Morita. Damping constants of Ni-Fe and Ni-Co alloy thin films. *IEEE Trans. Magn.*, 42(10):2372–2374, 2006.

- [228] S. Serrano-Guisan, H.-C. Wu, C. Boothman, M. Abid, B. S. Chun, I. V. Shvets, and H. W. Schumacher. Thickness dependence of the effective damping in epitaxial Fe<sub>3</sub>O<sub>4</sub>/MgO thin films. *J. Appl. Phys.*, 109(1):013907, 2011.
- [229] G. Wang, C. Dong, C. Jiang, G. Chai, and D. Xue. Effect of nanoparticle size on magnetic damping parameter in Co<sub>92</sub>Zr<sub>8</sub> soft magnetic films. *J. Magn. Magn. Mater.*, 324(18):2840 – 2843, 2012.
- [230] A. H. Morrish. *The physical principles of magnetism*, volume 1. 2001.
- [231] K. Butter, P. Bomans, P. Frederik, G. Vroege, and A. Philipse. Direct observation of dipolar chains in iron ferrofluids by cryogenic electron microscopy. *Nat. Mater.*, 2(2): 88–91, 2003.
- [232] S. Mørup and E. Tronc. Superparamagnetic relaxation of weakly interacting particles. *Phys. Rev. Lett.*, 72(20):3278, 1994.
- [233] O. Iglesias and A. Labarta. Magnetic relaxation in terms of microscopic energy barriers in a model of dipolar interacting nanoparticles. *Phys. Rev. B*, 70:144401, 2004.
- [234] O. Laslett, S. Ruta, R. Chantrell, J. Barker, G. Friedman, and O. Hovorka. Consistent energy barrier distributions in magnetic particle chains. *Physica B*, 486:173 – 176, 2016.
- [235] S. Bogren, A. Fornara, F. Ludwig, M. del Puerto Morales, U. Steinhoff, M. F. Hansen, O. Kazakova, and C. Johansson. Classification of magnetic nanoparticle systems: Synthesis, standardization and analysis methods in the nanomag project. *Int. J. Mol. Sci.*, 16(9):20308–20325, 2015.
- [236] F. Ludwig, H. Remmer, C. Kuhlmann, T. Wawrzik, H. Arami, R. M. Ferguson, and K. M. Krishnan. Self-consistent magnetic properties of magnetite tracers optimized for magnetic particle imaging measured by ac susceptometry, magnetorelaxometry and magnetic particle spectroscopy. *J. Magn. Magn. Mater.*, 360:169 – 173, 2014.
- [237] J. Dieckhoff, M. Schilling, and F. Ludwig. Fluxgate based detection of magnetic nanoparticle dynamics in a rotating magnetic field. *Appl. Phys. Lett.*, 99(11):112501, 2011.
- [238] R. Kötzitz, P. Fannin, and L. Trahms. Time domain study of Brownian and Néel relaxation in ferrofluids. *J. Magn. Magn. Mater.*, 149(1-2):42–46, 1995.
- [239] F. Ludwig, O. Kazakova, L. Fernandez Barquin, A. Fornara, L. Trahms, U. Steinhoff, P. Svedlindh, E. Wetterskog, Q. Pankhurst, P. Southern, P. Morales, M. Fougat Hansen, C. Frandsen, E. Olsson, S. Gustafsson, N. Gehrke, K. Ludtke-Buzug, C. Gruttner, C. Jonasson, and C. Johansson. Magnetic, structural, and particle size analysis of single- and multi-core magnetic nanoparticles. *IEEE Trans. Magn.*, 50(11):1–4, 2014.

- [240] O. Laslett, S. Ruta, J. Barker, R. Chantrell, G. Friedman, and O. Hovorka. Interaction effects enhancing magnetic particle detection based on magneto-relaxometry. *Appl. Phys. Lett.*, 106(1):012407, 2015.
- [241] F. Ahrentorp, A. Astalan, J. Blomgren, C. Jonasson, E. Wetterskog, P. Svedlindh, A. Lak, F. Ludwig, L. J. van IJzendoorn, F. Westphal, C. Grüttner, N. Gehrke, S. Gustafsson, E. Olsson, and C. Johansson. Effective particle magnetic moment of multi-core particles. *J. Magn. Magn. Mater.*, 380:221 – 226, 2015.
- [242] M. Bode, O. Pietzsch, A. Kubetzka, and R. Wiesendanger. Shape-dependent thermal switching behavior of superparamagnetic nanoislands. *Phys. Rev. Lett.*, 92:067201, 2004.
- [243] W. Wernsdorfer, B. Doudin, D. Mailly, K. Hasselbach, A. Benoit, J. Meier, J. P. Ansermet, and B. Barbara. Nucleation of magnetization reversal in individual nanosized nickel wires. *Phys. Rev. Lett.*, 77(9):1873–1876, 1996.
- [244] T. Cheung, K. Kavanagh, and U. Ribary. A new technique for magnetic nanoparticle imaging using magnetoencephalography frequency data. In S. Supek and A. Susac, editors, *17th International Conference on Biomagnetism Advances in Biomagnetism - Biomag2010*, volume 28 of *IFMBE Proceedings*, pages 443–446. Springer Berlin Heidelberg, 2010.
- [245] S. Machlup. Noise in semiconductors: Spectrum of a two-parameter random signal. *J. Appl. Phys.*, 25(3):341–343, 1954.
- [246] M. B. Weissman.  $1/f$  noise and other slow, nonexponential kinetics in condensed matter. *Rev. Mod. Phys.*, 60(2):537, 1988.
- [247] J. Bork, H. Hahlbohm, R. Klein, and A. Schnabel. The 8-layered magnetically shielded room of the PTB: Design and construction. In *Biomag2000, Proc. 12th Int. Conf. on Biomagnetism*, pages 970–73. Espoo, Finland, 2001.
- [248] M. Helsen. *Radial spin wave modes in magnetic vortex structures*. PhD thesis, Ghent University, 2015.
- [249] S. Neveu, A. Bee, M. Robineau, and D. Talbot. Size-selective chemical synthesis of tartrate stabilized cobalt ferrite ionic magnetic fluid. *J. Colloid Interface Sci.*, 255(2): 293–298, 2002.
- [250] B. Fischer, L. Mao, M. Gungormus, C. Tamerler, M. Sarikaya, and H. Koser. Ferro-microfluidic device for pathogen detection. In *Nano/Micro Engineered and Molecular Systems, 2008. NEMS 2008. 3rd IEEE International Conference on*, pages 907–910, 2008.
- [251] G. S. D. Beach, C. Nistor, C. Knutson, M. Tsoi, and J. L. Erskine. Dynamics of field-driven domain-wall propagation in ferromagnetic nanowires. *Nat. Mater.*, 4:741–744, 2005.

- 
- [252] E. Martinez, S. Emori, N. Perez, L. Torres, and G. S. D. Beach. Current-driven dynamics of Dzyaloshinskii domain walls in the presence of in-plane fields: Full micromagnetic and one-dimensional analysis. *J. Appl. Phys.*, 115(21):213909, 2014.
- [253] O. Boulle, J. Kimling, P. Warnicke, M. Kläui, U. Rüdiger, G. Malinowski, H. J. M. Swagten, B. Koopmans, C. Ulysse, and G. Faini. Nonadiabatic spin transfer torque in high anisotropy magnetic nanowires with narrow domain walls. *Phys. Rev. Lett.*, 101: 216601, 2008.
- [254] J. Rahmer, A. Halkola, B. Gleich, I. Schmale, and J. Borgert. First experimental evidence of the feasibility of multi-color magnetic particle imaging. *Phys. Med. Biol.*, 60(5):1775, 2015.
- [255] K. Nakata, Y. Hu, O. Uzun, O. Bakr, and F. Stellacci. Chains of superparamagnetic nanoparticles. *Adv. Mater.*, 20(22):4294–4299, 2008.
- [256] M. Helsen, A. Gangwar, A. Vansteenkiste, and B. Van Waeyenberge. Magneto-optical spectrum analyzer. *Rev. Sci. Instrum.*, 85(8):083902, 2014.
- [257] J. C. Butcher. *Numerical methods for ordinary differential equations*. John Wiley & Sons, 2008.
- [258] L. Euler. *Institutiones calculi integralis*, volume 3. 1768-1770.
- [259] H. Lamba. An adaptive timestepping algorithm for stochastic differential equations. *J. Comp. Appl. Math.*, 161(2):417 – 430, 2003.
- [260] K.-D. Lee, Y. M. Kim, H.-S. Song, C.-Y. You, J.-I. Hong, and B.-G. Park. Speed and stability of magnetic chiral motion in a chain of asymmetric thin nanodots. *Appl. Phys. Expr.*, 8(10):103003, 2015.



---

## List of constants and symbols

---

### List of constants

$e$	electron charge	$1.6022 \times 10^{-19} \text{ C}$
$\gamma$	gyromagnetic ratio	$1.76086 \times 10^{11} \text{ rad/Ts}$
$\gamma_0$	$\mu_0 \gamma$	$2.21 \times 10^5 \text{ m/As}$
$\hbar$	reduced Planck constant	$1.0546 \times 10^{-34} \text{ Js}$
$k_B$	Boltzmann constant	$1.3087 \times 10^{-23} \text{ J/K}$
$m_e$	electron mass	$9.109 \times 10^{-31} \text{ kg}$
$\mu_0$	vacuum permeability	$4\pi \times 10^{-7} \text{ Tm/A}$
$\mu_B$	Bohr magneton	$9.274 \times 10^{-24} \text{ Am}^2$

### List of symbols

#### Mathematical operators

$\nabla a$	gradient
$\langle a \rangle$	time average or ensemble average
$\langle ab \rangle$	correlation
$\langle\langle a \rangle\rangle$	spatial average over computational domain
$\dot{a}$	time derivative
$\ a\ $	norm

#### Roman symbols

$A_{\text{ex}}$	exchange stiffness constant
$b$	$\frac{P\mu_B}{eM_s(1+\beta^2)}$
$\mathbf{B}$	magnetic flux

$\mathbf{c}_{1,2,3}$	cubic anisotropy axes
$D$	diameter
$D_c$	core diameter
$D_h$	hydrodynamic diameter
$\mathcal{D}$	geometrical factor used in the derivation of the 1D-model
$DF$	dilution factor
$e$	electron charge
$\mathbf{e}_N$	unit vector normal to a surface
$\mathbf{e}_{x,y,z}$	unit vectors in a Cartesian coordinate system
$E$	energy
$E_{\text{anisotropy}}$	anisotropy energy
$E_{\text{exchange}}$	exchange energy
$E_{\text{magnetostatic}}$	magnetostatic energy
$E_{\text{total}}$	total energy
$E_{\text{Zeeman}}$	Zeeman energy
$\mathcal{E}$	energy density
$\mathcal{E}_{\text{anisotropy}}$	anisotropy energy density
$\mathcal{E}_{\text{exchange}}$	exchange energy density
$\mathcal{E}_{\text{magnetostatic}}$	magnetostatic energy density
$\mathcal{E}_{\text{Zeeman}}$	Zeeman energy density
$f$	frequency or rate
$f_0$	attempt frequency
$f_{\text{dep}}$	depinning force
$g$	Landé factor
$g(\nu)$	a rate dependent function
$h$	notation for timestep used in <a href="#">appendix A</a>
$\hbar$	reduced Planck constant
$\hat{\mathcal{H}}_{\text{exchange}}$	Heisenberg exchange Hamiltonian
$\mathbf{H}_{\text{ext}}$	external magnetic field
$H_{\text{ext},x,y,z}$	x, y and z component of the external magnetic field
$\mathbf{H}_{\text{anisotropy}}$	anisotropy field
$\mathbf{H}_{\text{demag}}$	demagnetising field
$\mathbf{H}_{\text{eff}}$	effective field
$H_K$	$2K/M_s$
$\mathbf{H}_{\text{th}}$	thermal field
$H_U$	magnetic field due to the potential energy profile
$H_x$	total x-component of all magnetic fields

$\mathbf{J}$	current density
$J_{x,y,z}$	x, y and z components of the current density $\mathbf{J}$
$\mathcal{J}$	quantum mechanical exchange interaction strength
$k_B$	Boltzmann constant
$K$	anisotropy constant
$K_s$	surface anisotropy constant
$l$	angular momentum
$l_{\text{ex}}$	exchange length
$L_{x,y,z}$	the x, y and z component of the size of the computational domain
$\mathcal{L}$	Langevin function
$m$	domain wall mass
$\mathbf{m}$	reduced magnetisation vector field
$m_D$	Döring mass
$m_e$	electron mass
$m_{x,y,z}$	the x,y and z component of $\mathbf{m}$ , respectively
$M$	$= \ \mathbf{M}\ $ , magnetisation
$\mathbf{M}$	magnetisation vector field
$M_0$	initial magnetisation
$M_s$	saturation magnetisation
$M_{x,y,z}$	the x,y and z component of $\mathbf{M}$ , respectively
$\mathfrak{M}$	magnetic moment
$\mathcal{N}$	demagnetising tensor
$\mathcal{N}_{\text{eff},x,y,z}$	effective demagnetising factors
$\mathcal{N}_{x,y,z}$	demagnetising factors
$\mathcal{O}$	order
$p$	viscosity
$P$	spin polarisation
$P(V)$	volume distribution
$P_{\text{switch,not}}$	the probability (not) to switch
$P_{\text{pin}}$	pinning probability
$P_{\text{u,d}}$	probability to find a moment in the up ( $u$ ) or down ( $d$ ) direction
$q$	$\frac{2k_B T \alpha}{M_s \gamma \mu_0^2 V}$
$r$	nanoparticle radius

$r^*$	a threshold length used in the calculation of the magnetostatic interaction in <a href="#">Vinamax</a>
$\mathbf{r}$	vector distance
$R$	the fraction between two volumes used in <a href="#">Chapter 4</a>
$R(s)$	autocorrelation at distance $s$
$\mathbf{R}_{\text{CM}}$	centre of magnetisation
$S$	surface
$S(f)$	noise power spectrum
$t$	time
$T$	temperature
$T_c$	critical temperature for superconductivity
$T_{\text{dep}}$	depinning temperature
$\mathbf{u}$	uniaxial anisotropy axis
$U$	potential energy profile
$v$	average velocity
$V$	volume
$V_c$	core volume
$V_h$	hydrodynamic volume
$x$	domain wall position
$\dot{x}$	instantaneous velocity
$\ddot{x}$	instantaneous acceleration
$\mathcal{Z}$	partition function

## Greek symbols

$\alpha$	Gilbert damping parameter
$\beta$	degree of non-adiabaticity
$\gamma$	gyromagnetic ratio
$\gamma_0$	$\mu_0\gamma$
$\gamma_c$	exponent used to describe the autocorrelation of the energy profile
$\Gamma$	measure for friction in domain wall motion
$\delta_{\text{D}}$	Dirac delta function
$\langle\langle\delta\rangle\rangle$	$\langle\langle m_y^2 + m_z^2 \rangle\rangle$ , a measure for the domain wall width

$\langle\langle\delta_{\text{eff}}\rangle\rangle$	effective domain wall width
$\Delta$	difference/deviation
$\Delta_{1\text{D}}$	domain wall width in the 1D-model
$\Delta E$	energy barrier
$\Delta t$	time step
$\epsilon$	error size
$\varepsilon_c$	standard deviation of potential energy profile
$\eta$	a random number with average 0 and standard deviation 1
$\boldsymbol{\eta}$	vector containing 3 random numbers $\eta$
$\theta$	spherical coordinate angle
$\Theta$	prefactor related to thermal fluctuations
$\lambda$	Landau-Lifshitz damping parameter
$\mu$	mean of the lognormal distribution
$\mu_0$	vacuum permeability
$\mu_{\text{B}}$	Bohr magneton
$\mu_{\text{creep}}$	creep exponent
$\nu_{\text{B}}$	Brownian relaxation rate
$\nu_{\text{eff}}$	effective relaxation rate
$\nu_{\text{N}}$	Néel relaxation rate
$\xi$	$\frac{\mu_0 M_s V H_{\text{ext}}}{k_{\text{B}} T}$
$\Xi$	prefactor related to current density
$\rho$	a length used in the calculation of the magnetostatic interaction in <a href="#">Vinamax</a>
$\sigma$	logarithm of the standard deviation in the lognormal distribution
$\hat{\sigma}$	quantum mechanical electron spin
$\Sigma$	disorder density
$\tau$	error tolerance
$\tau_0$	$\frac{1}{2f_0}$
$\tau_{\text{B}}$	Brownian relaxation time constant
$\tau_{\text{N}}$	Néel relaxation time constant
$\tau_{\text{N}0}$	relaxation time constant without interactions
$v$	A random number, uniformly distributed in $[0.0, 1.0)$

---

$\phi$	spherical coordinate angle or local out-of-plane angle of the magnetisation
$\phi_N$	the fraction of particles relaxing by the Néel mechanism
$\Phi_{1D}$	out-of-plane tilting angle of the domain wall in the 1D-model
$\chi_a$	susceptibility

- 1D-model, [35](#)
- adaptive time step, [138](#)
- adiabatic, [22](#)
- anisotropy, [15](#)
- anisotropy energy, [18](#)
- antivortex core, [32](#)
- antivortex domain wall, [32](#)
- asymmetric transverse domain walls, [31](#)
- Barkhausen, [11](#)
- Barkhausen noise, [11](#)
- Bean, [96](#)
- biomedical applications, [97](#)
- bistable regime, [87](#)
- Bitter, [11](#)
- Bloch, [11](#)
- Bloch wall, [30](#)
- blocked, [97](#)
- blocking temperature, [97](#)
- Bogacki-Shampine method, [138](#)
- Bohr magneton, [9](#)
- Brillouin, [95](#)
- Brown, R., [96](#)
- Brown, W. F., [11](#)
- Brownian motion, [96](#)
- Brownian relaxation, [96](#)
- Brownian relaxation time, [96](#)
- brute force method, [102](#)
- bubble memory, [48](#)
- Butcher, [141](#)
- Butcher tableaux, [141](#)
- chirality, [33](#)
- circulation, [32](#)
- cluster moment superposition model, [117](#)
- computers, [12](#)
- conservation of energy, [20](#)
- creep, [78](#)
- cubic anisotropy, [16](#)
- Curie temperature, [24](#)
- current-driven domain wall motion, [42](#)
- Döring, [12](#)
- damping, [12](#)
- degree of non-adiabaticity, [22](#)
- demagnetising factors, [19](#)
- demagnetising field, [18](#)
- depinning current threshold, [43](#)
- diffusion, [74](#)
- dipole approximation method, [102](#)
- dipole-dipole interaction, [18](#)
- disease detection, [97](#)
- domain wall mass, [69](#)
- domain walls, [30](#)
- domain-wall logic, [47](#)
- domains, [11](#)
- Dormand-Prince method, [140](#)
- Dzyaloshinskii-Moriya interaction, [19](#)
- edge charges, [32](#)

- edge roughness, 57
- effective field, 19
- effective wall width, 73
- Einstein, 96
- electron, 9
- Electron Paramagnetic Resonance, 98
- electronics, 46
- energy densities, 14
- energy profile, 68
- equation of motion, 69
- Euler, 137
- Euler backward, 138
- Euler forward, 138
- Euler's method, 137
- exchange energy, 14
- exchange interaction, 14
- exchange length, 15
- exchange stiffness constant, 15
- explicit solver, 138
- extrinsic pinning, 58
  
- fast Fourier transform, 25
- fast multipole method, 25
- fermions, 10
- ferromagnetic resonance, 98
- field-driven domain wall motion, 39
- field-like torque, 22
- finite difference cells, 24
- first-same-as-last, 138
- fluctuation-dissipation theorem, 22
- flux loops, 18
- flux-closed magnetisation, 28
- fourth order Runge-Kutta method, 140
- Frenkel and Dorfman, 92
- frustration, 135
  
- giant magnetoresistive effect, 21
- Gilbert, 12
- Gilbert damping parameter, 20
- grain boundaries, 53
- graphics cards, 12
- Guillaud, 92
- gyromagnetic ratio, 9
  
- handedness, 33
- hard materials, 17
- head-to-head, 31
- Heisenberg, 11
- Heun's method, 138
- high-friction limit, 69
- hotspin, 24
- hyperthermia, 98
- hysteresis loop, 115
  
- implicit solvers, 138
- intrinsic pinning, 43
  
- Joule heating, 48
- jump noise process, 24
  
- Kittel, 92
  
- Landau and Lifshitz, 11
- Landau state, 28
- Landau-Lifshitz equation, 20
- Landau-Lifshitz-Baryakhtar equation, 24
- Landau-Lifshitz-Bloch equation, 24
- Landau-Lifshitz-Gilbert equation, 20
- Langevin, 95
- Langevin function, 95
- Larmor frequency, 20
- locked state, 86
- lognormal distribution, 105
- long-range interaction, 18
- Lorentzian, 125
- Lyberatos, 22
  
- magnetic nanoparticles, 91
- Magnetic Particle Imaging, 98
- magneto-optical spectrum analyser, 135
- magnetocrystalline anisotropy, 17
- magnetoelastic energy, 19
- magnetorelaxometry, 98
- magnetostatic energy, 18
- magnetostatic field, 18
- magnetostatic interaction, 18
- magnetostriction, 19
- material grains, 53



- Maxwell's equations, 18
- micromagnetic simulations, 24
- micromagnetics, 11
- micromagnetism, 11
- moment superposition model, 113
- monodomain, 29
- multi-colour, 134
- multicore particles, 91
- MuMax3, 25
  
- Néel, 92
- Néel relaxation, 97
- Néel relaxation time, 97
- Néel wall, 30
- nanostrips, 30
- nanowires, 30
- noise spectrum, 124
- non-adiabatic, 22
- nonzero temperatures, 22
  
- orbital angular momentum, 9
- Ordinary Differential Equations, 137
  
- paramagnetism, 10
- Parkin, 47
- Pauli's exclusion principle, 10
- permalloy, 17
- perpendicular magnetic anisotropy, 17
- pinning potential, 50
- PMA, 17
- polarity, 32
- polycrystalline, 53
- potential wells, 50
  
- quenched, 10
  
- racetrack memory, 47
- Rashba effect, 63
- real-world applications, 46
- running state, 86
  
- saturation magnetisation, 14
- Schryer and Walker, 35
- seeds, 53
- seventh order Fehlberg method, 141
  
- shape anisotropy, 19
- single core particles, 91
- single-domain, 29
- single-domain particles, 91
- sixth order Fehlberg method, 140
- Sixtus and Tonks, 11
- skyrmion, 34
- soft material, 17
- solvers, 137
- spin, 10
- spin angular momentum, 10
- spin ices, 135
- spin polarisation, 21
- spin-Hall effect, 63
- spin-polarised current, 21
- spin-transfer torque, 21
- spintronics, 46
- stochastic field, 104
- stochastic switching, 104
- Stoner and Wolfarth, 92
- superparamagnetic limit, 98
- superparamagnetism, 96
- surface anisotropy, 17
- surface roughness, 57
- symmetric transverse walls, 31
  
- tail-to-tail, 31
- targeted drug delivery, 97
- thermal fluctuations, 22
- Thiaville, 35
- third order Runge-Kutta method, 140
- topological charge, 31
- transverse domain wall, 31
- two-state approximation, 95
  
- uniaxial anisotropy, 15
- unpaired electrons, 10
  
- vacuum permeability, 15
- Vinamax, 100
- Voronoi cell, 54
- Voronoi centres, 54
- Voronoi tessellation, 54
- vortex core, 32

vortex domain wall, [32](#)

vortex state, [28](#)

Walker breakdown, [40](#)

Weiss, [11](#)

Weiss molecular field, [11](#)

winding number, [31](#)

Zeeman energy, [15](#)

Zhang and Li, [22](#)

## Papers

- **J. Leliaert**, B. Van de Wiele, A. Vansteenkiste, L. Laurson, G. Durin, L. Dupré, and B. Van Waeyenberge. A numerical approach to incorporate intrinsic material defects in micromagnetic simulations. *J. Appl. Phys.*, 115(17):17D102, 2014.
- **J. Leliaert**, B. Van de Wiele, A. Vansteenkiste, L. Laurson, G. Durin, L. Dupré, and B. Van Waeyenberge. Influence of material defects on current-driven vortex domain wall mobility. *Phys. Rev. B*, 89:064419, 2014.
- **J. Leliaert**, B. Van de Wiele, A. Vansteenkiste, L. Laurson, G. Durin, L. Dupré, and B. Van Waeyenberge. Current-driven domain wall mobility in polycrystalline permalloy nanowires: A numerical study. *J. Appl. Phys.*, 115(23):233903, 2014.
- **J. Leliaert**, A. Coene, G. Crevecoeur, A. Vansteenkiste, D. Eberbeck, F. Wiekhorst, B. Van Waeyenberge, and L. Dupré. Regarding the Néel relaxation time constant in magnetorelaxometry. *J. Appl. Phys.*, 116(16):163914, 2014.
- **J. Leliaert**, A. Vansteenkiste, A. Coene, L. Dupré, and B. Van Waeyenberge. Vinamax: a macrospin simulation tool for magnetic nanoparticles. *Med. Biol. Eng. Comput.*, 53(4):309–317, 2015.
- **J. Leliaert**, B. Van de Wiele, J. Vandermeulen, A. Coene, A. Vansteenkiste, L. Laurson, G. Durin, B. Van Waeyenberge, and L. Dupré. Thermal effects on transverse domain wall dynamics in magnetic nanowires. *Appl. Phys. Lett.*, 106(20):202401, 2015.
- **J. Leliaert**, A. Coene, M. Liebl, D. Eberbeck, U. Steinhoff, F. Wiekhorst, B. Fischer, L. Dupré, and B. Van Waeyenberge. Thermal magnetic noise spectra of nanoparticle ensembles. *Appl. Phys. Lett.*, 107(22):222401, 2015.
- **J. Leliaert**, B. Van de Wiele, A. Vansteenkiste, L. Laurson, G. Durin, L. Dupré, and B. Van Waeyenberge. Creep turns linear in narrow ferromagnetic nanostrips. *Sci. Rep.*, 6:20472, 2016.
- A. Vansteenkiste, **J. Leliaert**, M. Dvornik, M. Helsen, F. Garcia-Sanchez, and B. Van Waeyenberge. The design and verification of MuMax3. *AIP Adv.*, 4(10):107133, 2014.

- A. Coene, G. Crevecoeur, **J. Leliaert**, and L. Dupré. Toward 2D and 3D imaging of magnetic nanoparticles using EPR measurements. *Med. Phys.*, 42(9):5007–5014, 2015.
- A. Coene, **J. Leliaert**, L. Dupré, and G. Crevecoeur. Quantitative model selection for enhanced magnetic nanoparticle imaging in magnetorelaxometry. *Med. Phys.*, 42(12):6853–6862, 2015.
- B. Van de Wiele, **J. Leliaert**, K. J. A. Franke, and S. van Dijken. Electric-field-driven dynamics of magnetic domain walls in magnetic nanowires patterned on ferroelectric domains. *New J. Phys.*, 18(3):033027, 2016.

### Presentations

- **J. Leliaert**, B. Van de Wiele, A. Vansteenkiste, L. Laurson, G. Durin, B. Van Waeyenberge and L. Dupré Influence of disorder on vortex domain wall mobility in magnetic nanowires *9th International symposium on hysteresis modelling and micromagnetics*, Taormina (Italy), May 15th, 2013.
- **J. Leliaert**, B. Van de Wiele, A. Vansteenkiste, L. Laurson, G. Durin, L. Dupré and B. Van Waeyenberge A numerical approach to incorporate intrinsic material defects in micromagnetic simulations *58th Annual conference on Magnetism and Magnetic Materials*, Denver, Colorado (USA), November 5th, 2013.
- **J. Leliaert** Including disorder in micromagnetic simulations: The road to imperfection *Il tempo della scienza, seminari tecnici*, Istituto Nazionale di Ricerca Metrologica, Torino (Italy), February 12th, 2014.
- A. Coene, G. Crevecoeur, **J. Leliaert** and L. Dupré Quantitative comparison of magnetorelaxometry models *15th German ferrofluid workshop*, Rostock (Germany), June 16th, 2015 .
- **J. Leliaert** The underlying physics of magnetic nanoparticles *Kolloquium der Abteilung 8*, Physikalisch-Technische Bundesanstalt, Berlin (Germany), August 13th, 2015.
- **J. Leliaert** Creep turns linear in narrow ferromagnetic nanostrips *PhD Symposium Faculty of Sciences*, Gent (Belgium), March 17th, 2016.

### Other

- **J. Leliaert** Understanding the influence of material defects: The key to future technologies *14th FEA PhD Symposium*, Gent (Belgium), December 6th, 2013 (Poster).
- **J. Leliaert**, A. Coene, G. Crevecoeur, L. Dupré and B. Van Waeyenberge Dipolar interactions between magnetic nanoparticles in magnetorelaxometry *19th International conference on biomagnetism*, Halifax (Canada), August 25th, 2014 (Poster).

- **J. Leliaert**, A. Coene, A. Vansteenkiste, G. Crevecoeur, B. Van Waeyenberge and L. Dupré Vinamax : a simulation tool for nanoparticle magnetisation dynamics *15th German ferrofluid workshop*, Rostock (Germany), June 16th, 2015 (Poster).